

Activity-dependent plasticity in the developing cortex

Jan Hendrik Kirchner

Vollständiger Abdruck der von der TUM School of Life Sciences der Technischen Universität München zur Erlangung des akademischen Grades eines

Doktors der Naturwissenschaften (Dr. rer. nat.)

genehmigten Dissertation.

Vorsitz: Prof. Dr. Mathias Wilhelm

Prüfende der Dissertation:

1. Prof. Julijana Gjorgjieva, Ph.D.
2. Prof. Dr. Simon N. Jacob
3. Prof. Dr. Matthias Kaschube

Die Dissertation wurde am 18. 05. 2022 bei der Technischen Universität München eingereicht und durch die TUM School of Life Sciences am 08.11.2022 angenommen.

Jan Hendrik Kirchner. *Activity-dependent plasticity in the developing cortex*. Dissertation, 2022.

Summary

The brain of a newborn animal needs to undergo an intricate developmental process involving multifold interactions of intrinsic and extrinsic factors before it can reliably instruct the animal's behavior in its environment. One central factor involved in the wiring of developing neural circuits is neural activity produced in the absence of sensory stimulation, called spontaneous activity. While we know that spontaneous activity is necessary for the formation of functional circuits through synaptic plasticity, our understanding of the mechanisms underlying the activity-dependent development of the brain remains limited.

In my dissertation, I investigate the interplay between spontaneous activity and synaptic plasticity across postnatal development at multiple scales: on the molecular, dendritic and network level. I used mathematical and computational modeling on the molecular and dendritic level to investigate the emergence of synaptic organization on individual developing neurons. The model revealed that an anatomical argument is sufficient to explain qualitatively different types of synaptic organization in different species. In collaboration with Dr. Marina Wosniack, we developed a computational model and performed data analysis of calcium imaging data to understand the adaptation of spontaneous activity at the level of neural circuits over prolonged developmental timescales. Using the model, we can explain how distinct types of spontaneous activity can contribute to circuit maturation. In collaboration with Dr. Paloma Maldonado, we examined the impact of the hormone oxytocin, released during maternal bonding and care, on the dynamics of spontaneous activity in the developing visual and somatosensory cortex through data analysis and computational modeling. Our model allowed us to synthesize insights from multiple sets of experiments into a consistent picture. Synthesizing this work, I highlight commonalities and differences and discuss the impact of the studies' results on the development of neural circuits and their function in general.

Contents

Summary	3
1 Introduction	7
Molecular level: Neurotrophic factors as key molecules for determining neuronal and synaptic fate	9
Dendrite level: Emergence of synaptic organization and dendritic maps during development	10
Circuit level: Structured spontaneous activity drives circuit maturation .	12
Behavioral level: Neuromodulatory control over spontaneous activity . .	15
2 Methods and mathematical framework	19
Molecular level: Neurotrophin plasticity model	19
Molecular level/Dendrite level: Generalized neurotrophin-inspired model	22
Dendrite level: From local dendritic to global somatic activity	22
Dendrite level/Circuit level: Backpropagating action potentials as global feedback signals	25
Circuit level/Behavioral level: GABAergic inputs control activity in a recurrent network	26
3 Results	31
Emergence of local and global synaptic organization on cortical dendrites	32
Emergence of synaptic organization and computation in dendrites	51
Adaptation of spontaneous activity in the developing visual cortex	62
Oxytocin shapes spontaneous activity patterns in the developing visual cortex	89
4 Discussion	109
Open Questions and Outlook	110

Contents

Impact of a single gene mutation on circuit structure and spontaneous activity in the developing cortex	111
Activity-dependent dendrite growth through formation and removal of synapses	113
Correlated spontaneous activity drives emergence of multi-sensory integration in the developing higher-order cortex	116
Simplicity in the developing brain	118
5 List of scientific communications	133
6 Acknowledgments	135
7 Appendix	137
Emergence of local and global synaptic organization on cortical dendrites	137
Emergence of synaptic organization and computation in dendrites	137
Adaptation of spontaneous activity in the developing visual cortex	137
Oxytocin Shapes Spontaneous Activity Patterns in the Developing Visual Cortex by Activating Somatostatin Interneurons	137

1 Introduction

When an animal is born, complex interactions between the animal's genes and its environment set up the neural circuitry that allows the animal to respond flexibly in different situations (Price *et al.*, 2017). The developing brain's genes do not specify every detail of how neurons ought to connect to produce an appropriate circuit; instead, they enable a large number of *potential* connections of which only a subset is realized (Price *et al.*, 2017; Witvliet *et al.*, 2021). The two major subtypes of neurons, excitatory and inhibitory, mature in synchrony to eventually establish a tight balance that is important for the brain's proper functioning (Naskar *et al.*, 2019; Okun *et al.*, 2008a). Neurons can form synapses throughout development when they come into contact with each other and the stability of these connections depends largely on extrinsic factors (Kirchner *et al.*, 2021; Lohmann *et al.*, 2005; Winnubst *et al.*, 2015). A major focus of experimental work has been identifying the extrinsic signals influencing circuit formation to understand how they can produce both normal function and pathology (El-Boustani *et al.*, 2018; Harward *et al.*, 2016; Hedrick *et al.*, 2016; Kleindienst *et al.*, 2011; Niculescu *et al.*, 2018; Winnubst *et al.*, 2015).

There are many extrinsic factors affecting development, including molecular signals exchanged between cells, neural activity patterns produced by local circuits or propagated from distinct brain regions, and modulatory signals reflecting the animal's state (Price *et al.*, 2017) (Fig. 1.1). Analyzing the contributions of individual extrinsic factors is complicated by multi-level interactions across the different levels of organization. For example, a single mutation in the FMR1 gene leads to subtle differences in circuit wiring and intrinsic properties of neurons (Bureau *et al.*, 2008; La Fata *et al.*, 2014), which in turn affect neural activity during early development (Cheyne *et al.*, 2019; Gonçalves *et al.*, 2013). These subtle differences might then amplify over time to contribute to more striking variations at the circuit level,

1 Introduction

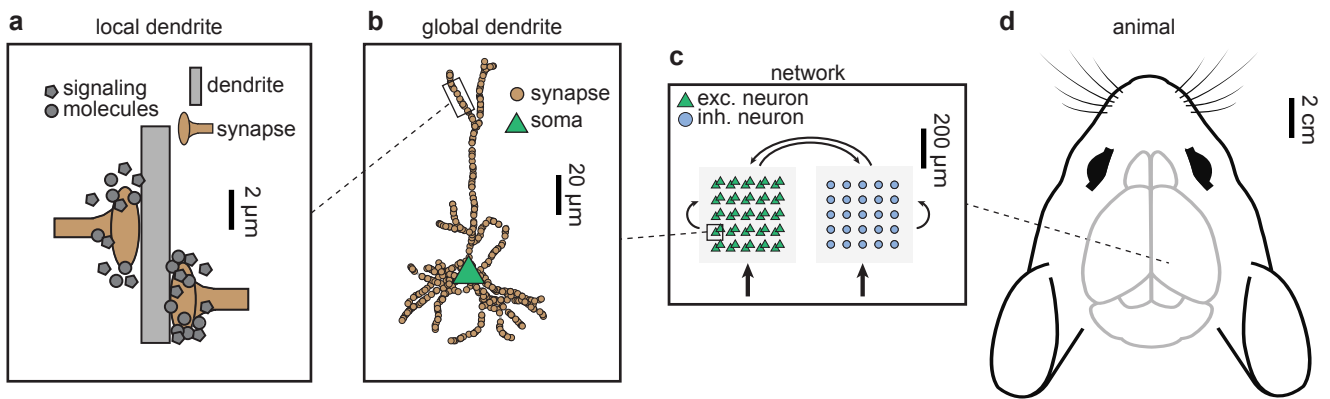


Figure 1.1: Investigating neuroscience questions at multiple interacting levels of abstraction. (a–d) Local dendritic level where nearby synapses interact through signaling molecules (a), global cellular level where signaling occurs between dendrites and the soma (b), network level where neural dynamics result from interactions between excitatory and inhibitory neurons (c), and animal level where network interactions produce behavior (d). Scale bars indicate orders of magnitude.

eventually leading to a wide range of altered behavioral characteristics of the autism spectrum disorder (Schneider *et al.*, 2009).

Disentangling the multi-level interactions driving circuit development requires systematic analysis of their relationships. While the description of neural processes exclusively in terms of their molecular constituents is the most accurate, its use would be as limited as that of Borges' map of the empire that is the size of the empire (Abbott, 2008; Borges *et al.*, 1946). To make statements that generalize beyond the particular model system at hand, we want to construct models that abstract away details that are not relevant to our particular questions (Levenstein *et al.*, 2020). Computational neuroscience aims to uncover the principles governing the development, structure, dynamics, and function of the nervous system through the use of computational and mathematical modeling (Dayan *et al.*, 2005). By using computational models capturing the essential properties of a complex system, computational neuroscience can bridge the gaps between research across different animal models, different experimental paradigms, and different scales of magnification (Marder, 2020). In the following sections, we explain how modeling at the level of molecular factors, cell properties, circuit activity, and behavior can help us understand neural circuit development and function.

Molecular level: Neurotrophic factors as key molecules for determining neuronal and synaptic fate

Out of a plethora of molecular factors involved in the development of the brain, the brain-derived neurotrophic factor (BDNF) stands out as one of the most versatile (Lu *et al.*, 2005). BDNF occurs in very small amounts in the brain but still exerts powerful control over brain development (Barde *et al.*, 1982). Deducing the amino acid sequence and cloning BDNF (Harward *et al.*, 2016), and continuously improving fluorescent sensors for BDNF and its receptor, Tropomyosin receptor kinase B (TrkB), (Leibrock *et al.*, 1989) has provided exciting insight into its action on developing neurons.

Similar to other signalling molecules involved in controlling cell development, BDNF is initially synthesized in an immature form (proBDNF), which binds primarily to the p75^{NTR} receptor (Yang *et al.*, 2009) (Fig. 1.2a). BDNF concentration varies with age (Katoh-Semba *et al.*, 1997; Yang *et al.*, 2009) and the relative balance between BDNF and proBDNF dynamically adapts to different developmental stages (Perovic *et al.*, 2013; Yang *et al.*, 2009). Mature BDNF promotes the survival of neurons, the growth of dendrites, and the formation and strengthening of synapses via TrkB signaling (Harward *et al.*, 2016; Hedrick *et al.*, 2016; Kowiański *et al.*, 2018). Intriguingly, its immature form, proBDNF, instead induces neural apoptosis, shrinkage of dendrites, and the removal or weakening of synapses via the p75^{NTR} signaling (Kowiański *et al.*, 2018; Teng *et al.*, 2005; Woo *et al.*, 2005) (Fig. 1.2b,c).

The antagonistic relationship between BDNF and proBDNF enables fine-grained, dynamic control over circuit development via regulating the local concentration of proBDNF and BDNF. In the developing circuit, both proBDNF and BDNF are secreted into extracellular space following neural activity, where proBDNF cleaving enzymes can further cleave proBDNF into BDNF (Lee *et al.*, 2001; Yang *et al.*, 2009) (Fig. 1.2b). Importantly, the amount of cleaving depends on neural activity (Je *et al.*, 2012). Consequently, the balance between proBDNF and BDNF dynamically adapts to the recent activation of a synapse, raising the possibility that proBDNF and BDNF might act as powerful levers for the activity-dependent sculpting of developing circuits (Lu *et al.*, 2014; Nagappan *et al.*, 2009). In fact, several recent

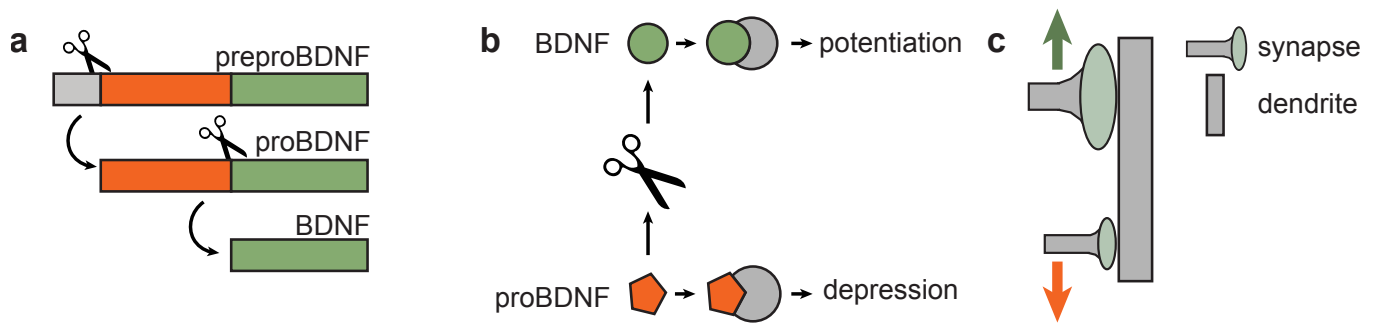


Figure 1.2: Push-pull interactions between the immature and mature forms of the brain-derived neurotrophic factor (BDNF). (a) Schematic illustrating the cleaving process (indicated by scissor) of the inactive preproBDNF into immature BDNF (proBDNF) and finally into mature BDNF. (b,c) Illustration of push-pull interactions between proBDNF and BDNF (b), which induce synaptic depression via activating the $p75^{\text{NTR}}$ receptor and potentiation via activating the TrkB receptor (c). Schematic adapted from (Kirchner *et al.*, 2021).

studies have implicated proBDNF and BDNF as central actors in controlling synaptic plasticity on developing dendrites (Kleindienst *et al.*, 2011; Niculescu *et al.*, 2018; Winnubst *et al.*, 2015).

Despite abundantly available experimental data on the action of neurotrophic factors, our understanding of their functional role in synaptic plasticity remains fragmented (Laviv *et al.*, 2021; Park *et al.*, 2013). In particular, we lack insight into how neurotrophic factors control the fate of individual synapses and dendrites. To address this question, we used computational methods to integrate disparate pieces of evidence into a unifying framework, test their compatibility, and efficiently generate experimental predictions (Kirchner *et al.*, 2021).

Dendrite level: Emergence of synaptic organization and dendritic maps during development

Above the level of molecular factors and synapses is the individual neuron with its soma, dendrite, and axon (Fig. 1.3a,b). By processing a barrage of synaptic inputs, individual neurons exhibit impressive computational capabilities, which sequentially emerge throughout development and allow them to integrate into complex neural circuits (Kirchner *et al.*, 2022; Stuart *et al.*, 2016).

Historically, the dendrite of a neuron was considered a passive conduit for trans-

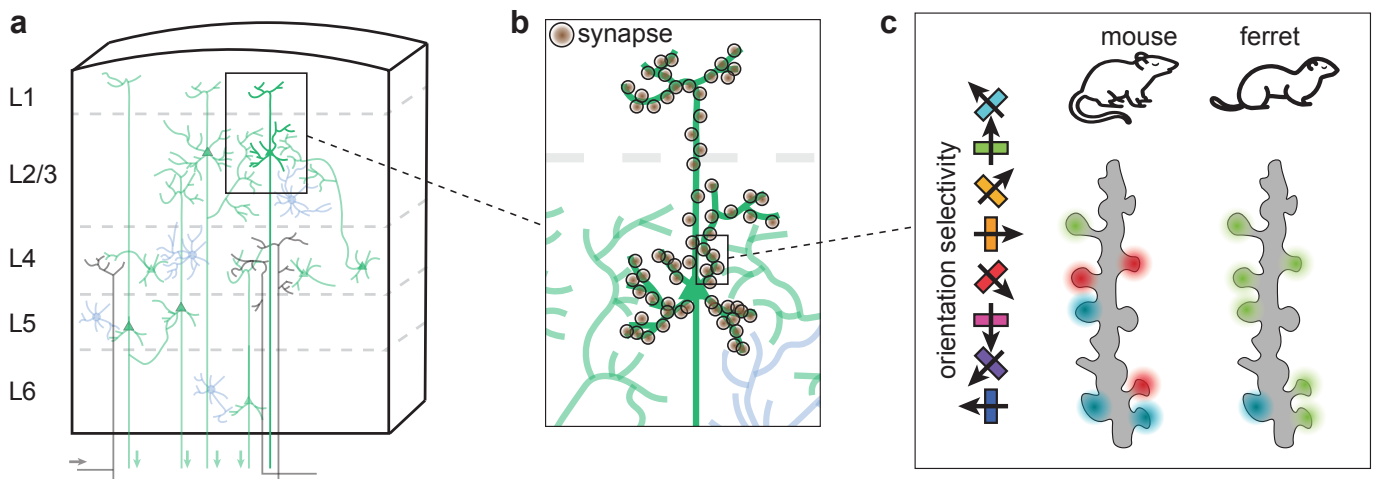


Figure 1.3: Emergence of synaptic organization on developing dendrites. (a) Schematic of six-layered cortex with excitatory (green) and inhibitory (blue) neurons, with a single pyramidal neuron in layer 2/3 highlighted. Arrows indicate flow of incoming (black) and outgoing (green) signals. Adapted from ref. (Naskar *et al.*, 2019). (b) Inset from a magnified, indicating distributed synaptic inputs on the developing dendrite. (c) Inset from b magnified, with synapses colored according to their orientation preference (left). Different species (e.g. mouse or ferret) exhibit qualitatively different types of synaptic organization (Iacaruso *et al.*, 2017; Wilson *et al.*, 2016). Adapted from ref. (Kirchner *et al.*, 2022).

porting electrical signals to the soma (Rall, 1962). After more than half a century of advances in imaging technology and cell electrophysiology, it is now clear that dendrites are not just passively but actively involved in information processing and communication between neurons (Payeur *et al.*, 2019; Poirazi *et al.*, 2020; Pulikkottil *et al.*, 2021). In particular, nearby synapses that activate in concert can cooperate to intricately transform an incoming signal (Poirazi *et al.*, 2003; Tzilivaki *et al.*, 2019), regulate each other's efficacy (El-Boustani *et al.*, 2018; Winnubst *et al.*, 2015), and share plasticity-related proteins (Okun *et al.*, 2008b; Redondo *et al.*, 2011). Consequently, the computational capabilities of neurons derive in part from the precise arrangement of synaptic inputs on the neurons' dendrites (Stuart *et al.*, 2016).

Synaptic organisation exists in different areas of the brain and in different species (Adoff *et al.*, 2021; Ashaber *et al.*, 2021; Frank *et al.*, 2018; Fu *et al.*, 2012; Gökçe *et al.*, 2016; Iacaruso *et al.*, 2017; Ju *et al.*, 2020; Kerlin *et al.*, 2019; Kim *et al.*, 2021; Kleindienst *et al.*, 2011; Lee *et al.*, 2019; McBride *et al.*, 2008; Niculescu *et al.*, 2018; Podgorski *et al.*, 2021; Scholl *et al.*, 2017; Takahashi *et al.*, 2012; Wilson *et al.*, 2016; Winnubst *et al.*, 2015), but the specific characteristics of the organiza-

1 Introduction

tion vary strongly across areas and species. In the ferret or macaque visual cortex nearby synapses tend to respond to moving gratings of the same orientation (Ju *et al.*, 2020; Scholl *et al.*, 2017; Wilson *et al.*, 2016). In the mouse visual cortex this shared orientation preference is not present. Instead, nearby synapses only tend to have overlapping, but not aligned, receptive fields (Iacaruso *et al.*, 2017; Jia *et al.*, 2010) (Fig. 1.3c). While these differences in synaptic organization might stem from differences in the experimental set-ups, species-specific differences in other forms of neural organization are well-established in the literature (Jang *et al.*, 2020).

Beyond the level of nearby synapses on the scale of tens of microns, converging lines of experimental evidence point towards a functional role of synaptic organization on the scale of entire dendrites (Bollmann *et al.*, 2009; El-Boustani *et al.*, 2018; Iacaruso *et al.*, 2017; Jia *et al.*, 2014; Kerlin *et al.*, 2019; Podgorski *et al.*, 2021; Wilson *et al.*, 2016). For example, in the tectum of *Xenopus* tadpoles and in the mouse visual cortex synapses are arranged according to visual location, with synapses near the soma responding to stimuli close to the centre of vision and those distant from the soma responding to stimuli further away (Bollmann *et al.*, 2009; El-Boustani *et al.*, 2018; Iacaruso *et al.*, 2017).

Having such a rich repertoire of experimental findings from different species invites the possibility of comparative studies that can reveal similarities and differences in function and thus uncover foundational principles of brain function (Laurent, 2020). While few labs have the resources to study multiple animal models simultaneously, computational modeling can synthesize existing data. A single model that explains results from several different species potentially captures a general principle that goes beyond individual experiments (Levenstein *et al.*, 2020). Thus, we used a computational model to explain the qualitatively different types of synaptic organization observed in ferrets and mice (Kirchner *et al.*, 2021).

Circuit level: Structured spontaneous activity drives circuit maturation

Despite the impressive computational abilities of individual neurons, the flexibility and versatility of the brain derive from the coordinated action of multiple cells connected into neural circuits (Hopfield *et al.*, 1986) (Fig. 1.4a). These neural circuits

emerge and become functional throughout brain development through an interplay of activity-dependent and -independent factors (Leighton *et al.*, 2016). After activity-independent, molecular factors establish a first, rough scaffold (McLaughlin *et al.*, 2005) (Fig. 1.4b), activity-dependent plasticity mechanisms refine the scaffold into a functioning, mature circuit (Fig. 1.4c). Despite decades of research, how this refinement occurs in detail and the relative importance of activity-dependent and activity-independent mechanisms remain unclear (Molnár *et al.*, 2020).

What type of activity drives circuit refinement? The eyelids of a newborn mouse stay closed for the first two weeks after birth and then open gradually over one or two days. But even though visual stimulation of the retina is strongly diminished during these early postnatal periods, the developing retina is still highly active (Stafford *et al.*, 2009; Tiriác *et al.*, 2018; Wong, 1999). The neural activity observed in this pre-sensory period is generated spontaneously and thus termed *spontaneous activity*. It is characterized by spatiotemporal patterns that resemble those seen in the mature animal (Berkes *et al.*, 2011; Ge *et al.*, 2021). Spontaneous activity occurs throughout the entire developing brain and exhibits variable characteristics depending on species, brain area, and developmental stage (Leighton *et al.*, 2016).

Spontaneous activity is crucial for the refinement of neural circuits (Kirkby *et al.*, 2013). Studies in a variety of model systems have shown that this activity can sculpt the connectivity of developing circuits by promoting the formation and elimination of synapses (Kleindienst *et al.*, 2011; Niculescu *et al.*, 2018; Takahashi *et al.*, 2012; Winnubst *et al.*, 2015). Exposing visually naive ferrets to several hours of visual input with unusual spatiotemporal can induce cortical neurons to become selective to this input, demonstrating the instructive role of spontaneous activity (Roy *et al.*, 2020). Disrupting spontaneous activity results in incorrect wiring and consequent dysfunction in the mature brain (Molnár *et al.*, 2020).

One prominent example of activity-dependent refinement of a cortical circuit is the refinement of thalamocortical afferents in the visual cortex (Kirkby *et al.*, 2013). In particular, activity-independent mechanisms can establish a rough topographically aligned mapping between neurons in the sensory periphery and neurons in the cortex (McLaughlin *et al.*, 2005). Besides extracting invariant features at high temporal and spatial resolution, spontaneous activity in conjunction with activity-dependent plasticity is required for refining the topography (Molnár *et al.*, 2020). Intrigu-

1 Introduction

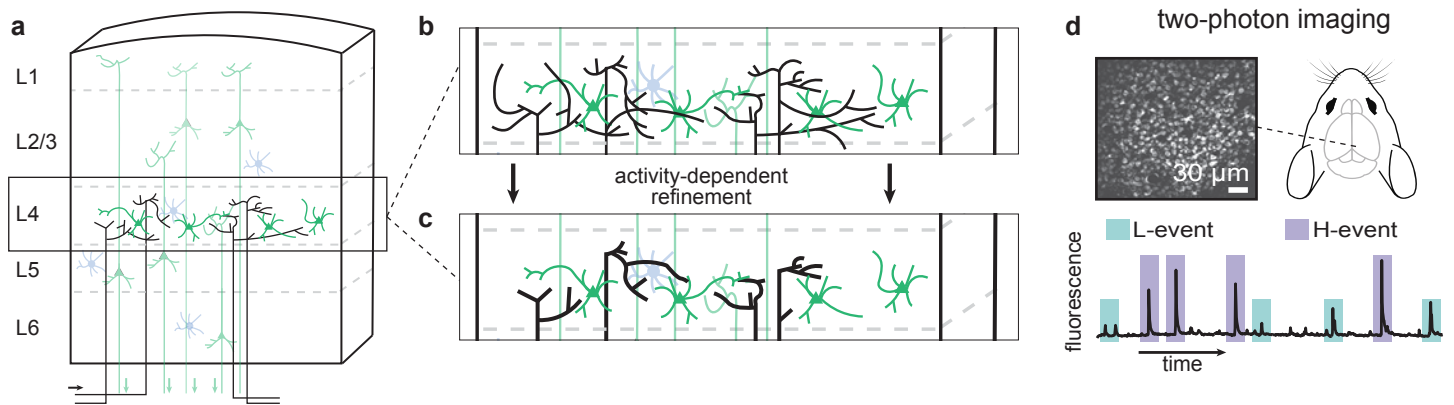


Figure 1.4: Activity-dependent refinement of thalamocortical afferents during development. (a) Schematic of six-layered cortex with excitatory (green) and inhibitory (blue) neurons. Thalamocortical afferents (black) project onto layer four neurons. (b) Inset from a magnified, highlighting the initially diffuse branching of thalamocortical axons. (c) Through activity-dependent refinement, thalamocortical input becomes more localized and specific to individual neurons. (d) Representative field of view from a two-photon calcium recording of neurons in L2/3 (top). Example of fluorescence trace (black; average over all cells) as a function of time, with two types of spontaneous activity (green and purple; low and high synchronicity) highlighted.

ingly, the developing cortex receives two qualitatively different types of spontaneous activity that might contribute to circuit refinement: peripherally-driven, low-synchronicity (L-)events and cortically-generated, high-synchronicity (H-events) (Fig. 1.4d) (Siegel *et al.*, 2012). While previous models establish that L-events can refine thalamocortical connections in a simplified set-up (Willshaw *et al.*, 1976), the resulting set-up is sensitive to perturbations and cannot incorporate the effect of H-events (Wosniack *et al.*, 2021). Thus, understanding how the presence of H-events might impact the emergence of topographically aligned maps in the developing visual cortex would increase our understanding of activity-dependent circuit refinement during development.

Alongside the initial description of H-events in 2012, Siegel *et al.* hypothesize that they might act as a homeostatic mechanism that helps maintain neural activity in a fixed range. We used a computational model of the developing visual system incorporating both L- and H-events to test this hypothesis. We characterized the conditions under which H-events can act to stabilize neural activity and generate concrete experimental predictions to substantiate the hypothesis.

Behavioral level: Neuromodulatory control over spontaneous activity

When investigating abstract computational properties of neural circuitry, it is important to remember that the circuit we study in controlled lab conditions is artificially constrained. Under natural conditions, circuits are constantly modulated by a variety of behavioral and ecological factors (Pollen *et al.*, 2007; Stringer *et al.*, 2019). Because mammalian infants require intensive care from their mothers to survive after birth, mother-pup interactions play a central role in the development of the brain (Lucion *et al.*, 2014). While there is considerable research focused on the perspective of the mother (Froemke *et al.*, 2021; Marlin *et al.*, 2015), little attention has been paid to how the presence or absence of the mother might affect circuit development in the pup (Miller *et al.*, 2015).

In the context of mother-pup interactions, oxytocin, the hormone often associated with social affiliation and the emotional bond, has emerged as a key neuromodulator (Miller *et al.*, 2015; Rajamani *et al.*, 2018; Vaidyanathan *et al.*, 2017). Expression of the oxytocin receptor (*Oxtr*) in mice is elevated during the first two weeks after birth, with its highest expression in the cortex observed at P14 (Hammock *et al.*, 2013; Vaidyanathan *et al.*, 2017). Our knowledge of how the oxytocin signaling pathway matures over development is incomplete, but converging lines of evidence highlight the importance of suckling behavior (Grinevich *et al.*, 2015) (Fig. 1.5a). One dominant hypothesis for the action of oxytocin centers on the possibility that oxytocin could be released in large quantities from the paraventricular nucleus of the brain of mouse pups. From the paraventricular nucleus, oxytocin might diffuse throughout the developing cortex (Grinevich *et al.*, 2015) where it modulates the activity of developing populations of neurons (Maldonado *et al.*, 2021; Zheng *et al.*, 2014) (Fig. 1.5b,c).

When investigating the impact of neuromodulators on neural activity, it is important to distinguish between different types of neurons. Neurons can be divided into excitatory (mostly signaling via glutamatergic synapses) or inhibitory (mostly signaling via GABAergic or glycinergic synapses) (Strata *et al.*, 1999) neurons. Excitatory and inhibitory activity is tightly regulated throughout development (Naskar *et al.*, 2019; Sutor *et al.*, 1995) and inhibitory activity can restrict spread of excita-

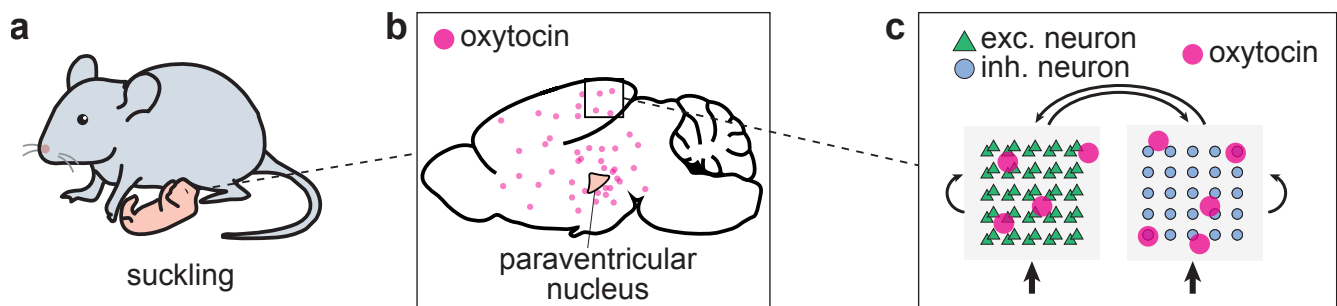


Figure 1.5: Possible behavioral trigger of intrinsic release of oxytocin. (a–c) Close interactions between mother and pup, like suckling behavior (a), can trigger the release of oxytocin from the paraventricular nucleus (b), which diffuses throughout the developing cortex and might affect dynamics of the developing circuit (c).

tory activity (Leighton *et al.*, 2021). Oxytocin can modulate both excitatory and inhibitory activity in the adult animal (Marlin *et al.*, 2015) and increase excitatory synaptic transmission in the developing somatosensory cortex (Zheng *et al.*, 2014).

Together with our collaborators from the Lohmann lab at the Netherlands Institute for Neuroscience, we explored whether and how oxytocin might affect spontaneous activity at the network level in the developing brain (Maldonado *et al.*, 2021). In a series of *in vivo* experiments, our collaborators demonstrated that oxytocin impacts neural activity at the population- and the single-cell level. In *in vitro* experiments, they furthermore demonstrate how oxytocin affects excitatory and inhibitory synaptic transmission and how it differentially acts on different neural subtypes. While both sets of experiments point at an inhibiting role of oxytocin, experimental data from *in vivo* and *in vitro* set-ups are difficult to compare (Prescott *et al.*, 2008). Thus, we developed a computational model of the developing visual cortex, calibrated with experimental data to test the compatibility of the two sets of experiments.

In this dissertation, I investigate the interactions between spontaneously generated activity and synaptic plasticity in the context of brain development. In particular, I introduce and contextualize three distinct projects concerned with

1. the emergence of synaptic organization on developing dendrites (Kirchner *et al.*, 2021, 2022),
2. the robust formation of topographic maps through adaptation of spontaneous activity (Wosniack *et al.*, 2021),
3. and the ability of neuromodulation to shape spontaneous activity through the differential regulation of inhibitory subnetworks (Maldonado *et al.*, 2021).

To further highlight commonalities and interactions between these projects, I demonstrate how the mathematical structures underlying these models interrelate. Finally, I discuss new research directions opened up by the work in this dissertation. Taken together, the results of my computational approach have revealed principles of organization that span multiple levels of abstraction with wide implications for developmental neuroscience.

2 Methods and mathematical framework

We used computational modeling to investigate properties of the brain across multiple levels of abstraction. In this chapter, we look at the mathematical equations underlying the models. In the published papers, we motivate the choice of these equations with an appeal to the corresponding biological process (Kirchner *et al.*, 2021; Maldonado *et al.*, 2021; Wosniack *et al.*, 2021). Here we will choose a different route and motivate the models by deriving the successively more abstract models starting at the molecular level.

Molecular level: Neurotrophin plasticity model

To demonstrate how the mathematical models at different levels of abstraction connect to the molecular model, we provide an introduction of the neurotrophin model (Kirchner *et al.*, 2021).

Neural exocytosis is the process by which neurons release neurotransmitters and other molecules into the synaptic cleft via the fusion of synaptic vesicles with the neuronal membrane. Exocytosis is linked to activity in the neuron, as the release of neurotransmitters can be triggered by an electrical signal called an action potential (Fig. 2.1a). We represent a sequence of presynaptic depolarizations arriving at the k -th synapse at times t_k as a sum of Dirac deltas, $x_k(t) = \sum_f \delta(t - t_k)$.

Presynaptic depolarization, x_k results in a temporary increase of the protease MMP9, $M(t)$, in the synaptic cleft (Je *et al.*, 2012) (Fig. 2.1b), which we model as a synapse-specific leaky integrator,

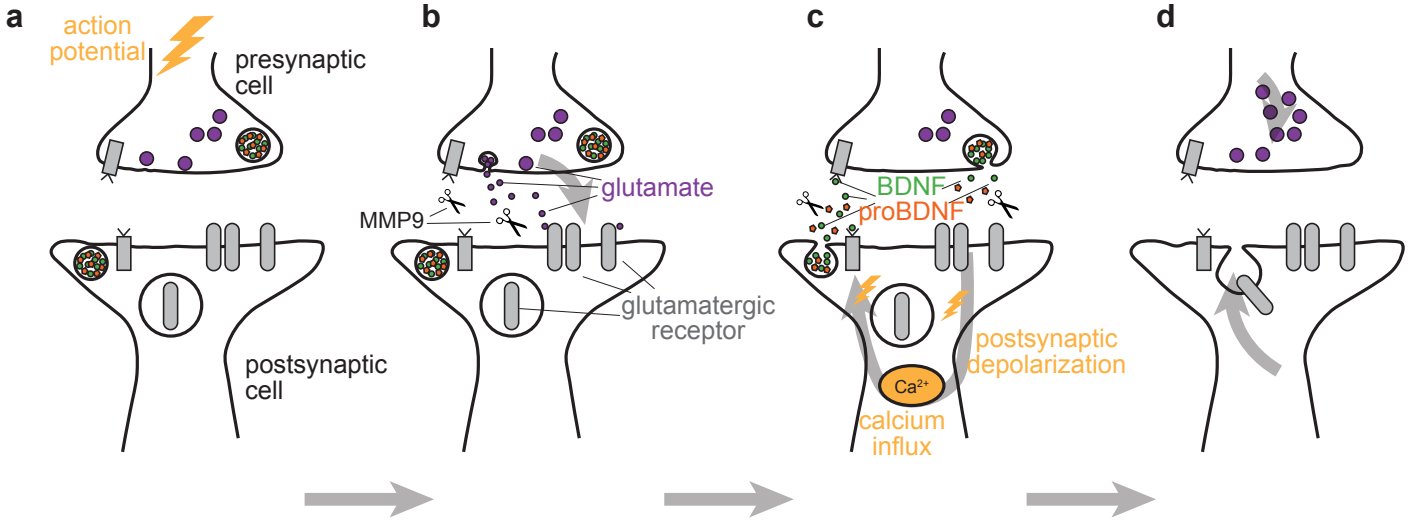


Figure 2.1: Possible neurotrophin signaling cascade leading to synaptic potentiation. (a–d) Presynaptic activation (a) leads to the release of glutamate and the protease MMP9 into the synaptic cleft (b). Glutamate binds to postsynaptic receptors and triggers an influx of calcium. Calcium, in turn, brings about the release of BDNF and proBDNF into the synaptic cleft (c). BDNF binds to pre- and postsynaptic receptors, which prompts an increase in presynaptic glutamate stores and the insertion of additional postsynaptic glutamate receptors (d).

$$\tau_M \frac{dM_k}{dt} = -M_k(t) + \phi x_k(t). \quad (2.1)$$

Here, ϕ is a constant that determines how efficiently MMP9 converts proBDNF into BDNF, and τ is always the time constant of the accumulator. The release of glutamate into the synaptic cleft furthermore activates postsynaptic glutamatergic receptors, which induces depolarization in the postsynapse (Fig. 2.1c). Consistent with experimental data (Lee *et al.*, 2016), we couple the postsynaptic calcium level, $Y(t)$, to the nearby synaptic inputs x_k ,

$$\tau_Y \frac{dY_k}{dt} = -Y_k(t) + \sum_{l=1}^N s_{kl} W_l(t) x_l(t). \quad (2.2)$$

To include distance-dependent attenuation of interactions between synapses, we weight synaptic inputs by their efficacies W_l and the distance-dependent factor s_{kl} , defined as a Gaussian kernel applied to the Euclidean distance $s_{kl} = e^{-d_{kl}^2/2\sigma_s^2}$. Here,

the calcium diffusion constant σ_s controls the spatial extent of lateral calcium diffusion. As postsynaptic calcium induces release of neurotrophins into the extracellular space (Harward *et al.*, 2016), we coupled extracellular proBDNF, $P(t)$, and BDNF, $B(t)$, to postsynaptic calcium (Fig. 2.1c),

$$\tau_P \frac{dP_k}{dt} = -P_k(t) + (1 - \eta)Y(t) - M_k(t)P_k(t), \quad (2.3)$$

$$\tau_B \frac{dB_k}{dt} = -B_k(t) + \eta Y(t) + M_k(t)P_k(t). \quad (2.4)$$

By including the product of the MMP9 accumulator and the proBDNF accumulator, $M_k(t)P_k(t)$, with different signs in the differential equations (2.3) and (2.4), we represent the ability of MMP9 to convert proBDNF to an equal amount of BDNF. The scaling factors $(1 - \eta)$ and η ensure that in the absence of MMP9, the ratio of BDNF to proBDNF remains close to the constitutive ratio η , i.e. the ratio observed when no extracellular cleaving occurs (Nagappan *et al.*, 2009).

One prominent hypothesis for how neurotrophins interact to induce synaptic plasticity is the Yin-Yang hypothesis of neurotrophin action (Lu *et al.*, 2005) which states that when BDNF binds to its receptor TrkB, the synapse strengthens, but when proBDNF binds to the p75NTR receptor, the synapse weakens. As in the depicted scenario (Fig. 2.1d), when BDNF outweighs proBDNF, the synapse increases in strength by e.g. recruiting additional glutamatergic receptors and increasing presynaptic vesicles with glutamate.

We incorporate the effect of this push-pull interaction between neurotrophic factors (Niculescu *et al.*, 2018) by coupling the change of synaptic efficacy, $W_k(t)$, to the difference of BDNF and proBDNF present in the synaptic cleft,

$$\tau_W \frac{dW_k}{dt} = B_k(t) - P_k(t). \quad (2.5)$$

Molecular level/Dendrite level: Generalized neurotrophin-inspired model

Here, we derive generalized neurotrophin model (Kirchner *et al.*, 2021). We can substantially simplify the system of equations (2.1)–(2.5) at the cost of the straightforward identifiability of the parameters. We obtain a synapse-specific presynaptic accumulator, $v_k(t)$, by relabeling of equation (2.1),

$$\tau_v \frac{dv_k}{dt} = -v_k(t) + \phi x_k(t), \quad (2.6)$$

and a locally shared postsynaptic accumulator, $u_k(t)$, by relabeling of equation (2.2),

$$\tau_u \frac{du_k}{dt} = -u_k(t) + \sum_{l=1}^N s_{kl} w_l(t) x_l(t). \quad (2.7)$$

We next make a steady-state assumption for the neurotrophin concentrations, $B_k(t)$ and $P_k(t)$, insert the resulting equation into the differential equation for the synaptic efficacy, $W_k(t)$, and linearize the resulting expression. We can then write the approximate change in efficacy compactly as a Hebbian learning rule (Gerstner *et al.*, 2014) that operates locally on the dendrite,

$$\tau_w \frac{dw_k}{dt} = u_k(t)(v_k(t) + \rho). \quad (2.8)$$

Here, $\rho = \frac{2\eta-1}{2(1-\eta)}$ and $\tau_w = \tau_W \frac{1}{2(1-\eta)}$.

Dendrite level: From local dendritic to global somatic activity

Next, we connect the detailed, local model of dendritic activity that we used in our work on synaptic organization (Kirchner *et al.*, 2021) with the rate-based model of neural activity we used in our research on connectivity refinement (Wosniack *et al.*, 2021) by performing a series of algebraic transformations.

While we focused on isolated stretches of dendrite in the previous section, a barrage of synaptic input arrives without pause across the entire dendrite. These synaptic inputs induce varying degrees of depolarization of the neuron’s membrane potential. Depending on the exact dendritic morphology and location of a given synapse, propagating the depolarization to the soma results in substantial attenuation of the synaptic signal. Interestingly, experiments indicate that this effect is compensated by an increase in conductance at distal synapses, which effectively normalizes the strength of synaptic inputs at the soma (termed synaptic democracy, Rumsey *et al.*, 2006; Sterratt *et al.*, 2012). We might thus approximate the somatic depolarization ($A(t)$) as the sum of individual postsynaptic activations (Kirchner *et al.*, 2021; Mel, 1991),

$$\tau_A \frac{dA}{dt} = -A(t) + \sum_{k=1}^N u_k(t) \approx -A(t) + \sum_{k=1}^N \sum_{l=1}^N s_{kl} w_l(t) x_l(t). \quad (2.9)$$

For the approximation in eq. (2.9), we have made a steady state assumption on the postsynaptic accumulator, $u_k \approx s_{kl} w_l(t) x_l(t)$. Interchanging the order of summation allows us to separate a term depending on local interactions from the inputs and synaptic weights,

$$\tau_A \frac{dA}{dt} = -A(t) + \sum_{l=1}^N w_l(t) x_l(t) \sum_{k=1}^N s_{kl}. \quad (2.10)$$

The term that depends on the local interactions, $\sum_{k=1}^N s_{kl}$, can be approximated as the product of the local interaction constant, σ_c , times the local density of inputs, ν_l , and scaled by a constant, $\sqrt{2\pi}$ (for details see section 4 of the Supplementary Notes of Kirchner *et al.*, 2021),

$$\tau_A \frac{dA}{dt} \approx -A(t) + \sum_{l=1}^N \sqrt{2\pi} \sigma_c \nu_l w_l(t) x_l(t). \quad (2.11)$$

We can summarize all synapse-specific terms into the connection weight, $\hat{w}_l(t) =$

2 Methods and mathematical framework

$\sqrt{2\pi}\sigma_s\nu_l w_l(t)$, and arrive at the well-established leaky integrator equation of the integrate-and-fire neuron model (Burkitt, 2006),

$$\tau_A \frac{dA}{dt} = -A(t) + \sum_{l=1}^N \hat{w}_l(t) x_l(t). \quad (2.12)$$

The dynamics of a integrate-and-fire unit, A , resemble the dynamics a rate-based unit, \bar{A} , in many biologically relevant settings (Gerstner *et al.*, 2014; Stevens *et al.*, 1995). Thus, we can write the time-dependent firing rate of the soma as a leaky accumulator of a nonlinear function of the input,

$$\tau_{\bar{A}} \frac{d\bar{A}}{dt} = -\bar{A}(t) + g \left[\sum_{l=1}^N \hat{w}_l(t) x_l(t) \right]. \quad (2.13)$$

Here, g is a nonlinear activation function that depends on the properties of the integrate-and-fire unit and the network connectivity (Gerstner *et al.*, 2014).

Given this set-up, we can interpret the weighted input, $\sum_{l=1}^N \hat{w}_l(t) x_l(t)$, as representing peripheral input arriving at the dendrites of pyramidal neurons of the developing cortex (Fig. 1.4). Beyond feedforward input from the periphery, these neurons also exhibit a second, distinct type of intrinsically generated spontaneous activity, $A^{\text{spont}}(t)$ (Siegel *et al.*, 2012),

$$\tau_{\bar{A}} \frac{d\bar{A}}{dt} = -\bar{A}(t) + g \left[\sum_{l=1}^N \hat{w}_l(t) x_l(t) \right] + A^{\text{spont}}(t). \quad (2.14)$$

Choosing the activation function, $g(\cdot)$, as the identity function, $\text{id}(\cdot)$, then produces the equation for the dynamics of the rate-based unit in eq. (1) of Wosniack *et al.* (2021),

$$\tau_{\bar{A}} \frac{d\bar{A}}{dt} = -\bar{A}(t) + \sum_{l=1}^N \hat{w}_l(t) x_l(t) + A^{\text{spont}}(t). \quad (2.15)$$

Dendrite level/Circuit level: Backpropagating action potentials as global feedback signals

After considering how local activity on the dendrite propagates to and accumulates at the soma, we now ask how somatic activity might affect synapses distributed across the dendrite. A natural candidate is the backpropagating action potential, the active propagation of depolarization produced by the initiation of an axonal action potential along the proximo–distal axis of the dendrite (Spruston *et al.*, 1995; Sterratt *et al.*, 2012). Following Kirchner *et al.* (2021), we can model the impact of a backpropagating action potential, $B(t)$, by including adding its effect to the local postsynaptic accumulator, eq. (2.7),

$$\tau_u \frac{du_k}{dt} = -u_k(t) + \sum_{l=1}^N s_{kl} w_l(t) x_l(t) + s_k B_{\text{amp}} B(t). \quad (2.16)$$

The impact of a backpropagating action potential depends on its initial amplitude, B_{amp} , as well as a distance–dependent scaling factor, $s_k = e^{-\frac{d_k^2}{2\sigma_s^2}}$, that attenuates the impact with increasing distance from the soma (Sterratt *et al.*, 2012), d_k . As in eq. (2.9), we again make a steady state assumption and insert the resulting expression into the differential equation describing the weight dynamics, eq. (2.8),

$$\tau_w \frac{dw_k}{dt} = \left(\sum_{l=1}^N s_{kl} w_l(t) x_l(t) + s_k B_{\text{amp}} B(t) \right) (v_k(t) + \rho). \quad (2.17)$$

As the depolarization induced by a backpropagating action potential tends to be much larger than the depolarization induced by nearby synaptic inputs, $s_k B_{\text{amp}} B(t) \gg \sum_{l=1}^N s_{kl} w_l(t) x_l(t)$, we can approximate the total change in weight by neglecting the impact of nearby synapses,

$$\tau_w \frac{dw_k}{dt} = (s_k B_{\text{amp}} B(t))(v_k(t) + \rho). \quad (2.18)$$

The resulting equation is a Hebbian learning rule with a distance-dependent term for the postsynaptic accumulator (Ebner *et al.*, 2019; Letzkus *et al.*, 2006). If we further assume that the impact of the attenuation can be neglected, as might be the case for most proximal synapses (Sterratt *et al.*, 2012), and that somatic firing is well approximated by a firing rate (compare eq. 2.13), we arrive at a simplified form of the equation for the change in weight,

$$\tau_w \frac{dw_k}{dt} = \bar{A}(t)(v_k(t) + \rho). \quad (2.19)$$

This expression matches, after appropriate relabeling of the variables, the equation describing the change in synaptic weight in a feedforward model, eq. (2) by Wosniack *et al.* (2021).

Circuit level/Behavioral level: GABAergic inputs control activity in a recurrent network

Synaptic inputs fall into two broad categories: glutamatergic excitatory and GABAergic inhibitory, depending on the neurotransmitter released and the effect on the postsynaptic neuron. While the excitatory synapses outnumber inhibitory synapses one to five (Iascone *et al.*, 2020), inhibitory synapses tend to compensate this numerical disadvantage by inducing a larger change in membrane potential (Maldonado *et al.*, 2021). To introduce inhibitory inputs into our model, we can split the input into the somatic accumulator, eq. (2.12), into excitatory and inhibitory input,

$$\tau_A \frac{dA}{dt} = -A(t) + \sum_{l=1}^N \hat{w}_{lE}(t)x_{lE}(t) + \sum_{m=1}^N \hat{w}_{mI}(t)x_{mI}(t), \quad (2.20)$$

$$= -A(t) + w_{E}^T x_E + w_{I}^T x_I \quad (2.21)$$

and constrain the weights to be positive and negative respectively, $w_l^E \geq 0$ and $w_m^I \leq 0$. In eq. (2.21), we have rewritten the equation as a vector product to simplify notation. With increasing postnatal age, recurrent connectivity within a cortical layer becomes more pronounced (Larsen *et al.*, 2006) until recurrent and thalamocortical inputs affect the postsynaptic neuron approximately equally (Schoonover *et al.*, 2014). To capture the dynamics of the network at this age, we can split the excitatory and inhibitory contributions further into recurrent (r) and feedforward (f) parts,

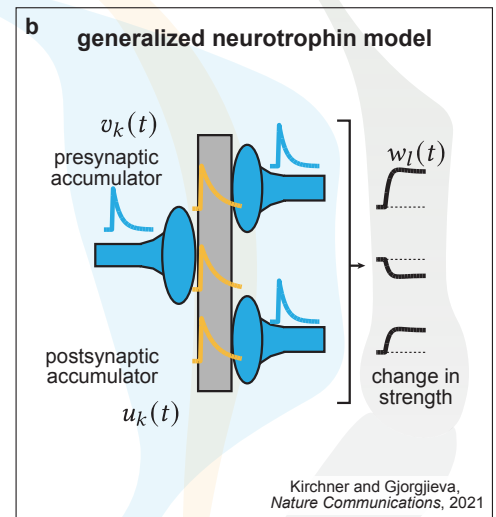
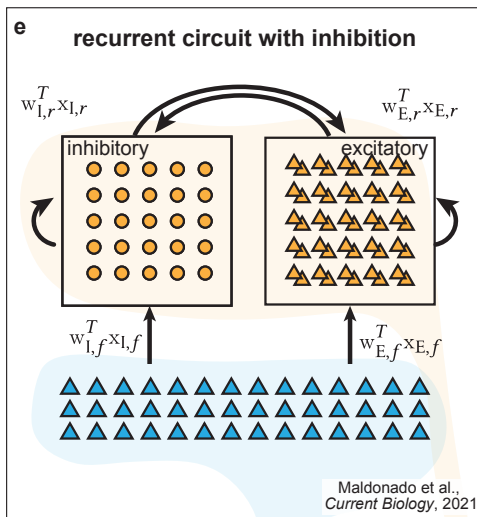
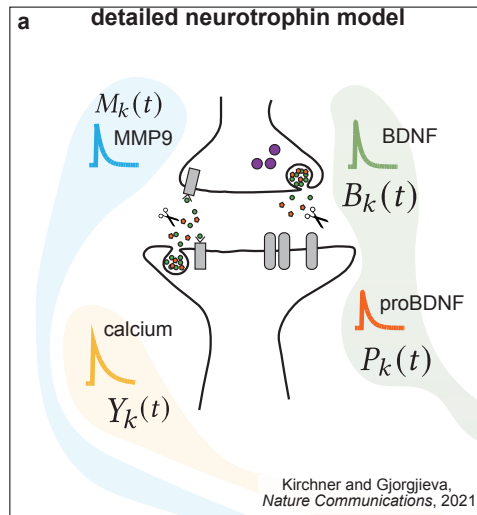
$$\tau_A \frac{dA}{dt} = -A(t) + w_{E,r}^T x_{E,r} + w_{E,f}^T x_{E,f} + w_{I,r}^T x_{I,r} + w_{I,f}^T x_{I,f}. \quad (2.22)$$

We thus arrive at a variation of the classical Wilson-Cowan model of excitatory and inhibitory interactions between populations of model neurons (Wilson *et al.*, 1972) where the activation function is again chosen as the identity function, $\text{id}(\cdot)$. In Maldonado *et al.* (2021) we complement this model by

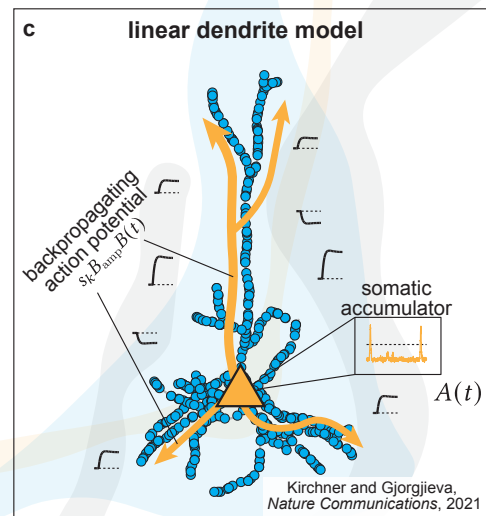
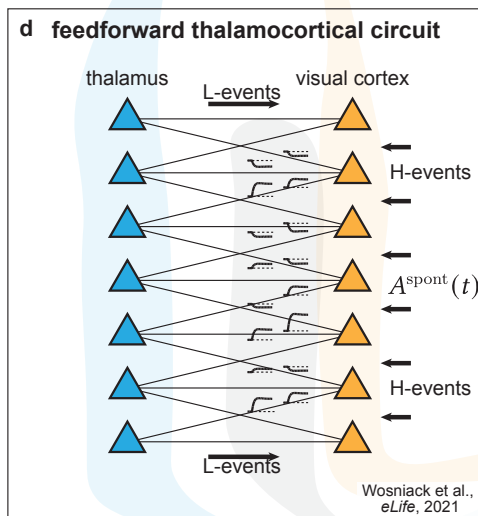
1. spatially structured connectivity within the cortex ($w_{E,r/f}^T, w_{I,r/f}^T$) and between the periphery and the cortex (Rossi *et al.*, 2020; Weiler *et al.*, 2022),
2. temporally structured feedforward input inspired by retinal wave activity (Wong, 1999),
3. biologically-realistic neuron parameters, including resting membrane potentials, spike thresholds, and membrane capacitance (Maldonado *et al.*, 2021).

Activation of the oxytocin receptor triggers a depolarizing inward current in somatostatin interneurons (Maldonado *et al.*, 2021). To model the effect of oxytocin activation, we can adapt the resting membrane potential of a portion of the inhibitory interneurons, from -60 mV to -55 mV, and arrive at the formulation of the model in Maldonado *et al.* (2021).

2 Methods and mathematical framework



← adding
inhibition
recurrent
connections



← adding
morphology

← linear activation
function ← strong
backpropagation

Figure 2.2: Model structure at different levels of abstraction. Schematic illustrating how synaptic plasticity (green, grey), and pre- and post-synaptic accumulators (blue and orange) manifest at different levels of abstraction. Individual boxes represent the systems described in equations (2.1-2.5) in box **a**, equations (2.6-2.8) in box **b**, equation (2.9) in box **c**, equations (2.15) and (2.19) in box **d**, and equation (2.22) in box **e**. Arrows between boxes indicate mathematical operation required to translate one model into the other. Reference in the bottom right of a box indicates the publication where we introduced the model.

3 Results

As part of my doctoral work, I have contributed to four peer-reviewed journal articles, using several distinct theoretical and computational techniques to answer different questions related to the interactions between spontaneous activity and synaptic plasticity (Kirchner *et al.*, 2021, 2022; Maldonado *et al.*, 2021; Wosniack *et al.*, 2021). I am the first author of two of the articles (Kirchner *et al.*, 2021, 2022) and a contributing author of the other two (Maldonado *et al.*, 2021; Wosniack *et al.*, 2021). I include a summary for each article, indicate my contribution, and reproduce the full text.

Emergence of local and global synaptic organization on cortical dendrites

In Kirchner *et al.* (2021), we propose a model for how the precise positioning of synapses on dendrites might emerge through the activity-dependent cooperation and competition between nearby synaptic inputs. We found that:

1. Brain-derived neurotrophic factor (BDNF) and its developmental precursor proBDNF can implement a biologically-realistic synaptic plasticity rule with distance-dependent competition and timing-dependent cooperation.
2. Combining this neurotrophin-inspired plasticity model with structural plasticity can explain the experimentally observed fine-scale organization of synaptic inputs in the developing and mature visual cortex called *synaptic clustering*.
3. Introducing a backpropagating somatic action potential can induce experimentally observed global organization of synaptic input across the entire dendritic tree.
4. By varying a single, species-specific anatomical factor (the animal's cortex size), we can produce qualitatively different local and global synaptic organizations in excellent agreement with the evidence from the cortices of mice and ferrets.

The work was completed in collaboration with my supervisor, Prof. Dr. Julijana Gjorgjieva. Together, we designed the research, prepared the figures, and wrote the manuscript. I created and analyzed the model, implemented model simulations, and wrote the first draft. I performed some preliminary research to motivate the model during my master thesis, which I completed under the supervision of Prof. Dr. Julijana Gjorgjieva. The full article was published on June 28th, 2021 in Nature Communications and is reproduced on the following pages under the Creative Commons Attribution 4.0 International License.




ARTICLE



<https://doi.org/10.1038/s41467-021-23557-3>

OPEN

Emergence of local and global synaptic organization on cortical dendrites

Jan H. Kirchner ^{1,2} & Julijana Gjorgjieva ^{1,2} 

Synaptic inputs on cortical dendrites are organized with remarkable subcellular precision at the micron level. This organization emerges during early postnatal development through patterned spontaneous activity and manifests both locally where nearby synapses are significantly correlated, and globally with distance to the soma. We propose a biophysically motivated synaptic plasticity model to dissect the mechanistic origins of this organization during development and elucidate synaptic clustering of different stimulus features in the adult. Our model captures local clustering of orientation in ferret and receptive field overlap in mouse visual cortex based on the receptive field diameter and the cortical magnification of visual space. Including action potential back-propagation explains branch clustering heterogeneity in the ferret and produces a global retinotopy gradient from soma to dendrite in the mouse. Therefore, by combining activity-dependent synaptic competition and species-specific receptive fields, our framework explains different aspects of synaptic organization regarding stimulus features and spatial scales.

¹Computation in Neural Circuits Group, Max Planck Institute for Brain Research, Frankfurt, Germany. ²School of Life Sciences, Technical University of Munich, Freising, Germany. ✉email: gjorgjieva@brain.mpg.de

Neurons in the developing brain become precisely connected before sensory organs mature. Spontaneous activity plays a major role in refining circuit connectivity to mature levels at the scale of single neurons and networks¹. During visual system development, for example, synaptic connections are established by matching molecular gradients and axonal targeting². Spatiotemporal correlations in spontaneous activity then instruct the development of various receptive field properties and visual feature maps, which are further fine-tuned by sensory activity³. In addition to refining developing networks at cellular precision, spontaneous activity can also establish fine-scale organization of individual synapses within the dendritic arborizations of single neurons^{4,5}. One striking example of such fine-scale organization is functional synaptic clustering: synapses onto dendrites of pyramidal neurons that receive correlated input or encode a common sensory feature are spatially grouped. Synaptic clustering has been observed across brain regions, developmental ages, and diverse species from rodent to primate^{4–12}, and has multiple functional benefits; it compartmentalizes the dendrites of single neurons, enables supralinear integration of inputs, shapes memory formation¹³, and can explain translation-invariance of complex cells in the visual cortex¹⁴. However, the mechanistic origins of synaptic clustering dependent on spontaneous activity during early postnatal development, and its relation to functional organization in the adult, remain elusive.

During development, recent experiments identified a molecular mechanism for the emergence of synaptic clustering based on the antagonistic interaction of brain-derived neurotrophic factor (BDNF) and its immature form, proBDNF. By binding to their corresponding receptors, BDNF and proBDNF can respectively promote synaptic potentiation and the survival of neurons, and synaptic depression and the apoptosis of axons and neurons¹⁵. While proBDNF is more prevalent than BDNF during early development¹⁶, the protease matrix metalloproteinase 9 (MMP9) controls the relative amounts of proBDNF and BDNF at a given synapse in an activity-dependent manner, and therefore regulates the plasticity of that synapse. This sets up a promising mechanistic implementation for the developmental formation of synaptic clusters based on neurotrophin interactions, yet the key computational properties that lead to the activity-dependent cooperation and competition of multiple synapses innervating a dendritic branch are unknown.

In the adult, several *in vivo* studies have reported clustering of different stimulus features in different species (but see refs. ^{17–20}). For example, dendritic branches in the ferret visual cortex exhibit local clustering of orientation selectivity but do not exhibit global organization of inputs according to spatial location and receptive field properties^{7,9}. In contrast, synaptic inputs in the mouse visual cortex do not cluster locally by orientation, but only by receptive field overlap, and exhibit a global retinotopic organization along the proximal-distal axis⁸. We presently do not understand the factors that underlie these scale- and species-specific differences and how they emerge during development.

Here we propose a computational framework to reconcile experimental findings about the fine-scale and global synaptic organization observed in the adult, and to make predictions about the key factors driving the emergence of this organization during development. We built a biophysically inspired model of synaptic plasticity based on the molecular mechanism of interacting neurotrophins required for synaptic clustering during development^{6,10}. We identified two important ingredients necessary to generate clustering with this model: timing-dependent cooperation and distance-dependent competition. Generalizing this neurotrophin model to an analytically tractable framework with these two characteristics enables us to study the

emergence of synaptic organization independent of the specific mechanistic implementation. When stimulated with spontaneous retinal waves in a realistic scenario of visual system development, the model generates clustering by orientation in the adult ferret visual cortex and clustering by receptive field overlap in the adult mouse visual cortex. Two key parameters determine the type of clustering: the diameter of receptive fields and the spread of receptive field centers in visual space, which depends on the cortical magnification factor of visual space. By introducing a backpropagating action potential to a reconstructed dendritic tree, the same model generates global organization across the entire tree. Therefore, a single computational framework motivated by molecular interactions in development can explain how circuits wire with the remarkable subcellular precision observed in adulthood, integrating many different facets of organization at the local and global scale.

Results

Distance- and timing-dependent synaptic plasticity in an activity-dependent neurotrophin model. To identify the driving factors for fine-scale dendritic organization of synaptic inputs, we formulated a computational model based on a local molecular mechanism implicated in the emergence of clustering during development. The mechanism implements an activity-dependent interaction between two signaling molecules: proBDNF and BDNF, and the conversion factor between them, MMP9 (Fig. 1a and Methods). Upon activation, a synapse in our model evokes the postsynaptic release of proBDNF and BDNF through the opening of voltage-gated calcium channels and the subsequent influx of calcium¹⁰, which spreads postsynaptically in the developing brain²¹. Through the lateral spread of calcium, the activated synapse can exert a direct effect on a different nearby synapse by triggering neurotrophin release independent of pre-synaptic stimulation of that synapse. MMP9 release is also coupled to neural activity²², but instead of spreading postsynaptically, it is co-localized with glutamatergic receptors in excitatory synapses²³. Therefore, we modeled MMP9 and calcium as synapse-specific and shared accumulators of neural activity, respectively (see Methods).

Analyzing the molecular interactions in the neurotrophin model revealed two prominent properties for sorting dendritic synaptic inputs into local clusters: timing-dependent cooperation and distance-dependent competition. Distance-dependent competition arises when considering the plasticity of two nearby synaptic inputs as a function of the distance between them and the stimulation frequency upon stimulating one of them (Fig. 1b–d). Driving one synapse with bursts, the units of information transmission during development^{6,24}, shifts the balance between proBDNF and BDNF²⁵ in favor of BDNF due to the activity-dependent release of MMP9 (Fig. 1b, c). Thus, the stimulated synapse potentiates. In contrast, the unstimulated synapse depresses by an amount depending on the distance between synapses, as it remains dominated by proBDNF due to the absence of MMP9 (Fig. 1d and Methods). Plasticity of an unstimulated synapse following the stimulation of another synapse is called heterosynaptic and can stabilize the positive feedback of Hebbian plasticity²⁶.

In addition to this distance-dependent heterosynaptic depression, the neurotrophin model exhibits timing-dependent cooperation by potentiating nearby coactive synapses. This can be best seen when implementing a classical plasticity induction paradigm where we quantified synaptic strength as a function of the timing between pre- and postsynaptic events (Fig. 1e). Using bursts as the natural activity patterns in development^{6,24}, we found that pre- and postsynaptic bursts with temporal offsets below 1 s yield

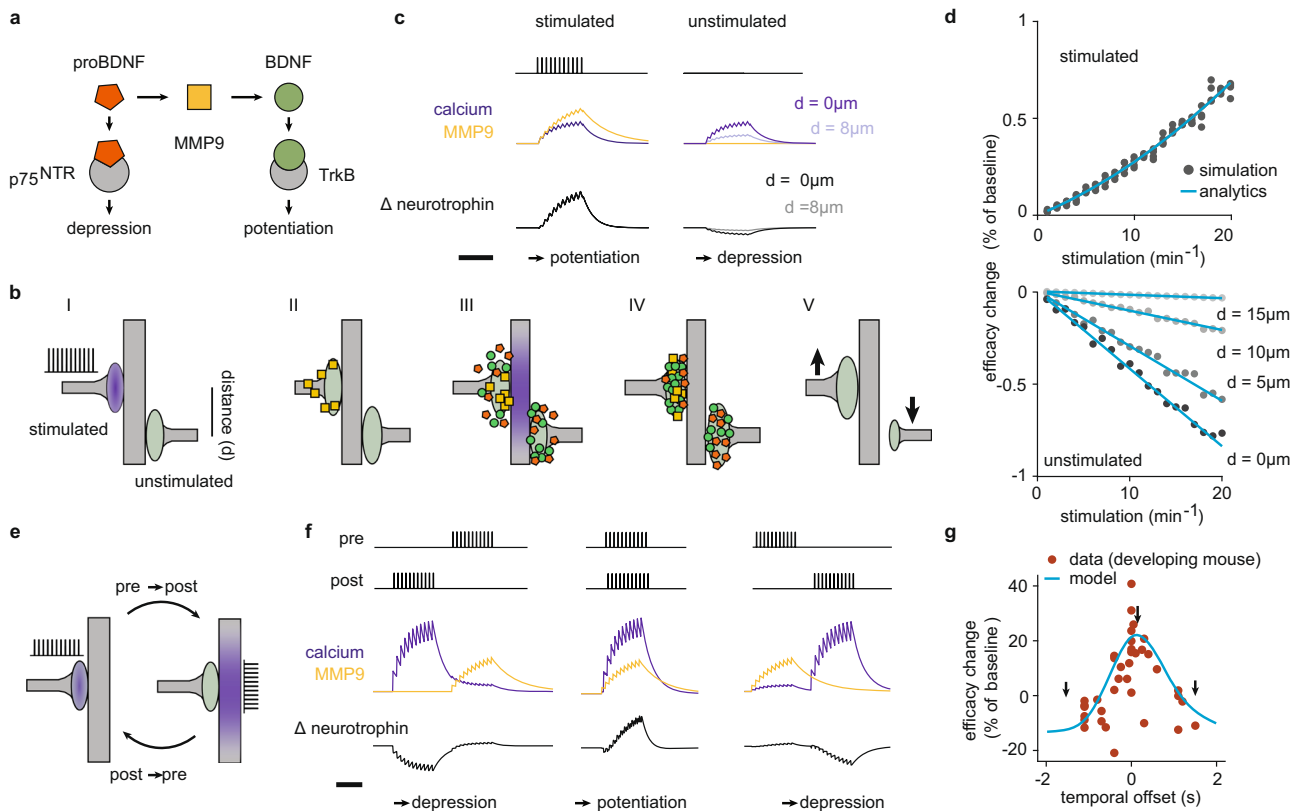


Fig. 1 Distance- and timing-dependent synaptic competition in the neurotrophin model. **a** Model schematic: interactions between neurotrophins (BDNF and proBDNF), neurotrophin receptors (TrkB and P75^{NTR}), and cleaving protease (MMP9). **b** Outcome of synaptic stimulation where two synapses separated by a distance d innervate the same dendrite: I. The left synapse is stimulated with a burst of action potentials. II. Presynaptic activation causes the local release of MMP9 (yellow). III. Signal transduction into the postsynapse results in the spatially extended influx of calcium (purple shading). Calcium triggers the exocytosis of proBDNF (orange) and BDNF (green) into extracellular space. IV. MMP9 differentially cleaves proBDNF into BDNF at the stimulated synapse. V. Repeating this pattern of stimulation potentiates the stimulated synapse and depresses the unstimulated synapse (arrows). Symbols as in **a**. **c** Variables (all unitless, see Methods) in **a** upon stimulation of one synapse only; the unstimulated synapse is distance d away, as in **b**. Δ neurotrophin is the difference between BDNF and proBDNF. Scale bar is 1 s. **d** Percentage change in synaptic efficacy (of baseline) of the stimulated synapse (top) and the unstimulated synapse (bottom) as a function of input rate (in bursts per minute, after 1 min of continuous stimulation) and distance d . The analytical solution follows from a linearized version of the model (see Methods). **e** A burst-timing-dependent plasticity induction protocol where the temporal offset between pre- and postsynaptic bursts is varied²⁷. A single synapse innervates the dendrite. Purple shading indicates either pre- (left) or postsynaptic (right) activation. **f** Accumulator and neurotrophin variables under the burst pairing protocol with temporal offsets -1.5 s (left), 0.05 s (middle), and 1.5 s (right). Scale bar is 0.5 s. We assumed that the calcium from direct postsynaptic stimulation is stronger than that released by stimulation of a synapse (compare to **c** and see Methods). **g** Percentage change in synaptic efficacy (of baseline) as a function of temporal offset (data represent change in EPSP size from developing mouse LGN reproduced from ref. ²⁷). The arrows mark the temporal offsets displayed in **f**.

synaptic potentiation due to the relative dominance of BDNF over proBDNF-induced signaling, while longer offsets lead to depression (Fig. 1f, g). This type of plasticity in the neurotrophin model can be matched to a timing-dependent Hebbian learning rule described in the developing visual system, burst-timing-dependent plasticity (BTDP)²⁷. According to this rule, synaptic change is sensitive to the overlap between pre- and postsynaptic bursts on the timescale of several hundred milliseconds. Remarkably, the dependence of the neurotrophin model on burst-timing as in the BTDP rule is robust to perturbations in most parameters of the model except for the proBDNF/BDNF ratio, which can shift the BTDP curve into depression and eliminate synaptic competition (Supplementary Fig. 1).

In summary, the proposed neurotrophin model provides a mechanistic implementation for (1) the distance-dependent competition between differentially stimulated synapses and (2) the timing-dependent potentiation when pre- and postsynaptic activity overlap over developmentally relevant timescales of several hundred milliseconds. Identifying these two ingredients provides a key step towards a general framework for establishing

synaptic organization in development^{6,10} and reconciling different aspects of synaptic organization observed in the adult⁷⁻⁹.

A generalized neurotrophin-inspired model captures out-of-sync-lose-your-link plasticity. To establish a framework for synaptic organization, we generalized the neurotrophin model to a local dendritic learning rule independent from a specific biophysical implementation. The generalized model derives directly from neurotrophin interactions, and hence retains the two key properties of timing- and distance-dependent plasticity (Supplementary Fig. 2). Synaptic efficacy change depends on the accumulated presynaptic (pre) and postsynaptic (post) activity and a constant heterosynaptic offset related to the initial ratio of proBDNF to BDNF in the absence of extracellular conversion through MMP9 (see Methods),

$$\text{change in synaptic efficacy} = \text{post} \times (\text{pre} - \text{offset}) \quad (1)$$

This generalized neurotrophin-inspired model has the advantage that it can be analyzed mathematically, can be flexibly

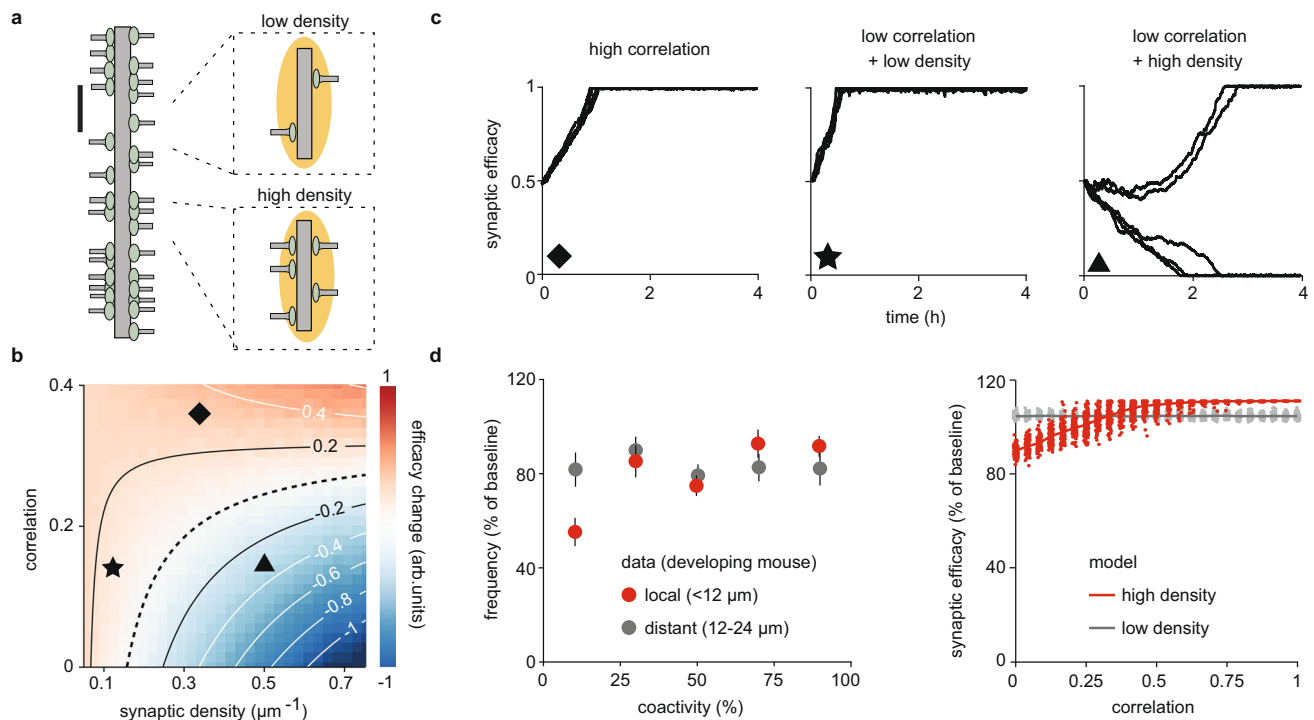


Fig. 2 Relating synaptic efficacy change to synaptic density and input correlation. **a** Schematic with randomly distributed synapses along a linear dendritic branch. All synapses receive Poisson input trains with identical pairwise correlations. Scale bar is 20 μm . **b** Average instantaneous change in synaptic efficacy as a function of input correlation and density. Contour lines are determined by analytics, while colors by simulation, averaging over time and synapses (negative synaptic efficacy change in blue, positive synaptic efficacy change in red). **c** Evolution of synaptic efficacy for five different synaptic inputs at various combinations of density and correlation as in **b** (diamond, star, and triangle at densities 0.312, 0.125, and 0.5 μm^{-1} and correlations 0.15, 0.35, and 0.15, respectively). For low correlation and high density, individual efficacy trajectories diverge due to random fluctuations in the inputs. As some synapses depress, the effective density decreases (the triangle moves to the left from a depression to a potentiation region as shown in **b**). **d** Left: Percentage change in synaptic transmission frequency after plasticity in the developing visual cortex relative to baseline as a function of coactivity for local (red) vs. distant (gray) synapses. Data from developing mouse visual cortex reproduced from ref. ⁶ and presented as mean values \pm SEM ($n = 11$ cells, pooled data of 352 synapses). Right: Percentage change in synaptic efficacy (of baseline) in our model as a function of correlation for synapses at high density (0.5 μm^{-1} , a synapse every 2 μm , red) and low density (0.05 μm^{-1} , a synapse every 20 μm , gray). Dots represent individual synapses.

implemented to apply to other signaling molecules, and hence, a broader cast of synaptic organization scenarios. This is especially important since the role of neurotrophins in the emergence of clustering of different stimulus features, as well as their interaction with plasticity-related proteins involved in tag-and-capture and synaptic crosstalk^{28–32} in adulthood, is unknown.

To determine how distance- and timing-dependent plasticity might drive the emergence of synaptic organization with respect to different stimulus features, we next investigated the consequences of these two model characteristics on the organization of multiple randomly distributed synaptic inputs on a linear dendritic branch. Under the assumption that synaptic efficacy changes on a much slower timescale than neural activity, the average change in synaptic efficacy can be expressed as a function of the synaptic input correlation (Eq. 11 in Methods). Therefore, the timing-dependent plasticity of synaptic inputs represented by the BTDP rule in our model translates into local plasticity that depends on input correlations³³. To investigate distance-dependent competition of multiple randomly distributed synaptic inputs on a dendritic branch, we varied the synaptic density. Locally, low synaptic density implies that pairs of synaptic inputs are on average far away from each other, while high synaptic density implies that pairs of synaptic inputs are on average near each other. Hence, local density relates to synaptic distance.

We derived the average change in synaptic efficacy as a function of two parameters: the input correlation and the synaptic density on the dendritic branch (Fig. 2a, b and Supplementary

Fig. 2). We identified three regimes: (i) at any synaptic density, if the synaptic input correlation is higher than a critical amount (Methods) then synapses stabilize (Fig. 2c, diamond), (ii) at low synaptic density, if the input correlation is lower than the same critical amount then synapses also stabilize (Fig. 2c, star), and (iii) at high synaptic density, if the input correlation is lower than the critical amount then synapses compete (Fig. 2c, triangle). Note that in regime (iii), synapses compete until a random subset is silenced, which reduces the effective density of the remaining synapses and eventually stabilizes them (Fig. 2b). The proposed generalization of the neurotrophin model thus implements Hebbian correlation-based plasticity at the single synapse³⁴ where synaptic efficacy is modulated by the local density of synaptic inputs on the dendrite, just like the implementation with interacting neurotrophins (Supplementary Fig. 2).

The generalized neurotrophin-inspired model for clustering enabled us to dissect how specific neurotrophin interactions influence the functional dependence of synaptic efficacy on input correlation and synaptic density. In particular, it is well established that BDNF can increase, while proBDNF can decrease the synaptic density on developing dendrites¹⁵. Applying those same perturbations to our model produces similar neurotrophin-induced changes in synaptic density, since the ratio of BDNF to proBDNF determines the synaptic density at which potentiation and depression are balanced through the heterosynaptic offset (Supplementary Fig. 3).

Additionally, the generalized model remains relevant for the emergence of synaptic organization in development. Key

properties that are accounted for are the slow timescales of the pre- and postsynaptic accumulators that respectively correspond to the time constants of MMP9 and postsynaptic calcium and give rise to the developmental BTDP plasticity rule (Supplementary Fig. 2). Additionally, the model implements the lateral postsynaptic spread of calcium, consistent with developmentally prevalent shaft synapses which can interact over long distances more easily than adult spine synapses³⁵.

As a result, the synaptic competition in our model (Fig. 2b, c) resembles a local out-of-sync-lose-your-link plasticity rule underlying the emergence of clustering in the developing visual cortex and hippocampus⁶. According to this rule, synaptic inputs on developing pyramidal dendrites either increase or decrease the success rate of synaptic transmission depending on their synchrony with their nearby, but not distant, neighbors (Fig. 2d, left). To directly compare our model to this experimental data, we visualized the synaptic efficacy as a measure of synaptic transmission success at two different densities (Fig. 2b): a high density of $0.5 \mu\text{m}^{-1}$ (a synapse every $2 \mu\text{m}$), which corresponds to local synapses in the data ($<12 \mu\text{m}$), and a low density of $0.05 \mu\text{m}^{-1}$ (a synapse every $20 \mu\text{m}$), which corresponds to distant synapses in the data ($12\text{--}24 \mu\text{m}$). Our model generates a similar out-of-sync-lose-your-link rule where local synaptic inputs (high density) are depressed if weakly correlated and potentiated if strongly correlated. In contrast, distant synaptic inputs (low density) are stabilized independent of correlation (Fig. 2d, right). A similar out-of-sync-lose-your-link structural plasticity, without the local postsynaptic component, has also been studied previously to solve more abstract classification tasks^{36–38}.

Taken together, our generalized model based on neurotrophin interactions with properties of timing- and distance-dependent competition provides a general framework to study the emergence of synaptic organization on dendritic branches innervated by multiple synaptic inputs. The model relates synaptic efficacy change to synaptic input correlation and local density and can capture the depression of weakly correlated neighboring inputs embodying out-of-sync-lose-your-link plasticity, implicated in the emergence of functional synaptic clustering during development.

Retinal wave input and synaptic turnover drive synaptic orientation clustering in a model of the ferret visual cortex. We next tested the potential of the above-developed model inspired by neurotrophin interactions to organize synaptic inputs in the developing visual cortex driven by spontaneous activity propagated from the sensory periphery^{39,40}. We simulated retinal waves⁴¹ and converted them to cortical synaptic input via a two-stage linear-nonlinear (LN) model (Fig. 3a and Methods). For the linear filter we used a spatially oriented Gabor with positive and negative elongated subregions based on receptive field measurements of individual spines on pyramidal neurons in the adult mouse visual cortex⁸. Each Gabor receptive field is characterized by three parameters: center, described in polar coordinates, diameter, and orientation, with a value between 0° and 360° (Fig. 3a). We inferred the receptive field diameter and center distribution for the visual cortex of two species, mouse and ferret (see Methods). An exponential nonlinearity converts the linearly filtered retinal waves into instantaneous firing rates from which activity is generated via a Poisson process (see Methods). Thus, in the LN model, a synapse probabilistically receives bursts of action potentials when the Gabor filter is stimulated by a retinal wave traveling in the direction that matches the filter orientation (Fig. 3a). Since activation of a synapse depends on the appropriate stimulation of its associated receptive field, synapses with nearby receptive field centers in visual space and a small difference in

orientation experience correlated input (Fig. 3b). White noise stimulation does not produce correlations for any orientation difference due to the lack of spatiotemporal structure to consistently activate nearby receptive fields (Fig. 3b).

Using a receptive field diameter and a center distribution from the ferret visual cortex⁹, we placed synaptic inputs with randomly oriented receptive fields on a non-branching, linear dendrite—as a model of small, approximately linear portions of real dendritic trees—and stimulated them with retinal waves⁴¹ filtered through an LN model. Neighboring synapses with mismatched orientations receive uncorrelated input as they are rarely activated by the same retinal wave and consequently depress. To prevent their irrevocable elimination, we modeled an activity-dependent mechanism of structural plasticity, which preserves the total number of synaptic inputs on a dendritic branch^{42,43} (Fig. 3c). Upon the removal of a synapse, a new synapse is placed at a random position on the dendritic branch with a randomly oriented receptive field and center in visual space sampled from the experimentally measured distribution in the ferret visual cortex⁹ (see Methods).

Throughout the simulation, synapses compete and are either stabilized or eliminated and turned over until nearby synapses share a similarly oriented receptive field (Fig. 3d). The number of turnovers per day decreases rapidly, with all remaining turnovers due to a small fraction of synapses (Fig. 3e). Despite substantial turnover during the first three days of the simulation, $\sim 60\%$ of synapses present at the beginning of the simulation do not experience any turnover and form a scaffold around which the remaining synapses stabilize (Fig. 3e, inset). Synapses that do not experience any turnover throughout the entire simulation tend to have a smaller-than-chance orientation difference from each other.

We found that all nearby synapses in the stable state share similarly oriented receptive fields, a type of clustering that we call orientation clustering (Fig. 3d right, f). Orientation clustering has been found in layer 2/3 of the adult ferret visual cortex *in vivo*^{7,9}. This orientation clustering further generates functional synaptic clustering in our simulations, where correlations between pairs of synapses trained with retinal wave input decay with distance at the same rate as during spontaneous activity in layer 2/3 of the adult ferret visual cortex (Fig. 3g). When using this relationship to characterize the size of the formed clusters, we found that cluster size strongly depends on the spatial spread constant of postsynaptic calcium (Fig. 3h and Supplementary Fig. 4). Therefore, we suggest that the different sizes of orientation clusters found in different species^{9,12}, variability across different cells of the same animal⁹, as well as potential differences in development vs. adulthood, could be the result of different amounts of postsynaptic calcium spread. Orientation clustering also emerges when we implement the full complement of neurotrophin interactions in our model (Supplementary Fig. 2). While we do not know whether neurotrophins directly drive the orientation clustering observed in the adult brain, our results show that slow developmental timescales of plasticity and input correlations together with timing- and distance-dependent synaptic competition are sufficient.

Orientation and functional clustering do not emerge with white noise stimulation (Fig. 3f), nor with a spike-timing-based plasticity (STDP) rule that induces synaptic change based on precise spike timing (Supplementary Fig. 5), due to the mismatch of timescales between the input patterns and the induction of plasticity^{24,27,33}. Including a dendritic nonlinearity preserves clustering and decreases the average nearest neighbor distance (Supplementary Fig. 6). Similarly, when requiring the synchronous activation of multiple neighboring synapses for the induction of plasticity^{26,34}, clustering persists when the timing

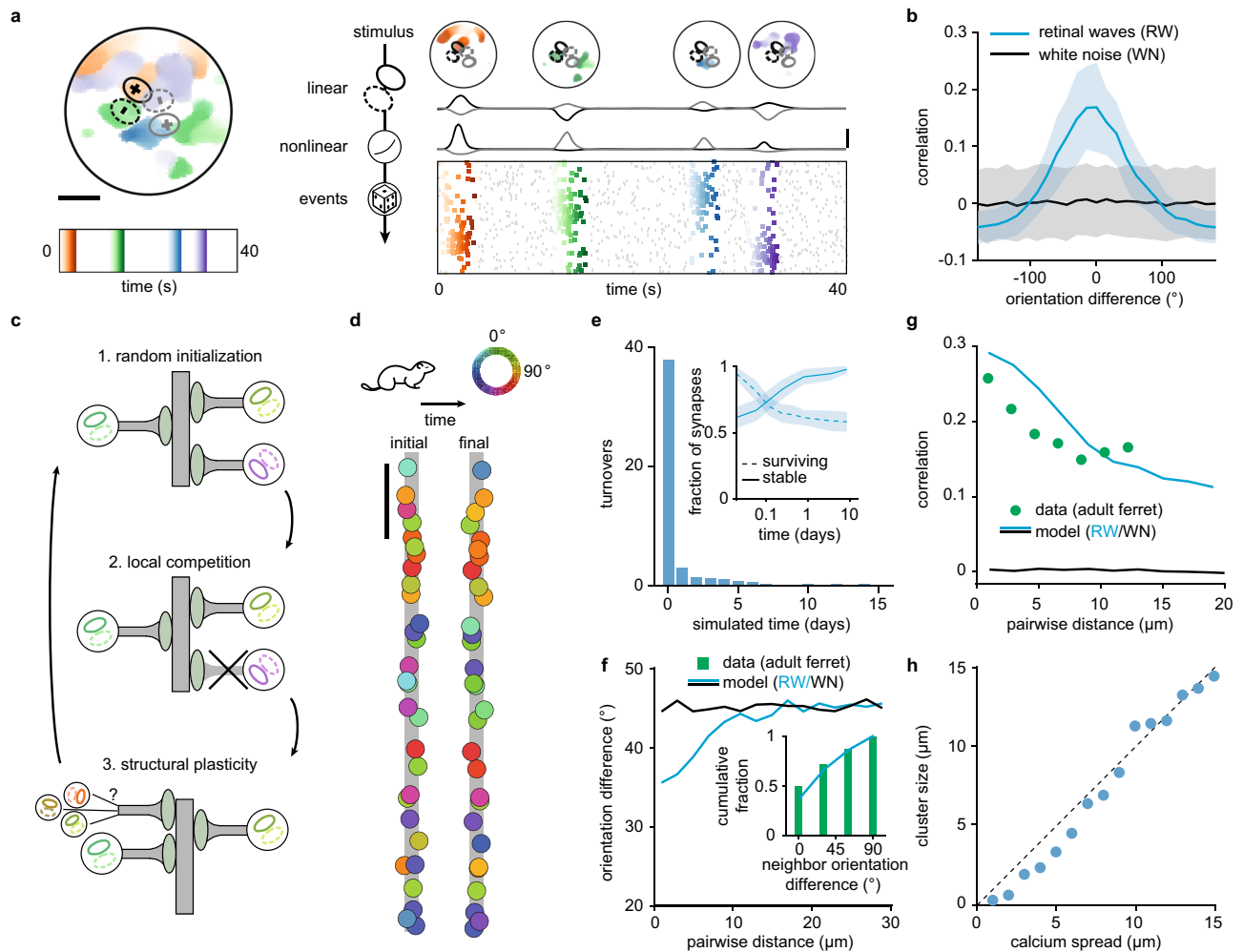


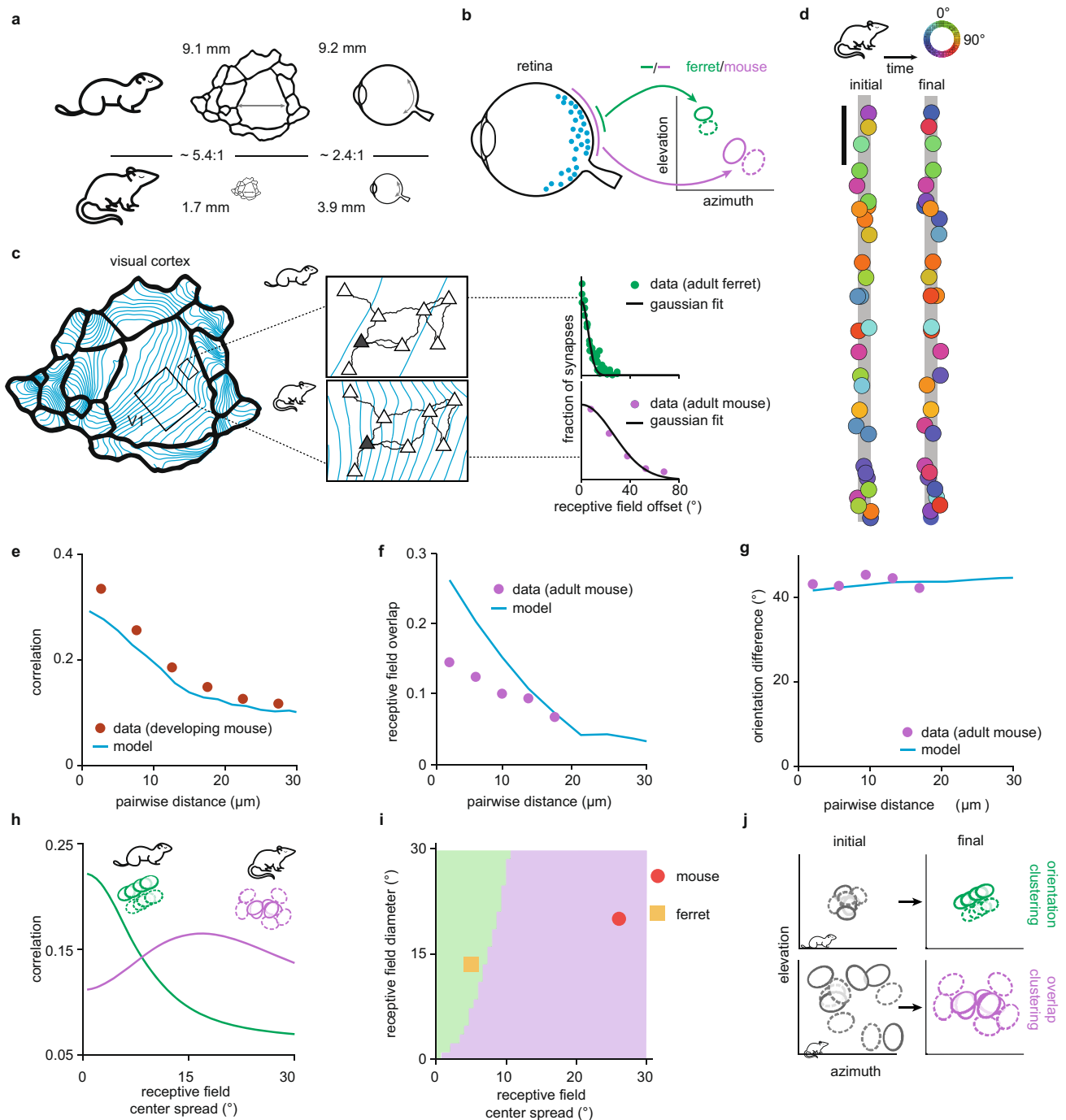
Fig. 3 Retinal wave input and synaptic turnover produce orientation clustering on a dendritic branch in a model of the ferret visual cortex. **a** (Left) Illustration of 40 s of retinal wave input. The color gradients indicate different time points. Scale bar is 30° in visual space. Superimposed are two schematics of Gabor receptive field filters with positive (full line) and negative (dashed line) components. (Right, from top) Four spontaneous retinal waves as stimuli, linearly filtered responses, and nonlinear outputs for the two oriented Gabors on the left. Scale bar is 1 Hz. Rows in raster plot correspond to firing events from different receptive fields, sorted from top to bottom by orientation. Gray events represent background noise. **b** Mean correlation as a function of the difference in orientation of receptive fields stimulated with retinal waves (RW) or white noise (WN) input. Shaded area indicates standard deviation. **c** Local correlation- and distance-dependent competition, together with structural plasticity, drive the formation of synaptic clusters. **d** Example of the emergence of orientation clustering on a linear dendrite using ferret cortex receptive field diameter and center distribution with retinal waves over 2 simulated weeks. Color of synapses indicates the orientation preference of the associated receptive field. Scale bar is $20\ \mu\text{m}$. **e** Number of turnovers as a function of simulated days. Inset: Semi-log plot of the mean survival fraction (synapses present at the beginning of simulation) and the stable fraction (synapses present at the end of the simulation) as a function of simulated days. Shaded area indicates standard deviation. **f** Orientation difference between pairs of synapses as a function of distance in the model with retinal waves or white noise. Inset: Cumulative fraction of orientation difference between an individual synapse and its nearby neighbors (less than $3\ \mu\text{m}$ away) in the model and experiments (data from adult ferret visual cortex reproduced from ref. 7). Difference computed after taking the orientation modulo 180° (see Methods). **g** Correlation between pairs of synaptic inputs in the model driven by retinal waves or white noise, and correlation between calcium signals of spontaneous synaptic activity (data from adult ferret visual cortex reproduced from ref. 9) as a function of distance. **h** Cluster size computed as the standard deviation of the best Gaussian fit to the pairwise correlation vs. distance (see Methods and g), as a function of the postsynaptic calcium spread. Dashed line indicates the identity line.

and spacing thresholds for such cooperative plasticity are consistently satisfied by the developmental slow timescales of activity and low synaptic density (Supplementary Fig. 6).

Otherwise, clustering is remarkably stable against perturbations of most model parameters (Supplementary Fig. 1). Clustering is, however, sensitive to changes in the heterosynaptic offset, which can shift plasticity into an exclusively potentiating or depressing regime (Supplementary Fig. 1). Since our model is based on neurotrophin interactions, we can interpret perturbations to the heterosynaptic offset as perturbations in the balance between BDNF and proBDNF signaling (Supplementary Fig. 3). For

instance, exogenous application of either proBDNF or BDNF can abolish clustering *in vitro* within minutes¹⁰. Our model also makes predictions for how additional perturbations to the conversion between the two neurotrophins, or the receptors to which they bind, might affect synaptic efficacy and clustering (Supplementary Fig. 3).

In summary, with a synaptic receptive field diameter and a center distribution from the ferret visual cortex, our model generates local clusters of similarly oriented and, therefore, functionally correlated synaptic inputs on a dendritic branch based on correlated input from retinal waves. Therefore, a



neurotrophin-inspired model for clustering supports the emergence of local synaptic organization in the ferret cortex.

Clustering of different stimulus features in mouse and ferret.

In contrast to the ferret, nearby synapses on pyramidal neuron dendrites in the mature mouse visual cortex do not share a preference for the same orientation^{8,19,20,44}. However, nearby synapses in the mouse visual cortex still exhibit correlated activity during development⁶, and hence are functionally clustered. We next investigated whether our modeling framework can also generate the functional clustering observed in the mouse.

One striking difference between mouse and ferret is the size of their retina and visual cortex, with each being about two vs. five times smaller in the mouse than in the ferret, respectively⁴⁵

(Fig. 4a). Consequently, the average receptive field diameter in the mouse visual cortex is about twice as large, and the cortical magnification of visual space about five times smaller than in the ferret⁹ (Fig. 4b, c). Consistent with these anatomical differences, a pyramidal neuron in the mouse visual cortex receives inputs from a considerably larger region of visual space than in the ferret⁹ (Fig. 4c, middle). The difference in the sampled region of visual space can be captured by the relative broadness of the distribution of receptive field centers characterized experimentally in the two species^{8,9}, a parameter that we call the receptive field center spread (Fig. 4c, right). We implemented our neurotrophin-inspired model for clustering using a larger receptive field diameter and center spread as measured in the mouse visual cortex⁸ to determine the synaptic organization driven by retinal waves (Fig. 4d). We observed functional synaptic clustering

Fig. 4 **Overlap clustering, but not orientation clustering, emerges on a dendritic branch in a model of the mouse visual cortex.** **a–c** Schematic of the anatomical argument for two qualitatively different types of clustering in mouse and ferret. Note that we depict ferret cortex as a scaled-version of mouse cortex. **a** Comparison of cortex and retina size in mouse and ferret (measures from ref. 45). **b** Schematic linking retina size (left) to receptive field diameter in the cortex (right). **c** Schematic linking cortex size to receptive field center spread. 1 mm of visual cortex spans a larger region of the total visual space (left, blue lines represent iso-contours at -7° 46) in the mouse than in the ferret. Since the dendritic trees of pyramidal neurons (triangles) in the two species are comparable in size, a target neuron (gray) pools input from a smaller region of visual space in ferret (top middle) than in mouse (bottom middle). The synaptic receptive fields on the dendritic tree of the target neuron are distributed in a small (ferret, top right) or large (mouse, bottom right) region in visual space. The receptive field spread is quantified by the standard deviation of the distribution of their centers (5.3° for ferret and 26° for mouse, data reproduced from refs. 8,9). **d** Example demonstrating lack of orientation clustering on a linear dendrite using mouse cortex receptive field spread and diameter with retinal waves over 2 simulated weeks. Scale bar is $20\ \mu\text{m}$. **e** Correlation between pairs of synaptic inputs in the model driven by retinal waves, and correlation between calcium signals of spontaneous synaptic activity (data from developing mouse visual cortex reproduced from ref. 6) as a function of distance. **f** Receptive field overlap for pairs of synaptic inputs as a function of distance in the model and experiments (data from adult mouse visual cortex reproduced from ref. 8). **g** Orientation difference between pairs of synapses as a function of distance in the model and experiments (data from adult mouse visual cortex reproduced from ref. 8). **h** Average correlation between nearby synapses as a function of receptive field center spread for simulated synaptic receptive fields that are either orientation clustered (green) or overlap clustered (purple). **i** Varying receptive field center spread and diameter in our model dichotomizes the area in which orientation clustering (green) or overlap clustering (purple) produces higher average correlation (see Methods). **j** Schematic showing how orientation (top) and overlap (bottom) clustering emerge from a combination of receptive field diameter and center spread.

during spontaneous activity, as measured during development⁶ (Fig. 4e). Interestingly, this functional organization is the result of synaptic clustering for receptive field overlap, rather than orientation (Fig. 4d–g). Such clustering of synapses with overlapping receptive fields is consistent with recent measurements in the adult mouse visual cortex⁸. We refer to this type of clustering as overlap clustering to contrast it with the orientation clustering observed in the ferret. Adding irregularities to the Gabor synaptic filters further improves the match between model and data (Supplementary Fig. 7).

To understand the principal factors that determine the type of clustering, we computed the correlations of synaptic activity resulting from the overlap of simulated synaptic receptive fields—that are either orientation clustered or overlap clustered—upon perturbing the spread of their centers on the dendritic branch (Fig. 4h). The orientation clustered receptive fields produce the highest correlations when the receptive field center spread is small ($\sim 5^\circ$, as in the ferret). With increasing spread, the overlap between the positive and negative components of the Gabor filter increases, which decreases correlations (Fig. 4h; green). Conversely, the receptive fields clustered by overlap produce the highest correlations when receptive field center spread is larger (~ 15 – 20° , as in the mouse) (Fig. 4h; purple).

Next, we determined the prevalence of orientation vs. overlap clustering by simultaneously varying the two anatomical parameters, the center spread, and the diameter of Gabor receptive fields in the visual cortex, and without modeling other differences in morphology, dendritic arborization, or synaptic density (Fig. 4i). Interestingly, for a very small receptive field diameter, only small receptive field center spread yields orientation clustering in our framework. Consistent with this, in the macaque visual cortex, which has a small receptive field diameter and receptive field center spread, orientation clustering has recently been reported¹². Therefore, our model explains the emergence of synaptic clustering with respect to different stimulus features in the mouse and ferret. Without modeling other differences in the visual systems, we find that clustering emerges from maximizing the amount of correlation as a function of the geometric arrangement of synaptic receptive fields in the different species (Fig. 4j).

Backpropagating action potentials establish global orientation clustering on ferret dendrites. We next asked whether the local organization of synaptic inputs achieved by our model also

supports the emergence of global organization of synaptic inputs on the dendritic tree. To probe interactions between the soma and synapses on different dendritic branches in a biologically realistic framework beyond the linear dendrites considered so far, we implemented our plasticity model on a morphologically realistic layer 2/3 pyramidal neuron (Fig. 5a). We modeled a somatic signal that affects the dendrite in the form of a backpropagating action potential (bAP) whenever the linearly summed input over all synapses exceeds a fixed threshold. The bAP results in a calcium influx into the proximal and distal dendritic branches that attenuates with distance from the soma (Fig. 5b, c)⁴⁷. As a result, the calcium signal at proximal synapses in our model neuron is dominated by somatic activity, while distal synapses are almost independent of the soma (Fig. 5c) as found experimentally⁴⁸.

Since bAPs are known to induce the release of neurotrophins⁴⁹, we investigated how an attenuating bAP affects the correlation- and distance-dependent competition when implementing the full complement of neurotrophin interactions. We found that a bAP naturally extends both mechanisms over larger spatial scales, so that synapses near the soma experience stronger depression than those farther away from the soma when they are activated asynchronously to the soma, and stronger potentiation when activated in synchrony with the soma (Supplementary Fig. 8). Therefore, the addition of a bAP should not affect local synaptic organization on branches far away from the soma, but reinforce it near the soma.

Using a small receptive field diameter and center spread for the ferret visual cortex, our model generates local orientation clusters along the entire dendritic tree just like on the linear dendrite (Fig. 5d, e and Supplementary Fig. 9). By including bAPs, global organization on the entire dendritic tree also emerges. Synaptic inputs on proximal dendritic branches acquire orientation preferences similar to the soma due to the weak decay of bAP signaling, while inputs on distal dendrites have orientation preferences that are independent of the soma due to the strong bAP attenuation (Fig. 5e). Therefore, including bAPs homogenizes proximal dendritic branches to the orientation preference of the soma while leaving distal synapses unconstrained (Fig. 5e, inset), and hence variable across individual simulations (Supplementary Fig. 9). We characterized the degree of branch heterogeneity by computing the circular dispersion, i.e., the difference between the orientation preference of individual synapses and the soma (Fig. 5d and Methods). We found that bAP attenuation controls the extent of cluster homogeneity along the dendritic tree, with weaker bAP attenuation leading to larger

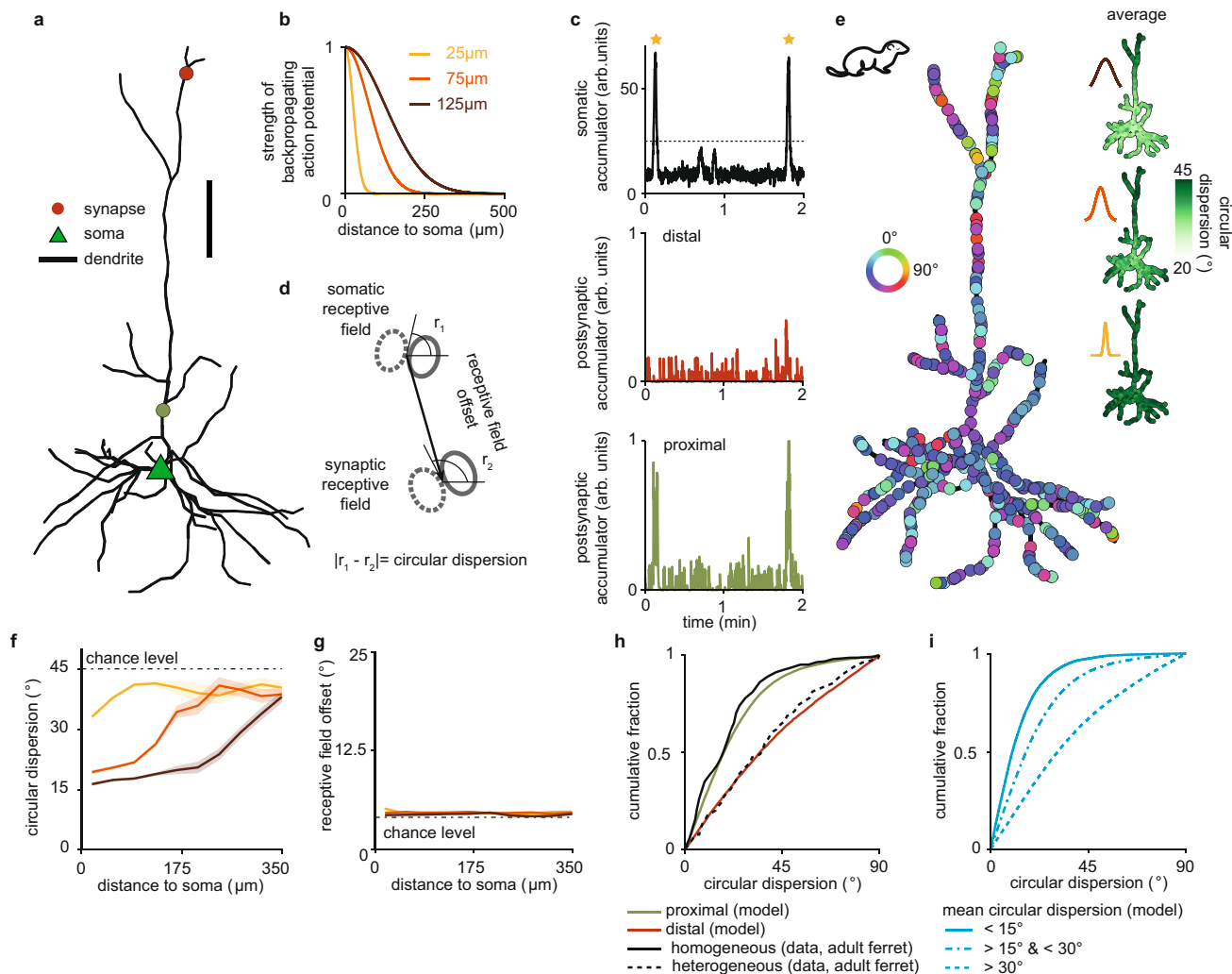


Fig. 5 A backpropagating somatic signal drives heterogeneously and homogeneously clustered dendritic branches in a model of the ferret visual cortex. **a** Illustration of a reconstructed pyramidal cell from layer 2/3 (Allen Cell Type database, ID 502269786). Triangle indicates soma. Circles indicate synaptic sites. Scale bar is 50 μm . **b** Strength of backpropagating action potentials (bAPs) for different attenuation factors as a function of path distance from the soma. **c** Top: Sample trace of somatic activation under retinal wave stimulation after five simulated days. Asterisks indicate the initiation of multiple global somatic signals in the form of a burst of bAPs after threshold crossing (dashed line). Middle, Bottom: Postsynaptic calcium traces of a distal (middle) and a proximal (bottom) synapse (indicated in **a**). **d** Schematic to illustrate circular dispersion and receptive field offset (see Methods). **e** Emergence of global organization of orientation preference on the reconstructed pyramidal cell using ferret cortex receptive field spread and diameter. Color of synapses indicates the orientation preference of the associated receptive field. Inset shows the circular dispersion averaged over 62 simulations for the three different attenuation factors in (**b**). **f, g** Circular dispersion (**f**) and receptive field offset (**g**) between synapse and soma for the three different bAP attenuation factors in (**b**) and as a function of path distance from the soma. Shaded areas indicate 95% confidence interval around the mean. **h** Cumulative fraction of circular dispersion for one bAP attenuation factor (75 μm) in the model, and different types of clustered branches in experiments (data from adult ferret visual cortex reproduced from ref. ⁷). **i** Same as **h** for branches with low (<15°), intermediate (15°–30°), and high (>30°) mean circular dispersion in the model.

homogeneous portions of the tree near the soma (Fig. 5f). Increasing bAP frequency controls the degree of homogeneity of the proximal tree (Supplementary Fig. 10). Consistent with experimental reports⁹, our model does not produce global organization of receptive field offsets, which are randomly distributed for synapses along the entire dendritic tree (Fig. 5g and Supplementary Fig. 9).

Different degrees of heterogeneity of synaptic orientation preference have been reported in the ferret visual cortex⁷, where experiments distinguished between homogeneous branches, with a mean circular dispersion below 15°, and heterogeneous branches, with a mean circular dispersion above 30°. We compared the cumulative distribution functions of the homogeneous and the heterogeneous branches to proximal (less than

two times the attenuation factor) and distal (more than two times the attenuation factor) synapses in our model, respectively, and found good quantitative agreement (Fig. 5h). Computing the distribution of circular dispersions of spines on branches with mean circular dispersion between 15° and 30° in our model revealed branches with intermediate heterogeneity (Fig. 5i). While from the experiments it is not clear whether homogeneous (heterogeneous) branches tend to be more proximal (distal) to the soma, our results predict the global organization of orientation selectivity and suggest that bAP attenuation in different neurons may underlie branch orientation heterogeneity.

In summary, the same modeling framework that produces local orientation clustering of synaptic inputs predicts global synaptic organization on a morphologically realistic model of a layer 2/3

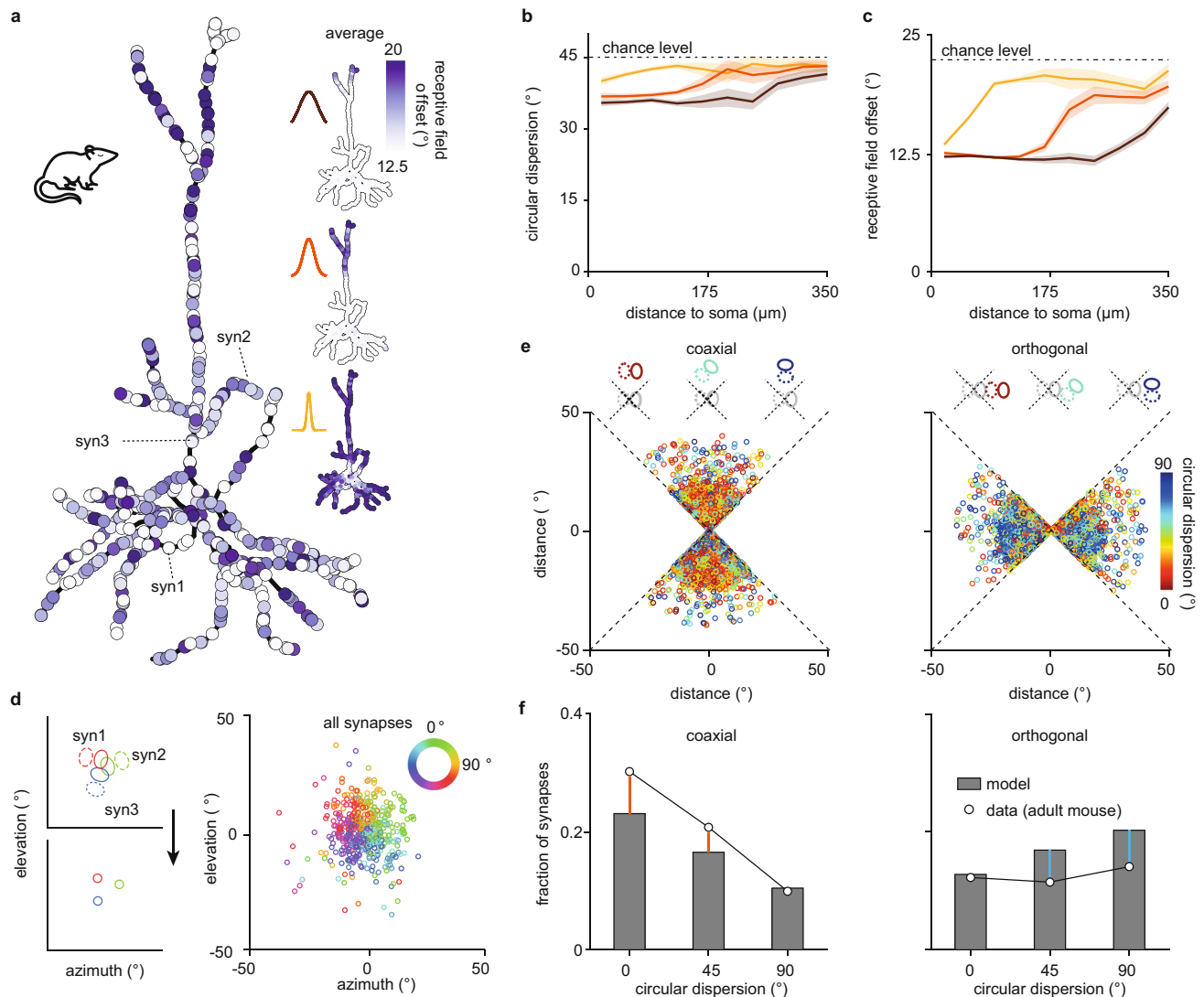


Fig. 6 Backpropagating action potentials establish a dendritic map of visual space in a model of the mouse visual cortex. **a** Receptive field offset on the reconstructed pyramidal cell with synapses with a large receptive field center spread corresponding to mouse. Color of synapses indicates the receptive field offset of the associated receptive field. Inset shows the receptive field offset averaged over 80 simulations for the three different attenuation factors (25, 75, and 125 μm) in Fig. 5b. **b, c** Circular dispersion (**b**) and receptive field offset (**c**) for the three different bAP attenuation factors in Fig. 5b and as a function of path distance from the soma. Shaded areas indicate 95% confidence interval around the mean. **d** (Left) Illustration of three synaptic receptive fields (see **a**) in visual space (top) and the same receptive fields represented as circles with color denoting orientation preference (bottom). (Right) All synaptic receptive fields from one simulation. **e** Receptive field centers in coaxial (left) and orthogonal (right) visual space colored according to their circular dispersion averaged over 80 simulations. Preferred orientation of the soma is vertical. **f** Histogram of circular dispersions between synaptic and somatic receptive fields in coaxial (left) and orthogonal (right) visual space in the model and experiments (data from adult mouse visual cortex reproduced from ref. ⁸). Preferred orientation of the soma in each schematic is always vertical, as indicated by a gray somatic receptive field in the center, while the preferred orientation of a synapse varies, as indicated by a colored receptive field either in coaxial or orthogonal space (see **e**).

pyramidal neuron with synapses on proximal dendrites sharing similar orientation preference with the soma. We suggest that an attenuating somatic signal is the main factor behind homogenizing some branches of the tree to the same orientation preference as the soma while leaving other branches more heterogeneous and uncorrelated to the soma as observed in the ferret visual cortex⁷.

Backpropagating action potentials establish visual topography of receptive field centers on mouse dendrites. To study emergent global organization in our model of a mouse pyramidal neuron, we considered a larger receptive field diameter and center spread as measured in the mouse (Fig. 4a) and investigated the

influence of a somatic bAP signal. Synaptic inputs on the reconstructed pyramidal neuron do not exhibit local orientation clustering, nor global homogenization of orientation preference except for a small bias, as observed experimentally^{8,19,20,44} (Fig. 6b and Supplementary Fig. 9). Synaptic inputs, however, do exhibit local overlap clustering as without a bAP, as well as global organization on the dendritic tree in the presence of a bAP, with synapses close to the soma having overlapping receptive fields with many other synapses close to the soma (Supplementary Fig. 9). As expected from the role of bAPs in reinforcing potentiation and depression near the soma (Supplementary Fig. 8), bAPs homogenize receptive field overlap close to the soma where the bAP influence is the strongest.

In the presence of a bAP, proximal synapses stabilize only if their receptive fields overlap with the somatic receptive field constraining their resulting receptive field offset to be small. Hence, the bAP brings receptive fields of proximal synapses to be on average centered closer to the somatic receptive field compared to the receptive fields of distal synapses (Fig. 6a, c). Distal synapses do not have this constraint, resulting in large cell-to-cell variability at distal branches (Supplementary Fig. 9). This relationship is modulated by bAP attenuation, with weak attenuation increasing the number of synapses centered near the somatic receptive field (Fig. 6c). We refer to this global organization as a dendritic map of visual space. Indeed, in pyramidal neurons of the mouse visual cortex, proximal vs. distal synapses respectively have a tendency to respond to more central vs. peripheral regions of visual space relative to the somatic receptive field center^{8,50}. This result is in contrast to the ferret⁹; also in our model, a bAP does not generate a dendritic map of visual space (Fig. 5g) because receptive fields of synaptic inputs proximal to the soma already overlap significantly due to their similar orientation preference to the soma. Hence, shifting their centers toward the somatic center does not increase their overlap and correlation as much as changing their orientation preference (Fig. 4h).

As a result of the global organization of receptive field overlap and dendritic maps generated in our model with bAPs of mouse visual cortex, synapses with nearby receptive field centers in visual space have a similarly oriented receptive field (Fig. 6d). We consequently observed that the distribution of receptive field orientations in different regions of visual space generated in the model has an interesting structure. In particular, synaptic receptive fields positioned along or close to the axis of the somatic receptive field, i.e., in the coaxial space^{8,51}, appear to have a similar orientation to the soma (Fig. 6e, left). This mirrors the distribution of circular dispersions in the coaxial region of visual space in the mouse visual cortex⁸ (Fig. 6f, left). The functionally specific organization in coaxial space agrees with the over-representation of edges with the same orientation along a common axis found in natural images called colinearity and could be used for the detection of elongated edges^{8,52,53}. Interestingly, in our model, synapses in the remaining region of visual space, called the orthogonal space⁸, are more likely to be oriented orthogonally to the soma (Fig. 6e, right). This over-representation of large circular dispersions compared to experimental data⁸ (Fig. 6f, right) is, however, consistent with another property found in natural images, called cocircularity, where two segments with different orientation have a tendency to be tangent to the same circle, and which could be used for the detection of continuous and smooth object boundaries^{52,53}. We believe that the discrepancy between experiments⁸ and our model might stem from undersampling in the experiments or from additional pruning of connections between cells with large orientation differences after eye opening⁵⁴. These results suggest that, even before the onset of vision, spontaneous activity contains sufficient spatiotemporal information to organize synaptic receptive fields into the orthogonal and coaxial portions of visual space for the detection of elongated edges or continuous boundaries in natural images. This has strong implications for the computational strategies of these neurons and their integration into local microcircuits.

Taken together, our model generates global, in addition to local, organization of synaptic inputs on the dendrites of cortical neurons in the mouse for different features than in the ferret by only including anatomical differences in their visual cortices in terms of the spread and diameter of synaptic receptive fields. In our framework, both the emergence of a retinotopic gradient along the dendritic tree, as well as the accumulation of co-aligned

(orthogonally-oriented) synapses in the coaxial (orthogonal) portion of visual space, can be explained through the homogenizing influence of bAPs. Therefore, our model explains the emergence of synaptic organization across scales and in two different species with respect to different stimulus features.

Discussion

Dendritic compartmentalization of synaptic inputs achieved by clustering has been postulated to enhance the computational capacity of neurons³⁷. Yet, direct experimental evidence of clustering during development^{4–6,10} and with respect to different stimulus features in different species in the adult^{8,9,12} has only recently emerged. At the same time, recent work has revealed disparate results regarding the global order of synaptic inputs on the entire dendritic tree^{8,9}. To reconcile these findings, we developed a computational framework supported by a specific biophysical implementation based on neurotrophins for the emergence of both local and global synaptic input organization on cortical dendrites in two different species. Combining developmentally inspired synaptic plasticity with retinal wave input and species-specific features of synaptic receptive fields, our framework supports the establishment of local functional clustering for orientation in the adult ferret vs. receptive field overlap in the adult mouse visual cortex^{8,9,12}. Including an attenuating somatic signal generates global organization of different features in the ferret and mouse cortex, establishing soma-to-dendrite maps of orientation selectivity and visual topography, respectively. We found that the interaction between two parameters, the cortical magnification factor of visual space and the receptive field diameter, drives these species-specific differences. Interestingly, these parameters can also explain the population-level (columnar vs. salt-and-pepper) organization in the ferret vs. mouse visual cortex⁴⁵, indicating that the same universal developmental process modulated by variations of cortex and retina size can produce both dendritic and population-level organization.

Relationship to previous modeling studies on clustering. While our work focuses on the establishment of stimulus feature tuning and its organization, previous modeling studies investigated other aspects of synaptic clustering. These include the robust and efficient encoding of memories through activity-dependent plasticity operating over hours^{37,38}, the increase of a cell's computational capacity⁵⁵, and the linking of multiple memories across extended periods⁵⁶. An alternative normative approach proposed the generation of synaptic clusters as the Bayes-optimal solution to a classical conditioning task with unreliable synaptic transmission⁵⁷. However, this model lacked a mechanism for clustering of correlated inputs from different axons. To our knowledge, our framework is the first to explain the emergence of activity-dependent synaptic organization of different stimulus features in a developmental setting and relate it to that in the adult.

Generality of our modeling framework. Since neurotrophins, calcium, and MMP9 have been implicated in the emergence of functional synaptic clustering during development^{6,10}, we based our model for clustering on interactions between these molecules, although additional signaling pathways are likely to be involved in synaptic organization^{58–60}. A generalization of this model that derives directly from neurotrophin interactions can be flexibly implemented to apply to other signaling molecules. Possible alternative mechanisms include synaptic tag-and-capture, where plasticity-related-proteins mediate activity-dependent cooperation and competition^{28–30}, synaptic crosstalk through the interaction of Rho-family GTPase-mediated proteins, which are in fact

modulated by BDNF and involved in structural plasticity^{31,32}, or the NMDAR-mediated amplification of calcium signals^{21,34}. For the local heterosynaptic depression of unstimulated synapses, alternatives to the neurotrophin mechanism include the activation of calcineurin, IP3Rs, and group I mGluRs²⁶ or Arc-targeting of inactive synapses^{50,61}. Similarly, the functional roles of MMP9 and calcium could equivalently be filled by postsynaptic depolarization, NMDAR activation, endocannabinoid or nitric oxide signaling, or by more complex diffusible plasticity-related products⁶². Thus, our predictions regarding the organization of synapses are not contingent on a specific biophysical implementation of our model, as long as it implements distance- and timing-dependent competition between synapses, and integrates slow developmental activity patterns matched to the timescales of plasticity.

Origin of clustered synaptic input. A prominent source of excitatory inputs to layer 2/3 pyramidal neurons comes from layer 4 neurons⁵¹, which likely obtain their orientation selectivity by combining On and Off center-surround receptive fields of thalamic feedforward inputs⁶³. Our modeling framework also supports the concurrent emergence and clustering of orientation selectivity in the cortex through the clustering of On and Off thalamocortical synapses (Supplementary Fig. 11). Also, pyramidal cells in the mouse and ferret visual cortex are already orientation-selective at⁵⁴ and before^{64,65} eye opening, providing another likely source of the synaptic Gabor receptive fields in our model.

Relationship between developing and mature cortex. Several factors make our model appropriate for the establishment of synaptic organization in development: the high turnover of synapses, the ability of synaptic inputs to interact over long distances, and the slow timescale of spontaneous activity and neurotrophin interactions. Therefore, in this developmental setting, STDP rules that operate on fast timescales involving several milliseconds do not generate clustering (Supplementary Fig. 5), in agreement with other studies of developmental plasticity^{24,27,33}. While early development is a particularly opportune time for the emergence of synaptic organization^{4–6,10}, it is currently unknown how clusters formed during development relate to those observed in the adult animal. Given the continued turnover of synapses in the adult brain⁴³ and the formation of new clusters following altered sensory experience⁵⁸ and learning^{59,60}, it is a priori unclear whether the clusters formed during early development persist into adulthood. Our developmentally inspired model for synaptic competition combined with correlated activity from retinal waves is sufficient to produce functional and feature-specific clustering as in the adult and can provide a backbone for clustering even when the density of synapses increases dramatically. Already-established clusters in our model can be preserved by decreasing the postsynaptic spread in calcium²¹ (Supplementary Fig. 12), although other changes (such as the onset of inhibition, postsynaptic thresholding through a nonlinearity, or a decrease in proBDNF level) would be equally suited. This supports an interpretation where development equips dendrites with basic building blocks such as feature selectivity from which other functional properties are derived in adulthood. It would be interesting to investigate whether context-specific clustering as in the retrosplenial⁶⁰ or the motor⁵⁹ cortex occur alongside (rather than in competition with) clusters formed during development, as described in the auditory system of the juvenile barnowl⁵⁸, and how our proposed plasticity mechanism might interact with STDP rules relevant in the adult⁶⁶.

Functional role of clustered synapses. We propose three situations where synaptic input clustering may be beneficial for a neuron. (1) The transient, precise synchronization of even a small group of synapses (the exact number of synapses required in vivo is unknown³⁴) can result in the nonlinear summation of synaptic activity⁶⁷, enhancing a neuron's computational capacity³⁷. These nonlinearities can furthermore counteract location-dependent gradients of conductances across synapses, effectively establishing a synaptic democracy^{11,68}. (2) Since synaptic transmission is highly variable⁶⁹, multiple synapses encoding a similar signal (in combination with local supralinear integration) increase tolerance for different types of noise, some of which cannot be removed by averaging⁷⁰. (3) Furthermore, since the translation of proteins is localized to individual dendritic compartments where nearby synapses share available proteins, synaptic clustering is also beneficial from the perspective of resource-preservation, consistent with the sharing of plasticity-related proteins in models like synaptic tag-and-capture^{29,71,72}.

Inhibitory synapses could form a backbone for excitatory clustering. Our modeling framework focused on the emergence of fine-scale organization of excitatory (glutamatergic) inputs, primarily due to lack of experimental data on the role of inhibitory (GABAergic) synapses on clustering. We speculate, however, that inhibitory synapses might shape the clustering of excitatory synapses on the dendritic tree. Indeed, while not being clustered themselves, GABAergic synapses can constrain the orientation preference of nearby excitatory clusters in our model (Supplementary Fig. 13). Since GABA might be excitatory early in postnatal development^{73,74}, we considered two scenarios in our model with GABA switching from excitatory to inhibitory or being inhibitory the entire time. The resulting excitatory clusters are tuned to the same orientation relative to nearby inhibitory synapses in the former case or tend to prefer the orthogonal orientation in the latter case (Supplementary Fig. 13). Thus, we predict that GABAergic synapses might be co-clustered with excitatory synapses. Provided that GABAergic synapses fire in synchrony with glutamatergic synapses, this co-clustering could allow them to dynamically switch a given cluster on or off⁷⁵. Additionally, since inhibitory synapses can cancel the effect of backpropagating action potentials⁷⁶, we expect that inhibitory synapses synchronized with somatic activation would be able to protect a cluster from the homogenizing effect of backpropagating somatic signals⁷⁷.

In summary, starting from several ingredients, including a species-specific receptive field model based on anatomical considerations, retinal wave input, and a developmentally inspired plasticity based on neurotrophins, our modeling framework generates species-specific outcomes regarding the emergence of local and global organization of dendritic synaptic inputs. These outcomes combine several experimental studies from the last decade on the emergence of functional synaptic organization across scales, and with respect to different stimulus features in two species. Therefore, our framework can explain how circuits wire up with subcellular precision, with paramount implications on the computational properties of cortical neurons and networks.

Methods

Neurotrophin model. We based the neurotrophin plasticity model on interactions between signaling molecules shown to drive the emergence of synaptic clustering during development^{4–6,10}: BDNF (**B**), its immature form, proBDNF (**P**), the cleaving protease MMP9 (**M**), and postsynaptic calcium (**Y**). W_k is the synaptic efficacy of a synapse with hard bounds at zero and one, and initial efficacy of 0.5. For a pair of synapses k and l separated by d_{kl} along the branch, we defined the

Table 1 Parameters of the proposed model along with nominal values used for simulations, unless stated otherwise.

Parameter	Variable	Value
Synaptic efficacy time constant	τ_W	6 s
proBDNF and BDNF time constants ³¹	τ_P, τ_B	5 ms
Postsynaptic calcium time constant ²¹	τ_Y, τ_u	300 ms
MMP9 time constant ⁸³	τ_M, τ_v	600 ms
Constitutive percent of BDNF of amount of total neurotrophins released ²⁵	η	45%
MMP9 efficiency constant ²²	ϕ	$\frac{3}{50} \text{ ms}^{-1}$
Heterosynaptic offset*	ρ	$\frac{2\eta-1}{2(1-\eta)}$
Synaptic efficacy time constant in the generalized neurotrophin-inspired model*	τ_w	$\tau_W \frac{1}{2(1-\eta)}$
Standard deviation of calcium spread ²¹	σ_c	6 μm
Density of synapses ⁸⁵	ν	0.2 μm^{-2}
Spread of receptive field centers for ferret and mouse ^{8,9} , in visual space	σ_p	5.3°, 26°
Diameter of Gabor receptive field mouse ⁸ , ferret ⁹ , and macaque ¹²		20°, 13.4°, 2°
LN model parameters ^{6,9}	a, b	0.2 Hz, 9.4
Turnover threshold below which a synapse is replaced	W_{thr}	0.02
Threshold for bAP generation ⁴⁸	B_{thr}	25
Unattenuated amplitude of bAP ^{47,48}	B_{amp}	5

Citations indicate a free parameter fitted to experimental data.
*Indicates a parameter that is derived from the other parameters.

proximity variables $s_{kl} = e^{-\frac{d_{kl}^2}{2\sigma_c^2}}$, where σ_c determines the spatial postsynaptic calcium spread constant.

Since the mechanism that produces synaptic clusters is activity-dependent, we modeled presynaptic and postsynaptic accumulators of synaptic activity. We modeled the presynaptic accumulator MMP9 as a synapse-specific leaky accumulator²² with dynamics

$$\tau_M \frac{dM_k}{dt} = -M_k(t) + \phi x_k(t) \quad (2)$$

Here,

$$x_k(t) = \int_0^\infty \sum_j \delta(s - s_k^j) (H(t - s) - H(t - x_{\text{dur}} - s)) ds \quad (3)$$

is the input event train to the k -th synapse with events at times t_k^j and where the Heaviside step function $H(t)$ is 0 when t is less than 0 and 1 when t is greater than or equal 0, so that events have duration x_{dur} . ϕ is an MMP9 efficiency constant that determines how efficiently MMP9 converts proBDNF into BDNF per unit of time. The postsynaptic accumulator was modeled by the local calcium variable Y that integrates activity from nearby synapses²¹, weighted by their efficacies W_l and the distance-dependent factor s_{kl} ,

$$\tau_Y \frac{dY_k}{dt} = -Y_k(t) + \sum_{l=1}^N s_{kl} W_l(t) x_l(t) \quad (4)$$

The lateral spread of calcium might be passive (during development many excitatory synapses form on the dendritic shaft⁷⁸ where calcium is less compartmentalized) or active (such as the calcium-induced calcium release characterized in the developing hippocampus²¹). Following experimental data^{10,31}, we coupled extracellular proBDNF and BDNF to postsynaptic calcium and let MMP9 convert proBDNF to an equal amount of BDNF,

$$\tau_P \frac{dP_k}{dt} = -P_k(t) + (1 - \eta) Y(t) - M_k(t) P_k(t) \quad (5)$$

$$\tau_B \frac{dB_k}{dt} = -B_k(t) + \eta Y(t) + M_k(t) P_k(t). \quad (6)$$

Here, the scaling factors $(1 - \eta)$ and η ensure that without MMP9 the ratio of BDNF to proBDNF remains close to the constitutive ratio η ²⁵ which is dominated by proBDNF (Table 1). By coupling the neurotrophin level to the local calcium level, inactive synapses experience an increase in extracellular neurotrophin following the activation of nearby activated synapses. While there is indirect evidence that activity-dependent BDNF release is not restricted to the activated synapse⁷⁹ and that stimulation of a synapse increases BDNF-receptor activation at another synapse³¹, much less is known about the activity-dependent release of proBDNF. For our model, we assumed that both BDNF and proBDNF release

depend only on an influx of postsynaptic calcium and can therefore also occur at unstimulated synapses when other nearby synapses are stimulated. According to the Yin-Yang hypothesis of neurotrophin action¹⁵, binding of BDNF to its receptor TrkB (tropomyosin receptor kinase B) leads to synaptic potentiation, while binding of proBDNF to p75^{NTR} receptor leads to depression. We assumed that the binding affinities of BDNF (α) and proBDNF (β), and corresponding magnitudes of induced plasticity are balanced, so that the synaptic efficacy can be written as the difference between BDNF and proBDNF,

$$\tau_w \frac{dW_k}{dt} = \alpha B_k(t) - \beta P_k(t), \quad (7)$$

with $\alpha = \beta = 1$ for all simulations except in Supplementary Fig. 3. τ always denotes the time constant for the variable in the corresponding subscript. Despite the model's biophysical motivation, in agreement with other modeling studies,^{56,80} all modeled variables are unitless, therefore, they are to be interpreted relative to each other.

Generalized neurotrophin-inspired model. We reduced the above neurotrophin model to a generalized model for clustering which is analytically tractable, assuming a tight coupling of proBDNF and BDNF to the postsynaptic calcium. We note, however, that this assumption is not critical (see Supplementary Fig. 1). We made a steady-state approximation of P_k and B_k in Eqs. (5) and (6), inserted these expressions into Eq. (7) for W_k and then linearized the resulting function around $M_k = 0$ to obtain the generalized model (see Supplementary Note 1 for details). We note that this linearization strips away some higher-order terms that have an attenuating effect on MMP9 in the full model (Supplementary Note 1). Hence, the effect of the presynaptic accumulation (a proxy for MMP9) in the generalized model is slightly amplified, shifting the system into a more potentiation driven regime. As a consequence, the generalized model experiences slightly less depression and competition compared to the full neurotrophin model, which results in fewer synaptic turnovers and slightly weaker clustering of synapses (Supplementary Fig. 2).

While we used upper case letters for the variables in the full neurotrophin model, we used lower case letters for the generalized model. The model consists of a synapse-specific presynaptic accumulator v_k (from now on we use the dot notation to denote the derivative, $\dot{v}_k = \frac{dv_k}{dt}$),

$$\tau_v \dot{v}_k = -v_k(t) + \phi x_k(t), \quad (8)$$

and a postsynaptic accumulator u_k that averages over nearby synapses in a weighted and distance-dependent manner,

$$\tau_u \dot{u}_k = -u_k(t) + \sum_{l=1}^N s_{kl} w_l(t) x_l(t). \quad (9)$$

The efficacy equation (Eq. 7) turns into a Hebbian equation that directly combines the pre- and postsynaptic accumulator with an additional offset constant ρ ,

$$\tau_w \dot{w}_k = u_k(t)(v_k(t) + \rho), \quad (10)$$

with $\rho = \frac{(\alpha + \beta)\eta - \beta}{(\alpha + \beta)(1 - \eta)}$ and $\tau_w = \tau_W \frac{1}{(\alpha + \beta)(1 - \eta)}$. This model cannot be reduced further without losing either the dependence on correlation through the link to the BTDP rule, or the dependence on distance.

Steady-state analysis of the generalized neurotrophin-inspired model. Combining the equations for the accumulators and the efficacy dynamics (Eqs. 8–10), taking the expected value over neurons (denoted by $\langle \cdot \rangle$) and over time (denoted by $\lim_{T \rightarrow \infty} \frac{1}{T} \int_0^T \cdot dt$), we can write the expected change in synaptic efficacy as (see Supplementary Note 2 for full derivation)

$$\lim_{T \rightarrow \infty} \frac{\tau_w}{T} \int_0^T \langle \dot{w}_k \rangle dt = \phi \sum s_{kl} w_l \left(\int_{-\infty}^{\infty} \bar{y}_{kl}(s) \Gamma(s) ds + \mu_k \mu_l \right) + \rho \sum s_{kl} w_l \mu_l. \quad (11)$$

Here, $\mu_k = \lim_{T \rightarrow \infty} \frac{1}{T} \int_0^T x_k(t) dt$ denotes the mean firing rate of the k -th input x_k , $\bar{y}_{kl}(t) = \lim_{T \rightarrow \infty} \frac{1}{T} \int_0^T (x_k(s) - \mu_k)(x_l(s - t) - \mu_l) ds$ denotes the covariance between inputs k and l at lag t and the kernel is given by $\Gamma(t) = \frac{1}{\tau_u + \tau_v} e^{-\frac{|t|}{\tau_u + \tau_v}}$.

When only one input is activated with burst events of duration x_{dur} and rate μ , we simplified Eq. (11) to write the change in synaptic efficacy for this input as $\langle \dot{w}_1 \rangle = K_1 \mu + K_2 \mu^2$, while the change in efficacy for a second inactive input at a

distance d_{12} is $\langle \dot{w}_2 \rangle = K_3 \mu e^{-\frac{d_{12}^2}{2\sigma_c^2}}$, with constants K_1, K_2 , and K_3 (see Supplementary Note 3 for details), as shown in Fig. 1d.

We considered the case with identical inputs on a linear dendrite with density ν , equal efficacies $w_k = w$ and rates $\mu_k = \mu$ for all k , and identical correlation $c_{kl} = c$ for all pairs $k \neq l$. In this setting, from Eq. (11) we derived the critical correlation c^* at which the system switches from the depression-dominated to the potentiation-dominated regime, $\langle \dot{w} \rangle(c^*) = 0$, as $c^* = \frac{\kappa S - 1}{S - 1}$ where $S_k = \sum_l s_{kl} \approx \sqrt{2\pi} \sigma_c \nu$, which is the same for all inputs k , thus $S = S_k$, and $\kappa = (-\frac{\rho}{\phi} - \mu)(\tau_u + \tau_v)$ is a constant (see Supplementary Note 4). S can be thought of as a measure of the total amount of activity in an area around a given synapse. Note that for high densities ν , the critical value c^* quickly approaches κ and is bounded above by it. The expression for c^* determines the dashed line in Fig. 2b, while the other contour lines come

directly from Eq. (11) and the approximation $S \approx \sqrt{2\pi}\sigma_c\nu$ (see Supplementary Fig. 14 and Supplementary Note 4). Whether a synapse becomes stabilized or depressed is thus determined by the balance of two factors: (1) A homosynaptic component, which depends only on the activation of the given synapse and is always stabilizing (Fig. 1d, top); (2) A heterosynaptic component, which depends only on the activation of synapses in the neighborhood of the activated synapse and can be either depressing or stabilizing. A synapse becomes depressed when the heterosynaptic component is depressing and outweighs the homosynaptic component. We first determined the correlation beyond which there is no competition between synapses, $\kappa = \left(-\frac{\rho}{\phi} - \mu\right)(\tau_u + \tau_v) \approx 0.32$, due to a stabilizing, rather than depressing, heterosynaptic component (see Supplementary Note 4 for details). Note that this parameter depends on the proBDNF to BDNF constitutive ratio, η (through ρ), on the MMP9 efficiency constant, ϕ , the stimulation rate of the synapse, μ , and the time constants of the pre- and postsynaptic accumulators in the model. Second, we found that when the heterosynaptic component is depressing for correlations below $\kappa \approx 0.32$, the synaptic density, ν , plays an additional role in determining whether the depressing heterosynaptic component outweighs the stabilizing homosynaptic component.

Parameters and data fitting. Many of the model parameters were extracted from published experimental data as follows.

Experimental work has shown that the binding affinity of BDNF to TrkB and proBDNF to p75^{NTR} is very high (see ref. 81 and references therein). Therefore, we assumed that the decay time constants of proBDNF and BDNF are small and, in the absence of evidence otherwise, equal ($\tau_p = \tau_b$). In our model, the decay time constants of proBDNF and BDNF describe the tightness of coupling between the level of postsynaptic calcium and of free (unbound) extracellular neurotrophin. This produces much longer effective decay time constants $\hat{\tau}_B \approx \hat{\tau}_p$, as measured in ref. 31 (Supplementary Fig. 15).

The synaptic efficacy time constant τ_W was chosen so that the total change in synaptic efficacy integrates the contribution of multiple pre- and postsynaptic events, yielding slow weight change compared to much faster neural activity, consistent with other computational models of synaptic plasticity⁸². The value for the time constant of postsynaptic calcium decay, τ_Y (300 ms), is in the experimentally measured range between 200–700 ms²¹. We based the decay time constant of extracellular MMP9 (τ_M) on a recent study which measured the decay of MMP9-GFP signal of a single exocytosis event in MCF-7 cells⁸³.

We assumed that the constitutive percentage of BDNF (η) of the total released neurotrophin is $\eta = 45\%$ based on estimates in the hippocampus⁸⁴, although it is possible that this ratio can change across different brain regions, over the course of development and depending on the stimulation protocol. Our sensitivity analysis (Supplementary Fig. 1) and perturbation simulations (Supplementary Fig. 3) demonstrate that the constitutive percentage of BDNF (η) is crucial in regulating the overall amount of potentiation and depression of synaptic efficacy, and therefore has a strong impact on the emergence and maintenance of synaptic organization. Therefore, although in our model stimulation of a given synapse leads to its potentiation consistent with some experimental data³¹ (Fig. 1), decreasing η could lead to the depression of the stimulated synapse in agreement with other experimental data⁶.

The MMP9 efficacy constant (ϕ) interacts closely with the constitutive percentage of BDNF (η). This relationship becomes clear in the generalized neurotrophin-inspired model, where ϕ and η trade off to maintain a given value of the critical correlation c^* and ensure the selective competition between strongly and poorly synchronized synapses. Since c^* depends on $\kappa = (-\rho/\phi - \mu)(\tau_u + \tau_v)$, ϕ needs to be proportional to $\rho = \frac{2\eta-1}{2(1-\eta)}$. We used $\phi = \frac{3}{50} \text{ms}^{-1}$ to obtain c^* with appropriate synaptic competition (Fig. 2b) given experimentally measured synaptic density. In particular, the density of synapses in the developing sensory cortex increases from $0.2 \mu\text{m}^{-1}$ to $0.8\text{--}1.2 \mu\text{m}^{-1}$ during postnatal development^{85,86}. We used a fixed density of $0.2 \mu\text{m}^{-1}$ for computational tractability as the runtime of our simulations scales as $\mathcal{O}(N^2)$ in the number of synapses N . However, we also found that synaptic clustering is not perturbed when synaptic density increases during simulated development (Supplementary Fig. 12). Here, we increased the density of synapses from $0.2 \mu\text{m}^{-1}$ to $0.8 \mu\text{m}^{-1}$ ⁸⁵ within four days, by adding a new synapse at a random position and with random receptive field orientation at regular time intervals of 64 min. Additionally, to conserve the total amount of postsynaptic calcium, we decreased the amount of calcium spread and the amount of released calcium per synaptic event with increasing time²¹.

To determine the standard deviation of calcium spread, σ_c , we referred to experimental studies that report mean propagation distances (defined as the full width at half maximum, FWHM) from individual synapses in dendrites of a developing pyramidal neuron, reporting values between $7.97 \mu\text{m}^{21}$ and $17.6 \mu\text{m}^4$. Assuming a Gaussian spread profile, these FWHM values translate into a standard deviation between $3.4 \mu\text{m}$ and $7.5 \mu\text{m}$, which validates our choice of $\sigma_c = 6 \mu\text{m}$.

The values for all parameters used in our simulations are listed in Table 1.

Sensitivity analysis. We performed a sensitivity analysis to determine the sensitivity of the central building blocks of our model, the shape of the resulting BTDP rule (Fig. 1), and the emergence of local clustering (Fig. 3), to perturbations of different model parameters. To quantify how uncertainty in the input parameters

propagates, we defined distributions over our model parameters that were chosen to be sufficiently broad to sometimes produce poor clustering (Supplementary Fig. 1). Many of the distributions were truncated from below because choosing extremely small values of any parameter is not biologically plausible and cannot be implemented in the model—but the distributions still cover one order of magnitude relative to the nominal parameter value. The prior distributions used for the sensitivity analysis are: $\tau_M, \tau_p \sim \mathcal{N}(600, 300)$ ms; truncated from below at 5 ms, $\tau_Y, \tau_u \sim \mathcal{N}(300, 150)$ ms; truncated from below at 5 ms, $\tau_b, \tau_p \sim \exp(\mathcal{N}(4, 1))$ ms; truncated from below at 1 ms, $\sigma_c \sim \mathcal{N}(8, 1) \mu\text{m}$; truncated from below at $4 \mu\text{m}$, $\phi \sim \mathcal{N}(\frac{3}{50}, \frac{3}{500})$, $\eta \sim \text{Uniform}([40\%, 50\%])$.

Retinal wave generation. To generate retinal waves with realistic spatiotemporal properties, we simulated 6 h of retinal waves from a published computational model with the parameter setting for mice (P0–P13)⁴¹ and looped the waves over the entire duration of the simulation. For consistency, we used the mouse retinal wave parameter settings for all simulations, since the parameter settings for ferret come from much younger animals (P2–P4)⁴¹. As a control we also generated white noise input by sampling each pixel independently from a normal distribution and applying a spatial Gaussian filter with a 2° standard deviation. Subsequently, we used each frame of the retinal wave or the white noise movie as input to a linear-nonlinear Poisson model of event generation.

Linear-nonlinear model. The linear filter consists of a Gabor linear filter \mathbf{H} , which we split into two components, a positive and a negative Gaussian with the same shape and opposite sign. We chose the semi-minor axis to be half as large as the semi-major axis so that the resulting Gabor is approximately equal in diameter along all axes. The receptive field diameter depends on the species and was extracted from published literature (Table 1). Synaptic receptive field centers in visual space have been measured to spread out in a small (for ferret⁹) or large (for mouse^{8,51}) neighborhood around the somatic receptive field center. The spread of the receptive field centers is inversely proportional to the size of the corresponding visual cortices, so that for the ferret visual cortex which is five times the size of the mouse visual cortex, the spread of receptive field centers in the ferret is one fifth the spread in the mouse. We interpret this anatomical argument to mean that the product of the receptive field spread and the diameter of the visual cortex is constant for the two species. For macaque we then use this relationship to infer the receptive field spread from the experimentally measured visual cortex diameter to obtain 2° . We defined the receptive field center spread σ_p to incorporate these differences and estimated σ_p from extracted experimental data in both species^{8,9} as the standard deviation of a Gaussian ($a_0 \exp(-x^2/(2\sigma_p^2))$) (Fig. 4a–c and Table 1). A synaptic receptive field center was drawn from a two-dimensional symmetric Gaussian with standard deviation σ_p and truncated to a circle of radius 50° to ensure that receptive fields fall within a region of visual space where they are modulated by the retinal waves. Each individual Gabor filter is rotated according to its orientation, θ , between 0° and 360° . For the simulations in Supplementary Fig. 11, we modeled On- and Off-selective receptive fields as Gaussians with a positive or negative sign and a diameter that is matched to typical mouse LGN neurons⁸⁷. The linearly filtered stimulus is passed through an exponential nonlinearity, $a \exp(bH)$, that produces an instantaneous firing rate from which we generate a Poisson input train with individual 50 ms-long events. The parameters (a, b) were chosen ($a = 0.2$ Hz, $b = 9.4$) to achieve a burst rate of around 15min^{-1} , as found experimentally⁴. For the simulations in Supplementary Fig. 11 we set the spontaneous background firing rate of Off-selective inputs to twice the value of On-selective inputs⁸⁸, $a = 0.4$ Hz.

Structural plasticity. To model synaptic turnover, we implemented a structural plasticity rule inspired by ref. 43 where each synapse whose efficacy falls below a fixed threshold W_{thr} is removed and replaced by a new synapse with a random position on the branch and a randomly oriented Gabor receptive field (Fig. 3d). The newly generated efficacy of a synapse through structural plasticity is the same as the initial efficacy at the onset of the simulation, i.e. 0.5, and the receptive field has orientation drawn from a uniform distribution over the interval $[0^\circ, 360^\circ]$. The turnover threshold is chosen arbitrarily to be sufficiently small to minimize the possibility of accidental removal of a synapse that is well-correlated with its neighbors. A novel synapse can potentially come from a pool of silent synapses, a type of synapse that lacks AMPA receptors but can become unsilenced through activity-dependent mechanisms⁸⁹.

Dendritic nonlinearity and cooperative plasticity. Inspired by experiments⁶⁷, we used a sigmoidal-like dendritic nonlinearity, $g(I) = \gamma \frac{c_1}{1 + \exp(-c_2(I - c_3))} + (1 - \gamma)I$ where the parameter $\gamma \in [0, 1]$ controls the strength of the nonlinearity and $c_1 = 0.5$, $c_2 = 35$, $c_3 = 0.125$ (Supplementary Fig. 6). This nonlinearity modifies the equation for the postsynaptic accumulation (Eq. 10),

$$\tau_u \dot{u}_k(t) = -u_k(t) + g\left(\sum_{i=1}^N s_{ki} w_i(t) x_i(t)\right). \quad (12)$$

The nonlinearity boosts the amount of postsynaptic calcium that is released through the simultaneous activation of multiple nearby synapses. This effectively

imposes the constraint that multiple synapses have to be active to generate a postsynaptic calcium event.

Similarly, we investigated whether synaptic organization can emerge when imposing a threshold for cooperativity, as recently described for NMDA-dependent cooperative potentiation^{34,90} and cooperative heterosynaptic depression²⁶ adulthood. We adapted Eq. (10) for the change in synaptic efficacy to include a spacing and a timing cooperativity threshold,

$$\tau_w \dot{w}_k(t) = \mathcal{F}(u_k(t)(v_k(t) + \rho)) \quad (13)$$

where $\mathcal{F}(x) = x$ when more than three synapses within a distance from synapse k smaller than a spacing threshold were activated within a timing threshold, and $\mathcal{F}(x) = 0$ otherwise. We chose three synapses guided by experimental data⁹⁰, but this number can be traded off with the spacing threshold.

Backpropagating somatic signal. To investigate the emergence of global order of synaptic inputs on an entire dendritic tree, we included a somatic accumulator which can produce backpropagating action potentials (bAPs) which attenuate with distance from the soma. Our somatic accumulator sums linearly over all postsynaptic accumulators, weighing them by their respective synaptic efficacy^{37,91}, $A(t) = \sum_{k=1}^N w_k(t)u_k(t)$. If the somatic accumulator crosses a threshold, A_{th} , there is a 25% probability that a bAP is generated, $B(t) \in \{0, 1\}$. These two parameters were chosen so that the burst rate of the soma is similar to the firing rate of synapses (15 min⁻¹) while avoiding step like activation patterns. The resulting somatic activation thus incorporates some aspects of the burst firing common for developing neurons, where the burst rate is modulated by the probability of generating a bAP (Supplementary Fig. 10). The bAP affects the postsynaptic accumulators of all synapses with attenuating effect over distance^{47,48}

$$\tau_u \dot{u}_k(t) = -u_k(t) + \sum_{l=1}^N s_{kl}x_l(t)w_l(t) + s_k B_{amp}B(t). \quad (14)$$

Here, B_{amp} is the unattenuated strength of the bAP and $s_k = e^{-\frac{d_k^2}{2\lambda^2}}$ is the attenuation factor of synapse k that depends on the distance to the soma d_k (Fig. 5b). We chose B_{amp} (Table 1) to reflect the experimental observation that the calcium influx through a bAP is larger than that caused by synaptic activation⁷. Additionally, a computational model⁴⁸ found that the peak calcium concentration at individual spines is around 29 μM (independent of distance) in a subthreshold stimulation protocol, while it is between 30 μM (distal synapse) and 100 μM (synapse at 150 μm from the soma). Extrapolating this to a distance of 0 μm makes a value of 5 for B_{amp} plausible, since this is five times as large as the synaptic level of calcium produced by presynaptic activation. Note that we did not include the term with $B(t)$ in the sum for the somatic accumulator $A(t)$ to avoid a positive feedback loop.

Since bAPs have been found to induce neurotrophin release in a calcium dependent manner⁴⁹, we also considered the case of including a bAP in the neurotrophin model by modifying the equation for the postsynaptic calcium (compare to Eq. 3),

$$\tau_Y \frac{dY_k}{dt} = -Y_k(t) + \sum_{l=1}^N s_{kl}x_l(t)W_l(t) + s_k B_{amp}B(t). \quad (15)$$

Placing a synaptic input at increasing distances away from the soma along the dendritic tree of the reconstructed layer 2/3 dendrite, we used either the distance-dependent competition or the burst-timing-dependent plasticity protocol from Fig. 1 to stimulate the soma and synaptic input (Supplementary Fig. 8).

Inhibitory clustering. To investigate the role of inhibitory synapses in synaptic clustering, we extended our neurotrophin model to also include plastic, GABAergic synapses. While it is commonly accepted that GABAergic synapses are plastic, the nature of the inhibitory plasticity is not well known, strongly depends on the cortical region and can easily be modulated by diverse neuromodulators⁹². During development, BDNF-TrkB signaling at excitatory synapses produces potentiation of nearby GABAergic synapses⁹³ and proBDNF-p75^{NTR} signaling results in the depression of nearby GABAergic synapses, provided that the p75^{NTR} activation occurs in concert with the opening of NMDA receptors⁹⁴. Therefore, we assumed that the strength of GABAergic synapses is homeostatically regulated to maintain a balance of excitation and inhibition⁹⁵. We postulated that the plastic change of inhibitory synapses, $\frac{dW_k^{GABA}}{dt}$, closely follows the average amount of plasticity of nearby excitatory synapses (Supplementary Fig. 13a),

$$\tau_W \frac{dW_k^{GABA}}{dt} = \sum_{l=1}^{N_l} s_{kl}(B_l(t) - P_l(t)), \quad (16)$$

where the sum runs over all the glutamatergic synapses l . Input to the GABAergic synapses, x_k^{GABA} and structural turnover of GABAergic synapses is implemented in the same way as for glutamatergic synapses. Since there is an ongoing debate on whether GABA during development is inhibitory⁹⁶, or whether it is initially excitatory and only later switches to being inhibitory^{73,74}, we considered two scenarios (Supplementary Fig. 13a):

A. GABAergic synapses hyperpolarize the postsynaptic membrane and are able to decrease postsynaptic calcium⁹⁷,

$$\tau_Y \frac{dY_k}{dt} = -Y_k(t) + \sum_{l=1}^{N_E} s_{kl}W_l x_l(t) - \sum_{l=1}^{N_I} s_{kl}W_l^{GABA} x_l^{GABA}(t), \quad (17)$$

B. GABAergic synapses are initially excitatory and are able to increase postsynaptic calcium,

$$\tau_Y \frac{dY_k}{dt} = -Y_k(t) + \sum_{l=1}^{N_E} s_{kl}W_l x_l(t) + \sum_{l=1}^{N_I} s_{kl}W_l^{GABA} x_l^{GABA}(t), \quad (18)$$

and only later in the simulation switch to being inhibitory and decreasing postsynaptic calcium⁷³, see Eq. (17).

Note that in the first scenario we needed to impose the biologically realistic condition $Y_k > 0$. In both scenarios, we scaled the amount of calcium increase per excitatory synaptic event so that the total amount of calcium in a neighborhood remains constant over time to stay in the same dynamic regime as in the exclusively glutamatergic case. We implemented the switch from excitation to inhibition in the second scenario after 4 days, although the exact day of the switch does not influence our results since the fraction of stable synapses increases at the same speed as in Fig. 3e.

Simulations. For the simulations in Fig. 1b, d, we distributed two synapses at varying distances ($\Delta d = 0 \mu\text{m}$ to $15 \mu\text{m}$) on a linear dendrite of length $L = 150 \mu\text{m}$ with periodic boundary conditions. Only one input was stimulated with a train of continuous bursts of activation whose rate varies from 1 to 20 min⁻¹. All bursts in our model have a duration of 50 ms ($x_{dur} = 50 \text{ms}$) unless stated otherwise. We fixed the synaptic efficacy to the initial value $W(t) = 0.5$ and computed the expected change in the efficacy of synapse k in Eq. (7) as the temporal average of $B_k(t) - P_k(t)$ over the 40 min duration of the simulation. For the simulations in Fig. 1f, g, we simulated only one synapse and provided either one (panel f) or ten (panel g) pairings of a pre- (t_{pre}) and a postsynaptic (t_{post}) burst event at a temporal offset of $\Delta T = t_{post} - t_{pre}$. Each burst event has a duration of 1 s and contains ten smaller 50 ms-long events. The postsynaptic burst contributes an additive term $I(t)$ with amplitude B_{amp} to the postsynaptic calcium, $\tau_Y \frac{dY_k}{dt} = -Y_k(t) + B_{amp}I(t)$. Note that in comparison to the calcium released by stimulating a synapse (Eq. 4), here B_{amp} provides a stronger contribution to the postsynaptic calcium (Table 1). We assumed that this postsynaptic signal comes from a bAP and hence is stronger than the synaptic signal⁴⁸. We indirectly varied B_{amp} in Supplementary Fig. 9 where we simulated Eq. (19) on a dendritic tree. We found that significantly weakening the calcium signal from direct postsynaptic stimulation preserves the shape of the BTDP curve (including the timing requirements for potentiation and depression) but makes it somewhat flatter.

For the simulations in Fig. 2b, c, we distributed $N = \lfloor L\nu \rfloor$ synapses on a branch of length L , where $\lfloor x \rfloor$ is the largest integer smaller or equal to x and where we choose L sufficiently long (30 μm in b and 64 μm in c) to avoid confounds from periodic boundary conditions. We varied the density ν between 0.05 and 0.75 μm⁻¹ to capture random and systematic fluctuations in local synaptic density⁹⁸. We generated 12 min in Fig. 2b (4 h in Fig. 2c) of correlated Poisson event trains⁹⁹, homogeneous across pairs, and with a fixed firing rate of 15 min⁻¹. To compute the instantaneous change in synaptic efficacy in Fig. 2b, we fixed the synaptic efficacy to the initial value and used Eq. (10) to compute the change from the same initial efficacy averaged over 12 min, as a proxy for the ensemble average over inputs. In Fig. 2c, the synaptic efficacy was not fixed to the initial value and evolved according to Eq. (10). For the simulations in Fig. 2d, we used an initial efficacy of 0.9 and, in line with the experimental paradigm⁶, generated 6 min of correlated Poisson input for synapses distributed at a high density ($\nu = 0.5 \mu\text{m}^{-1}$) or low density ($\nu = 0.05 \mu\text{m}^{-1}$).

In Figs. 3 and 4, we simulated a branch with length L of over 15 days. All synaptic receptive fields were initialized with an orientation drawn from a uniform distribution over the interval $[0^\circ, 360^\circ]$. For the simulations in Figs. 5 and 6, we tested a morphologically realistic dendrite model by using a reconstructed pyramidal cell from layer 2/3 of the mouse visual cortex (Allen Cell Type database, ID 502269786) which we resampled into equally sized segments of 10 μm using the TREES toolbox¹⁰⁰. We used this dendritic tree for both types of simulations, ferret and mouse, since to our knowledge no morphological reconstruction of a pyramidal layer 2/3 neuron from the ferret visual cortex is openly available. We do not expect this to influence our results, since the specific branching structure of the dendritic tree does not matter in our model. Our results depend on the anatomical argument of receptive field diameter and center spread and do not consider other factors, for instance, differences in morphology and electrophysiology across species. Furthermore, we did not include any differences between synaptic inputs on the apical vs. basal parts of the dendritic tree. Although apical and basal dendrites likely receive different inputs^{101,102}, no location-dependent differences in orientation or overlap clustering have been reported^{8,9}. Therefore, our model only considers synaptic differences pertaining to distance from the soma and their effect on global synaptic organization in the ferret and mouse. Because of the increased computational complexity, the duration for the simulations with the morphologically realistic dendrite model was 5 days, which is sufficient for most of the synapses to reach a stable state.

For the simulations with spike-timing-dependent plasticity in Supplementary Fig. 5, we used faster time scales of our pre- and postsynaptic accumulators ($\tau_M = 60$ ms, $\tau_Y = 1$ ms), and further changed $\eta = 0.3$ and $\phi = \frac{3}{5} \text{ms}^{-1}$. As we demonstrated analytically in Supplementary Note 5, the issue with generating clustering using this rule is its short integration time window (tens of milliseconds) rather than the exact choice of parameters³³.

Statistics. All correlations were computed as Pearson correlation coefficients, i.e., for two random variables X and Y we compute $\frac{(X-\mu_X)(Y-\mu_Y)}{\sigma_X\sigma_Y}$, where μ and σ denote the mean and the standard deviation. In Fig. 2b, for each pair of correlation and synaptic density we computed the average change in synaptic efficacy over all synapses in 50 simulations.

To compute the correlations in Figs. 3b, g and 4f, we first applied a boxcar filter of length 3 s to generate signals consistent with the slow calcium dynamics in experimental imaging studies¹⁹. The experiments from ref. 6 reproduced in Figs. 2e and 4f report coactivity—the fraction of events at a given synapse that occurs in concert with events at nearby synapses. Coactivity is closely related to the Pearson correlation coefficient when it is only applied to pairs of synapses (see Supplementary Note 6). To estimate the spatial decay of correlations as a function of distance, λ , in Supplementary Fig. 4, we computed the average correlation between pairs of synapses Δd apart, then subtracted the average correlation between pairs of synapses more than $50 \mu\text{m}$ apart and fit a Gaussian function with shape $A_0 \exp(-\Delta d^2 / (2\lambda^2))$ to the resulting curve⁹.

We computed the receptive field overlap in Fig. 4e as the spatial receptive field correlation⁸, i.e., the pixel-wise Pearson correlation coefficient between Gabor filters associated with pairs of synapses. The correlation for different receptive field center spreads in Fig. 4h, i was computed by first multiplying the coordinates of the receptive field center position with a scalar and then calculating the overlap o_{ij} between all pairs of synapses i and j . Next we computed a weighted average overlap for each synapse with its neighbors using the proximity values s_{ij} as $\sum_j s_{ij} o_{ij} / \sum_j s_{ij}$ and related it to the correlation, which is a monotonically increasing function of the overlap (Supplementary Fig. 7). In Supplementary Fig. 7, we generated a Gaussian noise image by drawing independent samples from a standard normal distribution and reshaping them into a matrix of the same shape as the receptive field filters (73×73 pixels). Then we applied a Gabor filter with random orientation, wavelength of 2 pixels per cycle and a ratio of the semi-major and semi-minor axes equal to $\frac{1}{2}$ to the resulting noise image. When computing the spatial overlap between receptive fields (Supplementary Fig. 7), we generated a filtered noise image for each receptive field and added the noise to the receptive field, scaled by a factor uniformly distributed between $\frac{1}{2}$ and 2.

The term orientation difference⁸ denotes the absolute difference in orientation between receptive fields of pairs of synapses modulo 180° ,

$$\min(|\theta'_i - \theta'_j|, 180^\circ - |\theta'_i - \theta'_j|), \quad (19)$$

where θ'_i is defined as $\text{mod}(\theta_i, 180^\circ)$. The term circular dispersion denotes the orientation difference between the receptive field of a given synapse and the soma, where the orientation preference of the soma is the circular average of all synaptic preferences⁷, $\arg\left(\frac{1}{N} \sum_{j=1}^N e^{i\theta_j}\right)$. We define the mean circular dispersion in Fig. 5i as the average circular dispersion of all synapses less than $50 \mu\text{m}$ apart. Analogously, the term receptive field offset denotes the Euclidean distance between the center of a given synaptic receptive field and the somatic receptive field center, defined as the average location of all synaptic receptive fields. The average circular dispersion and average receptive field offset in Figs. 5 and 6 were computed as the average over synapses within dendritic segments. The coaxial space⁸ (Fig. 6f, g) is defined as the portion of space up to 45° on either side of the axis extending along the average orientation of all synaptic receptive fields. Conversely, the orthogonal space is the remaining visual space that is not coaxial.

Reporting summary. Further information on research design is available in the Nature Research Reporting Summary linked to this article.

Data availability

The morphological reconstruction that supports the findings of this study is available from the Allen Cell Type database, ID 502269786.

Code availability

We used the openly available TREES toolbox (<https://www.treestoolbox.org>, v1.15) and the toolbox for generating correlated Poisson trains (<https://de.mathworks.com/matlabcentral/fileexchange/20591-sampling-from-multivariate-correlated-binary-and-poisson-random-variables>, v1.0). To generate retinal waves, we used open source code (<https://swindale.ecc.ubc.ca/home-page/software/retinal-wave-models/>). We extracted all displayed experimental data from the appropriately referenced publications using open source software¹⁰³. The code for this modeling study was written by Jan H. Kirchner using the MATLAB 2019a programming environment. The relevant code to generate the figures of this paper is publicly available at <https://github.com/comp-neural-circuits/synaptic-organization> (<https://doi.org/10.5281/zenodo.4630142>).

Received: 19 February 2021; Accepted: 3 May 2021;

Published online: 28 June 2021

References

- Blankenship, A. G. & Feller, M. B. Mechanisms underlying spontaneous patterned activity in developing neural circuits. *Nat. Rev. Neurosci.* **11**, 18–29 (2010).
- Cang, J. & Feldheim, D. A. Developmental mechanisms of topographic map formation and alignment. *Annu. Rev. Neurosci.* **36**, 51–77 (2013).
- Ackman, J. B. & Crair, M. C. Role of emergent neural activity in visual map development. *Curr. Opin. Neurobiol.* **24**, 166–175 (2014).
- Kleindienst, T., Winnubst, J., Roth-Alpermann, C., Bonhoeffer, T. & Lohmann, C. Activity-dependent clustering of functional synaptic inputs on developing hippocampal dendrites. *Neuron* **72**, 1012–1024 (2011).
- Takahashi, N. et al. Locally synchronized synaptic inputs. *Science* **335**, 353–356 (2012).
- Winnubst, J., Cheyne, J. E., Niculescu, D. & Lohmann, C. Spontaneous activity drives local synaptic plasticity in vivo. *Neuron* **87**, 399–410 (2015).
- Wilson, D. E., Whitney, D. E., Scholl, B. & Fitzpatrick, D. Orientation selectivity and the functional clustering of synaptic inputs in primary visual cortex. *Nat. Neurosci.* **19**, 1003–1009 (2016).
- Iacaruso, F. M., Gasler, I. T. & Hofer, S. B. Synaptic organization of visual space in primary visual cortex. *Nature* **547**, 449–452 (2017).
- Scholl, B., Wilson, D. E. & Fitzpatrick, D. Local order within global disorder: synaptic architecture of visual space. *Neuron* **96**, 1127–1138 (2017).
- Niculescu, D. et al. A BDNF-mediated push-pull plasticity mechanism for synaptic clustering. *Cell Rep.* **24**, 2063–2074 (2018).
- Kerlin, A. et al. Functional clustering of dendritic activity during decision-making. *Elife* **8**, e46966 (2019).
- Ju, N. et al. Spatiotemporal functional organization of excitatory synaptic inputs onto macaque V1 neurons. *Nat. Commun.* **11**, 1–11 (2020).
- Kastellakis, G., Cai, D. J., Mednick, S. C., Silva, A. J. & Poirazi, P. Synaptic clustering within dendrites: an emerging theory of memory formation. *Prog. Neurobiol.* **126**, 19–35 (2015).
- Mel, B. W., Ruderman, D. L. & Archie, K. A. Translation-invariant orientation tuning in visual “complex” cells could derive from intradendritic computations. *J. Neurosci.* **18**, 4325–4334 (1998).
- Lu, B., Pang, P. T. & Woo, N. H. The Yin and Yang of neurotrophin action. *Nat. Rev. Neurosci.* **6**, 603–614 (2005).
- Yang, J. et al. proBDNF negatively regulates neuronal remodeling, synaptic transmission, and synaptic plasticity in hippocampus. *Cell Rep.* **7**, 796–806 (2014).
- Varga, Z., Jia, H., Sakmann, B. & Konnerth, A. Dendritic coding of multiple sensory inputs in single cortical neurons in vivo. *Proc. Natl Acad. Sci. USA* **108**, 15420–15425 (2011).
- Chen, X., Leischner, U., Rochefort, N. L., Nelken, I. & Konnerth, A. Functional mapping of single spines in cortical neurons in vivo. *Nature* **475**, 501–505 (2011).
- Chen, T.-W. et al. Ultrasensitive fluorescent proteins for imaging neuronal activity. *Nature* **499**, 295–300 (2013).
- Jia, H., Rochefort, N. L., Chen, X. & Konnerth, A. Dendritic organization of sensory input to cortical neurons in vivo. *Nature* **464**, 1307–1312 (2010).
- Lee, K. F. H., Soares, C., Thivierge, J.-P. & Béique, J.-C. Correlated synaptic inputs drive dendritic calcium amplification and cooperative plasticity during clustered synapse development. *Neuron* **89**, 784–799 (2016).
- Je, H. S. et al. Role of pro-brain-derived neurotrophic factor (proBDNF) to mature BDNF conversion in activity-dependent competition at developing neuromuscular synapses. *Proc. Natl Acad. Sci. USA* **109**, 15924–15929 (2012).
- Gawlak, M. et al. High resolution in situ zymography reveals matrix metalloproteinase activity at glutamatergic synapses. *Neuroscience* **158**, 167–176 (2009).
- Butts, D. A. & Kanold, P. O. The applicability of spike time dependent plasticity to development. *Front. Synaptic Neurosci.* **2**, 30 (2010).
- Nagappan, G. et al. Control of extracellular cleavage of ProBDNF by high frequency neuronal activity. *Proc. Natl Acad. Sci. USA* **106**, 1267–1272 (2009).
- Oh, W. C., Parajuli, L. K. & Zito, K. Heterosynaptic structural plasticity on local dendritic segments of hippocampal CA1 neurons. *Cell Rep.* **10**, 162–169 (2015).
- Butts, D. A., Kanold, P. O. & Shatz, C. J. A burst-based ‘Hebbian’ learning rule at retinogeniculate synapses links retinal waves to activity-dependent refinement. *PLoS Biol.* **5**, 0651–0661 (2007).
- Fonseca, R., Nägerl, U. V., Morris, R. G. M. & Bonhoeffer, T. Competing for memory: hippocampal LTP under regimes of reduced protein synthesis. *Neuron* **44**, 1011–1020 (2004).

29. Govindarajan, A., Israely, I., Huang, S.-Y. & Tonegawa, S. The dendritic branch is the preferred integrative unit for protein synthesis-dependent LTP. *Neuron* **69**, 132–146 (2011).
30. Redondo, R. L. & Morris, R. G. M. Making memories last: the synaptic tagging and capture hypothesis. *Nat. Rev. Neurosci.* **12**, 17–30 (2011).
31. Harward, S. C. et al. Autocrine BDNF-TrkB signalling within a single dendritic spine. *Nature* **538**, 99 (2016).
32. Hedrick, N. G. et al. Rho GTPase complementation underlies BDNF-dependent homo- and heterosynaptic plasticity. *Nature* **538**, 104–108 (2016).
33. Gjorgjieva, J., Toyoizumi, T. & Eglon, S. J. Burst-time-dependent plasticity robustly guides ON/OFF segregation in the lateral geniculate nucleus. *PLoS Comput. Biol.* **5**, e1000618 (2009).
34. Weber, J. P. et al. Location-dependent synaptic plasticity rules by dendritic spine cooperativity. *Nat. Commun.* **7**, 11380 (2016).
35. Michaelsen, K. & Lohmann, C. Calcium dynamics at developing synapses: Mechanisms and functions. *Eur. J. Neurosci.* **32**, 218–223 (2010).
36. Roy, S. & Basu, A. An online unsupervised structural plasticity algorithm for spiking neural networks. *IEEE Trans. Neural Netw. Learn. Syst.* **28**, 900–910 (2016).
37. Mel, B. W. The clusteron: toward a simple abstraction for a complex neuron. In *Advances in Neural Information Processing Systems* 35–42 (Morgan Kaufmann, 1992).
38. Poirazi, P. & Mel, B. Impact of active dendrites and structural plasticity on the memory capacity of neural tissue. *Neuron* **29**, 779–796 (2001).
39. Ackman, J. B., Burbridge, T. J. & Crair, M. C. Retinal waves coordinate patterned activity throughout the developing visual system. *Nature* **490**, 219–225 (2012).
40. Siegel, F., Heimel, J. A., Peters, J. & Lohmann, C. Peripheral and central inputs shape network dynamics in the developing visual cortex in vivo. *Curr. Biol.* **22**, 253–258 (2012).
41. Godfrey, K. B. & Swindale, N. V. Retinal wave behavior through activity-dependent refractory periods. *PLOS Comput. Biol.* **3**, 1–13 (2007).
42. Keck, T. et al. Massive restructuring of neuronal circuits during functional reorganization of adult visual cortex. *Nat. Neurosci.* **11**, 1162 (2008).
43. Holtmaat, A. & Svoboda, K. Experience-dependent structural synaptic plasticity in the mammalian brain. *Nat. Rev. Neurosci.* **10**, 647 (2009).
44. Lee, K.-S., Vandemark, K., Mezey, D., Shultz, N. & Fitzpatrick, D. Functional synaptic architecture of callosal inputs in mouse primary visual cortex. *Neuron* **101**, 421–428 (2019).
45. Jang, J., Song, M. & Paik, S.-B. Retino-cortical mapping ratio predicts columnar and salt-and-pepper organization in mammalian visual cortex. *Cell Rep.* **30**, 3270–3279 (2020).
46. Garrett, M. E., Nauhaus, I., Marshel, J. H. & Callaway, E. M. Topography and areal organization of mouse visual cortex. *J. Neurosci.* **34**, 12587–12600 (2014).
47. Spruston, N., Schiller, Y., Stuart, G. & Sakmann, B. Activity-dependent action potential invasion and calcium influx into hippocampal CA1 dendrites. *Science* **268**, 297–300 (1995).
48. Sterratt, D. C., Groen, M. R., Meredith, R. M. & Van Ooyen, A. Spine calcium transients induced by synaptically-evoked action potentials can predict synapse location and establish synaptic democracy. *PLoS Comput. Biol.* **8**, e1002545 (2012).
49. Kuzewski, N. et al. Backpropagating action potentials trigger dendritic release of BDNF during spontaneous network activity. *J. Neurosci.* **28**, 7013–7023 (2008).
50. El-Boustani, S. et al. Locally coordinated synaptic plasticity of visual cortex neurons in vivo. *Science* **360**, 1349–1354 (2018).
51. Rossi, L. F., Harris, K. D. & Carandini, M. Spatial connectivity matches direction selectivity in visual cortex. *Nature* **588**, 648–652 (2020).
52. Sigman, M., Cecchi, G. A., Gilbert, C. D. & Magnasco, M. O. On a common circle: local scenes and Gestalt rules. *Proc. Natl Acad. Sci. USA* **98**, 1935–1940 (2001).
53. Geisler, W. S., Perry, J. S., Super, B. J. & Gallogly, D. P. Edge co-occurrence in natural images predicts contour grouping performance. *Vis. Res.* **41**, 711–724 (2001).
54. Ko, H. et al. The emergence of functional microcircuits in visual cortex. *Nature* **496**, 96 (2013).
55. Poirazi, P., Brannon, T. & Mel, B. W. Pyramidal neuron as two-layer neural network. *Neuron* **37**, 989–999 (2003).
56. Kastellakis, G., Silva, A. J. & Poirazi, P. Linking memories across time via neuronal and dendritic overlaps in model neurons with active dendrites. *Cell Rep.* **17**, 1491–1504 (2016).
57. Hiratani, N. & Fukai, T. Redundancy in synaptic connections enables neurons to learn optimally. *Proc. Natl Acad. Sci. USA* **115**, E6871–E6879 (2018).
58. McBride, T. J., Rodriguez-Contreras, A., Trinh, A., Bailey, R. & DeBello, W. M. Learning drives differential clustering of axodendritic contacts in the barn owl auditory system. *J. Neurosci.* **28**, 6960–6973 (2008).
59. Fu, M., Yu, X., Lu, J. & Zuo, Y. Repetitive motor learning induces coordinated formation of clustered dendritic spines in vivo. *Nature* **483**, 92–95 (2012).
60. Frank, A. C. et al. Hotspots of dendritic spine turnover facilitate clustered spine addition and learning and memory. *Nat. Commun.* **9**, 422 (2018).
61. Okuno, H. et al. Inverse synaptic tagging of inactive synapses via dynamic interaction of Arc/Arg3.1 with CaMKII β . *Cell* **149**, 886–898 (2012).
62. Foncelle, A. et al. Modulation of spike-timing dependent plasticity: towards the inclusion of a third factor in computational models. *Front. Comput. Neurosci.* **12**, 49 (2018).
63. Priebe, N. J. Mechanisms of orientation selectivity in the primary visual cortex. *Annu. Rev. Vis. Sci.* **2**, 85–107 (2016).
64. White, L. E., Coppola, D. M. & Fitzpatrick, D. The contribution of sensory experience to the maturation of orientation selectivity in ferret visual cortex. *Nature* **411**, 1049 (2001).
65. Chapman, B., Gödecke, I. & Bonhoeffer, T. Development of orientation preference in the mammalian visual cortex. *J. Neurobiol.* **41**, 18–24 (1999).
66. Tazerart, S., Mitchell, D. E., Miranda-Rottmann, S. & Araya, R. A spike-timing-dependent plasticity rule for dendritic spines. *Nat. Commun.* **11**, 4276 (2020).
67. Polsky, A., Mel, B. W. & Schiller, J. Computational subunits in thin dendrites of pyramidal cells. *Nat. Neurosci.* **7**, 621 (2004).
68. Rumsey, C. C. & Abbott, L. F. Synaptic democracy in active dendrites. *J. Neurophysiol.* **96**, 2307–2318 (2006).
69. Branco, T. & Staras, K. The probability of neurotransmitter release: variability and feedback control at single synapses. *Nat. Rev. Neurosci.* **10**, 373 (2009).
70. Poleg-Polsky, A. Dendritic spikes expand the range of well tolerated population noise structures. *J. Neurosci.* **39**, 9173–9184 (2019).
71. Frey, U. & Morris, R. G. Synaptic tagging and long-term potentiation. *Nature* **385**, 533 (1997).
72. Sajikumar, S., Morris, R. G. M. & Korte, M. Competition between recently potentiated synaptic inputs reveals a winner-take-all phase of synaptic tagging and capture. *Proc. Natl Acad. Sci. USA* **111**, 12217–12221 (2014).
73. Ben-Ari, Y. Excitatory actions of GABA during development: the nature of the nurture. *Nat. Rev. Neurosci.* **3**, 728 (2002).
74. Kirmse, K. et al. GABA depolarizes immature neurons and inhibits network activity in the neonatal neocortex in vivo. *Nat. Commun.* **6**, 7750 (2015).
75. Boivin, J. R. & Nedivi, E. Functional implications of inhibitory synapse placement on signal processing in pyramidal neuron dendrites. *Curr. Opin. Neurobiol.* **51**, 16–22 (2018).
76. Müllner, F. E., Wierenga, C. J. & Bonhoeffer, T. Precision of inhibition: dendritic inhibition by individual GABAergic synapses on hippocampal pyramidal cells is confined in space and time. *Neuron* **87**, 576–589 (2015).
77. Cichon, J. & Gan, W.-B. Branch-specific dendritic Ca²⁺ spikes cause persistent synaptic plasticity. *Nature* **520**, 180 (2015).
78. Dufour, A., Rollenhagen, A., Sätzler, K. & Lübke, J. H. R. Development of synaptic boutons in layer 4 of the barrel field of the rat somatosensory cortex: a quantitative analysis. *Cereb. Cortex* **26**, 838–854 (2016).
79. Hartmann, M., Heumann, R. & Lessmann, V. Synaptic secretion of BDNF after high-frequency stimulation of glutamatergic synapses. *EMBO J.* **20**, 5887–5897 (2001).
80. Clopath, C., Büsing, L., Vasilaki, E. & Gerstner, W. Connectivity reflects coding: a model of voltage-based STDP with homeostasis. *Nat. Neurosci.* **13**, 344–352 (2010).
81. Sasi, M., Vignoli, B., Canossa, M. & Blum, R. Neurobiology of local and intercellular BDNF signaling. *Pflügers Arch. J. Physiol.* **469**, 593–610 (2017).
82. Gerstner, W., Kempter, R., van Hemmen, J. L. & Wagner, H. A neuronal learning rule for sub-millisecond temporal coding. *Nature* **383**, 76–78 (1996).
83. Stephens, D. C. et al. Spatiotemporal organization and protein dynamics involved in regulated exocytosis of MMP-9 in breast cancer cells. *J. Gen. Physiol.* **151**, 1386–1403 (2019).
84. Yang, J. et al. Neuronal release of proBDNF. *Nat. Neurosci.* **12**, 113–115 (2009).
85. Naskar, S. et al. The development of synaptic transmission is time-locked to early social behaviors in rats. *Nat. Commun.* **10**, 1195 (2019).
86. Kroon, T., van Hugte, E., van Linge, L., Mansvelter, H. D. & Meredith, R. M. Early postnatal development of pyramidal neurons across layers of the mouse medial prefrontal cortex. *Sci. Rep.* **9**, 1–16 (2019).
87. Tang, J., Jimenez, S. C. A., Chakraborty, S. & Schultz, S. R. Visual receptive field properties of neurons in the mouse lateral geniculate nucleus. *PLoS ONE* **11**, e0146017 (2016).
88. Piscopo, D. M., El-Danaf, R. N., Huberman, A. D. & Niell, C. M. Diverse visual features encoded in mouse lateral geniculate nucleus. *J. Neurosci.* **33**, 4642–4656 (2013).
89. Kerchner, G. A. & Nicoll, R. A. Silent synapses and the emergence of a postsynaptic mechanism for LTP. *Nat. Rev. Neurosci.* **9**, 813–825 (2008).

90. Magó, Á., Weber, J. P., Ujfalussy, B. B. & Makara, J. K. Synaptic plasticity depends on the fine-scale input pattern in thin dendrites of CA1 pyramidal neurons. *J. Neurosci.* **40**, 2593–2605 (2020).
91. Bernander, O., Koch, C. & Douglas, R. J. Amplification and linearization of distal synaptic input to cortical pyramidal cells. *J. Neurophysiol.* **72**, 2743–2753 (1994).
92. Hennequin, G., Agnes, E. J. & Vogels, T. P. Inhibitory plasticity: balance, control, and codependence. *Annu. Rev. Neurosci.* **40**, 557–579 (2017).
93. Kuczewski, N. et al. Spontaneous glutamatergic activity induces a {BDNF}-dependent potentiation of GABAergic synapses in the newborn rat hippocampus. *J. Physiol.* **586**, 5119–5128 (2008).
94. Langlois, A., Diabira, D., Ferrand, N., Porcher, C. & Gaiarsa, J.-L. NMDA-dependent switch of proBDNF actions on developing GABAergic synapses. *Cereb. Cortex* **23**, 1085–1096 (2012).
95. Liu, G. Local structural balance and functional interaction of excitatory and inhibitory synapses in hippocampal dendrites. *Nat. Neurosci.* **7**, 373 (2004).
96. Valeeva, G., Tressard, T., Mukhtarov, M., Baude, A. & Khazipov, R. An optogenetic approach for investigation of excitatory and inhibitory network GABA actions in mice expressing channelrhodopsin-2 in GABAergic neurons. *J. Neurosci.* **36**, 5961–5973 (2016).
97. Higley, M. J. Localized GABAergic inhibition of dendritic Ca²⁺ signalling. *Nat. Rev. Neurosci.* **15**, 567 (2014).
98. Mataga, N., Mizuguchi, Y. & Hensch, T. K. Experience-dependent pruning of dendritic spines in visual cortex by tissue plasminogen activator. *Neuron* **44**, 1031–1041 (2004).
99. Macke, J. H., Berens, P., Ecker, A. S., Tolias, A. S. & Bethge, M. Generating spike trains with specified correlation coefficients. *Neural Comput.* **21**, 397–423 (2009).
100. Cuntz, H., Forstner, F., Borst, A. & Häusser, M. The TREES toolbox—probing the basis of axonal and dendritic branching. *Neuroinformatics* **9**, 91–96 (2011).
101. Larkum, M. E., Nevian, T., Sandler, M., Polsky, A. & Schiller, J. Synaptic integration in tuft dendrites of layer 5 pyramidal neurons: a new unifying principle. *Science* **325**, 756–760 (2009).
102. Takahashi, N., Oertner, T. G., Hegemann, P. & Larkum, M. E. Active cortical dendrites modulate perception. *Science* **354**, 1587–1590 (2016).
103. Rohatgi, A. (WebPlotDigitizer, 2011).

Acknowledgements

We thank N. Hedrick, M. Jüngling, M. Kaschube, G. Laurent, J. Letzkus, C. Lohmann, C. Miehl, L. Richter, B. Scholl, E. Schuman, M. Silies, and M. E. Wosniack for comments, discussions, and feedback on the manuscript. This work was supported by the Max Planck Society, the SMART START training program in computational neuroscience (to J.H.K.), and the Behrens-Weise Foundation (to J.G.). This project has received funding

from the European Research Council (ERC) under the European Union's Horizon 2020 research and innovation program (Grant agreement No. 804824).

Author contributions

J.H.K. and J.G. designed the research. J.H.K. analyzed the model and performed model simulations. J.H.K. and J.G. prepared the figures and wrote the manuscript.

Funding

Open Access funding enabled and organized by Projekt DEAL.

Competing interests

The authors declare no competing interests.

Additional information

Supplementary information The online version contains supplementary material available at <https://doi.org/10.1038/s41467-021-23557-3>.

Correspondence and requests for materials should be addressed to J.G.

Peer review information *Nature Communications* thanks the anonymous reviewers for their contribution to the peer review of this work.

Reprints and permission information is available at <http://www.nature.com/reprints>

Publisher's note Springer Nature remains neutral with regard to jurisdictional claims in published maps and institutional affiliations.



Open Access This article is licensed under a Creative Commons Attribution 4.0 International License, which permits use, sharing, adaptation, distribution and reproduction in any medium or format, as long as you give appropriate credit to the original author(s) and the source, provide a link to the Creative Commons license, and indicate if changes were made. The images or other third party material in this article are included in the article's Creative Commons license, unless indicated otherwise in a credit line to the material. If material is not included in the article's Creative Commons license and your intended use is not permitted by statutory regulation or exceeds the permitted use, you will need to obtain permission directly from the copyright holder. To view a copy of this license, visit <http://creativecommons.org/licenses/by/4.0/>.

© The Author(s) 2021

Emergence of synaptic organization and computation in dendrites

In Kirchner *et al.* (2022), we review recent scientific literature on how the precise positioning of excitatory and inhibitory synapses on dendrites might develop and which functions this positioning might support. We review experimental evidence and computational studies and focus on:

1. The synaptic clustering of excitatory synapses on a local spatial scale called *synaptic clustering*. We find that while synaptic clustering appears to be near-ubiquitous across brain areas and species, the qualitative characteristics of clustering can vary strongly.
2. The global organization of excitatory synapses. We find that recently published studies provide a converging picture of how global synaptic organization might be important for learning and dynamic computations in single neurons.
3. The local organization of inhibitory synapses. We find evidence that the precise coordination and co-location of excitatory and inhibitory synapses can enable flexible routing and signal amplification of synaptic inputs.

The work was completed in collaboration with my supervisor, Prof. Dr. Julijana Gjorgjieva. Together, we prepared the figures and wrote the manuscript. I performed the literature review and wrote the first draft. The full review was published on December 31st, 2021 in Neuroforum and is reproduced on the following pages under the Creative Commons Attribution 4.0 International License.

Review article

Jan H. Kirchner and Julijana Gjorgjieva*

Emergence of synaptic organization and computation in dendrites

<https://doi.org/10.1515/nf-2021-0031>

Abstract: Single neurons in the brain exhibit astounding computational capabilities, which gradually emerge throughout development and enable them to become integrated into complex neural circuits. These capabilities derive in part from the precise arrangement of synaptic inputs on the neurons' dendrites. While the full computational benefits of this arrangement are still unknown, a picture emerges in which synapses organize according to their functional properties across multiple spatial scales. In particular, on the local scale (tens of microns), excitatory synaptic inputs tend to form clusters according to their functional similarity, whereas on the scale of individual dendrites or the entire tree, synaptic inputs exhibit dendritic maps where excitatory synapse function varies smoothly with location on the tree. The development of this organization is supported by inhibitory synapses, which are carefully interleaved with excitatory synapses and can flexibly modulate activity and plasticity of excitatory synapses. Here, we summarize recent experimental and theoretical research on the developmental emergence of this synaptic organization and its impact on neural computations.

Keywords: cortex; dendrite; development; organization; synaptic plasticity.

Zusammenfassung: Einzelne Neuronen im Gehirn weisen erstaunliche Rechenfähigkeiten auf, die sich im Laufe der Entwicklung allmählich entwickeln und es den Neuronen ermöglichen, in komplexe neuronale Schaltkreise integriert zu werden. Diese Fähigkeiten leiten sich unter anderem von

der genauen Anordnung der Synapsen auf den Dendriten der Neuronen ab. Während der genaue rechnerische Nutzen dieser Anordnung noch unbekannt ist, zeichnet sich ein Bild ab, in dem Synapsen nach ihren funktionellen Eigenschaften über mehrere räumliche Ebenen hinweg organisiert sind. Während auf der lokalen Ebene (zehn Mikrometer) exzitatorische synaptische Eingänge dazu neigen, Cluster entsprechend ihrer funktionalen Ähnlichkeit zu bilden, zeigen synaptische Eingänge auf der Ebene einzelner Dendriten oder des gesamten Baums "dendritic maps", bei denen die Funktion exzitatorischer Synapsen gleichmäßig mit der Position auf dem Dendriten variiert. Die Entwicklung dieser Organisation wird durch inhibitorische Synapsen unterstützt, die präzise mit exzitatorischen Synapsen verflochten sind und die Aktivität und Plastizität exzitatorischer Synapsen flexibel modulieren können. Hier fassen wir aktuelle experimentelle und theoretische Forschung über die Entstehung dieser synaptischen Organisation in der Entwicklung und ihren Einfluss auf neuronale Berechnungen zusammen.

Schlüsselwörter: Kortex; Dendrit; Entwicklung; Organisation; synaptische Plastizität.

Introduction

Neurons process information in the form of electrical signals called action potentials. These signals are transmitted via synapses from one neuron to another. At a synapse, an electrical signal induces the release of neurotransmitters which affect the receiving neuron's membrane potential. The majority of synapses are found on dendrites, branch-like extensions of a neuron that receive electrical stimulation from other neurons and carry it to the neuron's cell body called the soma. Depending on the neurotransmitter a synapse releases, a synapse is either excitatory, i.e., usually depolarizing the membrane potential via the release of acetylcholine or glutamate, or inhibitory, i.e., usually hyperpolarizing the membrane potential via the release of gamma-aminobutyric acid (GABA) or glycine. The exact arrangement of excitatory and inhibitory synapses influences the generation of action potentials at the soma,

*Corresponding author: Julijana Gjorgjieva, Computation in Neural Circuits Group, Max Planck Institute for Brain Research, Max-von-Laue-Str. 4, 60438 Frankfurt, Germany; and Technical University of Munich, School of Life Sciences, 85354 Freising, Germany, E-mail: gjorgjieva@brain.mpg.de
<https://orcid.org/0000-0001-7118-4079>

Jan H. Kirchner, Computation in Neural Circuits Group, Max Planck Institute for Brain Research, Max-von-Laue-Str. 4, 60438 Frankfurt, Germany; and Technical University of Munich, School of Life Sciences, 85354 Freising, Germany, E-mail: jan.kirchner@brain.mpg.de
<https://orcid.org/0000-0002-9126-0558>

and hence the transmission of information to other neurons, and is of central importance for information processing in the brain (Stuart et al., 2016).

During early development, various single neuron and neural circuit properties, such as the organization of synapses, emerge through the interaction of multiple factors, including genetically regulated cell specification and activity-dependent circuit formation and refinement. Since many of the sensory organs in the developing brain are immature, much of the early neural activity is generated *spontaneously* in the absence of sensory stimulation. Almost all neural circuits in the developing brain can generate spontaneous activity, including the sensory cortex on which we focus here (Leighton and Lohmann, 2016). Spontaneous activity is usually highly structured and contains spatio-temporal correlations to instruct the formation, the removal, and the changes in strength of synaptic inputs. The developing retina exhibits one of the best studied examples of spontaneous activity known as retinal waves, which directly influence connectivity refinement and receptive field tuning in downstream visual areas such as the superior colliculus and the thalamus (Blankenship and Feller, 2010). Specific activity-dependent plasticity mechanisms drive this connectivity refinement (Richter and Gjorgjieva, 2017). The exact form of these plasticity mechanisms and their functional implications are an active area of research (Agnes and Vogels, 2021; Hiratani and Fukai, 2018; Kirchner and Gjorgjieva, 2021; Mikulasch et al., 2021; Sezener et al., 2021).

There are different computational and theoretical approaches to investigate the emergence of organization in the developing brain. In one approach, neurons are modeled as so-called *point neurons* that conceptualize neurons as single points without spatial extent. Often, point neurons are assumed to directly integrate synaptic inputs and transform them into spiking outputs while ignoring the transformations implemented by dendrites. Point neurons have the advantage that they are amenable to mathematical analysis while still capturing the ability of the neuron to generate action potentials and can be easily connected when simulating large networks. At the other end of the spectrum, multicompartiment neuron models include fully reconstructed dendrites to carefully incorporate the influence on the soma of individual synaptic inputs across the dendritic tree. Multicompartiment models are often equipped with a variety of ion channels, allowing them to produce a wide range of local, nonlinear transformations of the input. While these models are typically mathematically intractable, they reveal the profound impact of synapses' distribution on dendritic, cellular, and network computations and neural information processing more generally (Poirazi et al., 2003).

Here, we adopt a third perspective, similar to the passive multicompartiment model, in which we retain the

dendrite's shape while abstracting away many details of a full biophysical model. We distinguish between different spatial scales of synaptic organization on a dendrite, local and global, and summarize recent experimental and theoretical progress on understanding the properties, functions, and developmental emergence of this organization. We highlight differences and commonalities between excitatory and inhibitory synapse organization and possible functional consequences of their interaction. Finally, based on experimental data from the developing retina, we propose a model for the developmental emergence of balanced excitation and inhibition.

Organization of excitatory synapses

Most of the synaptic inputs that reach a neuron arrive on its dendrites. How these signals are integrated and finally transformed into action potentials is of central importance for understanding neuronal information processing (Spruston et al., 2016). Dendrites can support information processing at multiple spatial scales (Figure 1). On the local scale, i.e., the fine-scale organization of synapses over tens of microns, dendrites affect information processing by organizing synapses with similar properties into *synaptic clusters* that boost a neuron's computational capacity through nonlinear integration (Kastellakis et al., 2015; Mel, 1992, 1993; Poirazi et al., 2003; Ujfalussy and Makara, 2020; Wilson et al., 2016). On the level of

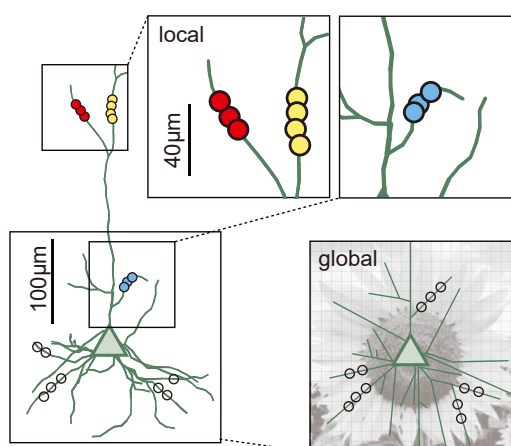


Figure 1: A schematic of a dendrite with synapses (colored dots). Synapses exhibit organization at multiple spatial scales. At the local scale of tens of microns (top right), synapses form clusters in which synapses with similar selectivity (indicated by the color) are in spatial proximity. At the global scale (bottom right), synapses form dendritic maps, where nearby locations in visual space, represented by the sunflower, are encoded by synapses at nearby locations on the dendrite (black circles).

individual branches, dendrites exhibit *dendritic maps* in which the tuning of synapses (or synaptic clusters) varies systematically across the dendritic tree (Bollmann and Engert, 2009; Iacaruso et al., 2017; Jia et al., 2014; Podgorski et al., 2021; Wilson et al., 2016). Finally, the dendrite's branching structure determines the extent to which synaptic inputs influence the soma (Ferrante et al., 2013; Jaffe and Carnevale, 1999; Tzilivaki et al., 2019; Vetter et al., 2001).

There is accumulating evidence that a substantial amount of the dendritic organization across these scales emerges already during early development (Kirchner and Gjorgjieva, 2021; Kleindienst et al., 2011; Lee et al., 2016; Niculescu et al., 2018; Takahashi et al., 2012; Winnubst et al., 2015). This early emergence is particularly noteworthy as neural activity during these early phases primarily arises spontaneously (Leighton and Lohmann, 2016), raising the question of how the brain can precisely arrange synaptic inputs across scales without sensory input. Investigating this question reveals essential facts about the mechanisms of brain development and provides a valuable perspective on how the adult brain works.

Synaptic clustering

In the case of local organization, synapses onto mouse pyramidal neurons arrange into clusters during early postnatal development (Kleindienst et al., 2011; Niculescu et al., 2018; Takahashi et al., 2012; Winnubst et al., 2015) (Figure 2a). Clustering refines over development (Takahashi et al., 2012) and cannot form when spontaneous activity is absent (Kleindienst et al., 2011; Takahashi et al., 2012). Further, experiments blocking individual molecules and their receptors implicate a family of signaling molecules called *neurotrophic factors* in this process (Kutsarova et al., 2021; Niculescu et al., 2018; Winnubst et al., 2015). Computational modeling demonstrates that the interactions between these neurotrophic factors effectively implement a local plasticity rule that can generate clustering (Kirchner and Gjorgjieva, 2021), where poorly synchronized synapses weaken and well-synchronized synapses stabilize (Niculescu et al., 2018; Winnubst et al., 2015). As the activity becomes driven by the senses and the animal encounters more complex situations, the substrate of plasticity becomes more complex over development. While the prevalence of the relevant

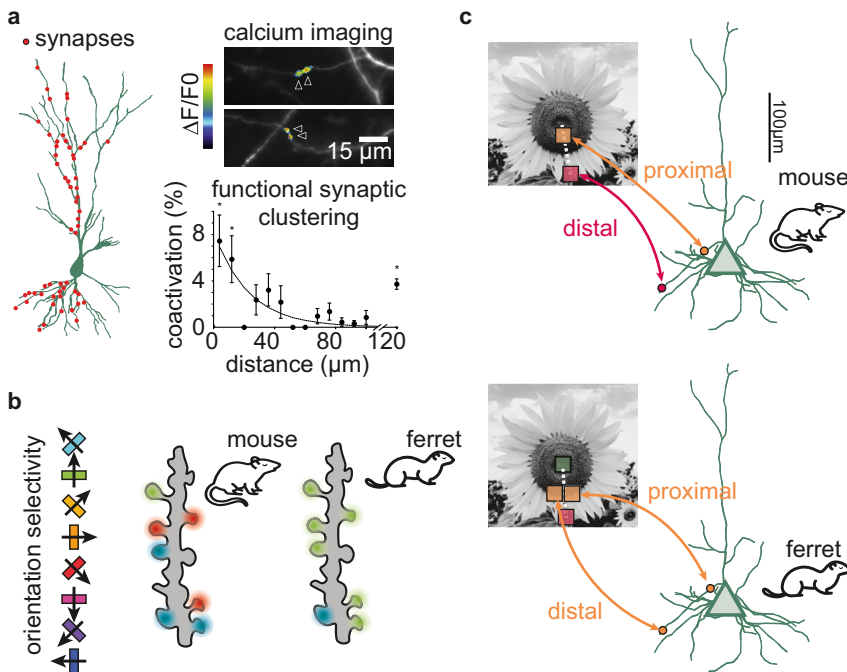


Figure 2: Species-specific local and global organization of excitatory synapses.

(a) Left: reconstruction of a CA3 pyramidal neuron with synaptic inputs indicated as red circles. Redrawn from ref (Kleindienst et al., 2011). Top right: calcium activity in clustered synaptic inputs in developing CA3 pyramidal cell dendrites. Redrawn from ref (Niculescu et al., 2018). Bottom right: synaptic coactivation as a function of intersynaptic distance. Redrawn from ref (Kleindienst et al., 2011). (b) Illustration of qualitatively different types of clustering in mouse and the ferret: the ferret shows clustering according to orientation, whereas the mouse does not and instead shows clustering according to receptive field overlap (Iacaruso et al., 2017; Wilson et al., 2016). (c) Illustration of a retinotopically organized dendritic map observed in the mouse (top) but not in the ferret (bottom).

neurotrophic factors decreases with age (Yang et al., 2009), there is evidence that the local plasticity rule also applies in the adult animal, possibly implemented by different sets of interacting molecules (El-Boustani et al., 2018; Harward et al., 2016; Hedrick et al., 2016; Oh et al., 2015; Tazerart et al., 2020). This parallel hints at the exciting possibility that the underlying principles of synaptic plasticity remain unchanged and form a foundation for more versatile plasticity during adult life (Ganguly and Poo, 2013; Lohmann and Kessels, 2014).

While synaptic clustering appears to be near-ubiquitous across brain areas and species (Adoff et al., 2021; Ashaber et al., 2021; Frank et al., 2018; Fu et al., 2012; Gökçe et al., 2016; Iacaruso et al., 2017; Ju et al., 2020; Kerlin et al., 2019; Kim et al., 2021; Kleindienst et al., 2011; Lee et al., 2019; McBride et al., 2008; Niculescu et al., 2018; Podgorski et al., 2021; Scholl et al., 2017; Takahashi et al., 2012; Wilson et al., 2016; Winnubst et al., 2015), there is striking variability in the qualitative characteristics of clusters. The receptive field of a synapse – the sensory feature encoded by the synaptic input – can be used to describe the properties of clusters. For example, synaptic clusters in the ferret or macaque visual cortex tend to have receptive fields that share a preference for moving gratings of the same orientation (Scholl et al., 2017; Wilson et al., 2016). This shared orientation preference is not present in the mouse visual cortex, where instead, synapses with spatially overlapping receptive fields tend to form a cluster (Iacaruso et al., 2017; Jia et al., 2010) (Figure 2b). Computational modeling demonstrates that the differences between the mouse, ferret, and macaque visual cortex might result from two simple factors: the anatomical size of the retina and the anatomical size of the visual cortex (Kirchner and Gjorgjieva, 2021; Scholl et al., 2017).

Thus, central aspects of the local synaptic organization can emerge without sensory stimulation, suggesting that development might equip dendrites with fundamental building blocks such as feature selectivity from which other functional properties derive in adulthood. Computational modeling stands out as a handy tool for investigating this hypothesis, as longitudinal experiments that monitor synaptic organization and function across development and into adulthood (Witvliet et al., 2021) are currently technically infeasible.

Dendritic maps

Beyond the fine-scale organization over tens of microns, there is also accumulating evidence for synaptic organization

on the level of entire dendritic branches (hundreds of microns). Concretely, synapses do not only cluster locally but also tend to organize along the entire dendritic tree, according to their function (Bollmann and Engert, 2009; El-Boustani et al., 2018; Iacaruso et al., 2017; Jia et al., 2014; Kerlin et al., 2019; Podgorski et al., 2021; Wilson et al., 2016). One striking example of this can be observed in the *Xenopus* tadpole tectum (Bollmann and Engert, 2009) and in the mouse visual cortex (El-Boustani et al., 2018; Iacaruso et al., 2017) where synapses are arranged retinotopically, i.e., proximal (distal) synapses tend to respond to stimulation of central (peripheral) locations in visual space (Figure 2c). We note, however, that the existing experimental data in the mouse and ferret visual cortex do not provide information about the relationship between synapse proximity and location on basal versus apical dendrites. A similar synaptic organization can be observed in the mouse barrel cortex, where proximal (distal) synapses tend to respond (not respond) to stimulation of the primary whisker of the corresponding barrel (Jia et al., 2014; Schoonover et al., 2014), and in the hippocampus, where individual branches respond to specific locations in space (Rashid et al., 2020). We term this type of global organization *dendritic maps* (Kirchner and Gjorgjieva, 2021) to highlight the similarity with *cortical maps* (White and Fitzpatrick, 2007). In the ferret visual cortex, this retinotopic organization is markedly absent (Scholl et al., 2017) (Figure 2c), and instead, synapses on the same dendritic branch tend to share the same preference for oriented gratings (Wilson et al., 2016).

While experimental evidence for dendritic maps abounds, their possible function is mostly unclear. One explanation for why different dendritic branches receive different inputs is that this separation allows the soma to weigh the inputs according to their reliability, enabling Bayes-optimal integration (Jordan et al., 2021). Alternatively, different dendritic branches might be gated on or off in a context-dependent fashion (Yang et al., 2016), allowing more powerful dendritic computations (Poirazi et al., 2003) and modifying only a subset of synapses while retaining the rest (Cichon and Gan, 2015; Sezener et al., 2021; Yaeger et al., 2019). A third hypothesis is that the feature selectivity of different synapses matches commonly co-occurring features in complex sensory inputs, allowing the neuron to perform more efficient feature detection (Hiratani and Fukai, 2018; Iacaruso et al., 2017; Kirchner and Gjorgjieva, 2021). Finally, the ability of dendrites to segregate feed forward and feedback information into different compartments (Larkum et al., 2009; Takahashi et al., 2016) might provide a biological substrate for

determining the contribution of individual inputs to the outcome of a computation, known as the credit assignment problem (Guerguiev et al., 2017; Richards and Lillicrap, 2019).

However, recent experiments have revealed that our understanding of dendritic computations is still limited. The somatic receptive field seems to be derived from only a handful of powerful synaptic connections (Cossell et al., 2015). Indeed, removing the entire basal or apical dendrites *in vivo* does not affect the functional selectivity of the soma (Park et al., 2019). Also, large dendritic events *in vivo* overwhelmingly co-occur with somatic events in typical recording setups (Beaulieu-Laroche et al., 2019; Francioni et al., 2019; Kerlin et al., 2019) and only become substantially decoupled when the animal is allowed to move freely (Voigts and Harnett, 2020). These observations indicate that proper investigation of structured and diverse synaptic input across the entire dendritic tree might require a richer set of stimuli (Laboy-Juárez et al., 2019) that engages the full cognitive potential of the animal.

How might dendritic maps be established? In contrast to synaptic clustering, there is only limited experimental evidence of the presence of dendritic maps in early development (Bollmann and Engert, 2009). Computational modeling suggests that local, structural plasticity in conjunction with an attenuating back-propagating action potential is sufficient to produce species-specific dendritic maps (Kirchner and Gjorgjieva, 2021). Alternatively, (Hiratani and Fukai, 2018) propose that dendritic maps might also arise during development from a combination of plasticity that depends on the location of the synapse on the dendritic tree (Froemke et al., 2005; Letzkus et al., 2006; Weber et al., 2016) and structural synaptic rewiring (Mel, 1992). Finally, recent experimental data demonstrate that dendritic growth is affected by synaptic activity (Podgorski et al., 2021), suggesting that changes to dendritic morphology might facilitate dendritic map formation. Since early development is characterized by the establishment of dendritic morphology (Richards et al., 2020) and by repeated and rapid synapse turnover (Holtmaat and Svoboda, 2009; Maletic-Savatic et al., 1999), it appears as a particularly opportune time for the formation of dendritic maps.

In summary, there is accumulating evidence that dendrites exhibit dendritic maps, i.e., topographically organized synaptic inputs across the entire dendritic tree. These dendritic maps exhibit substantial qualitative variability across areas and species. While their function is still unclear, computational models generate several testable predictions and provide hypotheses that can guide the direction of future experimental research.

Organization of inhibitory synapses

Most studies on synaptic organization focus on excitatory synapses. This focus is traditionally attributable to the relative abundance of glutamatergic synapses and the better availability of markers for glutamatergic synapses (Chen et al., 2012). Even though inhibitory synapses, which represent 12% of all dendritic synapses (Iascone et al., 2020), have been relatively neglected by comparison, they play an essential role in neural information processing (Boivin and Nedivi, 2018).

Local balance of excitatory and inhibitory synapses

The balance of excitation and inhibition is a characteristic feature of cortical dynamics (Okun and Lampl, 2008). Still, it is an open question on just how *detailed* this balance is (Hennequin et al., 2017): does the balance extend to the dendritic tree, individual branches, or even local stretches on the dendrite (Figure 3a)? These questions are the center of new experimental studies on inhibitory synapse organization and dynamics.

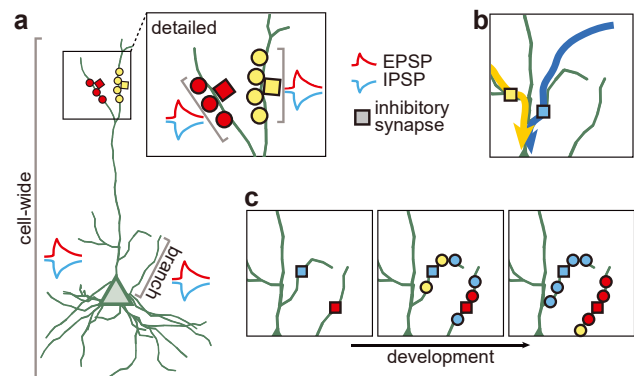


Figure 3: Function and origin of locally balanced excitation and inhibition.

(a) Illustration of the balance of excitation and inhibition at different spatial scales. Balance might exist cell-wide (excitation and inhibition matched at the soma), on individual branches, or local stretches of the dendrite (detailed balance, inset, top right). (b) Inhibitory synapses (colored squares) might gate dendritic signals by selectively inhibiting some branches but not others (Boivin and Nedivi, 2018). Yellow and blue arrows indicate incoming signals from two different branches. (c) Model of the emergence of excitatory and inhibitory balance over development, based on experiments in the mouse retina (Bleckert et al., 2013; Johnson et al., 2003; Soto et al., 2011). Inhibitory synapses form first (left) and provide a scaffold around which excitatory synapses organize (middle). Structural and functional plasticity rearranges excitatory synapses to establish a detailed dendritic balance (right).

On the local scale, inhibitory synapses exhibit a substantial amount of organization (Chen et al., 2012; Iascone et al., 2020; Liu, 2004; Villa et al., 2016). In contrast to excitatory synapses, which primarily reside on dendritic spines, inhibitory synapses can be found both on spines and the dendritic shaft (Iascone et al., 2020). The density of inhibitory synapses closely tracks the density of excitatory synapses (Iascone et al., 2020), and 25–30% of all inhibitory synapses share a dendritic spine with an excitatory synapse (Chen et al., 2012; Iascone et al., 2020), an arrangement called *dually innervated spines*. Excitatory synapses on dually innervated spines are extraordinarily stable and experience almost no turnover (Villa et al., 2016). By contrast, inhibitory synapses on dually innervated spines experience increased remodeling, repeatedly appearing and disappearing on the same spine (Villa et al., 2016). Experimental stimulation of clustered excitatory synapses triggers the *de novo* formation of inhibitory synapses (Hu et al., 2019). Also, during normal visual experience, whenever excitatory synapses are stable, nearby inhibitory synapses within 10 μm are also stable (Chen et al., 2012). Finally, experiments in a hippocampal culture provide evidence for a push–pull plasticity mechanism that can carefully balance excitatory and inhibitory strength (Liu, 2004). Thus, a detailed balance of excitation and inhibition on local stretches of dendrites appears entirely consistent with the experimental data.

Based on their location on specific parts of the dendritic tree, inhibitory synapses can effectively shape dendritic signal detection and integration by restricting both voltage and calcium signaling of excitatory synapses (Boivin and Nedivi, 2018; Higley, 2014; Liu, 2004) (Figure 3b). Computational modeling proposes several possible benefits of this property of inhibitory synapses. Consistent with experiments (Wang and Maffei, 2014), modulating local inhibition can change the shape of the learning rule for excitatory synapses (Agnes and Vogels, 2021; Hiratani and Fukai, 2017; Mikulasch et al., 2021). Based on the relative timing and strength of the inhibitory input, potentiation and depression of excitatory synapses can be attenuated (Agnes and Vogels, 2021) or even fully inverted (Hiratani and Fukai, 2017; Mikulasch et al., 2021). This inhibitory control over excitatory plasticity might enable the recalibration of selectivity of excitatory synapses in the visual cortex when input from one eye is lost (Hiratani and Fukai, 2017). Alternatively, local inhibition can help to avoid redundancies in the neural code and lead to more efficient and diverse feature representations (Mikulasch et al., 2021). Finally, gating excitatory plasticity through local inhibition can allow for the rapid reorganization of excitatory synapses during periods of

disinhibition, while keeping excitatory organization stable (Agnes and Vogels, 2021; Sezener et al., 2021).

How a highly detailed balance of excitation and inhibition emerges in the cortex is still an open question, but studying the emergence of detailed balance in the mouse retina (Bleckert et al., 2013; Jain et al., 2020; Johnson et al., 2003; Soto et al., 2011) might provide important insights. In the retina, inhibitory synapses form slightly before excitatory synapses (Johnson et al., 2003); the density of both types of synapses increases gradually until eye opening (Soto et al., 2011); and excitatory synapses are more likely to form nearby inhibitory synapses (Bleckert et al., 2013). These constraints postulate a model in which inhibitory synapses form a stable backbone around which excitatory synapses cluster (Kirchner and Gjorgjieva, 2021). Once the density of excitatory and inhibitory synapses has stabilized, a local plasticity rule can further rearrange synapses and establish synaptic clusters to enable flexible computations and efficient learning (Agnes and Vogels, 2021; Hiratani and Fukai, 2017; Kirchner and Gjorgjieva, 2021; Mikulasch et al., 2021) (Figure 3c).

While less is known about the organization of inhibitory synapses than of excitatory synapses, recent experiments and modeling studies paint a picture in which both types of synapses interact closely. Inhibitory synapses can exercise tight control over excitatory activity and plasticity, allowing for more flexible and diverse neural computations. During development, inhibitory synapses might form a backbone that substantially constrains and guides the emergence of excitatory synapse organization.

Discussion

The precise organization of synapses across the dendritic tree makes us hopeful that the daunting amount of detail present in biological dendrites as the branches that enable neurons to connect and transmit information might eventually lead to the discovery of unifying principles. Synaptic clustering, dendritic maps, and detailed excitatory–inhibitory balance all share the hallmark features of organization of the cortex at large: nearby neurons tend to share functional properties (Dombeck et al., 2009), neurons across the cortical sheet arrange into cortical maps (White and Fitzpatrick, 2007), and excitatory and inhibitory activity at the level of the soma is balanced (Okun and Lampl, 2008). We are excited to see if further parallels will emerge as experimental methods become more powerful (Podgorski et al., 2021).

While we focused on the organization of synapses on dendrites, conversely, dendrites' shape is affected by the availability of suitable synaptic partners (Niell et al., 2004; Podgorski et al., 2021; Stuart et al., 2016). As a consequence, a mature dendrite's shape might not only affect its possible inputs and thereby its computational capacities but also be the result of activity-dependent plasticity processes during early development. A time-lapsed optical imaging of dendrite growth during spontaneous activity or in conjunction with sensory stimulation (Podgorski et al., 2021) will be able to ascertain the degree to which activity affects dendrite growth and vice versa.

A wide range of further distinctions is possible beyond the broad separation of synapses into excitatory and inhibitory. Inhibitory interneurons fall into several genetically characterized subtypes, which differ in their biophysical properties and subcellular specificity (Tremblay et al., 2016). While fast-spiking, parvalbumin-positive interneurons tend to form synapses onto the soma and the proximal dendrite, other interneuron types prefer the distal basal or the apical tuft. While research on circuit implications of interneuron diversity is well underway, functional implications of different interneuron subtypes on different parts of the dendrite are only just shifting into focus (Vercruyse et al., 2021).

Author contributions: All the authors have accepted responsibility for the entire content of this submitted manuscript and approved submission.

Research funding: This work was supported by the Max Planck Society, the Behrens-Weise Foundation (to J.G.) and the European Research Council (ERC) under the European Union's Horizon 2020 research and innovation program (grant agreement no. 804824).

Conflict of interest statement: The authors declare no conflicts of interest regarding this article.

References

- Adoff, M.D., Climer, J.R., Davoudi, H., Marvin, J.S., Looger, L.L., and Dombeck, D.A. (2021). The functional organization of excitatory synaptic input to place cells. *Nat. Commun.* **12**, 3558.
- Agnes, E.J. and Vogels, T.P. (2021). Interacting synapses stabilise both learning and neuronal dynamics in biological networks. *BioRxiv*. <https://doi.org/10.1101/2021.04.01.437962>
- Ashaber, M., Tomina, Y., Kassraian, P., Bushong, E.A., Kristan, W.B., Ellisman, M.H., and Wagenaar, D.A. (2021). Anatomy and activity patterns in a multifunctional motor neuron and its surrounding circuits. *ELife* **10**, e61881.
- Beaulieu-Laroche, L., Toloza, E.H.S., Brown, N.J., and Harnett, M.T. (2019). Widespread and highly correlated somato-dendritic activity in cortical layer 5 neurons. *Neuron* **103**, 235–241.e4.
- Blankenship, A.G. and Feller, M.B. (2010). Mechanisms underlying spontaneous patterned activity in developing neural circuits. *Nat. Rev. Neurosci.* **11**, 18–29.
- Bleckert, A., Parker, E.D., Kang, Y., Pancaroglu, R., Soto, F., Lewis, R., Craig, A.M., and Wong, R.O.L. (2013). Spatial relationships between GABAergic and glutamatergic synapses on the dendrites of distinct types of mouse retinal ganglion cells across development. *PLoS One* **8**, e69612.
- Boivin, J.R. and Nedivi, E. (2018). Functional implications of inhibitory synapse placement on signal processing in pyramidal neuron dendrites. *Curr. Opin. Neurobiol.* **51**, 16–22.
- Bollmann, J.H. and Engert, F. (2009). Subcellular topography of visually driven dendritic activity in the vertebrate visual system. *Neuron* **61**, 895–905.
- Chen, J.L., Villa, K.L., Cha, J.W., So, P.T.C., Kubota, Y., and Nedivi, E. (2012). Clustered dynamics of inhibitory synapses and dendritic spines in the adult neocortex. *Neuron* **74**, 361–373.
- Cichon, J. and Gan, W.-B. (2015). Branch-specific dendritic Ca²⁺ spikes cause persistent synaptic plasticity. *Nature* **520**, 180–185.
- Cossell, L., Iacaruso, M.F., Muir, D.R., Houlton, R., Sader, E.N., Ko, H., Hofer, S.B., and Mrsic-Flogel, T.D. (2015). Functional organization of excitatory synaptic strength in primary visual cortex. *Nature* **518**, 399–403.
- Dombeck, D.A., Graziano, M.S., and Tank, D.W. (2009). Functional clustering of neurons in motor cortex determined by cellular resolution imaging in awake behaving mice. *J. Neurosci.* **29**, 13751–13760.
- El-Boustani, S., Ip, J.P.K., Breton-Provencher, V., Knott, G.W., Okuno, H., Bito, H., and Sur, M. (2018). Locally coordinated synaptic plasticity of visual cortex neurons in vivo. *Science* **360**, 1349–1354.
- Ferrante, M., Migliore, M., and Ascoli, G.A. (2013). Functional impact of dendritic branch-point morphology. *J. Neurosci.* **33**, 2156–2165.
- Francioni, V., Padamsey, Z., and Rochefort, N.L. (2019). High and asymmetric somato-dendritic coupling of V1 layer 5 neurons independent of visual stimulation and locomotion. *ELife* **8**, e49145.
- Frank, A.C., Huang, S., Zhou, M., Gdalyahu, A., Kastellakis, G., Silva, T.K., Lu, E., Wen, X., Poirazi, P., Trachtenberg, J.T., et al. (2018). Hotspots of dendritic spine turnover facilitate clustered spine addition and learning and memory. *Nat. Commun.* **9**, 422.
- Froemke, R.C., Poo, M., and Dan, Y. (2005). Spike-timing-dependent synaptic plasticity depends on dendritic location. *Nature* **434**, 221–225.
- Fu, M., Yu, X., Lu, J., and Zuo, Y. (2012). Repetitive motor learning induces coordinated formation of clustered dendritic spines in vivo. *Nature* **483**, 92–95.
- Ganguly, K. and Poo, M. (2013). Activity-dependent neural plasticity from bench to bedside. *Neuron* **80**, 729–741.
- Gökçe, O., Bonhoeffer, T., and Scheuss, V. (2016). Clusters of synaptic inputs on dendrites of layer 5 pyramidal cells in mouse visual cortex. *ELife* **5**, e09222.

- Guerguiev, J., Lillicrap, T.P., and Richards, B.A. (2017). Towards deep learning with segregated dendrites. *ELife* 6, e22901.
- Harward, S.C., Hedrick, N.G., Hall, C.E., Parra-Bueno, P., Milner, T.A., Pan, E., Laviv, T., Hempstead, B.L., Yasuda, R., and McNamara, J.O. (2016). Autocrine BDNF–TrkB signalling within a single dendritic spine. *Nature* 538, 99–103.
- Hedrick, N.G., Harward, S.C., Hall, C.E., Murakoshi, H., McNamara, J.O., and Yasuda, R. (2016). Rho GTPase complementation underlies BDNF-dependent homo- and heterosynaptic plasticity. *Nature* 538, 104–108.
- Hennequin, G., Agnes, E.J., and Vogels, T.P. (2017). Inhibitory plasticity: balance, control, and codependence. *Annu. Rev. Neurosci.* 40, 557–579.
- Higley, M.J. (2014). Localized GABAergic inhibition of dendritic Ca²⁺ signalling. *Nat. Rev. Neurosci.* 15, 567–572.
- Hiratani, N. and Fukai, T. (2017). Detailed dendritic excitatory/inhibitory balance through heterosynaptic spike-timing-dependent plasticity. *J. Neurosci.* 37, 12106–12122.
- Hiratani, N. and Fukai, T. (2018). Redundancy in synaptic connections enables neurons to learn optimally. *Proc. Natl. Acad. Sci. USA* 115, E6871–E6879.
- Holtmaat, A. and Svoboda, K. (2009). Experience-dependent structural synaptic plasticity in the mammalian brain. *Nat. Rev. Neurosci.* 10, 647–658.
- Hu, H.Y., Kruijssen, D.L.H., Frias, C.P., Rózsa, B., Hoogenraad, C.C., and Wierenga, C.J. (2019). Endocannabinoid signaling mediates local dendritic coordination between excitatory and inhibitory synapses. *Cell Rep.* 27, 666–675.e5.
- Iacaruso, M.F., Gasler, I.T., and Hofer, S.B. (2017). Synaptic organization of visual space in primary visual cortex. *Nature* 547, 449–452.
- Iascone, D.M., Li, Y., Sümbül, U., Doron, M., Chen, H., Andreu, V., Goudy, F., Blockus, H., Abbott, L.F., Segev, I., et al. (2020). Whole-neuron synaptic mapping reveals spatially precise excitatory/inhibitory balance limiting dendritic and somatic spiking. *Neuron* 106, 566–578.e8.
- Jaffe, D.B. and Carnevale, N.T. (1999). Passive normalization of synaptic integration influenced by dendritic architecture. *J. Neurophysiol.* 82, 3268–3285.
- Jain, V., Murphy-Baum, B.L., deRosenroll, G., Sethuramanujam, S., Delsey, M., Delaney, K.R., and Awatramani, G.B. (2020). The functional organization of excitation and inhibition in the dendrites of mouse direction-selective ganglion cells. *ELife* 9, e52949.
- Jia, H., Rochefort, N.L., Chen, X., and Konnerth, A. (2010). Dendritic organization of sensory input to cortical neurons in vivo. *Nature* 464, 1307–1312.
- Jia, H., Varga, Z., Sakmann, B., and Konnerth, A. (2014). Linear integration of spine Ca²⁺ signals in layer 4 cortical neurons in vivo. *Proc. Natl. Acad. Sci. USA* 111, 9277–9282.
- Johnson, J., Tian, N., Caywood, M.S., Reimer, R.J., Edwards, R.H., and Copenhagen, D.R. (2003). Vesicular neurotransmitter transporter expression in developing postnatal rodent retina: GABA and glycine precede glutamate. *J. Neurosci.* 23, 518–529.
- Jordan, J., Sacramento, J., Wybo, W.A.M., Petrovici, M.A., and Senn, W. (2021). Learning Bayes-optimal dendritic opinion pooling. *arXiv: 2104.13238v1 [q-bio.NC]*.
- Ju, N., Li, Y., Liu, F., Jiang, H., Macknik, S.L., Martinez-Conde, S., and Tang, S. (2020). Spatiotemporal functional organization of excitatory synaptic inputs onto macaque V1 neurons. *Nat. Commun.* 11, 697.
- Kastellakis, G., Cai, D.J., Mednick, S.C., Silva, A.J., and Poirazi, P. (2015). Synaptic clustering within dendrites: an emerging theory of memory formation. *Prog. Neurobiol.* 126, 19–35.
- Kerlin, A., Mohar, B., Flickinger, D., MacLennan, B.J., Dean, M.B., Davis, C., Spruston, N., and Svoboda, K. (2019). Functional clustering of dendritic activity during decision-making. *ELife* 8, e46966.
- Kim, N., Bahn, S., Choi, J.H., Kim, J.S., and Rah, J.-C. (2021). Synapses from the motor cortex and a high-order thalamic nucleus are spatially clustered in proximity to each other in the distal tuft dendrites of mouse somatosensory cortex. *Cerebr. Cortex*, <https://doi.org/10.1093/cercor/bhab236>.
- Kirchner, J.H. and Gjorgjieva, J. (2021). Emergence of local and global synaptic organization on cortical dendrites. *Nat. Commun.* 12, 4005.
- Kleindienst, T., Winnubst, J., Roth-Alpermann, C., Bonhoeffer, T., and Lohmann, C. (2011). Activity-dependent clustering of functional synaptic inputs on developing hippocampal dendrites. *Neuron* 72, 1012–1024.
- Kutsarova, E., Schohl, A., Munz, M., Wang, A., Zhang, Y.Y., Bilash, O.M., and Ruthazer, E.S. (2021). BDNF signaling in Hebbian and Stentian structural plasticity in the developing visual system, *BioRxiv*. <https://doi.org/10.1101/2021.10.07.463583>
- Laboy-Juárez, K.J., Langberg, T., Ahn, S., and Feldman, D.E. (2019). Elementary motion sequence detectors in whisker somatosensory cortex. *Nat. Neurosci.* 22, 1438–1449.
- Larkum, M.E., Nevian, T., Sandler, M., Polsky, A., and Schiller, J. (2009). Synaptic integration in tuft dendrites of layer 5 pyramidal neurons: a new unifying principle. *Science* 325, 756–760.
- Lee, K.F.H., Soares, C., Thivierge, J.-P., and Béique, J.-C. (2016). Correlated synaptic inputs drive dendritic calcium amplification and cooperative plasticity during clustered synapse development. *Neuron* 89, 784–799.
- Lee, K.-S., Vandemark, K., Mezey, D., Shultz, N., and Fitzpatrick, D. (2019). Functional synaptic architecture of callosal inputs in mouse primary visual cortex. *Neuron* 101, 421–428.e5.
- Leighton, A.H. and Lohmann, C. (2016). The wiring of developing sensory circuits—from patterned spontaneous activity to synaptic plasticity mechanisms. *Front. Neural Circ.* 10, 71.
- Letzkus, J.J., Kampa, B.M., and Stuart, G.J. (2006). Learning rules for spike timing-dependent plasticity depend on dendritic synapse location. *J. Neurosci.* 26, 10420–10429.
- Liu, G. (2004). Local structural balance and functional interaction of excitatory and inhibitory synapses in hippocampal dendrites. *Nat. Neurosci.* 7, 373–379.
- Lohmann, C. and Kessels, H.W. (2014). The developmental stages of synaptic plasticity. *J. Physiol.* 592, 13–31.
- Maletic-Savatic, M., Malinow, R., and Svoboda, K. (1999). Rapid dendritic morphogenesis in ca1 hippocampal dendrites induced by synaptic activity. *Science* 283, 1923–1927.

- McBride, T.J., Rodriguez-Contreras, A., Trinh, A., Bailey, R., and DeBello, W.M. (2008). Learning drives differential clustering of axodendritic contacts in the barn owl auditory system. *J. Neurosci.* *28*, 6960–6973.
- Mel, B.W. (1992). The clusteron: Toward a simple abstraction for a complex neuron. *NeurIPS*, 35–42.
- Mel, B.W. (1993). Synaptic integration in an excitable dendritic tree. *J. Neurophysiol.* *70*, 1086–1101.
- Mikulasch, F.A., Rudelt, L., and Priesemann, V. (2021). Local dendritic balance enables learning of efficient representations in networks of spiking neurons. *Proc. Natl. Acad. Sci. USA* *118*, e2021925118.
- Niculescu, D., Michaelsen-Preusse, K., Güner, Ü., van Dorland, R., Wierenga, C.J., and Lohmann, C. (2018). A BDNF-mediated push-pull plasticity mechanism for synaptic clustering. *Cell Rep.* *24*, 2063–2074.
- Niell, C.M., Meyer, M.P., and Smith, S.J. (2004). In vivo imaging of synapse formation on a growing dendritic arbor. *Nat. Neurosci.* *7*, 254–260.
- Oh, W.C., Parajuli, L.K., and Zito, K. (2015). Heterosynaptic structural plasticity on local dendritic segments of hippocampal ca1 neurons. *Cell Rep.* *10*, 162–169.
- Okun, M. and Lampl, I. (2008). Instantaneous correlation of excitation and inhibition during ongoing and sensory-evoked activities. *Nat. Neurosci.* *11*, 535–537.
- Park, J., Papoutsis, A., Ash, R.T., Marin, M.A., Poirazi, P., and Smirnakis, S.M. (2019). Contribution of apical and basal dendrites to orientation encoding in mouse V1 L2/3 pyramidal neurons. *Nat. Commun.* *10*, 5372.
- Podgorski, K., Toth, T.D., Coleman, P., Opushnyev, S., Brusco, J., Hogg, P., Edgcumbe, P., and Haas, K. (2021). Comprehensive imaging of synaptic activity reveals dendritic growth rules that cluster inputs. *BioRxiv* <https://doi.org/10.1101/2021.02.11.430646>.
- Poirazi, P., Brannon, T., and Mel, B.W. (2003). Pyramidal neuron as two-layer neural network. *Neuron* *37*, 989–999.
- Rashid, S.K., Pedrosa, V., Dufour, M.A., Moore, J.J., Chavlis, S., Delatorre, R.G., Poirazi, P., Clopath, C., and Basu, J. (2020). The dendritic spatial code: branch-specific place tuning and its experience-dependent decoupling. *BioRxiv*.
- Richards, B.A. and Lillicrap, T.P. (2019). Dendritic solutions to the credit assignment problem. *Curr. Opin. Neurobiol.* *54*, 28–36.
- Richards, S.E.V., Moore, A.R., Nam, A.Y., Saxena, S., Paradis, S., and Hooser, S.D.V. (2020). Experience-dependent development of dendritic arbors in mouse visual cortex. *J. Neurosci.* *40*, 6536–6556.
- Richter, L.M. and Gjorgjieva, J. (2017). Understanding neural circuit development through theory and models. *Curr. Opin. Neurobiol.* *46*, 39–47.
- Scholl, B., Wilson, D.E., and Fitzpatrick, D. (2017). Local order within global disorder: synaptic architecture of visual space. *Neuron* *96*, 1127–1138.e4.
- Schoonover, C.E., Tapia, J.-C., Schilling, V.C., Wimmer, V., Blazeski, R., Zhang, W., Mason, C.A., and Bruno, R.M. (2014). Comparative strength and dendritic organization of thalamocortical and corticocortical synapses onto excitatory layer 4 neurons. *J. Neurosci.* *34*, 6746–6758.
- Sezener, E., Grabska-Barwińska, A., Kostadinov, D., Beau, M., Krishnagopal, S., Budden, D., Hutter, M., Veness, J., Botvinick, M., Clopath, C., et al. (2021). A rapid and efficient learning rule for biological neural circuits. *BioRxiv*. <https://doi.org/10.1101/2021.03.10.434756>.
- Soto, F., Bleckert, A., Lewis, R., Kang, Y., Kerschensteiner, D., Craig, A.M., and Wong, R.O. (2011). Coordinated increase in inhibitory and excitatory synapses onto retinal ganglion cells during development. *Neural Dev.* *6*, 31.
- Spruston, N., Stuart, G., and Häusser, M. (2016). Principles of dendritic integration. *Dendrites* *351*, 1.
- Stuart, G., Spruston, N., and Häusser, M. (2016). *Dendrites* Oxford University Press: United Kingdom.
- Takahashi, N., Kitamura, K., Matsuo, N., Mayford, M., Kano, M., Matsuki, N., and Ikegaya, Y. (2012). Locally synchronized synaptic inputs. *Science* *335*, 353–356.
- Takahashi, N., Oertner, T.G., Hegemann, P., and Larkum, M.E. (2016). Active cortical dendrites modulate perception. *Science* *354*, 1587–1590.
- Tazerart, S., Mitchell, D.E., Miranda-Rottmann, S., and Araya, R. (2020). A spike-timing-dependent plasticity rule for dendritic spines. *Nat. Commun.* *11*, 4276.
- Tremblay, R., Lee, S., and Rudy, B. (2016). GABAergic interneurons in the neocortex: from cellular properties to circuits. *Neuron* *91*, 260–292.
- Tzilivaki, A., Kastellakis, G., and Poirazi, P. (2019). Challenging the point neuron dogma: FS basket cells as 2-stage nonlinear integrators. *Nat. Commun.* *10*, 1–14.
- Ujfalussy, B.B. and Makara, J.K. (2020). Impact of functional synapse clusters on neuronal response selectivity. *Nat. Commun.* *11*, 1413.
- Vercruyssen, F., Naud, R., and Sprekeler, H. (2021). Self-organization of a doubly asynchronous irregular network state for spikes and bursts. *BioRxiv*, <https://doi.org/10.1371/journal.pcbi.1009478>.
- Vetter, P., Roth, A., and Häusser, M. (2001). Propagation of action potentials in dendrites depends on dendritic morphology. *J. Neurophysiol.* *85*, 926–937.
- Villa, K.L., Berry, K.P., Subramanian, J., Cha, J.W., Oh, W.C., Kwon, H.-B., Kubota, Y., So, P.T.C., and Nedivi, E. (2016). Inhibitory synapses are repeatedly assembled and removed at persistent sites in vivo. *Neuron* *89*, 756–769.
- Voigts, J. and Harnett, M.T. (2020). Somatic and dendritic encoding of spatial variables in retrosplenial cortex differs during 2D navigation. *Neuron* *105*, 237–245.e4.
- Wang, L. and Maffei, A. (2014). Inhibitory plasticity dictates the sign of plasticity at excitatory synapses. *J. Neurosci.* *34*, 1083–1093.
- Weber, J.P., Andrásfalvy, B.K., Polito, M., Magó, Á., Ujfalussy, B.B., and Makara, J.K. (2016). Location-dependent synaptic plasticity rules by dendritic spine cooperativity. *Nat. Commun.* *7*, 11380.
- White, L.E. and Fitzpatrick, D. (2007). Vision and cortical map development. *Neuron* *56*, 327–338.
- Wilson, D.E., Whitney, D.E., Scholl, B., and Fitzpatrick, D. (2016). Orientation selectivity and the functional clustering of synaptic inputs in primary visual cortex. *Nat. Neurosci.* *19*, 1003–1009.
- Winnubst, J., Cheyne, J.E., Niculescu, D., and Lohmann, C. (2015). Spontaneous activity drives local synaptic plasticity in vivo. *Neuron* *87*, 399–410.

- Witvliet, D., Mulcahy, B., Mitchell, J.K., Meirovitch, Y., Berger, D.R., Wu, Y., Liu, Y., Koh, W.X., Parvathala, R., Holmyard, D., et al. (2021). Connectomes across development reveal principles of brain maturation. *Nature* 596, 257–261.
- Yaeger, C.E., Ringach, D.L., and Trachtenberg, J.T. (2019). Neuromodulatory control of localized dendritic spiking in critical period cortex. *Nature* 567, 100–104.
- Yang, G.R., Murray, J.D., and Wang, X.-J. (2016). A dendritic disinhibitory circuit mechanism for pathway-specific gating. *Nat. Commun.* 7, 12815.
- Yang, J., Siao, C.-J., Nagappan, G., Marinic, T., Jing, D., McGrath, K., Chen, Z.-Y., Mark, W., Tessarollo, L., Lee, F.S., et al. (2009). Neuronal release of proBDNF. *Nat. Neurosci.* 12, 113–115.

University in Freiburg. He joined the IMPRS program for a Ph.D. in Computational Neuroscience in Frankfurt, where he is now working toward his Ph.D. in Computational Neuroscience in the research group of Dr. Julijana Gjorgjieva. He is researching interactions between activity, plasticity, and circuit structure during the early development of the brain.



Julijana Gjorgjieva

Computation in Neural Circuits Group, Max Planck Institute for Brain Research, Max-von-Laue-Str. 4, 60438 Frankfurt, Germany
 Technical University of Munich, School of Life Sciences, 85354 Freising, Germany
gjorgjieva@brain.mpg.de
<https://orcid.org/0000-0001-7118-4079>

Bionotes



Jan H. Kirchner

Computation in Neural Circuits Group, Max Planck Institute for Brain Research, Max-von-Laue-Str. 4, 60438 Frankfurt, Germany
 Technical University of Munich, School of Life Sciences, 85354 Freising, Germany
jan.kirchner@brain.mpg.de
<https://orcid.org/0000-0002-9126-0558>

Jan H. Kirchner did a B.Sc. in Cognitive Science at the University of Osnabrück and an M.Sc. in Neuroscience at the Albert-Ludwigs

University in Freiburg. He joined the IMPRS program for a Ph.D. in Computational Neuroscience in Frankfurt, where he is now working toward his Ph.D. in Computational Neuroscience in the research group of Dr. Julijana Gjorgjieva. He is researching interactions between activity, plasticity, and circuit structure during the early development of the brain.

Julijana Gjorgjieva obtained her Ph.D. in Computational Neuroscience at Cambridge in 2011 and did postdoctoral training at Harvard and Brandeis University. In 2016, she established her independent research group at the Max Planck Institute for Brain Research in Frankfurt and will join the Technical University of Munich as a W3 professor in 2022. She is the 2021 recipient of the Eric Kandel Young Neuroscientists Prize, has co-chaired the Bernstein Conference in 2020 and 2021, and is a FENS-Kavli Network of Excellent Scholar. Her work investigates how organization and computation emerge in neural circuits during development, and how they are maintained throughout learning in adulthood.

Adaptation of spontaneous activity in the developing visual cortex

In Wosniack *et al.* (2021), we investigate how two distinct sources of spontaneous activity combine in the developing visual cortex to enable the maturation of connectivity between the eye and the cortex. We find that:

1. Introducing biologically-realistic spontaneous activity disrupts connectivity in a classical model of receptive field maturation.
2. we can prevent Disruption of connectivity by dynamically adapting the strength of cortically-generated activity to the strength of preceding activity.
3. Reanalyzing experimental data reveals hallmarks of adaptive spontaneous activity.
4. Adaptive spontaneous activity can promote the sparsification of cortical activity throughout development.

The work was completed in collaboration with Dr. Marina Wosniack, Prof. Dr. Julijana Gjorgjieva, Prof. Dr. Christian Lohmann, Dr. Nawal Zabouri, and Dr. Ling-Ya Chao. I contributed to three figures (Fig. 1A-C, Fig. 5A-C, and Figure 7C) and contributed to the first draft of the entire manuscript. I was also involved throughout the research process by contributing mathematical derivations, data analysis, discussions, and feedback. The full article was published on March 16th, 2021 in eLife and is reproduced on the following pages under the Creative Commons Attribution 4.0 International License.

Adaptation of spontaneous activity in the developing visual cortex

Marina E Wosniack^{1,2}, Jan H Kirchner^{1,2}, Ling-Ya Chao¹, Nawal Zabouri³, Christian Lohmann^{3,4}, Julijana Gjorgjieva^{1,2*}

¹Computation in Neural Circuits Group, Max Planck Institute for Brain Research, Frankfurt, Germany; ²School of Life Sciences Weihenstephan, Technical University of Munich, Freising, Germany; ³Netherlands Institute for Neuroscience, Amsterdam, Netherlands; ⁴Center for Neurogenomics and Cognitive Research, Vrije Universiteit, Amsterdam, Netherlands

Abstract Spontaneous activity drives the establishment of appropriate connectivity in different circuits during brain development. In the mouse primary visual cortex, two distinct patterns of spontaneous activity occur before vision onset: local low-synchronicity events originating in the retina and global high-synchronicity events originating in the cortex. We sought to determine the contribution of these activity patterns to jointly organize network connectivity through different activity-dependent plasticity rules. We postulated that local events shape cortical input selectivity and topography, while global events homeostatically regulate connection strength. However, to generate robust selectivity, we found that global events should adapt their amplitude to the history of preceding cortical activation. We confirmed this prediction by analyzing *in vivo* spontaneous cortical activity. The predicted adaptation leads to the sparsification of spontaneous activity on a slower timescale during development, demonstrating the remarkable capacity of the developing sensory cortex to acquire sensitivity to visual inputs after eye-opening.

*For correspondence:

gjorgjieva@brain.mpg.de

Competing interests: The authors declare that no competing interests exist.

Funding: See page 21

Received: 30 July 2020

Accepted: 03 February 2021

Published: 16 March 2021

Reviewing editor: Andrew J King, University of Oxford, United Kingdom

© Copyright Wosniack et al. This article is distributed under the terms of the [Creative Commons Attribution License](https://creativecommons.org/licenses/by/4.0/), which permits unrestricted use and redistribution provided that the original author and source are credited.

Introduction

The impressive ability of the newborn brain to respond to its environment and generate coordinated output without any prior experience suggests that brain networks undergo substantial organization, tuning and coordination even as animals are still in the womb, driven by powerful developmental mechanisms. These broadly belong to two categories: activity-independent mechanisms, involving molecular guidance cues and chemoaffinity gradients which establish the initial coarse connectivity patterns at early developmental stages (*Feldheim and O'Leary, 2010; Goodhill, 2016*), and activity-dependent plasticity mechanisms which continue with refinement of this initially imprecise connectivity into functional circuits that can execute diverse behaviors in adulthood (*Ackman and Crair, 2014; Richter and Gjorgjieva, 2017; Thompson et al., 2017*). Non-random patterns of spontaneous activity drive these refinements and act as training inputs to the immature circuits before the onset of sensory experience. Many neural circuits in the developing brain generate spontaneous activity, including the retina, hippocampus, cortex, and spinal cord (reviewed in *Blankenship and Feller, 2010; Wang and Bergles, 2015*). This activity regulates a plethora of developmental processes such as neuronal migration, ion channel maturation, and the establishment of precise connectivity (*Huberman et al., 2008; Moody and Bosma, 2005; Kirkby et al., 2013; Godfrey and Swindale, 2014*), and perturbing this activity impairs different aspects of functional organization and axonal refinement (*Cang et al., 2005a; Xu et al., 2011; Burbridge et al., 2014*). These studies firmly demonstrate that spontaneous activity is necessary and instructive for the emergence of specific and distinct patterns of neuronal connectivity in the developing nervous system.

Recent *in vivo* recordings in the developing sensory cortex have found that the spatiotemporal properties of spontaneous activity, including frequency, synchronicity, amplitude and spatial spread, depend on the studied region and developmental age (Golshani *et al.*, 2009; Rochefort *et al.*, 2009; Gribizis *et al.*, 2019). These studies have shown that the generation and propagation of spontaneous activity in the intact cortex depend on input from different brain areas. For instance, activity from the sensory periphery substantially contributes to the observed activity patterns in the developing cortex, but there are other independent sources of activity within the cortex itself (Ackman *et al.*, 2012; Siegel *et al.*, 2012; Hanganu *et al.*, 2006; Gribizis *et al.*, 2019). Two-photon imaging of spontaneous activity in the *in vivo* mouse primary visual cortex before eye-opening (post-natal days, P8-10) has demonstrated that there are two independently occurring patterns of spontaneous activity with different sources and spatiotemporal characteristics. Peripheral events driven by retinal waves (Feller *et al.*, 1996; Blankenship and Feller, 2010) spread in the cortex as low-synchronicity local events (L-events), engaging a relatively small number of the recorded neurons. In contrast, events intrinsic to the cortex that are unaffected by manipulation of retinal waves spread as highly synchronous global events (H-events), activating a large proportion of the recorded neurons (Siegel *et al.*, 2012).

We know relatively little about the information content of these local and global patterns of spontaneous cortical activity relevant for shaping local and brain-wide neural circuits. Specifically, it is unknown whether spontaneous activity from different sources affects distinct aspects of circuit organization, each providing an independent instructive signal, or if L- and H-events cooperate to synergistically guide circuit organization. Therefore, using experimentally characterized properties of spontaneous activity in the visual cortex *in vivo* at P8-10, we developed a biologically plausible, yet analytically tractable, theoretical framework to determine the implications of this activity on normal circuit development with a focus on the topographic refinement of connectivity and the emergence of stable receptive fields.

We postulated that peripheral L-events play a key role in topographically organizing receptive fields in the cortex, while H-events regulate connection strength homeostatically, operating in parallel to network refinements by L-events. We considered that H-events are ideally suited for this purpose because they maximally activate many neurons simultaneously, and hence lack topographic information that can be used for synaptic refinement. We studied two prominent activity-dependent plasticity rules to investigate the postulated homeostatic function of H-events, the Hebbian covariance rule (Miller *et al.*, 1989; Miller, 1994; Lee *et al.*, 2002; Sejnowski, 1977) and the Bienenstock-Cooper-Munro (BCM) rule (Bienenstock *et al.*, 1982). In the Hebbian covariance rule, simultaneous pre- and postsynaptic activation (e.g. during L-events) triggers the selective potentiation of synaptic connections, while postsynaptic activation without presynaptic input (e.g. during H-events) leads to the unselective depression of all connections. In the BCM rule, H-events dynamically regulate potentiation and depression. However, both rules generate receptive fields that have either refinement or topography defects. Therefore, we proposed that H-events might be self-regulating, with amplitudes that adapt to the levels of recent cortical activity. Indeed, we found evidence of this adaptation in spontaneous activity recorded in the developing visual cortex (Siegel *et al.*, 2012). Besides generating topographically refined receptive fields, this adaptation leads to the sparsification of cortical spontaneous activity over a prolonged timescale of development as in the visual and somatosensory cortex (Rochefort *et al.*, 2009; Golshani *et al.*, 2009). Therefore, our work proposes that global, cortically generated activity in the form of H-events rapidly adapts to ongoing network activity, supporting topographic organization of connectivity and maintaining synaptic strengths in an operating regime.

Results

A network model for connectivity refinements driven by spontaneous activity

How spontaneous activity instructs network refinements between the sensory periphery and the visual cortex depends on two aspects: the properties of spontaneous activity and the activity-dependent learning rules that translate these properties into specific changes in connectivity. We first characterized spontaneous activity in the mouse primary visual cortex before eye-opening, and

investigated two prominent learning rules to organize connectivity in a network model of the thalamus and visual cortex.

Spontaneous activity recorded *in vivo* using two-photon Ca^{2+} imaging exhibits two independently occurring patterns: network events originating in the retina and propagating through the thalamus, and network events generated in the cortex (Siegel *et al.*, 2012; Figure 1A). These two types of events were first identified by a cluster analysis based on event amplitude and jitter (a measure of synchrony; Siegel *et al.*, 2012). The analysis identified a participation rate criterion to separate network events into local low-synchronicity (L-) events generated in the retina, where 20–80% of the neurons in the field of view are simultaneously active, and global high-synchronicity (H-) events intrinsic to the cortex, where nearly all (80–100%) cortical neurons are simultaneously active. This same 80% participation rate criterion was recently validated both at the single-cell and population levels (Leighton *et al.*, 2020). We first confirmed differences in specific features of the recorded spontaneous events (Siegel *et al.*, 2012), and also characterized novel aspects (Figure 1B). In particular, L-events have a narrow distribution of amplitudes and inter-event intervals (IEI, the inverse of firing frequency) that follow an exponential-like distribution. H-events have a broader distribution of amplitudes with higher values and IEIs that follow a long-tailed distribution with higher values relative to L-events. We found that L- and H-events have similar durations.

Next, we built a model that incorporates these two different patterns of spontaneous activity to investigate the potentially different roles that L- and H-events might play in driving connectivity refinements between the thalamus and the visual cortex (Figure 1C). We used a one-dimensional feedforward network model – a microcircuit motivated by the small region of cortex imaged experimentally – composed of two layers, an input (presynaptic) layer corresponding to the sensory periphery (the thalamus) and a target (postsynaptic) layer corresponding to the primary visual cortex (Figure 2A). Cortical activity v in the model is generated by two sources (Figure 2B; Table 1). First, L-events, u , activate a fraction between 20% and 80% of neighboring thalamic cells (also referred to as the L-event size) and drive the cortex through the weight matrix, W . Second, H-events, v^{spont} , activate the majority of the cortical cells (a fraction between 80% and 100%, also referred to as the

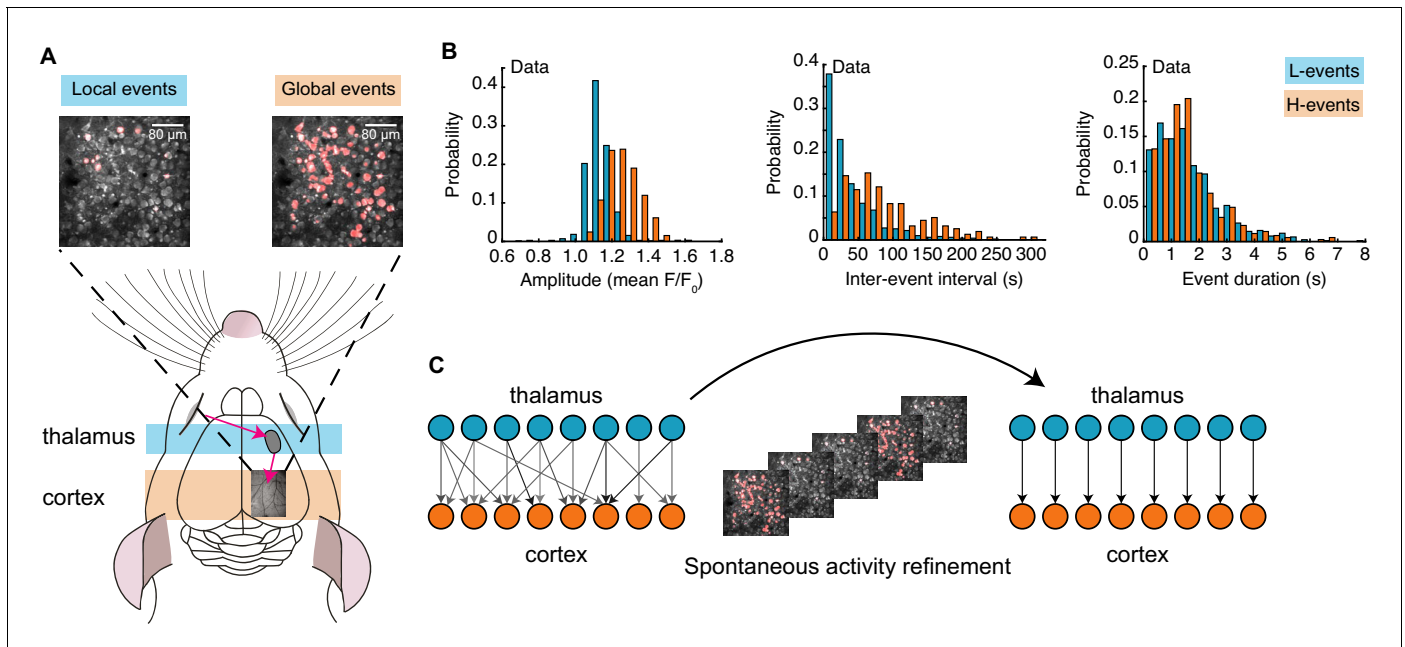


Figure 1. Spontaneous activity patterns in early postnatal development. (A) Two distinct patterns of spontaneous activity recorded *in vivo* in the visual cortex of young mice before eye-opening (P8-10). Blue shading denotes local low-synchronicity (L-) events generated by the retina; orange shading denotes global high-synchronicity (H-) events generated by the cortex. Activated neurons during each event are shown in red. (B) Distributions of different event properties (amplitude, inter-event interval, and event duration). Amplitude was measured as changes in fluorescence, relative to baseline, F/F_0 . (C) Network schematic: thalamocortical connections are refined by spontaneous activity. The initially broad receptive fields with weak synapses evolve into a stable configuration with strong synapses organized topographically.

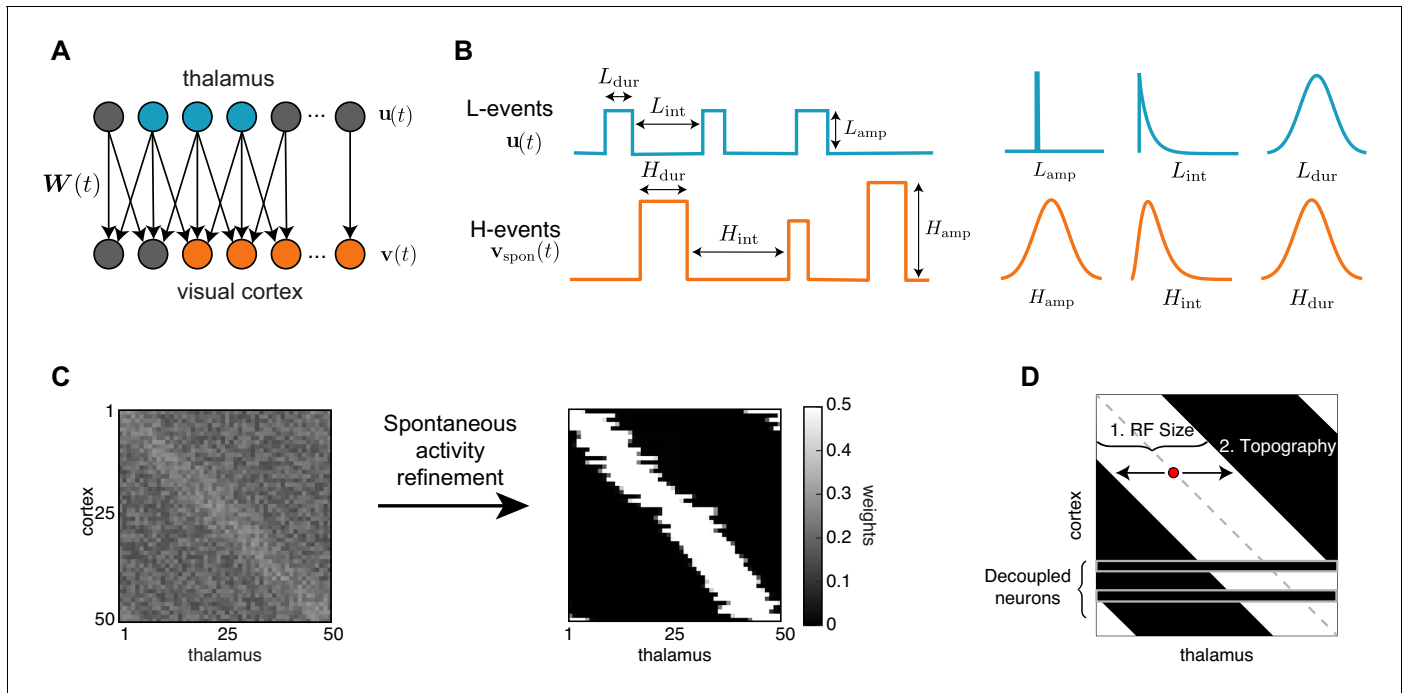


Figure 2. A network model of thalamocortical connectivity refinements. (A) A feedforward network with an input layer of thalamic neurons $u(t)$ connected to an output layer of cortical neurons $v(t)$ by synaptic weights $W(t)$. (B) Properties of L- and H-events in the model (amplitude L_{amp} , H_{amp} , inter-event interval L_{int} , H_{int} and duration L_{dur} , H_{dur}) follow probability distributions extracted from data (Siegel et al., 2012) (see Table 1). (C) Initially weak all-to-all connectivity with a small topographic bias along the diagonal (left) gets refined by the spontaneous activity events (right). (D) Evaluating network refinement through receptive field statistics (see Materials and methods). We quantify two properties: (1) the receptive field size and (2) the topography, which quantifies on average how far away the receptive field center of each cortical cell (red dot) is from the diagonal (dashed gray line).

H-event size). We used a rate-based unit with a membrane time constant τ_m and linear activation function consistent with the coarse temporal structure of spontaneous activity during development, carrying information on the order of hundreds of milliseconds (Gjorgjieva et al., 2009; Butts and Kanold, 2010; Richter and Gjorgjieva, 2017):

$$\tau_m \frac{dv(t)}{dt} = -v(t) + W(t)u(t) + v^{spon}(t). \tag{1}$$

To investigate the refinement of network connectivity during development, we studied the evolution of synaptic weights using plasticity rules operating over long timescales identified experimentally (Butts et al., 2007; Winnubst et al., 2015). First, we examined a classical Hebbian plasticity rule where coincident presynaptic thalamic activity and postsynaptic cortical activity in the form of L-events leads to synaptic potentiation. We postulated that H-events act homeostatically and maintain synaptic weights in an operating regime by depressing the majority of synaptic weights in the absence of peripheral drive. Because they activate most cortical neurons simultaneously, H-events lack the potential to drive topographical refinements. Their postulated homeostatic action resembles synaptic depression through downscaling, as observed in response to highly correlated network activity, for instance, upon blocking inhibition (Turrigiano and Nelson, 2004), or during slow-wave sleep (Tononi and Cirelli, 2006). Therefore, to the Hebbian rule we added a non-Hebbian term that depends only on the postsynaptic activity, with a proportionality constant that controls the relative amount of synaptic depression. This differs from other Hebbian covariance plasticity rules for the generation of weight selectivity, which include non-Hebbian terms that depend on both pre- and postsynaptic activity (Lee et al., 2002; Mackay and Miller, 1990) and is mathematically related to models of heterosynaptic plasticity (Chistiakova et al., 2014; Lynch et al., 1977; Zenke et al., 2015). Hence, the change in synaptic weight between cortical neuron j and thalamic neuron i is given by:

Table 1. List of parameters used in the model unless stated otherwise.

Name	Value/Distribution	Description
Network		
N_u	50	Number of thalamic neurons
N_v	50	Number of cortical neurons
T	50,000	Simulation length [s]
Weights		
w_{ini}	U(0.15,0.25)	Range of initial weights (U: uniform dist.)
s	0.05	Amplitude of Gaussian bias
σ_s	4	Spread of Gaussian bias
w_{max}	0.5	Weight saturation limit
L-events		
L_{amp}	1.0	Amplitude (equivalently, binary neuron)
L_{pct}	U(20%,80%)	Percentage of thalamic cells activated
L_{dur}	$\mathcal{N}(0.15, 0.015)$	Mean duration [s] (\mathcal{N} : Gaussian dist.)
L_{int}	Exp(1.5)	Mean inter-event interval [s] (Exp: exponential dist.)
H-events		
H_{amp}	$\mathcal{N}(6, 2)$	Amplitude
H_{pct}	U(80%,100%)	Percentage of cortical cells activated
H_{dur}	$\mathcal{N}(0.15, 0.015)$	Mean duration [s]
H_{int}	Gamma(3.5, 1.0)	Mean inter-event interval [s] (Gamma: Gamma dist.)
Time constants		
τ_m	0.01	Membrane time constant [s]
τ_w	500	Weight-change time constant for Hebbian covariance rule [s]
τ_w	1000	Weight-change time constant for BCM rule [s]
τ_θ	20	Output threshold time constant for BCM rule [s]
τ_η	1	Adaptation time constant [s]

$$\tau_w \frac{dw_{ji}(t)}{dt} = v_j(t)(u_i(t) - \theta_u), \quad (2)$$

where τ_w is the learning time constant and θ_u the proportionality constant in the non-Hebbian term, which we refer to as the ‘input threshold’. The activity time constant τ_m is much faster than the learning time constant, $\tau_m \ll \tau_w$, which allows us to separate timescales and to study how network activity on average affects learning (see Appendix). Interestingly, in this Hebbian covariance rule, the input threshold together with H-events effectively implement a subtractive constraint (see Appendix: ‘Normalization constraints’). Subtractive normalization preserves the sum of all weights by subtracting from each weight a constant amount independent of each weight strength and is known to generate selectivity and refined receptive fields (Miller and MacKay, 1994). This is in contrast to the alternative multiplicative normalization, which generates graded and unrefined receptive fields where most correlated inputs are represented (Miller and MacKay, 1994) and hence was not considered here.

Additionally, we investigated the BCM learning rule, which can induce weight stability and competition without imposing constraints in the weights, and hence generate selectivity in postsynaptic neurons which experience patterned inputs (Bienenstock et al., 1982). For instance, the BCM framework can explain the emergence of ocular dominance (neurons in primary visual cortex being selective for input from one of the two eyes) and orientation selectivity in the visual system (Cooper et al., 2004). An important property of the BCM rule is its ability to homeostatically regulate the balance between potentiation and depression of all incoming inputs into a given neuron

depending on how far away the activity of that neuron is from some target level. The change in synaptic weight between cortical neuron j and thalamic neuron i is given by:

$$\tau_w \frac{dw_{ji}(t)}{dt} = v_j(t)u_i(t)(v_j(t) - \theta_v^j(t)), \quad (3)$$

where

$$\tau_\theta \frac{d\theta_v^j(t)}{dt} = -\theta_v^j(t) + \frac{v_j^2(t)}{v_0} \quad (4)$$

describes the threshold $\theta_v^j(t)$ between depression and potentiation which slides as a function of postsynaptic activity, v_0 is the target rate of the cortical neurons and τ_θ the sliding threshold time constant. According to this rule, synaptic weight change is Hebbian in that it requires coincident pre- and postsynaptic activity, as is only the case during L-events. H-events induce no direct plasticity in the network because of the absence of presynaptic activation, but they still trigger synaptic depression indirectly by increasing the threshold between potentiation and depression.

Based on experimental measurements of the extent of thalamocortical connectivity at different developmental ages (López-Bendito, 2018), we assumed that initial network connectivity was weak and all-to-all, such that each cortical neuron was innervated by all thalamic neurons. To account for the activity-independent stage of development guided by molecular guidance cues and chemoaffinity gradients, a small bias was introduced to the initial weight matrix to generate a coarse topography in the network, where neighboring neurons in the thalamus project to neighboring neurons in the cortex and preserve spatial relationships (Figure 2C, left). Following connectivity refinements through spontaneous activity and plasticity, a desired outcome is that the network achieves a stable topographic configuration (Figure 2C, right) where each cortical neuron receives input only from a neighborhood of thalamic neurons.

To evaluate the success of this process, we quantified two properties. First, the receptive field size defined as the average number of thalamic neurons that strongly innervate a cortical cell (Figure 2D). We normalized the receptive field size to the total number of thalamic cells, so that it ranges from 0 (no receptive field, all cortical cells decouple from the thalamus) to 1 (each cortical cell receives input from all the thalamic cells, all weights potentiate leading to no selectivity). We also quantified the topography of the final receptive field (Figure 2D and Materials and methods), which evaluates how well the initial bias is preserved in the final network connectivity. The topography ranges from 0 (all cortical neurons connect to the same set of thalamic inputs) to 1 (perfect topography relative to the initial bias). We note that the lack of initial connectivity bias did not disrupt connectivity refinements and receptive field formation but could not on its own establish topography (Figure 3—figure supplement 1A).

Spontaneous cortical H-events disrupt topographic connectivity refinement in the Hebbian covariance and BCM plasticity rules

Both the Hebbian and the BCM learning rules are known to generate selectivity with patterned input stimuli (Mackay and Miller, 1990; Bienenstock et al., 1982), and we confirmed that L-events on their own can refine receptive fields in both scenarios (Figure 3—figure supplement 2). We found that including H-events in the Hebbian covariance rule requires that the parameters of the learning rule and the properties of H-events (the input threshold θ_u and the inter-event interval H_{int}) follow a tight relationship to generate selective and refined receptive fields (Figure 3A,C, left). For a narrow range of H_{int} , weight selectivity emerges, but with some degree of decoupling between pre- and postsynaptic neurons (Figure 3A, middle). Outside of this narrow functional range, individual cortical neurons are either non-selective (Figure 3A, left) or decoupled from the thalamus (Figure 3A, right). These results are robust to changes in the participation rates of L- and H-events. For instance, when H-events involve 70–100% of cortical neurons, the percent of outcomes with selective receptive fields increases slightly to 19.8% (compared to 14.0% when H-events involve 80–100% of cortical neurons), while the percent of outcomes with decoupled cortical neurons increases to 60.4% (compared to 43.6% when H-events involve 80–100% of cortical neurons), reinforcing the idea that H-events are detrimental to receptive field refinements. In comparison, including H-events in the BCM learning rule does not decouple pre- and postsynaptic neurons (Figure 3B) and selectivity can

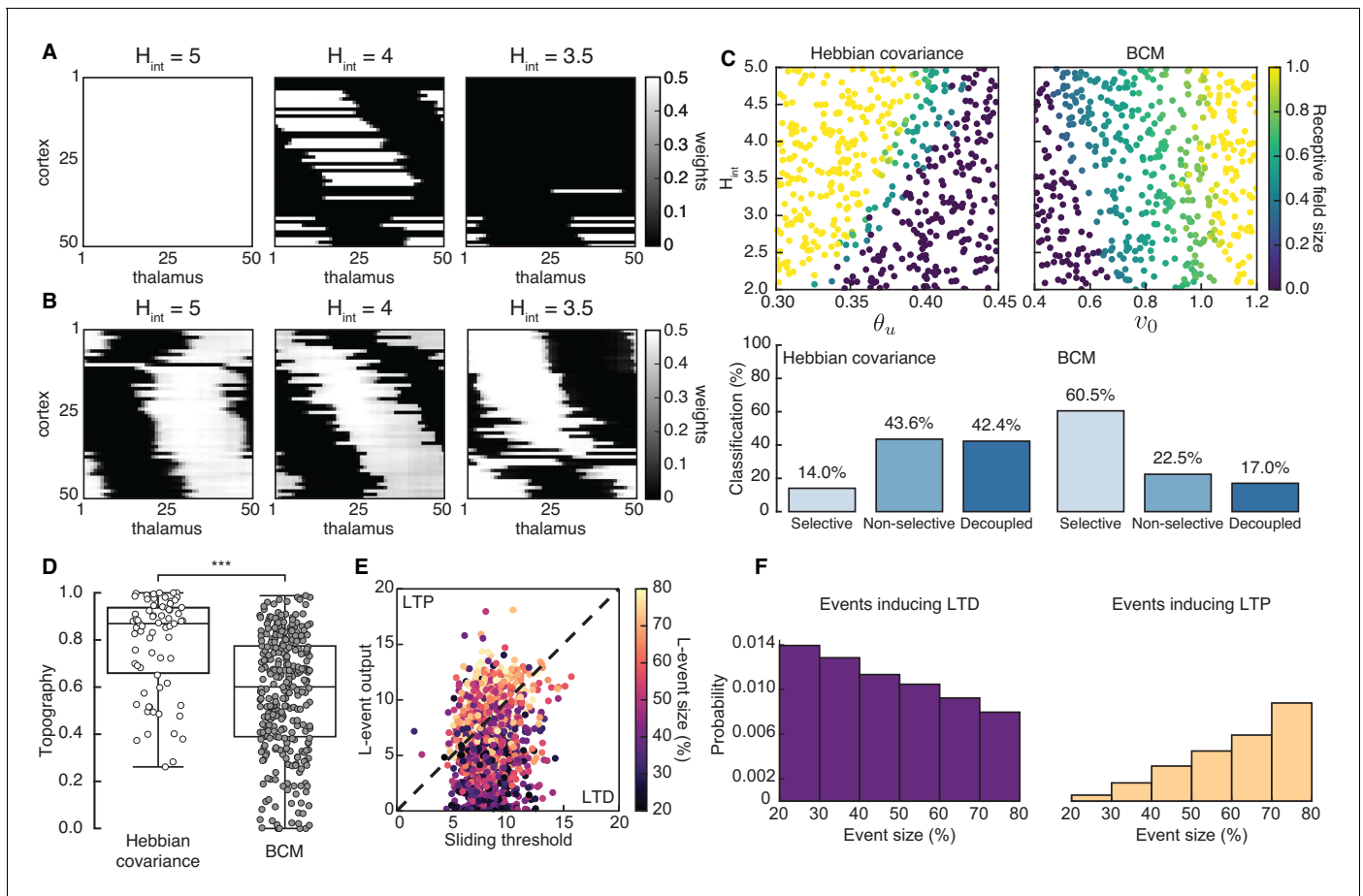


Figure 3. Spontaneous cortical events disrupt receptive field refinement. (A) Receptive fields generated by the Hebbian covariance rule with input threshold $\theta_u = 0.4$ and decreasing H_{int} . (B) Receptive fields generated by the BCM rule with target rate $v_0 = 0.7$ and decreasing H_{int} . (C) Top: Receptive field sizes obtained from 500 Monte Carlo simulations for combinations of H_{int} and θ_u for the Hebbian covariance rule (left) and H_{int} and v_0 for the BCM rule (right). Bottom: Percentage of simulation outcomes classified as ‘selective’ when the average receptive field size is smaller than one and larger than 0, ‘non-selective’ when the average receptive field size is equal to 1, and ‘decoupled’ when the average receptive field size is 0 for the two rules. (D) Topography of receptive fields classified as selective in C. Horizontal line indicates median, the box is drawn between the 25th and 75th percentile, whiskers extend above and below the box to the most extreme data points that are within a distance to the box equal to 1.5 times the interquartile range and points indicate all data points. Distributions are significantly different (***) as measured by a two-sample Kolmogorov-Smirnov test ($n = 70,302$ selective outcomes for each rule out of 500; $p < 10^{-10}$; $D = 0.45$). (E) The response of a single cortical cell to L-events of different sizes (color) as a function of the sliding threshold for the BCM rule with $H_{int} = 3.5$ and $v_0 = 0.7$. The cell’s incoming synaptic weights from presynaptic thalamic neurons undergo LTP or LTD depending on L-event size. (F) Probability of L-event size contributing to LTD (left) and LTP (right) for the BCM rule with the same parameters as in E.

The online version of this article includes the following figure supplement(s) for figure 3:

Figure supplement 1. Effect of initial bias on receptive field refinements and topography.

Figure supplement 2. Peripheral L-events generate robust receptive field refinement in the absence of H-events.

be generated over a wider range of H-inter-event-intervals H_{int} and target rates v_0 for the BCM rule (Figure 3C, right).

Despite this apparent advantage of the BCM rule, it generates receptive fields with much worse topography than the Hebbian covariance rule (Figure 3D). The underlying reason for this worse topography of the BCM rule is the sign of synaptic change evoked by L-events of different sizes corresponding to different participation rates. In particular, small L-events with low participation rates generate postsynaptic cortical activity smaller than the sliding threshold and promote long-term synaptic depression (LTD), while large L-events with high participation rates generate cortical activity larger than the sliding threshold and promote long-term synaptic potentiation (LTP) (Figure 3E,F).

Therefore, the amount of information for connectivity refinements present in the small L-events is limited in the BCM learning rule resulting in poor topographic organization of receptive fields.

Taken together, our results confirm that H-events can operate in parallel to network refinements by L-events and homeostatically regulate connection strength as postulated. However, the formation of receptive fields by the Hebbian covariance rule is very sensitive to small changes in event properties (e.g. inter-event intervals), which are common throughout development (Rocheffort *et al.*, 2009). In this case, H-events are disruptive and lead to the elimination of all thalamocortical synapses, effectively decoupling the cortex from the sensory periphery. In the BCM rule, including H-events prevents the decoupling of cortical cells from the periphery because the amount of LTD is dynamically regulated by the sliding threshold on cortical activity. However, L-events lose the ability to instruct topography because they generate LTP primarily when they are large. Therefore, neither learning rule seems suitable to organize network connectivity between the thalamus and cortex during development.

Adaptive H-events achieve robust selectivity

After comparing the distinct outcomes of the Hebbian and BCM learning rules in the presence of L- and H-events, we proposed that a mechanism that regulates the amount of LTD during H-events based on cortical activity, similar to the sliding threshold of the BCM rule, could be a biologically plausible solution to mitigate the decoupling of cortical cells in the Hebbian covariance rule. This mechanism combined with the Hebbian learning rule could lead to refined receptive fields that also have good topographic organization. Hence, we postulated that H-events adapt by assuming that during H-events cortical cells scale their amplitude to the average amplitude of the preceding recent events. In particular, for each cortical cell j an activity trace η_j integrates the cell's firing rate v_j over a timescale τ_η slower than the membrane time constant:

$$\tau_\eta \frac{d\eta_j(t)}{dt} = -\eta_j(t) + v_j(t). \quad (5)$$

This activity trace η_j then scales the intrinsic firing rate of the cortical cells during an H-event, $H_{\text{amp}} \rightarrow \eta_j H_{\text{amp}}$, making it dependent on its recent activity. The activity trace η_j might biophysically be implemented through a calcium-dependent signaling pathway that is activated upon sufficient burst depolarization and that is able to modulate a cell's excitability in the form of plasticity of intrinsic excitability (Desai *et al.*, 1999; Daoudal and Debanne, 2003; Tien and Kerschensteiner, 2018). A fast, activity-dependent mechanism that decreases single-neuron excitability following a prolonged period of high network activity has been identified in spinal motor neurons of neonatal mice (Lombardo *et al.*, 2018). However, there might be other ways to implement this adaptation (see Discussion).

Using adaptive H-events, we investigated the refinement of receptive fields in the network with the same Hebbian covariance rule (Figure 4A). In sharp contrast to the Hebbian covariance rule with non-adaptive H-events (Figure 3A), we observed that changing the average inter-event interval of H-events in a wider and more biologically realistic range (from the data, $H_{\text{int}} \sim 3L_{\text{int}}$) yields selectivity and appropriately refined receptive fields (Figure 4A). Increasing θ_u or decreasing H_{int} yields progressively smaller receptive fields while mitigating cortical decoupling (Figure 4B). The refined receptive fields also have a very good topography because L-events in the Hebbian learning rule carry nearest-neighbor information for the topographic refinements (Figure 4C). The proportion of selective receptive fields for adaptive H-events, however, is much higher than for their non-adaptive counterparts (390 vs. 70 out of 500 simulations). These results persist when the participation rates of L- and H-events change. For instance, when H-events involve 70–100% of cortical neurons, the percent of outcomes with selective receptive fields (75.0%) and the percent of outcomes with decoupled cortical neurons (0%) remain similar.

Next, we investigated how the proposed adaptive mechanism scales H-event amplitude by modulating the relative strength of H-events. For the Hebbian covariance rule, we calculated the analytical solution for weight development with L- and H-events by reducing the dimension of the system to two: one being the average of the weights that potentiate and form the receptive field, w_{RF} , and the other being the average of the remaining weights, which we called 'complementary' to the receptive field, w_{C} (Figure 4D; see Appendix, Materials and methods). We calculated the phase

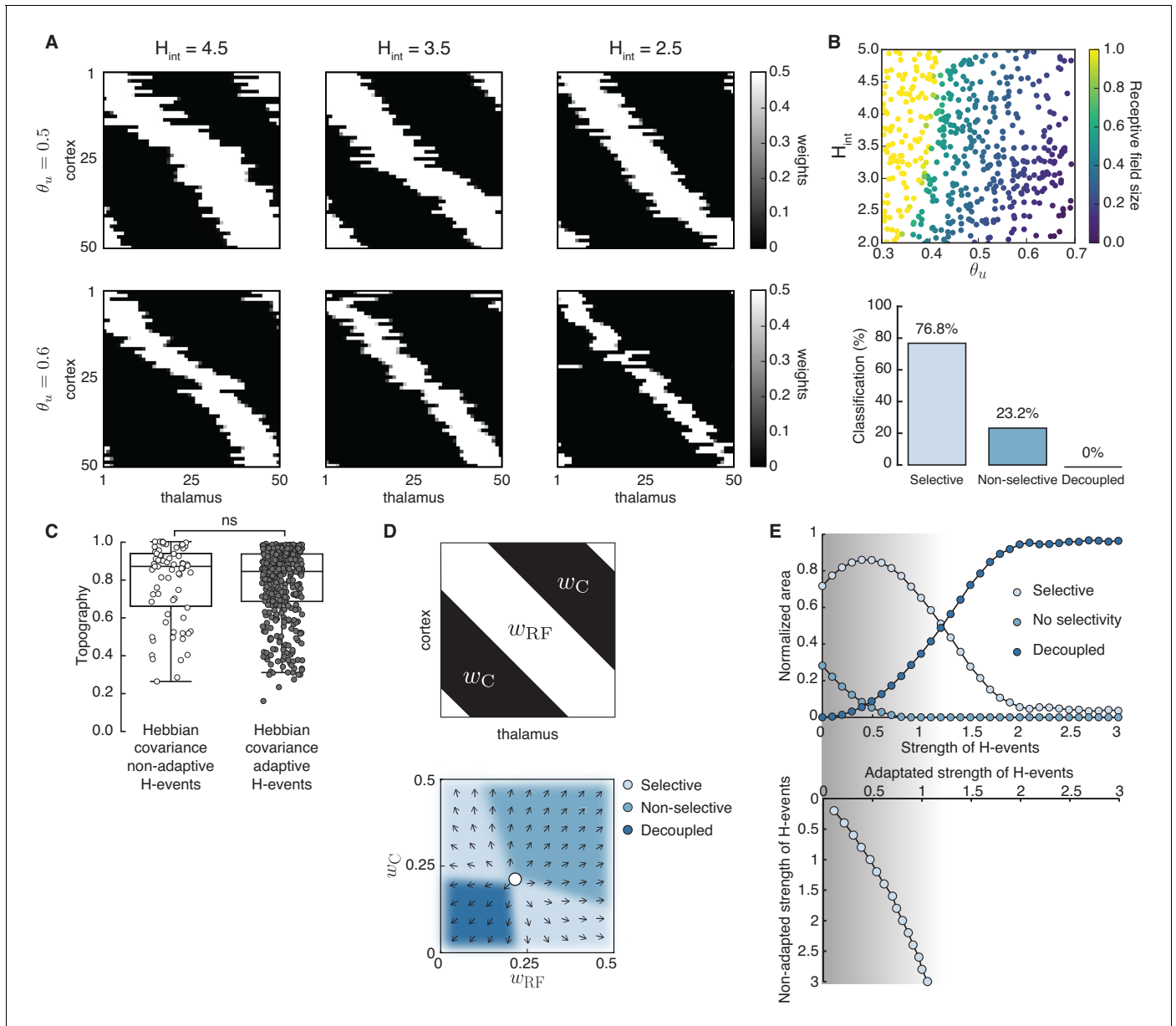


Figure 4. Adaptive cortical events refine thalamocortical connectivity. (A) Receptive field refinement with adaptive H-events and different H-inter-event intervals, H_{int} . Top: $\theta_u = 0.5$; bottom: $\theta_u = 0.6$. (B) Receptive field sizes from 500 Monte Carlo simulations for combinations of H_{int} and θ_u . Bottom: Percentage of simulation outcomes classified as ‘selective’ when the average receptive field size is smaller than one and larger than 0, ‘non-selective’ when the average receptive field size is equal to 1, and ‘decoupled’ when the average receptive field size is 0 for the two rules. (C) Topography of receptive fields classified as selective in B. Horizontal line indicates median, the box is drawn between the 25th and 75th percentile, whiskers extend above and below the box to the most extreme data points that are within a distance to the box equal to 1.5 times the interquartile range and points indicate all data points. Distributions are not significantly different (ns) as measured by a two-sample Kolmogorov-Smirnov test ($n = 70,390$ selective outcomes for each rule out of 500; $p = 0.41$; $D = 0.45$). (D) Top: Reduction of the full weight dynamics into two dimensions. Two sets of weights were averaged: those which potentiate and form the receptive field, w_{RF} , and the complementary set of weights that depress, w_C . Bottom: Initial conditions in the reduced two-dimensional phase plane were classified into three outcomes: ‘selective’, ‘non-selective’, and ‘decoupled’. We sampled 2500 initial conditions which evolved according to Equation 16 until the trajectories reached one of the selective fixed points, $(w_{max}, 0)$ and $(0, w_{max})$, or resulted in no selectivity either because both weights depressed to $(0, 0)$ or potentiated to (w_{max}, w_{max}) . The normalized number of initial coordinates generating each region can be interpreted as the area of the phase plane that results in each outcome. (E) Top: Normalized area of the phase plane of the reduced two-dimensional system that resulted in ‘selective’, ‘non-selective’, and ‘decoupled’ outcomes for $\theta_u = 0.53$ as a function of H-event strength. The darker shading indicates ranges of non-adapted H-event strength where the selectivity area is maximized. Bottom: The corresponding adapted strength of H-events was calculated in simulations with adaptive H-events and plotted as a function of the nominal, non-adapted strength of H-events. Figure 4 continued on next page

Figure 4 continued

The range of adapted H-event strengths (bottom) corresponds to the range of non-adaptive values that maximize the selectivity area (top). Each point shows the average over 10 runs and the bars the standard deviation (which are very small).

plane area of the reduced two-dimensional system with non-adaptive H-events (calculated as the proportion of initial conditions) that results in selectivity, potentiation or depression (**Figure 4D**, bottom). We found that adaptively modulating the strength of H-events maximizes the area of the phase plane that results in selectivity (**Figure 4E**, shaded region). The range of H-event strengths that maximizes the selective area for each input threshold in the reduced two-dimensional system can be related to the scaling of H-event amplitude in the simulations (Methods). In particular, the adaptation reliably shifts the H-event amplitude that would have occurred without adaptation, which we call ‘non-adapted strength of H-events’, into the regime of amplitudes that maximizes selectivity, which we call ‘adapted strength of H-events’ (**Figure 4E**). Therefore, the adaptation of H-event amplitudes controls the selective refinement by peripheral L-events by modulating the cortical depression by adapted H-events.

In vivo spontaneous cortical activity shows a signature of adaptation

To determine whether spontaneous cortical activity contains a signature of our postulated adaptation mechanism of H-event amplitudes, we reanalyzed published *in vivo* two-photon Ca^{2+} imaging data recorded in the visual cortex of young mice (P8-10) (**Siegel et al., 2012**). We combined multiple consecutive ~ 300 s long recordings for up to 40 mins of data from a given animal. First, we tested for long-term fluctuations in cortical excitability in the concatenated recordings of the same animal. We identified L- and H-events based on previously established criteria (**Siegel et al., 2012**). We found that the average amplitude of all (L and H) events is not significantly different across consecutive recordings of the same animal (**Figure 5—figure supplement 1A**). Additionally, across different animals and ages, individual event amplitudes remain uncorrelated between successive recordings at this timescale (**Figure 5—figure supplement 1B**). This suggests that there are no prominent long-term amplitude fluctuations, and therefore, the correlations cannot be explained by such fluctuations. Even so, slow amplitude fluctuations would not be able to generate refined receptive fields in the model (**Figure 5—figure supplement 2**).

Next, we investigated the relationship between the amplitude of a given H-event and the average activity preceding it. For each detected H-event, we extracted all spontaneous (L- or H-) events that preceded this H-event up to $T_{\max} = 300$ s before it. We then scaled the amplitude of each previous event multiplying it by an exponential kernel with a decay time constant of $\tau_{\text{decay}} = 1000$ s, which is sufficiently long to integrate many preceding spontaneous events (compared with the inter-event intervals in **Figure 1B**), and averaged these scaled amplitudes to get an aggregate quantity over amplitude and frequency (see Materials and methods).

We found that this aggregate amplitude of L- and H-events preceding a given H-event is significantly correlated ($r = 0.44$, $p < 10^{-10}$) to the amplitude of the selected H-event (**Figure 5B**). Consequently, a strong (weak) H-event follows strong (weak) average preceding network activity (**Figure 5C**), suggesting that cortical cells adapt their spontaneous firing rates as a function of their previous activity levels. The correlations are robust to variations in the inclusion criteria, maximum time T_{\max} to integrate activity and the exponential decay time constant τ_{decay} (**Figure 5—figure supplement 3**).

Modulating spontaneous activity properties affects receptive field refinements

Our results make relevant predictions for the refinement of receptive fields upon manipulating spontaneous activity. For example, H-event frequency can be experimentally reduced by a gap junction blocker (carbenoxolone) (**Siegel et al., 2012**). Our work demonstrates a trade-off between H-event frequency and the learning rule’s threshold between potentiation and depression on receptive field size; hence, less frequent H-events will need a somewhat higher threshold to achieve the same receptive field size (**Figure 4**).

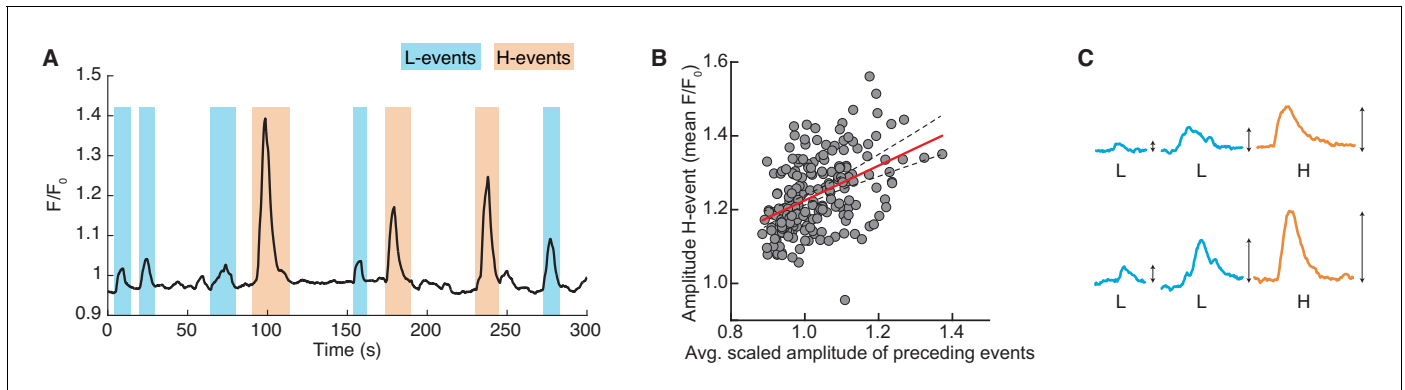


Figure 5. Spontaneous events in developing cortex adapt to recent activity. (A) Calcium trace of a representative recording with L- (blue) and H-events (orange) (Siegel et al., 2012). (B) The amplitude of an H-event shown as a function of the aggregate amplitude of preceding L- and H-events up to $T_{\max} = 300$ s before it, scaled by an exponential kernel with a decay time constant of 1000 s ($N = 195$ events from nine animals). Animals with fewer than 12 H-events preceded by activity within T_{\max} were excluded from this analysis (see Materials and methods). The Pearson correlation coefficient is $r = 0.44$, $p < 10^{-10}$, CI = (0.32, 0.54). Red line indicates regression line with 95% confidence bounds as dashed lines. (C) Schematic of the postulated adaptation: A weak (strong) H-event is more likely to be preceded by weak (strong) spontaneous events.

The online version of this article includes the following figure supplement(s) for figure 5:

Figure supplement 1. Fluctuations in cortical activity cannot generate correlations between event amplitude and average preceding activity.

Figure supplement 2. Long-term fluctuations in the amplitudes of L- and H-events cannot guide proper network refinement.

Figure supplement 3. Robustness of correlation under variations in the inclusion criteria, T_{\max} and τ_{decay} .

Similarly, L-events can also be experimentally manipulated, for instance, by altering inhibitory signaling (Leighton et al., 2020), or the properties of retinal waves which propagate as L-events into the cortex. We performed Monte Carlo simulations with a range of input thresholds θ_i and variable participation rates of thalamic neurons in L-events, using the Hebbian covariance rule with adaptive H-events (Figure 6A). Larger L-events in our model produce less refined, that is, larger receptive fields in the cortical network (Figure 6B,C, left). This result is not surprising given the proposed role of L-events in guiding receptive field refinements, and is consistent with the imprecise and unrefined receptive fields observed in the visual cortex of animals where retinal wave properties have been modified. For instance, a prominent example of retinal wave manipulations are $\beta 2$ knockout mice, which lack expression of the $\beta 2$ subunit of the nicotinic acetylcholine receptor ($\beta 2$ -nAChR) that mediates spontaneous retinal waves in the first postnatal week. In these animals, retinal waves are consistently larger as characterized by the increased correlation with distance (Sun et al., 2008; Stafford et al., 2009; Cutts and Eglén, 2014), in addition to other features. As a result, there are measurable defects in the retinotopic map refinement of downstream targets (Grubb et al., 2003; Cang et al., 2005b; Burbridge et al., 2014). Smaller L-events also refine receptive fields with better topographic organization (Figure 6C, right) and do not impair connectivity refinements. This result could be linked to experiments where the expression of $\beta 2$ -nAChR is limited to the ganglion cell layer of the retina, resulting in smaller retinal waves than those in wild-type and undisturbed retinotopy in the superior colliculus (Xu et al., 2011), although the effects in the cortex are unknown.

Therefore, we suggest that certain manipulations that modulate the size of sensory activity from the periphery have a profound impact on the precision of receptive field refinement in downstream targets, making predictions to be tested experimentally. In contrast to retinal wave manipulations, the effect of altered inhibitory signaling on receptive field refinements is still unknown. It is likely that such manipulations will also affect H-events (Leighton et al., 2020), as well as shape ongoing plasticity in the network (Wu et al., 2020), and hence have less predictable effects on receptive field size and topography.

Adaptive H-events promote the developmental event sparsification of cortical activity

Thus far, we focused on the development of the network connectivity in our model driven by spontaneous activity based on properties measured during a few postnatal days (P8-10, Figure 4A).

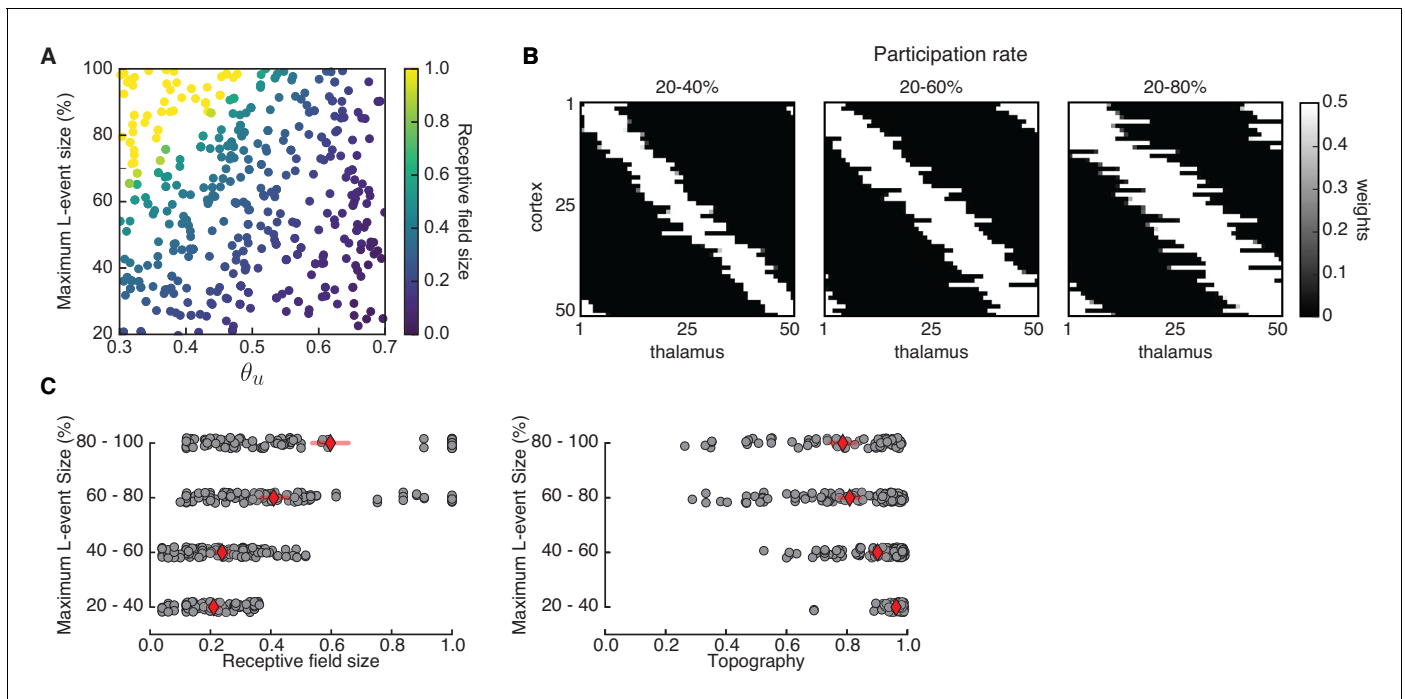


Figure 6. Receptive field refinement depends on the properties of L-events. (A) Receptive field sizes from 500 Monte Carlo simulations for different sizes of L-events where the minimum participation rate was 20%, and the maximum participation rate was varied. The input threshold was taken from the range $0.3 \leq \theta_u \leq 0.7$, while the adaptive H-events had a fixed inter-event-interval $H_{\text{int}} = 3.5$. (B) Individual receptive fields for different L-event maximum participation rates and $\theta_u = 0.50$. As the upper bound of the participation rate progressively increases from 40% to 80%, receptive fields get larger. (C) Left: Receptive field sizes from A binned according to the maximum L-event size. Right: Corresponding topography of selective receptive fields for different sizes of L-events. Diamonds in red indicate the mean, while horizontal bars indicate the 95% confidence interval.

However, *in vivo* spontaneous activity patterns are not static, but dynamically regulated during development by ongoing activity-dependent plasticity which continuously reshapes network connectivity that lasts several days (Rochefort et al., 2009; Golshani et al., 2009; Frye and MacLean, 2016). Moreover, it is unclear if the same criteria based on event participation rates and amplitude can be used to separate the spontaneous events into L and H at later developmental ages. Hence, we next asked how our observed modifications in network connectivity that are the result of receptive field refinement further modify spontaneous activity patterns on a much longer developmental timescale of several days in our model. Therefore, we analyzed all spontaneous events of simulated cortical neurons during the process of receptive field refinement in the presence of adaptive H-events (Figure 4B). Since the input threshold θ_u of the Hebbian learning rule is related to receptive field size (Figure 4B), we used θ_u as a proxy for time of development in the model: low θ_u corresponds to earlier developmental stages when receptive fields are large, while high θ_u corresponds to late developmental stages when receptive fields are refined. This assumption is also in line with the fact that the input resistance of neurons in V1 and S1 decreases during development (Etherington and Williams, 2011; Golshani et al., 2009), so that the depolarizing current necessary to trigger an action potential increases with age.

At an early developmental stage in the model ($\theta_u = 0.45$), the unrefined receptive fields of cortical neurons in our network model propagate thalamic activity into the cortex as very broad spontaneous events, while adaptive H-events remain intrinsic to the cortical layer. As in the data (Figure 7A,C; Siegel et al., 2012), the amplitude of events with 20–80% participation rate is approximately half the amplitude of events with greater than 80% participation rate (Figure 7B,D, left). Moreover, we also observed a high proportion of large events with greater than 80% participation rate (Figure 7—figure supplement 1A), suggesting that in the network model large spontaneous events are very frequent. At an intermediate developmental stage in the model ($\theta_u = 0.50$), as receptive fields refine

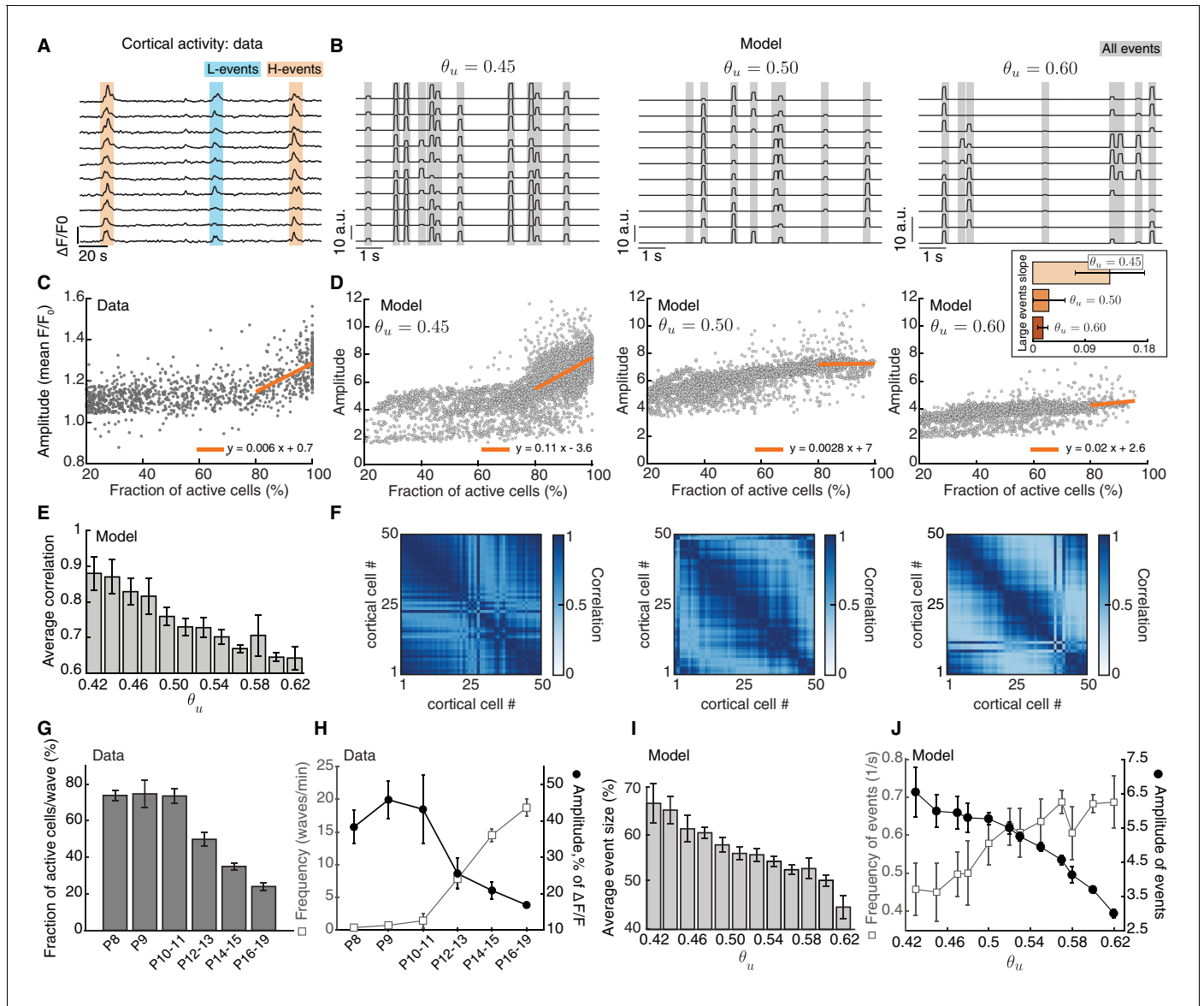


Figure 7. Adaptive H-events promote sparsification of cortical activity during development. (A) Spontaneous activity in the mouse visual cortex recorded *in vivo* at P8-10 (Siegel et al., 2012). Each activity trace represents an individual cortical cell. Blue and orange shading denotes L-events and H-events, respectively, as identified by Siegel et al., 2012. (B) Sample traces of cortical activity for different values of θ_u (as a proxy for developmental age). Gray shading denotes all events detected in our networks. (C) Amplitude vs. participation rate plot from the data (Siegel et al., 2012). The regression line for the amplitude vs. participation rate in H-events has a positive slope. (D) Amplitude vs. participation rate plots from the model, for different values of θ_u . Inset: The regression line for the amplitude vs. participation rate in large events with greater than 80% participation rate has a slope that decreases with θ_u . Error bars represent standard deviation. (E) Correlation between cortical neurons decreases as a function of the input threshold θ_u in the model, a proxy for developmental time. (F) Correlation matrices of simulated cortical neuron activity corresponding to D. (G,H). Event sizes and the relationship between frequencies (open squares) and amplitudes (filled circles) of spontaneous events at different postnatal ages (data reproduced from Rochefort et al., 2009). Error bars represent standard error of the mean (number of animals used at each age is provided in the original reference). (I) Spontaneous event sizes as a function of the input threshold θ_u . (J) Frequencies (squares) and amplitudes (circles) of events with 20–80% participation rate in the model at different input thresholds. Error bars represent the standard error of the mean of 10 simulations. The online version of this article includes the following figure supplement(s) for figure 7:

Figure supplement 1. Developmental event sparsification in the model.

and peripheral events activate fewer cortical neurons, our proposed adaptation of H-event amplitudes decreases the overall level of intrinsic activity in the cortical layer. This changes the relationship between effective amplitude and participation rate (**Figure 7D**, middle), with large events decreasing their amplitudes and density (**Figure 7—figure supplement 1A**). Finally, at late developmental stages in the model ($\theta_u = 0.60$), the relationship between effective amplitude and participation rate is almost absent (**Figure 7D**, right). Overall event amplitude is much lower resulting in far fewer large events with greater than 80% participation rate (**Figure 7—figure supplement 1B**). Therefore, due to the progressive receptive field refinements and the continued H-event adaptation in response to resulting activity changes, spontaneous events in our model progressively sparsify during ongoing development, whereby spontaneous events become smaller in size with fewer participating cells. This finding suggests that spontaneous events in the cortex at later developmental ages can no longer be separated into L and H using the same criteria of participation rate and amplitude as during early development. We also found that the mean pairwise correlation of all cortical neurons in the model decreases as a function of developmental age (θ_u ; **Figure 7E,F**), which further supports the trend of progressive sparsification already observed in the event sizes.

Interestingly, such event sparsification of spontaneous activity has been observed experimentally in the mouse barrel cortex during postnatal development from P4 to P26 (**Golshani et al., 2009**) and in the visual cortex from P8 to P79 (**Rocheftort et al., 2009**). During this period, in the visual cortex, the size of spontaneous events decreases (**Figure 7G**), the amplitude of the participating cells also decreases, while event frequency increases (**Figure 7H; Rocheftort et al., 2009**). This progressive event sparsification of cortical activity is generated by mechanisms intrinsic to the cortex, and does not seem to be sensory-driven (**Rocheftort et al., 2009; Golshani et al., 2009**). We found the same relationships in our model using θ_u as a proxy for developmental time (**Figure 7I,J**).

In summary, our framework for activity-dependent plasticity and receptive field refinement between thalamus and cortex with adaptive H-events can tune the properties of cortical spontaneous activity and provide a substrate for the event sparsification of cortical activity during development on a much longer timescale than receptive field refinement. This sparsification has been found in different sensory cortices, including visual (**Rocheftort et al., 2009**), somatosensory (**Golshani et al., 2009**), and auditory (**Frye and MacLean, 2016**), suggesting a general principle that underlies network refinement. However, the event sparsification we observe is different from sparse network activity implicated in sparse efficient coding, which interestingly seems to decrease during development (**Berkes et al., 2009; Berkes et al., 2011**). Our modeling predicts that cortical event sparsification is primarily due to the suppression of cortically-generated H-events in the Hebbian covariance rule, which switches cortical sensitivity to input from the sensory periphery after the onset of sensory experience.

Discussion

We examined the information content of spontaneous activity for refining local microcircuit connectivity during early postnatal development. In contrast to classical works on activity-dependent refinements, which used mathematically convenient formulations of spontaneous activity (**Willshaw and von der Malsburg, 1976; Mackay and Miller, 1990**), we used spontaneous activity patterns characterized in the mouse visual cortex *in vivo* before the onset of vision (P8-10), which revealed its rich structure. Specifically, we explored the joint contribution of two distinct patterns of spontaneous activity recorded in the mouse visual cortex before the onset of vision, local (L-events) and global (H-events), on establishing topographically refined receptive fields between the thalamus and the cortex without decoupling in a model network with activity-dependent plasticity. Because of their spatially correlated activity, we proposed that peripherally generated L-events enable topographic refinement, while H-events regulate connection strength homeostatically. We investigated two Hebbian learning rules – the Hebbian covariance and the BCM rules – which use joint pre- and postsynaptic activity to trigger synaptic plasticity. First, we studied the Hebbian covariance rule that induces global synaptic depression in the presence of only postsynaptic activity (i.e. H-events). Second, we studied the BCM rule, which is known to establish the emergence of ocular dominance and orientation selectivity in the visual system. Although L-events successfully instruct topographic receptive field refinements in the Hebbian covariance rule, naively including H-events provides too much depression, eliminating selectivity in the network despite fine-tuning (**Figure 3**). In contrast, in the

BCM rule, H-events are indeed homeostatic, regulating the threshold between depression and potentiation. However, small L-events, which carry precise information for topographic connectivity refinements, mostly cause long-term depression in the synaptic weights and disrupt topography. Inspired by the sliding threshold in the BCM rule, we proposed a similar adaptive mechanism operating at the single-cell level in the Hebbian covariance rule. This mechanism regulates the amplitude of the cortically generated H-events according to the preceding average activity in the network to homeostatically balance local increases and decreases in activity, and can successfully refine receptive fields with excellent topography (**Figure 4**). Without any additional fine-tuning, this mechanism can also explain the long-term event sparsification of cortical activity as the circuit matures and starts responding to visual input (**Figure 7**). Therefore, we propose that L- and adaptive H-events cooperate to synergistically guide circuit organization of thalamocortical synapses during postnatal development.

The origin of cortical event amplitude adaptation

After a re-examination of spontaneous activity recorded in the developing cortex *in vivo* between postnatal days 8 and 10 (**Siegel et al., 2012**), we found evidence for the proposed H-event amplitude adaptation (**Figure 5**). This mechanism is sufficiently general in its formulation that it could be realized at the cellular, synaptic or network level. At the cellular level, the adaptation mechanism resembles the plasticity of intrinsic excitability. Typically, plasticity of intrinsic excitability has been reported in response to long-term perturbations in activity or persistent changes in synaptic plasticity like LTP and LTD, where the intrinsic properties of single neurons are adjusted in an activity-dependent manner (**Daoudal and Debanne, 2003; Desai et al., 1999**). During plasticity of intrinsic excitability, neurons can alter the number and expression levels of ion channels to adjust their input-output function either by modifying their firing thresholds or response gains, which could represent the substrate for H-event amplitude regulation. Our adaptation mechanism is consistent with the fast plasticity of intrinsic excitability operating on the timescale of several spontaneous events supported by many experimental studies. For instance, intrinsic excitability of spine motoneurons is depressed after brief but sustained changes in spinal cord network activity in neonatal mice (**Lombardo et al., 2018**). Similarly, hippocampal pyramidal neurons also exhibit a rapid reduction of intrinsic excitability in response to sustained depolarizations lasting up to several minutes (**Sánchez-Aguilera et al., 2014**). In addition to reduced excitability, in the developing auditory system, enhanced intrinsic excitability has been reported in the cochlea followed by reduced synaptic excitatory input from hair cells in a model of deafness, although this change is slower than our proposed adaptation mechanism (**Babola et al., 2018**).

At the synaptic level, our adaptation mechanism can be implemented by synaptic scaling, a process whereby neurons regulate their activity by scaling incoming synaptic strengths in response to perturbations (**Turrigiano et al., 1998**). A second possibility is short-term depression, which appears to underlie the generation of spontaneous activity episodes in the chick developing spinal cord (**Tabak et al., 2001; Tabak et al., 2010**). Similarly, release probability suppression has been reported to strongly contribute to synaptic depression during weak activity at the calyx of Held (**Xu and Wu, 2005**), which is more pronounced at immature synapses where morphological development renders synaptic transmission less effective (**Renden et al., 2005; Nakamura and Takahashi, 2007**). This is also the case in the cortex, where short-term synaptic plasticity in young animals is stronger (**Oswald and Reyes, 2008**). Beyond chemical synapses, plasticity of gap junctions, which are particularly prevalent in development (**Niculescu and Lohmann, 2014**), could also be a contributing mechanism that adapts overall network activity (**Cachope et al., 2007; Haas et al., 2011**).

Finally, at the network level, the development of inhibition could be a substrate for amplitude adaptation of cortically generated events. The main inhibitory neurotransmitter, GABA, is thought to act as a depolarizing neurotransmitter, excitatory in early postnatal days (**Ben-Ari, 2002**), although recent evidence argues that GABAergic neurons have an inhibitory effect on the cortical network already in the second postnatal week (**Murata and Colonnese, 2020; Kirmse et al., 2015; Valeeva et al., 2016**). Thus, the local maturation of inhibitory neurons – of which there are several types (**Tremblay et al., 2016**) – that gradually evolve to balance excitation and achieve E/I balance (**Dornn et al., 2010**) could provide an alternative implementation of the proposed H-event adaptation.

Developmental sparsification of cortical activity

On a longer timescale than receptive field refinement, we demonstrated that the adaptation of H-event amplitude can also bring about the event sparsification of cortical activity, as global, cortically generated H-events are attenuated and become more localized (**Figure 7**). The notion of 'sparse neural activity' has received significant attention in experimental and theoretical studies of sensory processing in the cortex, including differing definitions and implementations (**Field, 1994; Willmore and Tolhurst, 2001; Berkes et al., 2009; Olshausen and Field, 2004; Zylberberg and DeWeese, 2013**). In particular, sparse activity in the mature cortex has been argued to be important for the efficient coding of sensory inputs of different modalities (**Olshausen and Field, 2004; Field, 1994**). Hence, the developmental process of receptive field refinement might be expected to produce sparser network activity over time. However, experiments directly testing this idea have found no, or even opposite, evidence for the developmental emergence of efficient sparse coding (**Berkes et al., 2009; Berkes et al., 2011**). In the context of our work, sparsification simply refers to an overall sparsification of network events (fewer active cells per event). Given that our data pertain to developmental spontaneous activity before eye-opening, in complete absence of stimulation, it is not straightforward to relate our event sparsification to the sparse efficient coding hypothesis.

Assumptions in the model

Our model is based on the assumption that L- and H-events have distinct roles during the development of the visual system. Retinal waves, the source of L-events, carry information downstream about the position and function of individual retinal ganglion cells (**Stafford et al., 2009**), hence they are ideally suited to serve as 'training patterns' to enable activity-dependent refinements based on spatiotemporal correlations (**Ko et al., 2011; Ackman and Crair, 2014; Thompson et al., 2017**). Since all cells are maximally active during H-events, these patterns likely do not carry much information that can be used for activity-dependent refinement of connectivity. In contrast, we assumed that H-events homeostatically control synaptic weights, operating in parallel to network refinements by L-events (**Figure 4**). Indeed, highly correlated network activity can cause homeostatic down-regulation of synaptic weights via a process known as synaptic scaling (**Turrigiano and Nelson, 2004**). The homeostatic role of H-events is also consistent with synaptic downscaling driven by slow waves during sleep, a specific form of synchronous network activity (**Tononi and Cirelli, 2006; Vyazovskiy et al., 2008**). Since during development sleep patterns are not yet regular, we reasoned that refinement (by L-events) and homeostasis (by H-events) occur simultaneously instead of being separated into wake and sleep states.

We focused on the role of spontaneous activity in driving receptive field refinements rather than study how spontaneous activity is generated. While the statistical properties of spontaneous activity in the developing cortex are well-characterized, the cellular and network mechanisms generating this activity remain elusive. In particular, while H-event generation has been shown to rely on gap junctions (**Siegel et al., 2012; Niculescu and Lohmann, 2014**), which recurrently connect developing cortical cells, not much is known about how the size of cortical events is modulated and how an L-event is prevented from spreading and turning into an H-event. It is likely that cortical inhibition plays a critical role in localizing cortical activity and shaping receptive field refinements (**Wood et al., 2017; Leighton et al., 2020**), for instance, through the plasticity of inhibitory connections by regulating E/I balance (**Dorn et al., 2010**). As new experiments are revealing more information about the cellular and synaptic mechanisms that generate spatiotemporally patterned spontaneous activity (**Fujimoto et al., 2019**), a full model of the generation and the effect of spontaneous activity might soon be feasible.

The threshold parameter in the Hebbian covariance rule in the presence of H-events implements an effective subtractive normalization that sharpens receptive fields (see Appendix). Despite the strong weight competition, subtractive normalization seems to be insufficient to stabilize receptive fields in the presence of non-adaptive H-events (**Figure 3**). Multiplicative normalization is an alternative normalization scheme, but it does not generate refined receptive fields (**Miller and MacKay, 1994**). Therefore, we also studied the BCM rule due to its ability to generate selectivity in postsynaptic neurons under patterned input. While the BCM rule successfully generates selectivity and receptive field refinement, the resulting topography is worse than in the Hebbian covariance rule (**Figure 3**). Both rules have an adaptive component: in the BCM rule it is the threshold between

potentiation and depression that slides as a function of postsynaptic activity, while in the Hebbian covariance rule it is the adaptive amplitude of H-events, while the rule itself is fixed. Although experiments have shown the stereotypical activity dependence of the BCM rule (Kirkwood *et al.*, 1996; Sjöström *et al.*, 2001), whether a sliding threshold for potentiation vs. depression exists is still debated. Moreover, the timescale over which the threshold slides to prevent unbounded synaptic growth needs to be much faster than found experimentally (Zenke *et al.*, 2017). Our proposed H-event amplitude adaptation operates on the fast timescale of several spontaneous events found experimentally (Siegel *et al.*, 2012; Sánchez-Aguilera *et al.*, 2014; Lombardo *et al.*, 2018). Hence, together with the better topography and the resulting event sparsification as a function of developmental stage that the Hebbian covariance rule with adaptive H-events generates, we propose it as the more likely plasticity mechanism to refine receptive fields in the developing visual cortex.

Finally, we have focused here on the traditional view that molecular gradients set up a coarse map that activity-dependent mechanisms then refine (Goodhill and Xu, 2005). In our model, this was implemented as a weak bias in the initial connectivity, which did not affect our results regarding the refinement of receptive fields. Both activity and molecular gradients may work together in interesting ways to refine receptive fields (Grimbert and Cang, 2012; Godfrey and Swindale, 2014; Naoki, 2017), and future work should include both aspects.

Predictions of the model

Our model makes several experimentally testable predictions. First, we showed that changing the frequency of H-events can affect the size of the resulting receptive fields under both the BCM (Figure 3) and the Hebbian covariance rule with adaptive H-events (Figure 4). The frequency of H-events can be experimentally manipulated using optogenetics or pharmacology. For instance, gap junction blocker (carbenoxolone) has been shown to specifically reduce the frequency of H-events (Siegel *et al.*, 2012), hence in that scenario our results predict broader receptive fields.

Additionally, L-events can also be experimentally manipulated. Recently, reduced inhibitory signaling by suppressing somatostatin-positive interneurons have been shown to increase the size of L-events in the developing visual cortex (Leighton *et al.*, 2020). With the effect of altered inhibitory signaling on receptive field refinements still unknown, our work predicts larger receptive fields and worse topography upon reduction of inhibition. L-events can also be experimentally manipulated by changing the properties of retinal waves, which can significantly affect retinotopic map refinement of downstream targets (Grubb *et al.*, 2003; Cang *et al.*, 2005b; Burbridge *et al.*, 2014). Indeed, $\beta 2$ knockout mice discussed earlier have larger retinal waves and less refined receptive fields in the visual cortex (Sun *et al.*, 2008; Stafford *et al.*, 2009; Cutts and Eglén, 2014). If we assume that these larger retinal waves manifest as larger L-events in the visual cortex following Siegel *et al.*, 2012, then these experimental observations are in agreement with our model results.

Third, our model predicts that as a result of receptive field refinement during development, network events sparsify as global, cortically generated events are attenuated and become more localized. Interestingly, the properties of spontaneous activity measured experimentally in different sensory cortices (Rochefort *et al.*, 2009; Frye and MacLean, 2016; Smith *et al.*, 2015; Ikezoe *et al.*, 2012; Shen and Colonnese, 2016; Golshani *et al.*, 2009) and in the olfactory bulb (Fujimoto *et al.*, 2019) change following a very similar timeline during development as predicted in our model. However, in many of these studies activity has not been segregated into peripherally driven L-events and cortically generated H-events. Therefore, our model predicts that the frequency of L-events would increase while the frequency of H-events would decrease over development.

Finally, we propose that for a Hebbian covariance rule to drive developmental refinements of receptive fields using spontaneous L- and H-event patterns recorded *in vivo* (Siegel *et al.*, 2012), H-events need to adapt to ongoing network activity. Whether a fast adaptation mechanism like the one we propose operates in the cortex requires prolonged and detailed activity recordings *in vivo*, which are within reach of modern technology (Ackman and Crair, 2014; Ji, 2017; Gribizis *et al.*, 2019). Our framework also predicts that manipulations that affect overall activity levels of the network, such as activity reduction by eye enucleation, would correspondingly affect the amplitude of ongoing H-events.

Conclusion

In summary, we studied the refinement of receptive fields in a developing cortex network model constrained by realistic patterns of experimentally recorded spontaneous activity. We proposed that adaptation of the amplitude of cortically generated spontaneous events achieves this refinement without additional assumptions on the type of plasticity in the network. Our model further predicts how cortical networks could transition from supporting highly synchronous activity modules in early development to sparser peripherally driven activity suppressing local amplification, which could be useful for preventing hyper-excitability and epilepsy in adulthood while enhancing the processing of sensory stimuli.

Materials and methods

Network model

We studied a feedforward, rate-based network with two one-dimensional layers, one of N_u thalamic neurons (u) and the other of N_v cortical neurons (v), with periodic boundary conditions in each layer to avoid edge effects. The initial connectivity in the network was all-to-all with uniformly distributed weights in the range $w_{\text{ini}} = [a, b]$. In addition, a topographic bias was introduced by modifying the initially random connectivity matrix to have the strongest connections between neurons at the matched topographic location, and which decay with a Gaussian profile with increasing distance (**Figure 2C**), with amplitude s and spread σ_s . During the evolution of the weights, soft bounds were applied on the interval $[0, w_{\text{max}}]$. We studied weight evolution under two activity-dependent learning rules: the Hebbian (**Equation 2**) and the BCM (**Equation 3**) rules. **Table 1** lists all parameters. Sample codes can be found at github.com/comp-neural-circuits/LH-events (Wosniack, 2021; copy archived at [swh: 1:rev:b90e189a9e1a4d0cdda097d435fa91b1236f1866](https://www.swh.io/rev/b90e189a9e1a4d0cdda097d435fa91b1236f1866)).

Generation of L- and H-events

We modeled two types of spontaneous events in the thalamic (L-events) and the cortical (H-events) layer of our model (Siegel et al., 2012). During L-events, the firing rates of a fraction (L_{pct}) of neighboring thalamic neurons were set to $L_{\text{amp}} = 1$ during a period L_{dur} and were otherwise 0. Similarly, during H-events, the firing rates of a fraction (H_{pct}) of cortical cells were set to H_{amp} during time H_{dur} . As a result, cortical neuron activity was composed of H-events and L-events transmitted from the thalamus. For each H-event, H_{amp} was independently sampled from a Gaussian distribution with mean H_{amp} and standard deviation $H_{\text{amp}}/3$. The inter-event intervals were L_{int} and H_{int} sampled from experimentally characterized distributions in Siegel et al., 2012, (Table 1). The event durations and inter-event intervals were shortened by a factor of 10 compared to the values measured in the data (Figure 1) to speed up our simulations, but the relationships observed in the data were preserved. We note that in the experiments, both L- and H-events were characterized in the primary visual cortex; in our model, we assume that L-events are generated in the retina and subsequently propagated through the thalamus to the cortex, where they manifest with the experimentally reported characteristics (see Figure 7B for example). This interpretation is supported by experimental evidence (Siegel et al., 2012), but we cannot exclude the possibility that the retina also generates H-events or that L-events are generated in the cortex.

Reduction of the weight dynamics to two dimensions

To reduce the full weight dynamics to a two-dimensional system, we averaged all the n weights belonging to the receptive field that are predicted to potentiate along the initial topological bias, as w_{RF} , and all the $N_u - n$ remaining weights, which we call complementary to the receptive field, as w_{C} . When all weights behaved the same, we arbitrarily split them into two groups of the same size. Details about the classification of weights as w_{RF} or w_{C} can be found in the Appendix.

Computing the strength of simulated H-events

To relate the reduced two-dimensional phase planes to the simulation results, we wrote down the steady state activity of neuron j (Equation 1), which contains the rate gain from H-events relative to L-events, $\langle R_{\text{H}} \rangle$ (also called 'Strength of H-events' in Figure 4E):

$$\langle R_H \rangle = \frac{\langle L_{\text{int}} \rangle \langle H_{\text{amp}} \rangle \langle H_{\text{dur}} \rangle}{\langle H_{\text{int}} \rangle \langle L_{\text{amp}} \rangle \langle L_{\text{dur}} \rangle} = \frac{L_{\text{int}}}{H_{\text{int}}} \langle H_{\text{amp}} \rangle \quad (6)$$

since $\langle L_{\text{dur}} \rangle = \langle H_{\text{dur}} \rangle$ and $\langle L_{\text{amp}} \rangle = 1$.

In the absence of adaptive H-events, for a fixed set of values for H_{amp} and L_{int} (as in **Table 1**) and a chosen $\langle R_H \rangle$ which we called ‘Non-adapted strength of H-events’ in **Figure 4E**, we used **Equation 6** to find the H_{int} value that satisfies the equation. Next, we ran simulations with the same H_{int} and L_{int} parameters, but adaptive H_{amp} . We fixed the inter-event intervals of both L- and H-events to their mean values L_{int} and H_{int} instead of sampling them from distributions in **Figure 4E**. Then we numerically estimated the average amplitude of H-events with adaptation, which we called ‘Adapted strength of H-events’ in **Figure 4E** at the end of the simulation (final 5% of the simulation time) when the dynamics were stationary.

Receptive field statistics

The following receptive field statistics were used to quantify properties of the weight matrix \mathbf{W} after the developing weights became stable.

Receptive field size

The receptive field of a cortical neuron is the group of weights from thalamic cells for which $w_{ij} > w_{\text{max}}/5$. The lower threshold was chosen to make the measurement robust to small fluctuations around 0, which are present because of the soft bounds. Mathematically, we compute the receptive field size of cortical neuron j as:

$$R_F(\mathbf{w}_j) = \frac{1}{N_u} \sum_{i=1}^{N_u} \mathcal{I}_i, \quad (7)$$

with the \mathcal{I} vector given by:

$$\mathcal{I}_i = \begin{cases} 1, & w_{ij} > w_{\text{max}}/5 \\ 0, & \text{otherwise.} \end{cases} \quad (8)$$

The normalized receptive field ranges from 0 corresponding to a total decoupling of the cortical cell from the input layer, to one corresponding to no selectivity due to the potentiation of all weights from the input layer to that neuron. To compute the average receptive field size of the network, we include only the cortical neurons (N^*) that have not decoupled:

$$R_F(\mathbf{W}) = \frac{1}{N^*} \sum_{j=1}^{N^*} R_F(\mathbf{w}_j). \quad (9)$$

If all the cortical cells have decoupled from the thalamus, we set $R_F(\mathbf{W}) = 0$.

Topography \mathcal{T}

The topography of the network is a measure of how much of the initially weak biased topography is preserved in the final receptive field. Due to our biased initial conditions, neighboring thalamic cells are expected to project to neighboring cortical cells, yielding a diagonal weight matrix. For each cortical neuron, we calculated how far the center of its receptive field is from the ideal diagonal. Mathematically, for each row j of \mathbf{W} , we determined the center of the receptive field c_j and calculated the smallest distance (while considering periodic boundary conditions) between the receptive field center and the diagonal element j . Then, we summed all the squared distances and calculated the average error of the topography:

$$\xi = \frac{1}{N_v} \sum_{j=1}^{N_v} |c_j - j|^2. \quad (10)$$

To normalize the topography, we compared ξ to the topography error Ξ of a column receptive field (**Figure 3—figure supplement 1A**) where the centers of all cortical receptive fields were the

same, $c_j = c$ (c a constant). For such a column receptive field, $\Xi = \frac{N_u^2}{12}$. Therefore, we define the topography score \mathcal{T} as:

$$\mathcal{T} = 1 - \frac{\xi}{\Xi}. \quad (11)$$

The topography will be close to one if the weight matrix is perfectly diagonal and 0 if the final receptive field is a column ($\xi = \Xi$).

Proportion of cortical decoupling \mathcal{D}

To quantify the cortical decoupling, we use **Equation 8** to compute the fraction of decoupled neurons divided by the number of neurons, $\frac{1}{N_u} \sum_{j=1}^{N_u} \prod_{i=1}^{N_u} (1 - \mathcal{I}_{ij})$. If the decoupling is 0, no cortical neuron has decoupled from the thalamus, while decoupling of 1 means that all the cortical neurons are decoupled from the thalamus.

Quantifying adaptation in the data

We first investigated if fluctuations in the activity across recordings could generate significant correlations. We analyzed consecutive recordings (each ~5 mins long) in the same animal of which we had between 3 and 14 in all 26 animals (separated by <5 mins due to experimental constraints on data collection) to identify possible fluctuations on a longer timescale. We found that the average amplitude of all (L and H) events is not significantly different across consecutive recordings of the same animal (**Figure 5—figure supplement 1A**, one-way ANOVA tests, $p > 0.05$ in 23 out of 26 animals). Across different animals and ages, individual event amplitudes remained uncorrelated between successive recordings at this timescale, which we confirmed by plotting the difference in event amplitude as a function of the time between recordings (**Figure 5—figure supplement 1B**), Kruskal-Wallis test, $p > 0.05$.

For our reanalysis of the spontaneous events (**Figure 5**), we only included events that recruited at least 20% of the cells in the imaging field of view following **Siegel et al., 2012**. We computed the average amplitude of all events that occurred within a time window T_{\max} before an H-event (consecutive recordings were concatenated) and compared it to the amplitude of the H-event. We excluded animals that had fewer than 12 H-events preceded by spontaneous activity within the time window T_{\max} (nine animals remained after exclusion). Next, we computed the correlation coefficient of the relationship between H-event amplitude and the average amplitude of preceding activity within T_{\max} with a leaky accumulator of time constant τ_{decay} . To estimate the 95% confidence interval, we performed a bootstrap analysis in which we generated 1000 bootstrap datasets by drawing without replacement from the valid pairs of H-event amplitudes and average amplitude of preceding activity. We repeated this analysis with different thresholds for excluding data (**Figure 5—figure supplement 3A,B**), different values of the time window T_{\max} within which events are averaged (**Figure 5—figure supplement 3C**) and for different decay time constants τ_{decay} (**Figure 5—figure supplement 3D**). All data and analysis code can be found at github.com/comp-neural-circuits/LH-events.

Spontaneous events identification in the model

To quantify the properties of spontaneous activity in the cortical layer of our model, we used the time series of activity of all the simulated cortical neurons (after weight stabilization is achieved) sampled in a high time resolution (0.01 s, **Figure 7B**). We defined a global activity threshold $\nu = v_{\max}/r$, where v_{\max} is the highest amplitude among the cortical cells in the recording and r is a fixed scaling constant ($r = 8$ for all recordings). For each cortical cell j , we labeled the intervals where the cell was active (1) or inactive (0) based on:

$$x_j(t) = \begin{cases} 1, & \text{if } v_j(t) \geq \nu, \\ 0, & \text{otherwise.} \end{cases} \quad (12)$$

We then used the trace $X(t) = \sum_{j=1}^N x_j(t)$ to define the number of active cortical cells at each time step t , that is, the participation rate. For each identified event, we averaged the amplitude of the active cells to obtain the amplitude vs. participation rate relationship.

Acknowledgements

This project has received funding from the European Research Council (ERC) under the European Union's Horizon 2020 research and innovation programme (Grant agreement No. 804824 to JG). This work was further supported by the Max Planck Society (MW, JHK, LYC, JG), a NARSAD Young Investigator Grant from the Brain and Behavior Research Foundation (JG), a Capes-Humboldt Research fellowship (MW), the Smart Start joint training program in computational neuroscience (JHK), and by grants of the Netherlands Organization for Scientific Research (NWO, ALW Open Program grants, no. 819.02.017, 822.02.006 and ALWOP.216; ALW Vici, no. 865.12.001) and the "Stichting Vrienden van het Herseninstituut" (NZ, CL). We thank Stephen Eglen for discussions and ideas in the initial stages of the project.

Additional information

Funding

Funder	Grant reference number	Author
Alexander von Humboldt-Stiftung		Marina E Wosniack
H2020 European Research Council	804824	Jan H Kirchner Julijana Gjorgjieva
Max-Planck-Gesellschaft		Marina E Wosniack Jan H Kirchner Ling-Ya Chao Julijana Gjorgjieva
Brain and Behavior Research Foundation	26253	Julijana Gjorgjieva
SMART START training program in computational neuroscience		Jan H Kirchner
Nederlandse Organisatie voor Wetenschappelijk Onderzoek	819.02.017	Nawal Zabouri Christian Lohmann
Stichting Vrienden van het Herseninstituut	805254845	Nawal Zabouri Christian Lohmann
Nederlandse Organisatie voor Wetenschappelijk Onderzoek	822.02.006	Nawal Zabouri Christian Lohmann
Nederlandse Organisatie voor Wetenschappelijk Onderzoek	ALWOP.216	Nawal Zabouri Christian Lohmann
Nederlandse Organisatie voor Wetenschappelijk Onderzoek	ALW Vici no. 865.12.001	Nawal Zabouri Christian Lohmann

The funders had no role in study design, data collection and interpretation, or the decision to submit the work for publication.

Author contributions

Marina E Wosniack, Conceptualization, Software, Formal analysis, Methodology, Writing - original draft, Writing - review and editing, Performing simulations; Jan H Kirchner, Methodology, Writing - original draft; Ling-Ya Chao, Software, Methodology; Nawal Zabouri, Data curation, Investigation; Christian Lohmann, Conceptualization, Resources, Writing - review and editing; Julijana Gjorgjieva, Conceptualization, Resources, Supervision, Funding acquisition, Methodology, Writing - original draft, Project administration, Writing - review and editing

Author ORCIDs

Marina E Wosniack  <https://orcid.org/0000-0003-2175-9713>

Jan H Kirchner  <https://orcid.org/0000-0002-9126-0558>

Ling-Ya Chao  <https://orcid.org/0000-0002-6706-5939>

Christian Lohmann  <https://orcid.org/0000-0002-1780-2419>

Julijana Gjorgjieva  <https://orcid.org/0000-0001-7118-4079>

Decision letter and Author response

Decision letter <https://doi.org/10.7554/eLife.61619.sa1>

Author response <https://doi.org/10.7554/eLife.61619.sa2>

Additional files

Supplementary files

- Transparent reporting form

Data availability

Sample codes and data are available at <https://github.com/comp-neural-circuits/LH-events> (copy archived at <https://archive.softwareheritage.org/swh:1:rev:b90e189a9e1a4d0cdda097d435-fa91b1236f1866/>).

References

- Ackman JB, Burbridge TJ, Crair MC. 2012. Retinal waves coordinate patterned activity throughout the developing visual system. *Nature* **490**:219–225. DOI: <https://doi.org/10.1038/nature11529>, PMID: 23060192
- Ackman JB, Crair MC. 2014. Role of emergent neural activity in visual map development. *Current Opinion in Neurobiology* **24**:166–175. DOI: <https://doi.org/10.1016/j.conb.2013.11.011>, PMID: 24492092
- Babola TA, Li S, Gribizis A, Lee BJ, Issa JB, Wang HC, Crair MC, Bergles DE. 2018. Homeostatic control of spontaneous activity in the developing auditory system. *Neuron* **99**:511–524. DOI: <https://doi.org/10.1016/j.neuron.2018.07.004>, PMID: 30077356
- Ben-Ari Y. 2002. Excitatory actions of gaba during development: the nature of the nurture. *Nature Reviews Neuroscience* **3**:728–739. DOI: <https://doi.org/10.1038/nrn920>, PMID: 12209121
- Berkes P, White B, Fiser J. 2009. No evidence for active sparsification in the visual cortex. In: Bengio Y, Schuurmans D, Lafferty J. D, Williams C. K, Culotta A (Eds). *Advances in Neural Information Processing Systems* 22. Curran Associates, Inc. p. 108–116.
- Berkes P, Orbán G, Lengyel M, Fiser J. 2011. Spontaneous cortical activity reveals hallmarks of an optimal internal model of the environment. *Science* **331**:83–87. DOI: <https://doi.org/10.1126/science.1195870>, PMID: 21212356
- Bienenstock EL, Cooper LN, Munro PW. 1982. Theory for the development of neuron selectivity: orientation specificity and binocular interaction in visual cortex. *The Journal of Neuroscience* **2**:32–48. DOI: <https://doi.org/10.1523/JNEUROSCI.02-01-00032.1982>, PMID: 7054394
- Blankenship AG, Feller MB. 2010. Mechanisms underlying spontaneous patterned activity in developing neural circuits. *Nature Reviews Neuroscience* **11**:18–29. DOI: <https://doi.org/10.1038/nrn2759>, PMID: 19953103
- Burbridge TJ, Xu HP, Ackman JB, Ge X, Zhang Y, Ye MJ, Zhou ZJ, Xu J, Contractor A, Crair MC. 2014. Visual circuit development requires patterned activity mediated by retinal acetylcholine receptors. *Neuron* **84**:1049–1064. DOI: <https://doi.org/10.1016/j.neuron.2014.10.051>, PMID: 25466916
- Butts DA, Kanold PO, Shatz CJ. 2007. A burst-based "Hebbian" learning rule at retinogeniculate synapses links retinal waves to activity-dependent refinement. *PLOS Biology* **5**:e61. DOI: <https://doi.org/10.1371/journal.pbio.0050061>, PMID: 17341130
- Butts DA, Kanold PO. 2010. The applicability of spike time dependent plasticity to development. *Frontiers in Synaptic Neuroscience* **2**:30. DOI: <https://doi.org/10.3389/fnsyn.2010.00030>, PMID: 21423516
- Cachope R, Mackie K, Triller A, O'Brien J, Pereda AE. 2007. Potentiation of electrical and chemical synaptic transmission mediated by endocannabinoids. *Neuron* **56**:1034–1047. DOI: <https://doi.org/10.1016/j.neuron.2007.11.014>, PMID: 18093525
- Cang J, Kaneko M, Yamada J, Woods G, Stryker MP, Feldheim DA. 2005a. Ephrin-as guide the formation of functional maps in the visual cortex. *Neuron* **48**:577–589. DOI: <https://doi.org/10.1016/j.neuron.2005.10.026>, PMID: 16301175
- Cang J, Rentería RC, Kaneko M, Liu X, Copenhagen DR, Stryker MP. 2005b. Development of precise maps in visual cortex requires patterned spontaneous activity in the retina. *Neuron* **48**:797–809. DOI: <https://doi.org/10.1016/j.neuron.2005.09.015>, PMID: 16337917
- Chistiakova M, Bannon NM, Bazhenov M, Volgushev M. 2014. Heterosynaptic plasticity: multiple mechanisms and multiple roles. *The Neuroscientist : A Review Journal Bringing Neurobiology, Neurology and Psychiatry* **20**: 483–498. DOI: <https://doi.org/10.1177/1073858414529829>, PMID: 24727248
- Cooper LN, Intrator N, Blais BS, Shouval HZ. 2004. *Theory of Cortical Plasticity*. Singapore: World Scientific.

- Cutts CS**, Eglén SJ. 2014. Detecting pairwise correlations in spike trains: an objective comparison of methods and application to the study of retinal waves. *Journal of Neuroscience* **34**:14288–14303. DOI: <https://doi.org/10.1523/JNEUROSCI.2767-14.2014>, PMID: 25339742
- Daoudal G**, Debanne D. 2003. Long-term plasticity of intrinsic excitability: learning rules and mechanisms. *Learning & Memory* **10**:456–465. DOI: <https://doi.org/10.1101/lm.64103>, PMID: 14657257
- Desai NS**, Rutherford LC, Turrigiano GG. 1999. Plasticity in the intrinsic excitability of cortical pyramidal neurons. *Nature Neuroscience* **2**:515–520. DOI: <https://doi.org/10.1038/9165>, PMID: 10448215
- Dornn AL**, Yuan K, Barker AJ, Schreiner CE, Froemke RC. 2010. Developmental sensory experience balances cortical excitation and inhibition. *Nature* **465**:932–936. DOI: <https://doi.org/10.1038/nature09119>, PMID: 20559387
- Etherington SJ**, Williams SR. 2011. Postnatal development of intrinsic and synaptic properties transforms signaling in the layer 5 excitatory neural network of the visual cortex. *Journal of Neuroscience* **31**:9526–9537. DOI: <https://doi.org/10.1523/JNEUROSCI.0458-11.2011>, PMID: 21715617
- Feldheim DA**, O’Leary DD. 2010. Visual map development: bidirectional signaling, bifunctional guidance molecules, and competition. *Cold Spring Harbor Perspectives in Biology* **2**:a001768. DOI: <https://doi.org/10.1101/cshperspect.a001768>, PMID: 20880989
- Feller MB**, Wellis DP, Stellwagen D, Werblin FS, Shatz CJ. 1996. Requirement for cholinergic synaptic transmission in the propagation of spontaneous retinal waves. *Science* **272**:1182–1187. DOI: <https://doi.org/10.1126/science.272.5265.1182>, PMID: 8638165
- Field DJ**. 1994. What is the goal of sensory coding? *Neural Computation* **6**:559–601. DOI: <https://doi.org/10.1162/neco.1994.6.4.559>
- Frye CG**, MacLean JN. 2016. Spontaneous activations follow a common developmental course across primary sensory Areas in mouse neocortex. *Journal of Neurophysiology* **116**:431–437. DOI: <https://doi.org/10.1152/jn.00172.2016>, PMID: 27146981
- Fujimoto S**, Leiwe MN, Sakaguchi R, Muroyama Y, Kobayakawa R, Kobayakawa K, Saito T, Imai T. 2019. Spontaneous activity generated within the olfactory bulb establishes the discrete wiring of mitral cell dendrites. *bioRxiv*. DOI: <https://doi.org/10.1101/625616>
- Gjorgjieva J**, Toyozumi T, Eglén SJ. 2009. Burst-time-dependent plasticity robustly guides ON/OFF segregation in the lateral geniculate nucleus. *PLOS Computational Biology* **5**:e1000618. DOI: <https://doi.org/10.1371/journal.pcbi.1000618>, PMID: 20041207
- Godfrey KB**, Swindale NV. 2014. Modeling development in retinal afferents: retinotopy, segregation, and ephrinA/EphA mutants. *PLOS ONE* **9**:e104670. DOI: <https://doi.org/10.1371/journal.pone.0104670>, PMID: 25122119
- Golshani P**, Gonçalves JT, Khoshkhoo S, Mostany R, Smirnakis S, Portera-Cailliau C. 2009. Internally mediated developmental desynchronization of neocortical network activity. *Journal of Neuroscience* **29**:10890–10899. DOI: <https://doi.org/10.1523/JNEUROSCI.2012-09.2009>, PMID: 19726647
- Goodhill GJ**. 2016. Can molecular gradients wire the brain? *Trends in Neurosciences* **39**:202–211. DOI: <https://doi.org/10.1016/j.tins.2016.01.009>, PMID: 26927836
- Goodhill GJ**, Xu J. 2005. The development of retinotectal maps: a review of models based on molecular gradients. *Network: Computation in Neural Systems* **16**:5–34. DOI: <https://doi.org/10.1080/09548980500254654>, PMID: 16353341
- Gray RM**. 2005. Toeplitz and circulant matrices: a review. *Foundations and Trends in Communications and Information Theory* **2**:155–239. DOI: <https://doi.org/10.1561/0100000006>
- Gribizis A**, Ge X, Daigle TL, Ackman JB, Zeng H, Lee D, Crair MC. 2019. Visual cortex gains independence from peripheral drive before eye opening. *Neuron* **104**:711–723. DOI: <https://doi.org/10.1016/j.neuron.2019.08.015>, PMID: 31561919
- Grimbert F**, Cang J. 2012. New model of retinocollicular mapping predicts the mechanisms of axonal competition and explains the role of reverse molecular signaling during development. *Journal of Neuroscience* **32**:9755–9768. DOI: <https://doi.org/10.1523/JNEUROSCI.6180-11.2012>, PMID: 22787061
- Grubb MS**, Rossi FM, Changeux J-P, Thompson ID. 2003. Abnormal functional organization in the dorsal lateral geniculate nucleus of mice lacking the $\beta 2$ subunit of the nicotinic acetylcholine receptor. *Neuron* **40**:1161–1172. DOI: [https://doi.org/10.1016/S0896-6273\(03\)00789-X](https://doi.org/10.1016/S0896-6273(03)00789-X), PMID: 14687550
- Haas JS**, Zavala B, Landisman CE. 2011. Activity-Dependent Long-Term depression of electrical synapses. *Science* **334**:389–393. DOI: <https://doi.org/10.1126/science.1207502>, PMID: 22021860
- Hanganu IL**, Ben-Ari Y, Khazipov R. 2006. Retinal waves trigger spindle bursts in the neonatal rat visual cortex. *Journal of Neuroscience* **26**:6728–6736. DOI: <https://doi.org/10.1523/JNEUROSCI.0752-06.2006>, PMID: 16793880
- Huberman AD**, Feller MB, Chapman B. 2008. Mechanisms underlying development of visual maps and receptive fields. *Annual Review of Neuroscience* **31**:479–509. DOI: <https://doi.org/10.1146/annurev.neuro.31.060407.125533>, PMID: 18558864
- Ikezoe K**, Tamura H, Kimura F, Fujita I. 2012. Decorrelation of sensory-evoked neuronal responses in rat barrel cortex during postnatal development. *Neuroscience Research* **73**:312–320. DOI: <https://doi.org/10.1016/j.neures.2012.05.009>, PMID: 22677628
- Ji N**. 2017. Adaptive optical fluorescence microscopy. *Nature Methods* **14**:374–380. DOI: <https://doi.org/10.1038/nmeth.4218>, PMID: 28362438
- Kirkby LA**, Sack GS, Firl A, Feller MB. 2013. A role for correlated spontaneous activity in the assembly of neural circuits. *Neuron* **80**:1129–1144. DOI: <https://doi.org/10.1016/j.neuron.2013.10.030>, PMID: 24314725

- Kirkwood A**, Rioult MC, Bear MF. 1996. Experience-dependent modification of synaptic plasticity in visual cortex. *Nature* **381**:526–528. DOI: <https://doi.org/10.1038/381526a0>, PMID: 8632826
- Kirmse K**, Kummer M, Kovalchuk Y, Witte OW, Garaschuk O, Holthoff K. 2015. GABA depolarizes immature neurons and inhibits network activity in the neonatal neocortex *in vivo*. *Nature Communications* **6**:7750. DOI: <https://doi.org/10.1038/ncomms8750>, PMID: 26177896
- Ko H**, Hofer SB, Pichler B, Buchanan KA, Sjöström PJ, Mrsic-Flogel TD. 2011. Functional specificity of local synaptic connections in neocortical networks. *Nature* **473**:87–91. DOI: <https://doi.org/10.1038/nature09880>, PMID: 21478872
- Lee CW**, Eglén SJ, Wong RO. 2002. Segregation of ON and OFF retinogeniculate connectivity directed by patterned spontaneous activity. *Journal of Neurophysiology* **88**:2311–2321. DOI: <https://doi.org/10.1152/jn.00372.2002>, PMID: 12424272
- Leighton AH**, Houwen GJ, Cheyne JE, Maldonado PP, Winter FD, Lohmann C. 2020. Control of spontaneous activity patterns by inhibitory signaling in the developing visual cortex. *bioRxiv*. DOI: <https://doi.org/10.1101/2020.02.21.959262>
- Lombardo J**, Sun J, Harrington MA. 2018. Rapid activity-dependent modulation of the intrinsic excitability through up-regulation of KCNQ/Kv7 channel function in neonatal spinal motoneurons. *PLOS ONE* **13**:e0193948. DOI: <https://doi.org/10.1371/journal.pone.0193948>, PMID: 29579068
- López-Bendito G**. 2018. Development of the thalamocortical interactions: past, present and future. *Neuroscience* **385**:67–74. DOI: <https://doi.org/10.1016/j.neuroscience.2018.06.020>, PMID: 29932982
- Lynch GS**, Dunwiddie T, Gribkoff V. 1977. Heterosynaptic depression: a postsynaptic correlate of long-term potentiation. *Nature* **266**:737–739. DOI: <https://doi.org/10.1038/266737a0>, PMID: 195211
- Mackay DJC**, Miller KD. 1990. Analysis of Linsker's application of Hebbian rules to linear networks. *Network: Computation in Neural Systems* **1**:257–297. DOI: https://doi.org/10.1088/0954-898X_1_3_001
- Miller KD**, Keller JB, Stryker MP. 1989. Ocular dominance column development: analysis and simulation. *Science* **245**:605–615. DOI: <https://doi.org/10.1126/science.2762813>, PMID: 2762813
- Miller KD**. 1994. Models of activity-dependent neural development. *Progress in Brain Research* **102**:303–318. DOI: [https://doi.org/10.1016/S0079-6123\(08\)60548-8](https://doi.org/10.1016/S0079-6123(08)60548-8), PMID: 7800821
- Miller KD**, MacKay DJC. 1994. The role of constraints in hebbian learning. *Neural Computation* **6**:100–126. DOI: <https://doi.org/10.1162/neco.1994.6.1.100>
- Moody WJ**, Bosma MM. 2005. Ion channel development, spontaneous activity, and activity-dependent development in nerve and muscle cells. *Physiological Reviews* **85**:883–941. DOI: <https://doi.org/10.1152/physrev.00017.2004>, PMID: 15987798
- Murata Y**, Colonnese MT. 2020. GABAergic interneurons excite neonatal Hippocampus *in vivo*. *Science Advances* **6**:eaba1430. DOI: <https://doi.org/10.1126/sciadv.aba1430>, PMID: 32582852
- Nakamura Y**, Takahashi T. 2007. Developmental changes in potassium currents at the rat Calyx of held presynaptic terminal. *The Journal of Physiology* **581**:1101–1112. DOI: <https://doi.org/10.1113/jphysiol.2007.128702>, PMID: 17331991
- Naoki H**. 2017. Revisiting chemoaffinity theory: chemotactic implementation of topographic axonal projection. *PLOS Computational Biology* **13**:e1005702. DOI: <https://doi.org/10.1371/journal.pcbi.1005702>, PMID: 28792499
- Niculescu D**, Lohmann C. 2014. Gap junctions in developing thalamic and neocortical neuronal networks. *Cerebral Cortex* **24**:3097–3106. DOI: <https://doi.org/10.1093/cercor/bht175>, PMID: 23843439
- Olshausen BA**, Field DJ. 2004. Sparse coding of sensory inputs. *Current Opinion in Neurobiology* **14**:481–487. DOI: <https://doi.org/10.1016/j.conb.2004.07.007>, PMID: 15321069
- Oswald AM**, Reyes AD. 2008. Maturation of intrinsic and synaptic properties of layer 2/3 pyramidal neurons in mouse auditory cortex. *Journal of Neurophysiology* **99**:2998–3008. DOI: <https://doi.org/10.1152/jn.01160.2007>, PMID: 18417631
- Renden R**, Taschenberger H, Puente N, Rusakov DA, Duvoisin R, Wang LY, Lehre KP, von Gersdorff H. 2005. Glutamate transporter studies reveal the pruning of metabotropic glutamate receptors and absence of AMPA receptor desensitization at mature Calyx of held synapses. *Journal of Neuroscience* **25**:8482–8497. DOI: <https://doi.org/10.1523/JNEUROSCI.1848-05.2005>, PMID: 16162930
- Richter LM**, Gjorgjieva J. 2017. Understanding neural circuit development through theory and models. *Current Opinion in Neurobiology* **46**:39–47. DOI: <https://doi.org/10.1016/j.conb.2017.07.004>, PMID: 28777957
- Rochefort NL**, Garaschuk O, Milos RI, Narushima M, Marandi N, Pichler B, Kovalchuk Y, Konnerth A. 2009. Sparsification of neuronal activity in the visual cortex at eye-opening. *PNAS* **106**:15049–15054. DOI: <https://doi.org/10.1073/pnas.0907660106>, PMID: 19706480
- Sánchez-Aguilera A**, Sánchez-Alonso JL, Vicente-Torres MA, Colino A. 2014. A novel short-term plasticity of intrinsic excitability in the hippocampal CA1 pyramidal cells. *The Journal of Physiology* **592**:2845–2864. DOI: <https://doi.org/10.1113/jphysiol.2014.273185>, PMID: 24756640
- Sejnowski TJ**. 1977. Storing covariance with nonlinearly interacting neurons. *Journal of Mathematical Biology* **4**:303–321. DOI: <https://doi.org/10.1007/BF00275079>, PMID: 925522
- Shen J**, Colonnese MT. 2016. Development of activity in the mouse visual cortex. *Journal of Neuroscience* **36**:12259–12275. DOI: <https://doi.org/10.1523/JNEUROSCI.1903-16.2016>, PMID: 27903733
- Siegel F**, Heimel JA, Peters J, Lohmann C. 2012. Peripheral and central inputs shape network dynamics in the developing visual cortex *in vivo*. *Current Biology* **22**:253–258. DOI: <https://doi.org/10.1016/j.cub.2011.12.026>, PMID: 22264606

- Sjöström PJ**, Turrigiano GG, Nelson SB. 2001. Rate, timing, and cooperativity jointly determine cortical synaptic plasticity. *Neuron* **32**:1149–1164. DOI: [https://doi.org/10.1016/S0896-6273\(01\)00542-6](https://doi.org/10.1016/S0896-6273(01)00542-6), PMID: 11754844
- Smith GB**, Sederberg A, Elyada YM, Van Hooser SD, Kaschube M, Fitzpatrick D. 2015. The development of cortical circuits for motion discrimination. *Nature Neuroscience* **18**:252–261. DOI: <https://doi.org/10.1038/nn.3921>, PMID: 25599224
- Stafford BK**, Sher A, Litke AM, Feldheim DA. 2009. Spatial-temporal patterns of retinal waves underlying activity-dependent refinement of retinofugal projections. *Neuron* **64**:200–212. DOI: <https://doi.org/10.1016/j.neuron.2009.09.021>, PMID: 19874788
- Sun C**, Warland DK, Ballesteros JM, van der List D, Chalupa LM. 2008. Retinal waves in mice lacking the beta2 subunit of the nicotinic acetylcholine receptor. *PNAS* **105**:13638–13643. DOI: <https://doi.org/10.1073/pnas.0807178105>, PMID: 18757739
- Tabak J**, Rinzel J, O'Donovan MJ. 2001. The role of activity-dependent network depression in the expression and self-regulation of spontaneous activity in the developing spinal cord. *The Journal of Neuroscience* **21**:8966–8978. DOI: <https://doi.org/10.1523/JNEUROSCI.21-22-08966.2001>, PMID: 11698607
- Tabak J**, Mascagni M, Bertram R. 2010. Mechanism for the universal pattern of activity in developing neuronal networks. *Journal of Neurophysiology* **103**:2208–2221. DOI: <https://doi.org/10.1152/jn.00857.2009>, PMID: 20164396
- Thompson A**, Gribizis A, Chen C, Crair MC. 2017. Activity-dependent development of visual receptive fields. *Current Opinion in Neurobiology* **42**:136–143. DOI: <https://doi.org/10.1016/j.conb.2016.12.007>, PMID: 28088066
- Tien NW**, Kerschensteiner D. 2018. Homeostatic plasticity in neural development. *Neural Development* **13**:9. DOI: <https://doi.org/10.1186/s13064-018-0105-x>, PMID: 29855353
- Tononi G**, Cirelli C. 2006. Sleep function and synaptic homeostasis. *Sleep Medicine Reviews* **10**:49–62. DOI: <https://doi.org/10.1016/j.smrv.2005.05.002>, PMID: 16376591
- Tremblay R**, Lee S, Rudy B. 2016. GABAergic interneurons in the neocortex: from cellular properties to circuits. *Neuron* **91**:260–292. DOI: <https://doi.org/10.1016/j.neuron.2016.06.033>, PMID: 27477017
- Turrigiano GG**, Leslie KR, Desai NS, Rutherford LC, Nelson SB. 1998. Activity-dependent scaling of quantal amplitude in neocortical neurons. *Nature* **391**:892–896. DOI: <https://doi.org/10.1038/36103>, PMID: 9495341
- Turrigiano GG**, Nelson SB. 2004. Homeostatic plasticity in the developing nervous system. *Nature Reviews Neuroscience* **5**:97–107. DOI: <https://doi.org/10.1038/nrn1327>, PMID: 14735113
- Valeeva G**, Tressard T, Mukhtarov M, Baude A, Khazipov R. 2016. An optogenetic approach for investigation of excitatory and inhibitory network GABA actions in mice expressing Channelrhodopsin-2 in GABAergic neurons. *The Journal of Neuroscience* **36**:5961–5973. DOI: <https://doi.org/10.1523/JNEUROSCI.3482-15.2016>, PMID: 27251618
- Vyazovskiy VV**, Cirelli C, Pfister-Genskow M, Faraguna U, Tononi G. 2008. Molecular and electrophysiological evidence for net synaptic potentiation in wake and depression in sleep. *Nature Neuroscience* **11**:200–208. DOI: <https://doi.org/10.1038/nn2035>, PMID: 18204445
- Wang HC**, Bergles DE. 2015. Spontaneous activity in the developing auditory system. *Cell and Tissue Research* **361**:65–75. DOI: <https://doi.org/10.1007/s00441-014-2007-5>, PMID: 25296716
- Willmore B**, Tolhurst DJ. 2001. Characterizing the sparseness of neural codes. *Network: Computation in Neural Systems* **12**:255–270. DOI: <https://doi.org/10.1080/net.12.3.255.270>, PMID: 11563529
- Willshaw DJ**, von der Malsburg C. 1976. How patterned neural connections can be set up by self-organization. *Proceedings of the Royal Society of London. Series B, Biological Sciences* **194**:431–445. DOI: <https://doi.org/10.1098/rspb.1976.0087>, PMID: 12510
- Winnubst J**, Cheyne JE, Niculescu D, Lohmann C. 2015. Spontaneous activity drives local synaptic plasticity *in vivo*. *Neuron* **87**:399–410. DOI: <https://doi.org/10.1016/j.neuron.2015.06.029>, PMID: 26182421
- Wood KC**, Blackwell JM, Geffen MN. 2017. Cortical inhibitory interneurons control sensory processing. *Current Opinion in Neurobiology* **46**:200–207. DOI: <https://doi.org/10.1016/j.conb.2017.08.018>, PMID: 28938181
- Wosniack ME**. 2021. LH-events. *Software Heritage*. swh:1:rev:b90e189a9e1a4d0cdda097d435fa91b1236f1866. <https://archive.softwareheritage.org/swh:1:dir:efa7beb842340f63b39cebacc246fc0f89dcc72fe;origin=https://github.com/comp-neural-circuits/LH-events;visit=swh:1:snp:2bbe495e9a398f2e628d82ad9638fa97bc3844fc;anchor=swh:1:rev:b90e189a9e1a4d0cdda097d435fa91b1236f1866/>
- Wu YK**, Hengen KB, Turrigiano GG, Gjorgjieva J. 2020. Homeostatic mechanisms regulate distinct aspects of cortical circuit dynamics. *PNAS* **117**:24514–24525. DOI: <https://doi.org/10.1073/pnas.1918368117>, PMID: 32917810
- Xu HP**, Furman M, Mineur YS, Chen H, King SL, Zenisek D, Zhou ZJ, Butts DA, Tian N, Picciotto MR, Crair MC. 2011. An instructive role for patterned spontaneous retinal activity in mouse visual map development. *Neuron* **70**:1115–1127. DOI: <https://doi.org/10.1016/j.neuron.2011.04.028>, PMID: 21689598
- Xu J**, Wu LG. 2005. The decrease in the presynaptic calcium current is a major cause of short-term depression at a calyx-type synapse. *Neuron* **46**:633–645. DOI: <https://doi.org/10.1016/j.neuron.2005.03.024>, PMID: 15944131
- Zenke F**, Agnes EJ, Gerstner W. 2015. Diverse synaptic plasticity mechanisms orchestrated to form and retrieve memories in spiking neural networks. *Nature Communications* **6**:6922. DOI: <https://doi.org/10.1038/ncomms7922>, PMID: 25897632
- Zenke F**, Gerstner W, Ganguli S. 2017. The temporal paradox of hebbian learning and homeostatic plasticity. *Current Opinion in Neurobiology* **43**:166–176. DOI: <https://doi.org/10.1016/j.conb.2017.03.015>, PMID: 28431369

Zylberberg J, DeWeese MR. 2013. Sparse coding models can exhibit decreasing sparseness while learning sparse codes for natural images. *PLoS Computational Biology* **9**:e1003182. DOI: <https://doi.org/10.1371/journal.pcbi.1003182>, PMID: 24009489

Oxytocin shapes spontaneous activity patterns in the developing visual cortex

In Maldonado *et al.* (2021), we investigate the role of the neuromodulator oxytocin in shaping spontaneous activity in the developing cortex by regulating somatostatin interneurons. We find that:

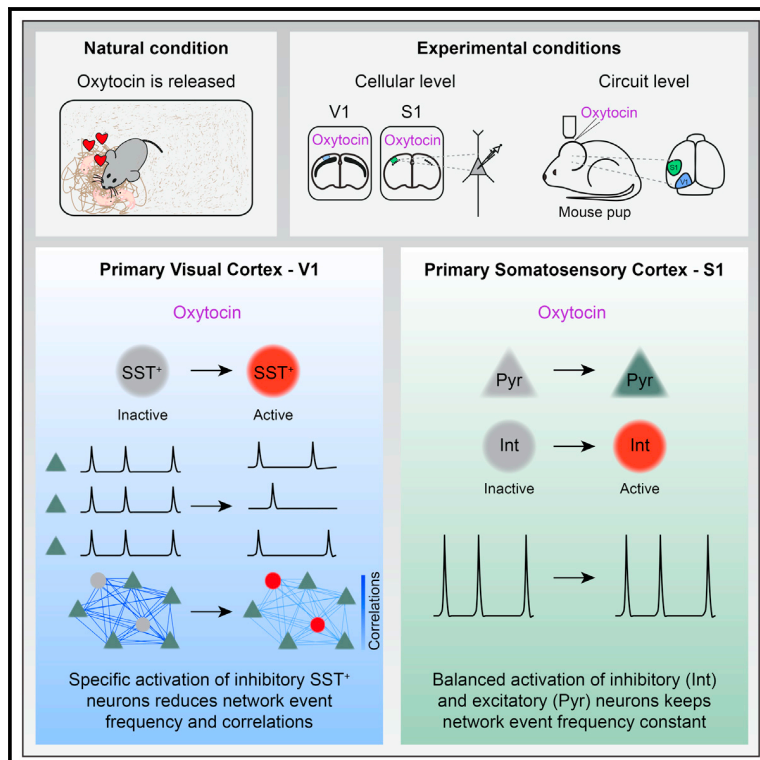
1. Topically applied oxytocin rapidly and strongly decreases the frequency of spontaneous activity in the developing mouse visual cortex.
2. Application of oxytocin furthermore desynchronizes network activity and induces a distance-dependent decrease in neural correlations.
3. Changes in network activity are mediated by the differential expression of the oxytocin receptor across sensory cortices and neuron types.
4. Our model demonstrates that the oxytocin-induced increase of excitability of somatostatin interneurons is sufficient to explain the observed network-level changes in spontaneous activity.

The work was completed in collaboration with Dr. Paloma Maldonado, Prof. Dr. Julijana Gjorgjieva, Prof. Dr. Christian Lohmann, Alvaro Nuno-Perez, and Prof. Dr. Elizabeth Hammock. I contributed to three figures (Fig. 2E-L, Figure 6G-L, and Figure S1C-D) and wrote the first draft for the corresponding portions of the results and the methods. I was also involved throughout the research process through discussions and feedback. The full article was published on January 25th, 2021 in *Current Biology* and is reproduced on the following pages under the Creative Commons Attribution 4.0 International License.

Current Biology

Oxytocin Shapes Spontaneous Activity Patterns in the Developing Visual Cortex by Activating Somatostatin Interneurons

Graphical Abstract



Authors

Paloma P. Maldonado,
Alvaro Nuno-Perez, Jan H. Kirchner,
Elizabeth Hammock,
Julijana Gjorgjieva, Christian Lohmann

Correspondence

c.lohmann@nin.knaw.nl (C.L.)

In Brief

Maldonado et al. uncover oxytocin's role in developing sensory cortices. *In vivo*, they show that oxytocin decreases the frequency and correlations of spontaneous activity patterns in V1 by specifically activating somatostatin⁺ interneurons. In S1, oxytocin increases both excitation and inhibition and does not affect spontaneous activity frequency.

Highlights

- Oxytocin modulates spontaneous activity event patterns in the developing V1
- Oxytocin increases inhibition by activating somatostatin⁺ interneurons
- SST⁺ neuron activity reduces event frequency and correlations, but not amplitude
- In S1, oxytocin increases excitation and inhibition and does not modulate frequency



Article

Oxytocin Shapes Spontaneous Activity Patterns in the Developing Visual Cortex by Activating Somatostatin Interneurons

Paloma P. Maldonado,¹ Alvaro Nuno-Perez,^{1,7} Jan H. Kirchner,^{3,4} Elizabeth Hammock,^{5,6} Julijana Gjorgjieva,^{3,4} and Christian Lohmann^{1,2,8,*}

¹Department of Synapse and Network Development, Netherlands Institute for Neuroscience, 1105 BA Amsterdam, the Netherlands

²Department of Functional Genomics, Center for Neurogenomics and Cognitive Research, VU University Amsterdam, 1081 HV Amsterdam, the Netherlands

³Max Planck Institute for Brain Research, Computation in Neural Circuits, 60438 Frankfurt am Main, Germany

⁴TUM School of Life Sciences, Technical University of Munich, 85354 Freising, Germany

⁵Program in Neuroscience, The Florida State University, Tallahassee, FL 32306, USA

⁶Department of Psychology, The Florida State University, Tallahassee, FL 32306, USA

⁷Present address: The Department of Fundamental Neuroscience, The University of Lausanne, Rue du Bugnon 9, Lausanne 1005, Switzerland

⁸Lead Contact

*Correspondence: p.maldonado@nin.knaw.nl (P.P.M.), alvaro.nunoperez@unil.ch (A.N.-P.), jan.kirchner@brain.mpg.de (J.H.K.), hammock@psy.fsu.edu (E.H.), gjorgjieva@brain.mpg.de (J.G.), c.lohmann@nin.knaw.nl (C.L.)

<https://doi.org/10.1016/j.cub.2020.10.028>

SUMMARY

Spontaneous network activity shapes emerging neuronal circuits during early brain development prior to sensory perception. However, how neuromodulation influences this activity is not fully understood. Here, we report that the neuromodulator oxytocin differentially shapes spontaneous activity patterns across sensory cortices. *In vivo*, oxytocin strongly decreased the frequency and pairwise correlations of spontaneous activity events in the primary visual cortex (V1), but it did not affect the frequency of spontaneous network events in the somatosensory cortex (S1). Patch-clamp recordings in slices and RNAscope showed that oxytocin affects S1 excitatory and inhibitory neurons similarly, whereas in V1, oxytocin targets only inhibitory neurons. Somatostatin-positive (SST⁺) interneurons expressed the oxytocin receptor and were activated by oxytocin in V1. Accordingly, pharmacogenetic silencing of V1 SST⁺ interneurons fully blocked oxytocin's effect on inhibition *in vitro* as well its effect on spontaneous activity patterns *in vivo*. Thus, oxytocin decreases the excitatory/inhibitory (E/I) ratio by recruiting SST⁺ interneurons and modulates specific features of V1 spontaneous activity patterns that are crucial for the wiring and refining of developing sensory circuits.

INTRODUCTION

In the developing brain, neuronal connections form with remarkable precision. First, axons grow to predetermined target areas guided by molecular cues. Subsequently, activity-dependent processes refine synaptic connections:^{1–3} already before the senses become active, spontaneous activity drives synaptic refinement to prepare the brain for interacting with the outside world. Finally, circuits adapt to the prevalent environmental conditions through sensory-experience-driven plasticity mechanisms.

Spontaneous activity is expressed in specific patterns, and these patterns are crucial for the appropriate wiring of neurons. For example, in the developing retina, waves of spontaneous activity travel at specific speeds, in various directions, and with different wave front shapes.^{4,5} Retinal waves drive highly structured activity patterns in the central visual system, including the primary visual cortex.^{6–8} Perturbing these activity patterns leads to miswiring of the central visual system.^{9–11}

During the period when synaptic connections are shaped by spontaneous activity, neuromodulators play an important role in the development of cortical circuits.^{12–14} One of them, oxytocin, is particularly prominently expressed in sensory cortices during the first 2 postnatal weeks and decreases thereafter until the end of the 3rd postnatal week, when it reaches adult levels.¹⁵ Similarly, oxytocin receptor ligand binding, immunolabeling, and mRNA expression in sensory cortices peak during the 2nd postnatal week and decrease thereafter.^{15–17} Thus, oxytocin is most likely required for the development of sensory circuits during the 1st postnatal weeks in addition to its roles in social sensory processing in adults, where oxytocin increases the sensitivity of auditory cortex neurons to pup calls,¹⁸ modulates odor processing in the olfactory and accessory systems,¹⁹ and shapes social sensory perception.^{20,21} Oxytocin modulates synaptic transmission in the developing forebrain. For example, oxytocin is required for cross-modal, experience-driven synaptic plasticity in the somatosensory cortex during the first 2 weeks of life.¹⁵ Moreover, oxytocin triggers a temporary switch of



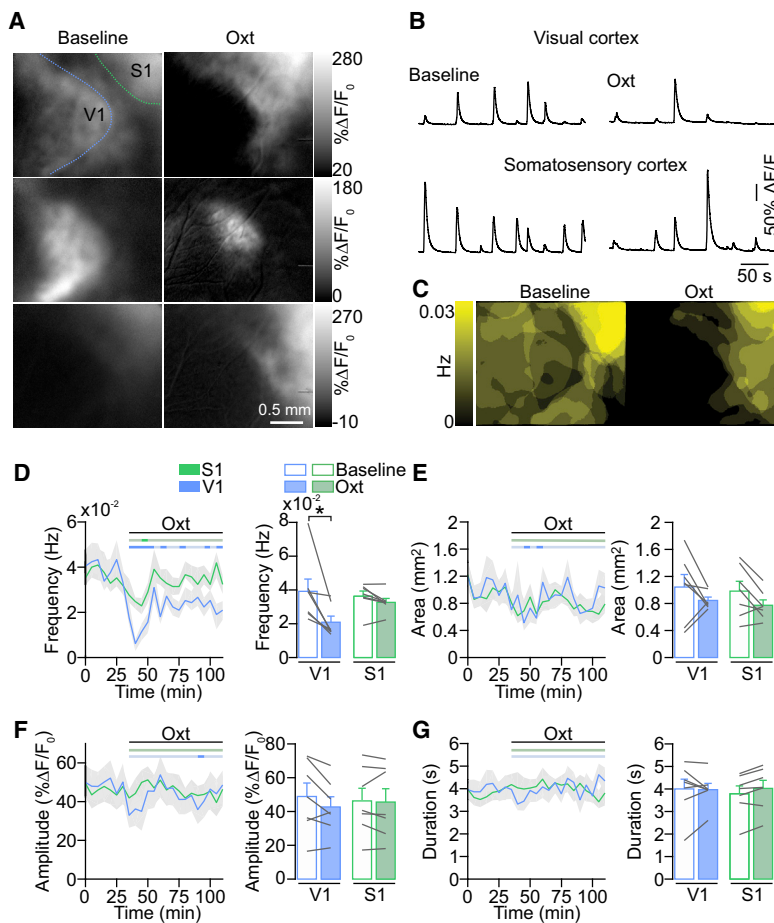


Figure 1. Oxytocin Affects Spontaneous Network Events Differentially across Sensory Cortices

(A) Wide-field calcium imaging of spontaneous activity in V1 and S1 before eye opening. (Left) Single-frame images depict network events activating V1 and/or S1 during baseline recordings before oxytocin application. (Right) Network events after oxytocin (Oxt) application are shown. (B) Traces show fluorescent changes in V1 and S1 before and after oxytocin application.

(C) Superimposition of all network events detected during a 5-min baseline recording (left) and after oxytocin application (right). Color code indicates the frequency of the detected events. V1 activity is strongly reduced.

(D) Network event frequency in V1 and S1 during baseline and after oxytocin application. Time courses represent 5-min averages. The horizontal bars above the line plots indicate the time points when the values for each time bin differed significantly from baseline (dark shades; paired two-tailed t test; $p < 0.05$; without multi-measurement correction). * $p = 0.016$ ($n = 7$ animals; Wilcoxon test).

(E) Network event area.

(F) Network event amplitude.

(G) Network event duration.

Data are represented as mean \pm SEM. See also Figure S6.

hippocampal GABA receptor action from excitatory to inhibitory.^{12,22} However, it has been unclear whether spontaneous activity patterns, which drive synaptic plasticity before experience-driven refinement occurs,²³ are regulated by oxytocin as well.

Here, we asked whether oxytocin signaling shapes neuronal activity patterns in the primary visual (V1) and somatosensory cortices (S1) during the 2nd postnatal week. We found that, while in S1, oxytocin activates inhibitory and excitatory neurons similarly and does not affect the frequency of network activity, in V1, oxytocin recruits specifically somatostatin-expressing (SST⁺) interneurons to control network activity frequency and correlation, properties known to determine the refinement of synaptic connections in V1 prior to eye opening.

RESULTS

Oxytocin Modulates Spontaneous Cortical Activity Differentially across Sensory Areas

To study the role of the neuromodulator oxytocin in developing sensory cortices, we first asked whether oxytocin receptor activation modulates large-scale spontaneous activity patterns. We used *in utero* electroporation to express the calcium sensor GCaMP6s in layer 2/3 pyramidal cells across V1, higher visual areas, and the barrel cortex. Then, we performed wide-field

in vivo calcium imaging in lightly anesthetized pups between postnatal days (P) 9 and 13. We observed spontaneous network activity in V1, S1, and higher visual areas (Figures 1A and 1B). Frequently, network events were confined to individual sensory regions but sometimes occurred across the entire field of view. After topical application of oxytocin (1 μ M) onto the cortical surface (for details, see STAR Methods), the occurrence of network events was strongly decreased in V1 but only modestly changed in S1 (Figures 1A–1D). Control application of cortex buffer without oxytocin did not change the frequency of calcium events (V1 mean frequency before cortex buffer 0.042 ± 0.002 Hz; after 0.044 ± 0.004 Hz; $p > 0.05$; $n = 4$; Wilcoxon test. S1 mean frequency before cortex buffer 0.042 ± 0.003 Hz; after 0.044 ± 0.004 Hz; $p > 0.05$; $n = 4$; Wilcoxon test). Surprisingly, the response of V1 and S1 differed significantly (percentage of change V1: $-43.5\% \pm 7.9\%$; S1: $-7.9\% \pm 5.2\%$; $p = 0.0026$; $n = 7$; unpaired two-tailed t test). Network event area, amplitude, or duration was not affected (Figures 1E–1G).

Oxytocin Desynchronizes Spontaneous V1 Network Activity

To evaluate how oxytocin modulates the activity of individual neurons in the developing cortical network, we performed *in vivo* two-photon calcium imaging in V1 of lightly anesthetized neonatal mice. Layer 2/3 cells were labeled with the calcium indicator Oregon Green BAPTA-1 (OGB-1) by bolus loading.²⁴ Oxytocin application decreased the frequency of calcium events transiently (Figures 2A–2C) without affecting their amplitude (Figure 2D), in line with our wide-field experiments. In control experiments, where we applied cortex buffer without oxytocin, frequency and amplitude were unaffected (Figures S1A and S1B).

Because the correlational structure of spontaneous network activity determines its role in network refinement,²⁵ we also investigated whether oxytocin affected the pairwise correlations between spontaneously active neurons. We observed that oxytocin application decreased the mean Pearson correlation coefficients across pairs of neurons (Figures 2E and 2F), whereas cortex buffer applications did not affect such correlations (Figures 2E and 2F). Next, we explored changes in correlations at the level of individual neurons after oxytocin application in more detail. We plotted pairwise correlations for all experiments during baseline against the correlations after oxytocin or cortex buffer application (Figures S1C and S1D). Again, we observed that oxytocin, but not cortex buffer application, strongly decreased correlations across the entire population. There were essentially no neuronal pairs that showed increased correlations (Figure S1C). We further found that oxytocin had a subtractive effect on neuronal correlations (Figures 2G and 2H), such that more distal pairs of neurons were proportionally decorrelated more strongly by oxytocin than nearby neuronal pairs (Figures 2I and 2J). Finally, we investigated whether the changes in correlations between all neurons occurred uniformly or whether specific pairs of neurons underwent changes in their correlations. To address this question, we first computed the correlation matrices at different time points (Figure 2K). Interestingly, we saw that, during late oxytocin, when the frequency of calcium events had returned to baseline (mean baseline: 0.032 ± 0.004 Hz; mean 125–135 min: 0.027 ± 0.003 Hz; $p = 0.14$; paired two-tailed t test), the correlation matrices exhibited sustained structural differences in the correlational structure of subsets of cells (Figure 2K, inset). To quantify these differences, we computed the mean squared distance (MSD) between the baseline matrix and the matrices computed at varying time points and found that networks treated with oxytocin exhibited a sustained higher distance compared to baseline ($p = 0.038$, repeated-measures one-way ANOVA; mean baseline: 0.1 ± 0.04 ; mean 60–70 min: 6.36 ± 1.56 , $p = 0.007$; mean 90–100 min: 4.52 ± 1.12 , $p = 0.008$; mean 125–135 min: 2.94 ± 0.6 , $p = 0.009$; post hoc paired two-tailed t test). Conversely, the MSD was unchanged with cortex buffer application ($p = 0.19$; repeated-measures one-way ANOVA; Figure 2L). These oxytocin-induced changes in network activity patterns may reflect differences in functional connectivity between the imaged neurons or their shared inputs, because response correlations are indicative of strong synaptic connections in the adult and probably common feedforward inputs in the developing visual cortex.^{26,27}

Oxytocin Affects the E/I Ratio Differentially across Sensory Areas

To investigate whether the differential modulation of V1 and S1 by oxytocin as described above (Figure 1) can be explained by differences in the distribution of the oxytocin receptor in these areas, we used RNAscope to detect *Oxtr*, *Sc17a7* (coding for VGLUT1), and *Gad1* mRNA in the cortex at P10. We found that *Oxtr* was expressed in V1 as well as in S1 (Figure 3). However, in V1, *Oxtr* co-localized almost exclusively with the *Gad1* signal (Figures 3B–3D), whereas in S1, the *Oxtr* signal co-localized with both the VGLUT1 and *Gad1* signal (Figures 3F–3H). These observations suggested that differences between V1 and S1 in

oxytocin receptor expression on the cellular level could explain oxytocin's differential effect in these areas. To test this idea functionally, we examined how oxytocin regulated excitatory and inhibitory synaptic transmission in V1 and S1. Whole-cell patch-clamp recordings of layer 2/3 pyramidal neurons in slices from V1 showed that oxytocin affected neither the frequency nor the amplitude of spontaneous excitatory postsynaptic currents (sEPSCs) (Figures 4A–4C). Next, we measured spontaneous inhibitory postsynaptic currents (sIPSCs) at the reversal potential of glutamate-receptor-mediated currents. We found that the frequency of sIPSCs, in contrast to that of sEPSCs, was strongly increased after oxytocin bath application (Figures 4D and 4E). The amplitude of sIPSCs was unaffected (Figure 4F). To test whether this increase in frequency was mediated by the specific activation of the oxytocin and not the vasopressin 1A receptor,²⁸ which can be activated by oxytocin as well,²⁹ we blocked the oxytocin receptor using its specific antagonist OTA.³⁰ OTA prevented the oxytocin-mediated increase in sIPSC frequency entirely (fold-change oxytocin only, Figure 4E: 4.95 ± 1.53 ; oxytocin + OTA, Figure S2: 0.98 ± 0.32 ; $p = 0.012$; unpaired two-tailed Mann-Whitney test), demonstrating that this effect was mediated by the oxytocin receptor. Thus, activation of the oxytocin receptor increased the inhibitory tone in V1 dramatically but did not affect excitatory synaptic transmission.

In contrast to V1, in S1, oxytocin bath application increased sEPSC frequency in layer 2/3 pyramidal cells (Figures 4H and 4I). Again, sEPSC amplitude was unaffected (Figure 4J). The frequency of sIPSCs was increased but less pronounced than in V1 (Figures 4K and 4L); amplitudes were unaffected (Figure 4M). Thus, oxytocin shifted the E/I ratio in V1 toward inhibition (Figure 4G; $p < 0.001$; repeated-measurement two-way ANOVA) but did not affect E/I significantly in S1 (Figure 4N). These experiments suggested that differences in the magnitude of inhibitory versus excitatory synaptic activity modulation accounted for the differences in the effect of oxytocin on spontaneous network activity in V1 versus S1.

Oxytocin Targets SST⁺ Interneurons in the Developing V1

Because we observed that oxytocin shaped spontaneous activity patterns effectively in V1, but not in S1, we focused next on the cellular mechanism of oxytocin-mediated facilitation of inhibition in V1. First, we measured miniature IPSCs (mIPSCs) before and after oxytocin bath application and found that mIPSC frequency and amplitude were unaffected by oxytocin (Figures 5A–5C). This indicated that the number of inhibitory synapses, the density of postsynaptic receptors, or changes in the presynaptic release machinery could not explain the increase in sIPSC frequency described above.

To search for alternative causes of the increased inhibitory activity, we performed voltage-clamp recordings in inhibitory interneurons. We used two mouse lines expressing TdTomato to target inhibitory neurons in general (GAD2-Cre;Rosa26-TdTomato) or somatostatin-expressing interneurons specifically (SST-Cre;Rosa26-TdTomato). We focused on SST⁺ interneurons for four reasons: (1) RNA sequencing (RNA-seq) data in adulthood showed that V1 oxytocin receptors are expressed primarily in SST⁺ interneurons (Figure S3A; Allen Brain Atlas data portal: <http://casestudies.brain-map.org/celltax>).³¹ (2) We found

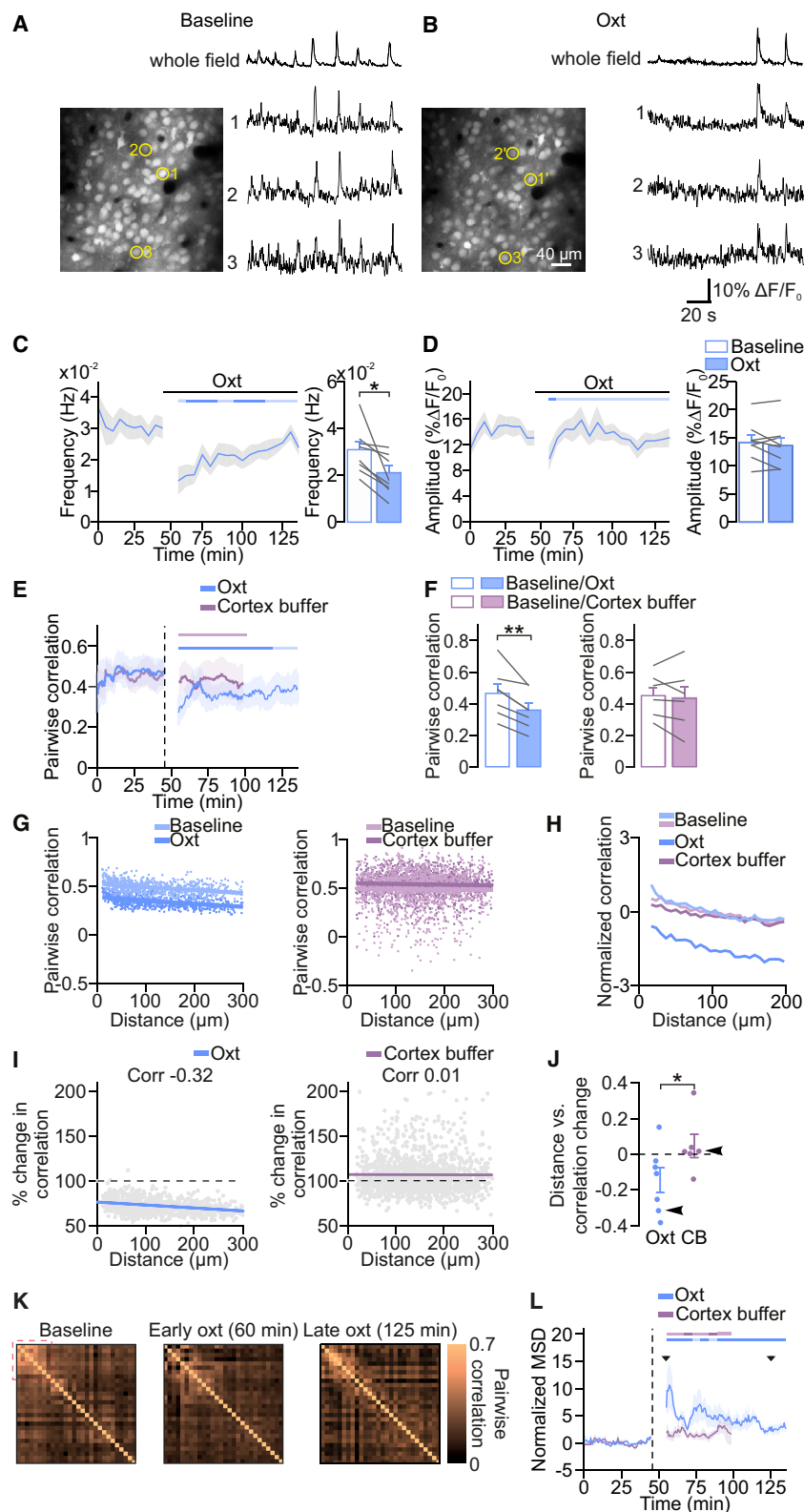


Figure 2. Oxytocin Desynchronizes Network Activity in V1

(A and B) V1 network activity before and after oxytocin application. (Left) Layer 2/3 neurons labeled with the calcium indicator Oregon Green-BAPTA 1 are shown. Traces show fluorescent changes of three example neurons and the average activity across all cells.

(C) Network event frequency during baseline and after oxytocin application. Imaging resumed approximately 10 min after oxytocin application. The frequency of network events was reduced after oxytocin application. The horizontal bar indicates significant deviations from baseline as in Figure 1 (dark shades; paired two-tailed t test; $p < 0.05$; without multi-measurement correction). * $p = 0.015$ ($n = 8$ animals; paired two-tailed t test).

(D) Network event amplitude during baseline and after oxytocin application.

(E) Time course of pairwise Pearson correlation coefficients before and after oxytocin and cortex buffer application. Dashed vertical line indicates the time point of oxytocin or cortex buffer application. Time course represents averages of sliding 7-min window (for details see STAR Methods). The horizontal bar indicates significant deviations from baseline as in Figure 1 (dark shades; paired two-tailed t test; $p < 0.05$; without multi-measurement correction).

(F) Mean correlations after oxytocin or cortex buffer control applications. ** $p = 0.003$ ($n = 7$ for oxytocin; $n = 6$ for cortex buffer; paired two-tailed t test).

(G) Pairwise correlations plotted against interneuronal distance for an example of oxytocin (left) and cortex buffer (right) conditions.

(H) Mean pairwise correlations in oxytocin and cortex buffer condition. Note that baseline condition and cortex buffer display the same profile.

(I) Change in pairwise correlations plotted against interneuronal distance for an example of oxytocin (left) and cortex buffer (right) conditions. Dashed lines indicate zero change in correlations. Colored lines indicate linear fits (left, $p < 10^{-10}$; right, $p = 0.47$; paired two-tailed t test).

(J) Pearson correlation coefficients between pairwise distances and percentages of change in correlations for all animals in oxytocin and cortex buffer condition. Arrowheads indicate the examples shown in (I). * $p = 0.037$ ($n = 7$ for oxytocin; $n = 6$ for cortex buffer; unpaired two-tailed t test).

(K) Correlation matrices computed baseline, early oxytocin (60 min), and late oxytocin (125 min). Red dotted square indicates an example of a subgroup of neurons that undergo structural changes.

(L) Normalized mean squared distances (MSDs) between the baseline matrix and the correlation matrices computed from a sliding 7-min window (see STAR Methods for details) as function of time for oxytocin and cortex buffer conditions.

Data are represented as mean \pm SEM. See also Figure S1.

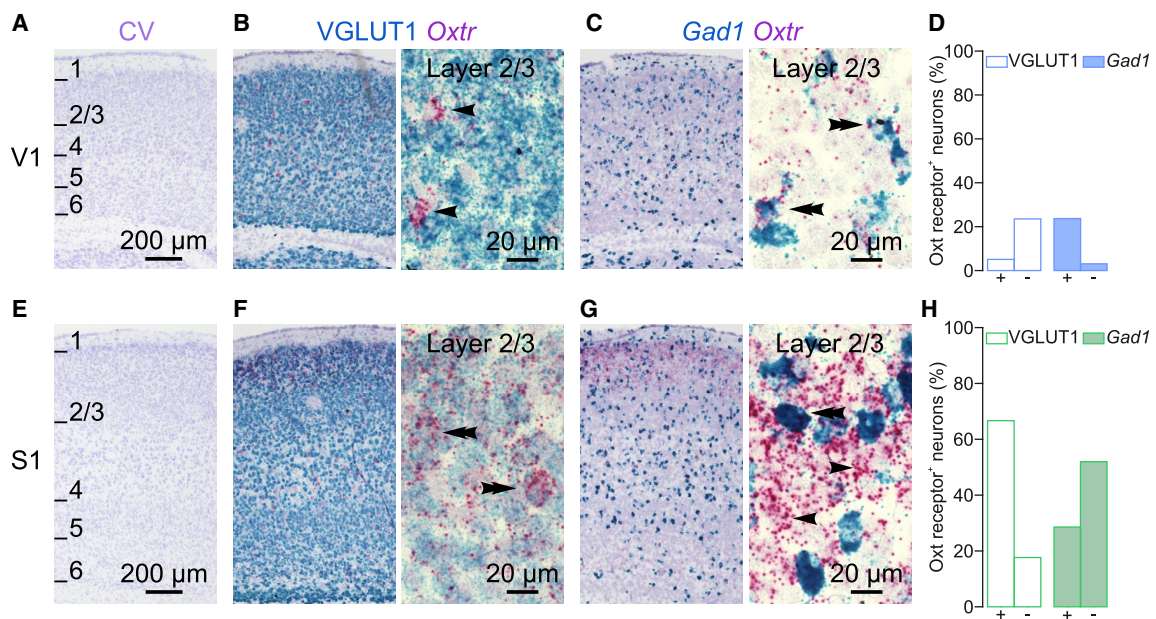


Figure 3. Oxytocin Receptor mRNA Is Differentially Expressed across Sensory Cortices

(A) Cresyl violet Nissl staining of a sagittal section from V1 at low magnification. Numbers indicate cortical layers. (B) Dual-color RNAscope staining of VGLUT1 and *Oxt* mRNA in a V1 sagittal section. Left: low magnification is shown. Right: high magnification is shown. Note that the *Oxt* signal was largely non-overlapping with the VGLUT1 signal (arrowheads indicate VGLUT1⁻/*Oxt*⁺ neurons). (C) Dual-color RNAscope staining of *Gad1* and *Oxt* mRNA in a V1 sagittal section. Left: low magnification is shown. Right: high magnification is shown; note that the *Oxt* signal co-localized with the *Gad1* signal (double arrowhead *Gad1*⁺/*Oxt*⁺) and not with *Gad1*⁻ neurons. (D) Quantification. (E) Cresyl violet Nissl staining of a sagittal section from S1 (same section as in A) at low magnification. Numbers indicate cortical layers. (F) Dual-color RNAscope staining of VGLUT1 and *Oxt* mRNA in an S1 sagittal section. Left: low magnification is shown. Right: high magnification is shown; note the superposition of the two signals (double arrowheads, VGLUT1⁺/*Oxt*⁺). (G) Dual-color RNAscope staining of *Gad1* and *Oxt* mRNA in an S1 sagittal section. Left: low magnification is shown. Right: high magnification is shown; note that the *Oxt* signal co-localized with both *Gad1*⁺ and *Gad1*⁻ signal (double arrowheads indicate *Gad1*⁺/*Oxt*⁺; arrowhead indicates *Gad1*⁻/*Oxt*⁺ neuron). (H) Quantification.

here that, already at P10, oxytocin receptor mRNA is expressed almost exclusively in SST⁺ interneurons in layer 2/3 of V1 (Figure 5D). (3) Decreases in network correlations similar to those described above can be induced by SST⁺ interneuron-mediated lateral inhibition.^{32,33} (4) We observed here that the rise rate of V1 and S1 sIPSCs increased in response to oxytocin application (Figure S3B). Because the sIPSC rise rate is larger for synapses that are located distally in the dendritic tree, this result indicated that oxytocin preferentially increased the frequency of inhibitory inputs at distal dendrites, which receive the majority of SST⁺ interneuron inputs.³⁴

Therefore, we investigated the effect of oxytocin on SST⁺ interneurons. We recorded from SST⁺ neurons in voltage-clamp mode at -60 mV and blocked NMDA, AMPA, and GABA_A receptor-mediated currents using D-AP5, NBQX, and SR95531, respectively, to prevent oxytocin-mediated network effects. In this configuration, we recorded oxytocin-mediated inward currents in almost all SST⁺ neurons (83%; amplitude: -27 ± 16 pA; Figures 5E–5G). Oxytocin did not trigger inward currents in any of the SST⁻ neurons in slices from the same SST-Cre;Rosa26-TdTomato mice. We concluded that oxytocin triggered depolarizing inward currents specifically in SST⁺ interneurons. Accordingly, we observed oxytocin induced inward currents in 29% of GAD2⁺ interneurons (Figure 5G), which is similar to the

proportion of SST⁺ neurons within the entire population of V1 interneurons (23%).³⁵

Together, these results indicated that oxytocin mediated the increase in inhibitory synaptic activity in V1 through activation of SST⁺ interneurons. To test this idea directly, we asked whether specifically downregulating SST⁺ interneurons might prevent the oxytocin-induced increase in overall inhibition (Figure 5H). We performed voltage-clamp recordings of layer 2/3 neurons in acute slices from V1 of transgenic neonatal mice where SST⁺ interneurons expressed inhibitory designer receptors activated by designer drugs (iDREADDs) (SSTCre;GiDreadd). Bath application of CNO, the activator of iDREADDs, did not affect the baseline frequency of sIPSCs (Figures 5I and 5J), suggesting that SST⁺ interneurons were only sparsely active in our slice preparation. Then, we applied oxytocin and found that it did not increase sIPSC frequency in the presence of CNO (Figures 5I and 5J), in contrast to our previous results in slices from wild-type (WT) mice (Figure 4E; fold-change WT: 4.95 ± 1.53; iDREADD: 0.95 ± 0.07; p < 0.0001; Mann-Whitney test). Additional control experiments showed that oxytocin did increase the frequency of sIPSCs in neurons from iDREADD-expressing animals in the absence of CNO, but not their amplitude (Figures 5J, inset; S4A; and S4B), and that CNO by itself did not change the sIPSC frequency (Figures S4C and S4D). These

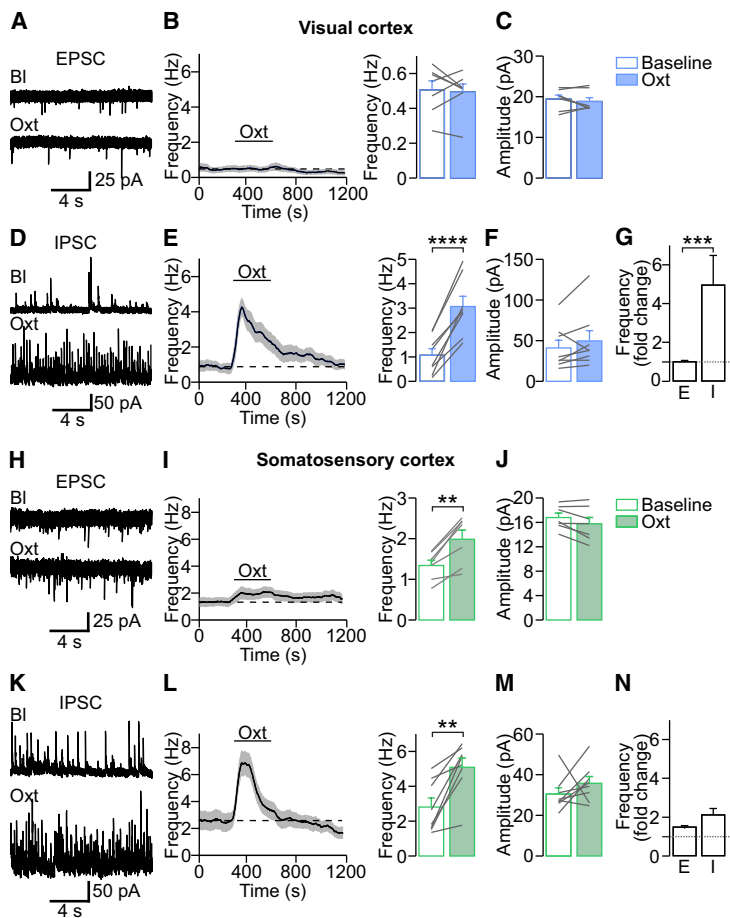


Figure 4. Oxytocin Affects Synaptic Activity Differentially across Sensory Cortices

(A) Voltage-clamp recordings of spontaneous excitatory postsynaptic currents (sEPSCs) during baseline (BI) and after oxytocin bath application in acute visual cortex slices. (B) Frequency of sEPSCs before, during, and after oxytocin application. In the visual cortex, oxytocin did not affect EPSC frequency. $p > 0.05$ ($n = 7$ cells; paired two-tailed t test). (C) Oxytocin did not affect sEPSC amplitude. $p > 0.05$ ($n = 7$ cells; paired two-tailed t test). (D) Spontaneous inhibitory postsynaptic currents (sIPSCs) before and after oxytocin application. (E) Oxytocin led to a strong increase in sIPSCs. $****p = 8.2 \times 10^{-5}$ ($n = 8$ cells; paired two-tailed t test). (F) Oxytocin did not affect the amplitude of sIPSCs. $p > 0.05$ ($n = 8$ cells; paired two-tailed t test). (G) In the visual cortex, oxytocin led to a 5 times increase of sIPSCs, but sEPSCs were unaffected. $***p = 0.0003$ ($n = 7$ and $n = 8$ cells for V1 sEPSCs and sIPSCs, respectively; Mann-Whitney test). (H) Voltage-clamp recordings of sEPSCs before and after oxytocin bath application in somatosensory cortex slices. (I) Application of oxytocin increased the frequency of sEPSCs in the somatosensory cortex slightly. $**p = 0.0014$ ($n = 7$; paired two-tailed t test). (J) Oxytocin did not affect the amplitude of sEPSCs. $p > 0.05$ ($n = 7$ cells; paired two-tailed t test). (K) sIPSCs before and after oxytocin application. (L) Oxytocin led to a transient increase in sIPSCs. $**p = 0.002$ ($n = 8$ cells; paired two-tailed t test). (M) Oxytocin did not affect the amplitude of sIPSCs. $p > 0.05$ ($n = 8$ cells; paired two-tailed t test). (N) In the somatosensory cortex, oxytocin led to similar increases in sIPSC and sEPSC frequency. $p = 0.11$ ($n = 7$ and $n = 8$ cells for S1 sEPSCs and sIPSCs, respectively; unpaired two-tailed t test). Data are represented as mean \pm SEM. See also Figure S2.

results showed that activation of SST⁺ interneurons is required for the oxytocin-induced increase in inhibition.

Oxytocin Enhances SST⁺ Neuron Excitability

Our results suggested that oxytocin triggered inward currents in SST⁺ interneurons (Figures 5E–5G) and that oxytocin-dependent enhancement of SST⁺ interneuron firing mediated its effect on network activity (Figures 5H–5J). Therefore, we investigated next whether and how oxytocin-induced inward currents enhanced SST⁺ neuron firing. In current-clamp mode, we injected a constant current to set the membrane potential of V1 layer 2/3 SST⁺ interneurons to -60 mV in the presence of the transmitter receptor blockers D-AP5, NBQX, and SR95531. Then, we applied oxytocin while keeping the holding current constant. We observed that oxytocin induced a depolarization of 4.5 ± 0.4 mV (Figure 6A), which exhibited the same transient temporal profile as the sIPSC frequency increase shown in Figure 4E. Current-clamp recordings (Figure 6B) revealed an increase in the firing rate of SST⁺ interneurons after oxytocin application (Figure 6C). We further studied how oxytocin affected the action potential (AP) properties of SST⁺ interneurons. Oxytocin (1) increased the AP amplitude and overshoot (Figures 6D and S5A; $+2.63 \pm 0.78$ mV and $+2.01 \pm 0.93$ mV, respectively), (2) broadened the AP width ($+0.18 \pm 0.03$ ms at half-maximum; Figures 6D and 6E), and (3) decreased the time required to generate

an AP from the onset of current injection (-1.97 ± 0.32 ms; Figure 6F). In addition, oxytocin modulated AP kinetics as it decreased the maximal speed of voltage change (dV/dt; Figures S5B and S5C). Thus, oxytocin increased the firing capacity and AP properties of V1 layer 2/3 SST⁺ neurons, most likely by depolarizing their resting membrane potential, as described for PV⁺ interneurons in the hippocampus.³⁶ Knowing how oxytocin affects SST⁺ interneuron activity, we used this information to better understand how oxytocin generated the observed distance-dependent change in correlations. We implemented a recurrent spiking neural network based on a multi-layer model of the thalamocortical system (Figure 6G).³⁷ To mimic the effect of oxytocin, we increased the resting membrane potential of 25% of the inhibitory neurons, corresponding to the population of SST⁺ interneurons (Figure 6H). This elevation in membrane potential increased the firing rate of SST⁺ interneurons for identical current injections (Figure 6I) similarly as observed in our data (Figure 6C). Consequently, in the simulated network, firing of excitatory neurons was strongly suppressed. Inhibitory neurons fired slightly less as well, because their excitatory inputs were largely diminished (Figure 6J). In addition, oxytocin strongly decreased the temporal synchronization of excitatory neurons (Figures 6K and 6L), generating a comparable decrease of correlations over distance as in our experimental data (Figures 2G–2J). This result supported the idea that the increased inhibitory drive produced by

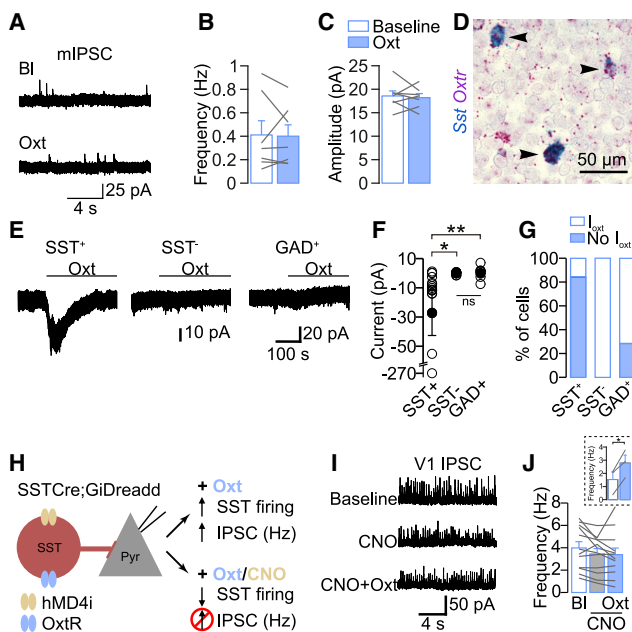


Figure 5. SST⁺ Interneurons Mediate the Oxytocin-Induced Increase in Inhibitory Synaptic Activity in V1

(A) Voltage-clamp recordings of spontaneous miniature synaptic excitatory postsynaptic currents (mIPSCs) in the presence of tetrodotoxin (TTX) (0.5 μ M) before and after oxytocin bath application in V1 slices.

(B) The frequency of mIPSCs was not affected by oxytocin. $p > 0.05$ ($n = 7$ cells; paired two-tailed t test).

(C) The amplitude of mIPSCs was not affected by oxytocin. $p > 0.05$ ($n = 7$ cells; paired two-tailed t test).

(D) V1 *Oxtr* and *Sst* mRNA transcripts. Note the superposition of the two signals (arrowhead: *Sst*⁺/*Oxtr*⁺ neurons: 93%; *Sst*⁻/*Oxtr*⁺ neurons: 2%).

(E) Examples of voltage-clamp recordings at holding potential of -60 mV from a somatostatin-expressing neuron (SST⁺) (SST-Cre;Rosa26-TdTomato), an unlabeled neuron (SST⁻), and a GAD2⁺ neuron (GAD2-Cre;Rosa26-TdTomato) before and after oxytocin application. Oxytocin induced an inward current in the SST⁺ neuron, but not in the unlabeled (most likely excitatory) neuron or in the GAD2⁺ neuron.

(F) Group data of oxytocin-induced inward currents: SST⁺ $n = 17$ cells; SST⁻ $n = 7$ cells; and GAD2⁺ $n = 7$ cells. * $p = 0.021$; ** $p = 0.0044$. Kruskal-Wallis test, followed by a Dunn test.

(G) Percentage of cells with oxytocin-induced inward currents. Almost all SST⁺ neurons show oxytocin-mediated currents (14/17 cells) but none of the SST⁻ neurons (0/7 cells) and a fraction of GAD2⁺ cells (2/7 cells).

(H) Schematic representation of the experimental paradigm: pyramidal neurons in slices from a transgenic mouse expressing inhibitory DREADDs specifically in SST⁺ interneurons (SST-Cre;Rosa26-Gi-hMD4i) were recorded in voltage-clamp mode. Oxytocin was applied while SST⁺ neuron activity was suppressed by CNO to test whether SST⁺ activation is required for the oxytocin-induced increase in inhibitory synaptic activity.

(I) Example recordings of sIPSCs in baseline condition, in the presence of CNO alone, and after bath application of oxytocin in the presence of CNO.

(J) Oxytocin did not increase sIPSC frequency in the presence of CNO. $p > 0.05$ ($n = 12$ cells; repeated-measurements one-way ANOVA). Inset: sIPSC frequency is shown. Oxytocin led to an increase in the frequency in the absence of CNO. * $p = 0.032$ ($n = 3$ cells; paired two-tailed t test).

Data are represented as mean \pm SEM. See also Figures S3 and S4.

oxytocin is sufficient to generate the here-observed effects of oxytocin applications on spontaneous activity patterns, including the distance-dependent changes in interneuronal correlations.

Activation of SST⁺ Interneurons Is Required for Oxytocin-Mediated Modulation of Spontaneous Activity Patterns

Finally, we asked whether the oxytocin-mediated decrease in the frequency of spontaneous network activity was the result of the activation of oxytocin receptors expressed in SST⁺ interneurons *in vivo*. We specifically inactivated SST⁺ interneurons by using a Cre-dependent inhibitory DREADD delivered by virus injection, which results in 80% of the SST⁺ interneurons expressing the hM4Di-DREADD construct.³³ We showed previously that bath application of clozapine *in vitro* reduced the excitability of SST⁺ interneurons,³³ replicating previous findings that hM4Di-DREADD activation reduces the excitability of developing layer 2/3 neurons.³⁸ We performed *in vivo* wide-field calcium imaging to monitor spontaneous network activity in V1 and then activated the iDREADD receptor by injecting clozapine subcutaneously (Figure 7A). 5 min after clozapine injection, oxytocin was applied topically (Figures 7A and 7B). In this condition, oxytocin failed to decrease the frequency of spontaneous network events compared with oxytocin application alone (Figure 7C, % of change clozapine + oxytocin: $-18.1 \pm 10.5\%$; Figure 1D, % of change oxytocin: $-49.2 \pm 6.2\%$; $p = 0.023$; unpaired two-tailed t test). Area, amplitude, and duration were not affected either (Figures 7D–7F). Therefore, SST⁺ neurons are required for the inhibitory effect of exogenous oxytocin on the frequency of spontaneous activity in the developing visual cortex.

We demonstrated here that oxytocin receptor activation can modulate spontaneous activity patterns by specifically activating SST⁺ interneurons; however, the source of oxytocin was exogenous. To evaluate whether endogenous oxytocin indeed modulates spontaneous activity patterns under physiological conditions, we performed wide-field *in vivo* calcium imaging recordings in awake animals, when SST⁺ interneurons are intrinsically active (SST⁺ interneurons are largely silent under anesthesia).³² When we blocked oxytocin receptors, we observed a small but significant increase in the frequency of calcium events (Figure 7G), whereas the amplitude remained unchanged (Figure 7H), as predicted based on our results after topical application of exogenous oxytocin. This result suggested that the oxytocin receptor is activated by its endogenous ligand and modulates spontaneous activity patterns. Finally, we verified that focal oxytocin application modulates spontaneous activity in the awake condition as well. As in anesthetized animals, we found that the frequency of network events was decreased although their amplitude remained unaffected (mean baseline frequency: 0.047 ± 0.007 ; mean oxytocin frequency: 0.036 ± 0.005 ; $p = 0.043$; paired two-tailed t test; $n = 6$ animals).

DISCUSSION

In adults, oxytocin is a potent modulator of brain activity and behavior, and it is important for brain development. Here, we demonstrate that, before eye opening, during the 2nd postnatal week, oxytocin modulates specific characteristics of spontaneous activity patterns in the visual cortex: it selectively increases SST⁺ interneuron excitability through oxytocin receptor activation and sparsifies and decorrelates neuronal activity in layer 2/3 of V1 without affecting event area, amplitude, or duration.

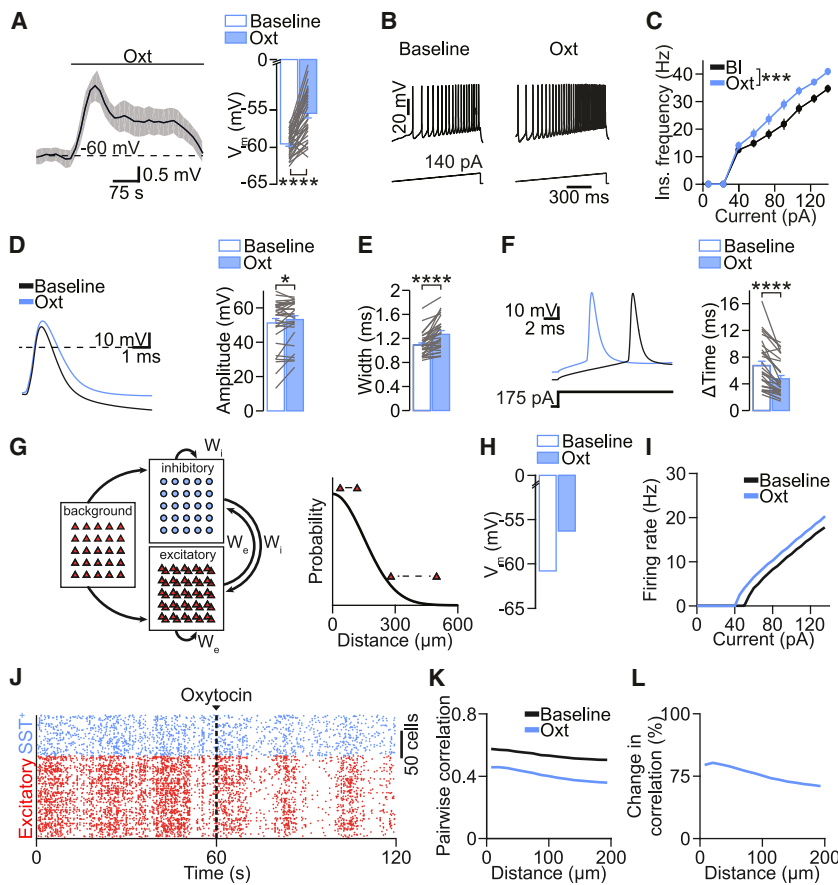


Figure 6. Oxytocin-Induced Increase of the Excitability of SST⁺ Interneurons Is Sufficient to Explain Distance-Dependent Changes in Correlation

(A) Average of current-clamp recordings of SST⁺ neurons before and after oxytocin bath application. Right: group data of SST⁺ interneuron membrane potential in baseline and oxytocin conditions are shown. ****p = 4.7×10^{-10} (n = 34 cells; paired two-tailed t test).

(B) Train of APs generated with a ramp protocol in current-clamp mode in baseline and oxytocin conditions.

(C) Instantaneous frequency versus current plot. ***p < 0.0001 (n = 34 cells; repeated-measurements two-way ANOVA).

(D) Left: single APs aligned to the peak in baseline and oxytocin conditions. Right: group data of AP amplitude in baseline and oxytocin conditions are shown. *p = 0.038 (n = 34 cells; paired two-tailed t test).

(E) AP width. ****p = 1.8×10^{-6} (paired two-tailed t test).

(F) AP. Left: single APs in response to a square current step in baseline and oxytocin conditions. The time required to elicit an action potential was strongly reduced in the presence of oxytocin. ****p = 8.9×10^{-7} (paired two-tailed t test). Data are represented as mean ± SEM.

(G) Left: schematic of the model with excitatory background input and recurrently connected excitatory (red) and inhibitory populations (blue). W_{e_i} , excitatory weight; W_{i_i} , inhibitory weight. Right: connection probability as a function of distance between cells is shown.

(H) Resting membrane potential of SST⁺ interneurons during baseline and oxytocin.

(I) Firing rate of inhibitory cells as a function of the input current in baseline and oxytocin.

(J) Spike raster plot of excitatory (red) and SST⁺ interneurons (blue) neuron populations before and after application of oxytocin (see STAR Methods).

(K) Correlation as a function of distance for baseline and oxytocin conditions. See STAR Methods for calculation details.

(L) Change in correlation as a function of distance.

See also Figure S5 and Table S1.

The Effect of Oxytocin Receptor Activation Differs between V1 and S1

A large body of evidence suggests that maternal care behaviors induce activation of hypothalamic neurons and release of oxytocin in the pup's brain (e.g., during mother-pup skin-to-skin contact,³⁹ anogenital stimulation,⁴⁰ or stroking stimuli,⁴¹ and most likely after milk suckling activity⁴²). Accordingly, somatosensory stimuli specifically activate parvocellular oxytocin neurons in the paraventricular nucleus (PVN).⁴³ How oxytocin reaches the developing cortex is not entirely clear. It might be released within V1, because hypothalamic oxytocin neurons project to the cortex, including V1, at least in adult mice.^{17,44} Alternatively, oxytocin may diffuse into the developing cortex after somatodendritic release from the hypothalamus into the third ventricle.^{15,28,42} To fully disentangle how oxytocin reaches the developing cortex and to induce endogenous release, it will be required to adapt technical approaches currently available in adults^{18,36,44} to neonatal animals. Nevertheless, our observation that blocking cortical oxytocin receptors increases the frequency of spontaneous network activity in V1 of awake animals indicates that the oxytocin receptor is activated by its

endogenous ligand and modulates spontaneous activity patterns during development.

Independently of the source of oxytocin, we find here that this neuropeptide strongly decreases spontaneous network activity in V1, although its effect on spontaneous network activity in S1 is comparably mild. The differences between oxytocin's effect on V1 and S1 network activity are consistent with differences in the expression of its receptor across cell types and their specific responses to oxytocin. Oxytocin receptor mRNA expression co-localizes with the interneuron marker GAD1 in both V1 and S1; however, its expression in excitatory neurons is higher in S1 than V1. Furthermore, oxytocin increases specifically inhibitory synaptic transmission in V1, but in S1, it results in a smaller and more-balanced activation of both spontaneous inhibitory and excitatory currents. Thus, the specific effect of oxytocin on inhibitory signaling is most likely responsible for its effect on network activity patterns in V1. In the adult, various brain regions differ in their responses to oxytocin due to differences in the distribution of the oxytocin receptor in inhibitory neurons as well;^{17,18,36,44–47} however, whether oxytocin signaling differs between V1 and S1 in adulthood too is currently unknown.

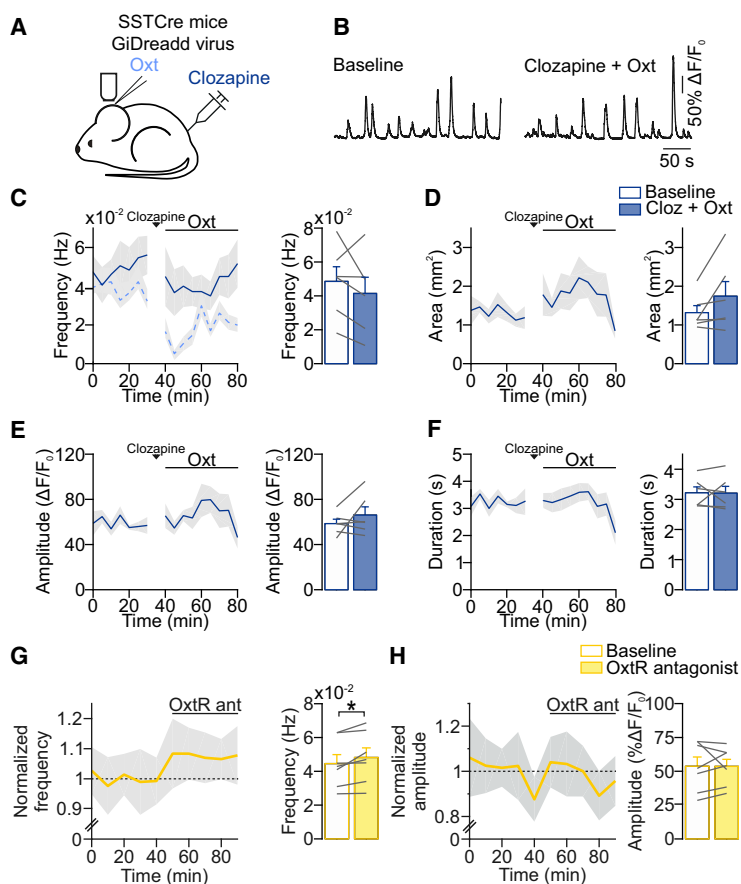


Figure 7. Role for SST⁺ Interneurons and Endogenous Oxytocin Receptor Activation in Modulating Network Activity In Vivo

(A) Schematic representation of the experimental design: wide-field calcium imaging of spontaneous network activity in SST-Cre mice where V1 neurons express GCaMP6s and GiDreadd after viral transduction.

(B) Fluorescent changes before and after clozapine + oxytocin application.

(C) Network event frequency during baseline and after oxytocin application. Time courses represent 5-min averages. Dashed light blue curve represents data shown in Figure 1D, V1, for comparison.

(D) Network event area.

(E) Network event amplitude.

(F) Network event duration. Data are represented as mean ± SEM. (G) Network event frequency during baseline and after oxytocin receptor antagonist application, in awake animals. *p = 0.037 (n = 7 animals; paired two-tailed t test). Data are represented as mean ± SEM.

(H) Network event amplitude during baseline and after oxytocin receptor antagonist application, in awake animals.

2 weeks after eye opening.⁵¹ Thus, oxytocin may be an important regulator of “phenotypic checkpoints” important for sensitive periods during postnatal development.⁵²

Oxytocin Desynchronizes the Network in a Structured Manner

We observed that oxytocin decreases pairwise correlations between neurons. This decorrelation is mediated most likely by oxytocin-induced activation

SST⁺ Interneuron Activation Accounts for the Oxytocin-Mediated Increase in V1 Inhibitory Transmission

We propose here that the specific activation of SST⁺ interneurons through oxytocin modulates spontaneous activity patterns in the developing V1 based on five observations: (1) the oxytocin receptor is transcribed in V1 SST⁺ interneurons but barely detected in other interneuron types, excitatory neurons, or glia cells.³¹ (2) Pharmacogenetic suppression of SST⁺ neurons prevents the oxytocin-mediated decrease in network event frequency *in vivo*. (3) Oxytocin induces an inward current in almost all SST⁺ interneurons and in a fraction of GAD2⁺ interneurons. (4) Oxytocin-mediated depolarization of SST⁺ interneurons increases the frequency of inhibitory synaptic inputs in pyramidal cells 5-fold, and (5) this increase is abolished entirely by SST⁺ interneuron inactivation.

Our finding that oxytocin increases inhibitory function through SST⁺ interneuron activation and decreases spontaneous activity during an important step in visual cortex development supports the idea that oxytocin modulation of inhibition facilitates the developmental progression across critical periods.^{19,48} During development, changes in the E/I balance are important, because they determine the opening or closure of critical periods, during which sensory pathways become sensitive to experience.⁴⁹ Furthermore, the maturation of inhibition may be required for decreasing spontaneous activity,⁵⁰ thereby increasing the relative importance of visually evoked activity. This relative increase in experience-driven activity could initiate the critical period

of SST⁺ interneurons, in agreement with previously published findings: activation of interneurons decreases neuronal correlations in general.^{53,54} More specifically, lateral inhibition, a role attributed to SST⁺ interneurons, decorrelates spike trains⁵⁵ or stimulus-evoked patterns,⁵⁶ and pharmacogenetic inactivation of SST⁺ interneurons increases pairwise correlations during spontaneous network activity in the developing visual cortex.³³ Our analyses and simulations suggest that correlations are downregulated in a spatially specific manner: correlation decreases are more pronounced between pairs of neurons that are farther apart. Neuronal correlations and the spatial extent of spontaneous network activity patterns determine their effectiveness in refining synaptic connections in the visual system.^{11,25,57,58} Therefore, the regulation of spatial correlations through oxytocin may be necessary to shape spontaneous activity patterns to drive the refinement of synaptic connections and to prepare the emerging network optimally for computing visual inputs after eye opening. It might be tempting to speculate that oxytocin contributes to improved visual acuity after tactile stimulation during development.⁵⁹

During the 2nd postnatal week, V1 activity patterns change from high-correlation, high-cell-participation patterns toward sparser and less-correlated activity. Sparsification of activity patterns has been shown to be largely pre-programmed.^{60–62} Because oxytocin signaling ramps up during the 2nd postnatal week and sparsifies activity patterns as discussed above,

oxytocin and potentially other neuromodulators may drive the sparsification and decorrelation seen in spontaneous activity patterns toward the onset of sensation. In this regard, it is interesting to note that activity patterns in the *Fmr1* knockout (KO) mouse, a model for the neurodevelopmental disorder fragile X syndrome, show increased correlations in the developing somatosensory and visual cortices compared to WT littermates.^{63,64} In addition, atypical oxytocin signaling has been implicated as a risk factor for neurodevelopmental disorders.^{65–67} Thus, oxytocin may be important for healthy brain development to specifically shape activity patterns for synaptic refinement by regulating SST⁺ interneuron function.

STAR★METHODS

Detailed methods are provided in the online version of this paper and include the following:

- **KEY RESOURCES TABLE**
- **RESOURCE AVAILABILITY**
 - Lead Contact
 - Materials Availability
 - Data and Code Availability
- **EXPERIMENTAL MODEL AND SUBJECT DETAILS**
 - Animal
- **METHOD DETAILS**
 - In utero electroporation and surgery
 - Virus injection
 - Wide-field imaging
 - 2-photon imaging
 - Patch-clamp experiments
 - RNAscope
 - Model
- **QUANTIFICATION AND STATISTICAL ANALYSIS**
 - 2-photon imaging analysis
 - Wide-field imaging analysis
 - Electrophysiological analysis
 - RNAscope analysis
 - Statistics

SUPPLEMENTAL INFORMATION

Supplemental Information can be found online at <https://doi.org/10.1016/j.cub.2020.10.028>.

ACKNOWLEDGMENTS

We thank Corette Wierenga, Nicole Ropert, and Marcus Howlett for critically reading the manuscript; Gertjan Houwen for his help with MATLAB coding; Maurice Manning for the donation of the oxytocin receptor antagonist; Monique van Mourik for performing the *in utero* electroporations and virus injection; Fred de Winter for the production of AAV-hSyn-DIO-hM4D(Gi)-mCherry virus; and Marko Popovic for sharing with us the Rapid LED Switching System for one-photon microscopy. We thank the Helmut Kessels lab for sharing equipment, The Allen Brain Institute for permission to reproduce their data in Figure S3, and Marian Verhage for helping with our mice colony. This work was supported by grants of the Netherlands Organization for Scientific Research (NWO, ALW Open Program grants nos. 819.02.017, 822.02.006, and ALWOP.216; ALW Vici, no. 865.12.001), the “Stichting Vrienden van het Herseninstituut” (all C.L.), and the Max Planck Society and European Research Council StG 804824 (J.G.).

AUTHOR CONTRIBUTIONS

Conceptualization, P.P.M. and C.L.; Experiments, P.P.M., A.N.-P., and E.H.; Analysis, P.P.M., A.N.-P., J.K., and J.G.; Writing, P.P.M. and C.L.

DECLARATION OF INTERESTS

The authors declare no competing interests.

Received: February 7, 2020

Revised: August 28, 2020

Accepted: October 9, 2020

Published: November 5, 2020

REFERENCES

1. Katz, L.C., and Shatz, C.J. (1996). Synaptic activity and the construction of cortical circuits. *Science* 274, 1133–1138.
2. Sanes, J.R., and Yamagata, M. (2009). Many paths to synaptic specificity. *Annu. Rev. Cell Dev. Biol.* 25, 161–195.
3. Kirkby, L.A., Sack, G.S., Firl, A., and Feller, M.B. (2013). A role for correlated spontaneous activity in the assembly of neural circuits. *Neuron* 80, 1129–1144.
4. Meister, M., Wong, R.O.L., Baylor, D.A., and Shatz, C.J. (1991). Synchronous bursts of action potentials in ganglion cells of the developing mammalian retina. *Science* 252, 939–943.
5. Feller, M.B., Wellis, D.P., Stellwagen, D., Werblin, F.S., and Shatz, C.J. (1996). Requirement for cholinergic synaptic transmission in the propagation of spontaneous retinal waves. *Science* 272, 1182–1187.
6. Ackman, J.B., Burbridge, T.J., and Crair, M.C. (2012). Retinal waves coordinate patterned activity throughout the developing visual system. *Nature* 490, 219–225.
7. Siegel, F., Heimel, J.A., Peters, J., and Lohmann, C. (2012). Peripheral and central inputs shape network dynamics in the developing visual cortex *in vivo*. *Curr. Biol.* 22, 253–258.
8. Colonnese, M.T., Shen, J., and Murata, Y. (2017). Uncorrelated neural firing in mouse visual cortex during spontaneous retinal waves. *Front. Cell. Neurosci.* 11, 289.
9. Weliky, M., and Katz, L.C. (1997). Disruption of orientation tuning in visual cortex by artificially correlated neuronal activity. *Nature* 386, 680–685.
10. Cang, J., Rentería, R.C., Kaneko, M., Liu, X., Copenhagen, D.R., and Stryker, M.P. (2005). Development of precise maps in visual cortex requires patterned spontaneous activity in the retina. *Neuron* 48, 797–809.
11. Burbridge, T.J., Xu, H.-P., Ackman, J.B., Ge, X., Zhang, Y., Ye, M.-J., Zhou, Z.J., Xu, J., Contractor, A., and Crair, M.C. (2014). Visual circuit development requires patterned activity mediated by retinal acetylcholine receptors. *Neuron* 84, 1049–1064.
12. Tyzio, R., Nardou, R., Ferrari, D.C., Tsintsadze, T., Shahrokhi, A., Eftekhari, S., Khalilov, I., Tsintsadze, V., Brouchoud, C., Chazal, G., et al. (2014). Oxytocin-mediated GABA inhibition during delivery attenuates autism pathogenesis in rodent offspring. *Science* 343, 675–679.
13. Hanganu, I.L., Staiger, J.F., Ben-Ari, Y., and Khazipov, R. (2007). Cholinergic modulation of spindle bursts in the neonatal rat visual cortex *in vivo*. *J. Neurosci.* 27, 5694–5705.
14. Sarro, E.C., Wilson, D.A., and Sullivan, R.M. (2014). Maternal regulation of infant brain state. *Curr. Biol.* 24, 1664–1669.
15. Zheng, J.-J., Li, S.-J., Zhang, X.-D., Miao, W.-Y., Zhang, D., Yao, H., and Yu, X. (2014). Oxytocin mediates early experience-dependent cross-modal plasticity in the sensory cortices. *Nat. Neurosci.* 17, 391–399.
16. Hammock, E.A., and Levitt, P. (2013). Oxytocin receptor ligand binding in embryonic tissue and postnatal brain development of the C57BL/6J mouse. *Front. Behav. Neurosci.* 7, 195.
17. Mitre, M., Marlin, B.J., Schiavo, J.K., Morina, E., Norden, S.E., Hackett, T.A., Aoki, C.J., Chao, M.V., and Froemke, R.C. (2016). A distributed

- network for social cognition enriched for oxytocin receptors. *J. Neurosci.* 36, 2517–2535.
18. Marlin, B.J., Mitre, M., D'amour, J.A., Chao, M.V., and Froemke, R.C. (2015). Oxytocin enables maternal behaviour by balancing cortical inhibition. *Nature* 520, 499–504.
 19. Grinevich, V., and Stoop, R. (2018). Interplay between oxytocin and sensory systems in the orchestration of socio-emotional behaviors. *Neuron* 99, 887–904.
 20. Burkett, J.P., Andari, E., Johnson, Z.V., Curry, D.C., de Waal, F.B.M., and Young, L.J. (2016). Oxytocin-dependent consolation behavior in rodents. *Science* 351, 375–378.
 21. Ferretti, V., Maltese, F., Contarini, G., Nigro, M., Bonavia, A., Huang, H., Gigliucci, V., Morelli, G., Scheggia, D., Managò, F., et al. (2019). Oxytocin signaling in the central amygdala modulates emotion discrimination in mice. *Curr. Biol.* 29, 1938–1953.e6.
 22. Tyzio, R., Cossart, R., Khalilov, I., Minlebaev, M., Hübner, C.A., Represa, A., Ben-Ari, Y., and Khazipov, R. (2006). Maternal oxytocin triggers a transient inhibitory switch in GABA signaling in the fetal brain during delivery. *Science* 314, 1788–1792.
 23. Winnubst, J., Cheyne, J.E., Niculescu, D., and Lohmann, C. (2015). Spontaneous activity drives local synaptic plasticity in vivo. *Neuron* 87, 399–410.
 24. Stosiek, C., Garaschuk, O., Holthoff, K., and Konnerth, A. (2003). In vivo two-photon calcium imaging of neuronal networks. *Proc. Natl. Acad. Sci. USA* 100, 7319–7324.
 25. Leighton, A.H., and Lohmann, C. (2016). The wiring of developing sensory circuits—from patterned spontaneous activity to synaptic plasticity mechanisms. *Front. Neural Circuits* 10, 71.
 26. Cossell, L., Iacaruso, M.F., Muir, D.R., Houlton, R., Sader, E.N., Ko, H., Hofer, S.B., and Mrsic-Flogel, T.D. (2015). Functional organization of excitatory synaptic strength in primary visual cortex. *Nature* 518, 399–403.
 27. Ko, H., Cossell, L., Baragli, C., Antolik, J., Clopath, C., Hofer, S.B., and Mrsic-Flogel, T.D. (2013). The emergence of functional microcircuits in visual cortex. *Nature* 496, 96–100.
 28. Chini, B., Verhage, M., and Grinevich, V. (2017). The action radius of oxytocin release in the mammalian CNS: from single vesicles to behavior. *Trends Pharmacol. Sci.* 38, 982–991.
 29. Schorscher-Petcu, A., Sotocinal, S., Ciura, S., Dupré, A., Ritchie, J., Sorge, R.E., Crawley, J.N., Hu, S.-B., Nishimori, K., Young, L.J., et al. (2010). Oxytocin-induced analgesia and scratching are mediated by the vasopressin-1A receptor in the mouse. *J. Neurosci.* 30, 8274–8284.
 30. Manning, M., Misicka, A., Olma, A., Bankowski, K., Stoev, S., Chini, B., Durroux, T., Mouillac, B., Corbani, M., and Guillon, G. (2012). Oxytocin and vasopressin agonists and antagonists as research tools and potential therapeutics. *J. Neuroendocrinol.* 24, 609–628.
 31. Tasic, B., Menon, V., Nguyen, T.N., Kim, T.K., Jarsky, T., Yao, Z., Levi, B., Gray, L.T., Sorensen, S.A., Dolbeare, T., et al. (2016). Adult mouse cortical cell taxonomy revealed by single cell transcriptomics. *Nat. Neurosci.* 19, 335–346.
 32. Adesnik, H., Bruns, W., Taniguchi, H., Huang, Z.J., and Scanziani, M. (2012). A neural circuit for spatial summation in visual cortex. *Nature* 490, 226–231.
 33. Leighton, A.H., Houwen, G.J., Cheyne, J.E., Maldonado, P.P., De Winter, F., and Lohmann, C. (2020). Control of spontaneous activity patterns by inhibitory signaling in the developing visual cortex. *bioRxiv*. <https://doi.org/10.1101/2020.02.21.959262>.
 34. van Versendaal, D., and Levitt, C.N. (2016). Inhibitory interneurons in visual cortical plasticity. *Cell. Mol. Life Sci.* 73, 3677–3691.
 35. Gonchar, Y., Wang, Q., and Burkhalter, A. (2008). Multiple distinct subtypes of GABAergic neurons in mouse visual cortex identified by triple immunostaining. *Front. Neuroanat.* 7, 3.
 36. Tirko, N.N., Eyring, K.W., Carcea, I., Mitre, M., Chao, M.V., Froemke, R.C., and Tsien, R.W. (2018). Oxytocin transforms firing mode of CA2 hippocampal neurons. *Neuron* 100, 593–608.e3.
 37. Hill, S., and Tononi, G. (2005). Modeling sleep and wakefulness in the thalamocortical system. *J. Neurophysiol.* 93, 1671–1698.
 38. Naskar, S., Narducci, R., Balzani, E., Cwetsch, A.W., Tucci, V., and Cancedda, L. (2019). The development of synaptic transmission is time-locked to early social behaviors in rats. *Nat. Commun.* 10, 1195.
 39. Kojima, S., Stewart, R.A., Demas, G.E., and Alberts, J.R. (2012). Maternal contact differentially modulates central and peripheral oxytocin in rat pups during a brief regime of mother-pup interaction that induces a filial huddling preference. *J. Neuroendocrinol.* 24, 831–840.
 40. Caba, M., Rovirosa, M.J., and Silver, R. (2003). Suckling and genital stroking induces Fos expression in hypothalamic oxytocinergic neurons of rabbit pups. *Brain Res. Dev. Brain Res.* 143, 119–128.
 41. Okabe, S., Yoshida, M., Takayanagi, Y., and Onaka, T. (2015). Activation of hypothalamic oxytocin neurons following tactile stimuli in rats. *Neurosci. Lett.* 600, 22–27.
 42. Grinevich, V., Desarménien, M.G., Chini, B., Tauber, M., and Muscatelli, F. (2015). Ontogenesis of oxytocin pathways in the mammalian brain: late maturation and psychosocial disorders. *Front. Neuroanat.* 8, 164.
 43. Tang, Y., Benusiglio, D., Lefevre, A., Hilfger, L., Althammer, F., Bludau, A., Hagiwara, D., Baudon, A., Darbon, P., Schimmer, J., et al. (2020). Social touch promotes interfemale communication via activation of parvocellular oxytocin neurons. *Nat. Neurosci.* 23, 1125–1137.
 44. Knobloch, H.S., Charlet, A., Hoffmann, L.C., Eliava, M., Khrulev, S., Cetin, A.H., Osten, P., Schwarz, M.K., Seeburg, P.H., Stoop, R., and Grinevich, V. (2012). Evoked axonal oxytocin release in the central amygdala attenuates fear response. *Neuron* 73, 553–566.
 45. Mühlethaler, M., Charpak, S., and Dreifuss, J.J. (1984). Contrasting effects of neurohypophysial peptides on pyramidal and non-pyramidal neurones in the rat hippocampus. *Brain Res.* 308, 97–107.
 46. Owen, S.F., Tuncdemir, S.N., Bader, P.L., Tirko, N.N., Fishell, G., and Tsien, R.W. (2013). Oxytocin enhances hippocampal spike transmission by modulating fast-spiking interneurons. *Nature* 500, 458–462.
 47. Nakajima, M., Görlich, A., and Heintz, N. (2014). Oxytocin modulates female sociosexual behavior through a specific class of prefrontal cortical interneurons. *Cell* 159, 295–305.
 48. Hammock, E.A.D. (2015). Developmental perspectives on oxytocin and vasopressin. *Neuropsychopharmacology* 40, 24–42.
 49. Hensch, T.K. (2005). Critical period plasticity in local cortical circuits. *Nat. Rev. Neurosci.* 6, 877–888.
 50. Colonnese, M.T. (2014). Rapid developmental emergence of stable depolarization during wakefulness by inhibitory balancing of cortical network excitability. *J. Neurosci.* 34, 5477–5485.
 51. Toyozumi, T., Miyamoto, H., Yazaki-Sugiyama, Y., Atapour, N., Hensch, T.K., and Miller, K.D. (2013). A theory of the transition to critical period plasticity: inhibition selectively suppresses spontaneous activity. *Neuron* 80, 51–63.
 52. Ben-Ari, Y., and Spitzer, N.C. (2010). Phenotypic checkpoints regulate neuronal development. *Trends Neurosci.* 33, 485–492.
 53. Cardin, J.A. (2018). Inhibitory interneurons regulate temporal precision and correlations in cortical circuits. *Trends Neurosci.* 41, 689–700.
 54. Giridhar, S., Doiron, B., and Urban, N.N. (2011). Timescale-dependent shaping of correlation by olfactory bulb lateral inhibition. *Proc. Natl. Acad. Sci. USA* 108, 5843–5848.
 55. Arevian, A.C., Kapoor, V., and Urban, N.N. (2008). Activity-dependent gating of lateral inhibition in the mouse olfactory bulb. *Nat. Neurosci.* 11, 80–87.
 56. Friedrich, R.W., and Laurent, G. (2001). Dynamic optimization of odor representations by slow temporal patterning of mitral cell activity. *Science* 291, 889–894.
 57. Xu, H.-P., Burbidge, T.J., Chen, M.-G., Ge, X., Zhang, Y., Zhou, Z.J., and Crair, M.C. (2015). Spatial pattern of spontaneous retinal waves instructs retinotopic map refinement more than activity frequency. *Dev. Neurobiol.* 75, 621–640.

58. Wosniak, M.E., Kirchner, J.H., Chao, L.-Y., Zabouri, N., Lohmann, C., and Gjorgjieva, J. (2020). Adaptive spontaneous activity in the developing visual cortex. *bioRxiv*. <https://doi.org/10.1101/2020.07.30.229559>.
59. Guzzetta, A., Baldini, S., Bancalè, A., Baroncelli, L., Ciucci, F., Ghirri, P., Putignano, E., Sale, A., Viegi, A., Berardi, N., et al. (2009). Massage accelerates brain development and the maturation of visual function. *J. Neurosci.* *29*, 6042–6051.
60. Che, A., Babij, R., Iannone, A.F., Fetcho, R.N., Ferrer, M., Liston, C., Fishell, G., and De Marco García, N.V. (2018). Layer I interneurons sharpen sensory maps during neonatal development. *Neuron* *99*, 98–116.e7.
61. Golshani, P., Gonçalves, J.T., Khoshkhou, S., Mostany, R., Smirnakis, S., and Portera-Cailliau, C. (2009). Internally mediated developmental desynchronization of neocortical network activity. *J. Neurosci.* *29*, 10890–10899.
62. Rochefort, N.L., Garaschuk, O., Milos, R.I., Narushima, M., Marandi, N., Pichler, B., Kovalchuk, Y., and Konnerth, A. (2009). Sparsification of neuronal activity in the visual cortex at eye-opening. *Proc. Natl. Acad. Sci. USA* *106*, 15049–15054.
63. Cheyne, J.E., Zabouri, N., Baddeley, D., and Lohmann, C. (2019). Spontaneous activity patterns are altered in the developing visual cortex of the *Fmr1* knockout mouse. *Front. Neural Circuits* *13*, 57.
64. Gonçalves, J.T., Anstey, J.E., Golshani, P., and Portera-Cailliau, C. (2013). Circuit level defects in the developing neocortex of fragile X mice. *Nat. Neurosci.* *16*, 903–909.
65. Hammock, E.A.D., and Young, L.J. (2006). Oxytocin, vasopressin and pair bonding: implications for autism. *Philos. Trans. R. Soc. Lond. B Biol. Sci.* *361*, 2187–2198.
66. Insel, T.R., O'Brien, D.J., and Leckman, J.F. (1999). Oxytocin, vasopressin, and autism: is there a connection? *Biol. Psychiatry* *45*, 145–157.
67. Muscatelli, F., Desarménien, M.G., Matarazzo, V., and Grinevich, V. (2018). Oxytocin signaling in the early life of mammals: link to neurodevelopmental disorders associated with ASD. *Curr. Top. Behav. Neurosci.* *35*, 239–268.
68. Evangelidis, G.D., and Psarakis, E.Z. (2008). Parametric image alignment using enhanced correlation coefficient maximization. *IEEE Trans. Pattern Anal. Mach. Intell.* *30*, 1858–1865.
69. Diesmann, M., and Gewaltig, M.-O. (2002). NEST: An Environment for Neural Systems Simulations (Beiträge zum Heinz-Billing-Preis), pp. 43–70.
70. Pologruto, T.A., Sabatini, B.L., and Svoboda, K. (2003). ScanImage: flexible software for operating laser scanning microscopes. *Biomed. Eng. Online* *2*, 13.
71. Battefeld, A., Popovic, M.A., van der Werf, D., and Kole, M.H.P. (2019). A versatile and open-source rapid LED switching system for one-photon imaging and photo-activation. *Front. Cell. Neurosci.* *12*, 530.
72. Chen, T.-W., Wardill, T.J., Sun, Y., Pulver, S.R., Renninger, S.L., Baohan, A., Schreiter, E.R., Kerr, R.A., Orger, M.B., Jayaraman, V., et al. (2013). Ultrasensitive fluorescent proteins for imaging neuronal activity. *Nature* *499*, 295–300.

STAR★METHODS

KEY RESOURCES TABLE

REAGENT or RESOURCE	SOURCE	IDENTIFIER
Bacterial and Virus Strains		
pAAV1-hSyn-DIO-hM4D(Gi)-mCherry	³³	N/A
pAAV1.Syn.GCaMP6s.WPRE.SV40	UPenn viral core	AV-1-PV2824
Chemicals, Peptides, and Recombinant Proteins		
Oregon Green 488 BAPTA-1 AM	Invitrogen	Thermo Fisher Scientific #O6807
Oxytocin	Sigma	O6379
desGly-NH ₂ ,d(CH ₂) ₅ [D-Tyr ² ,Thr ⁴]OVT	Synthesized and given by Dr. Maurice Manning, University of Toledo ³⁰	N/A
Clozapine N-oxide	Tocris	#0444
Clozapine	Tocris	#4936
SR95531	Tocris	#1262
NBQX	Tocris	#1044
D-AP5	Tocris	#0103
TTX	Tocris	#1078
Critical Commercial Assays		
RNAscope 2.5HD Duplex Assay	Advanced Cell Diagnostics	#322430
Experimental Models: Organisms/Strains		
Mouse: C57B/6J	Janvier	N/A
<i>Sst</i> ^{Cre}	The Jackson Laboratory	013044
<i>Gad2</i> ^{Cre}	The Jackson Laboratory	010802
<i>Gt(ROSA)26Sor^{CAG-tdTomato}</i>	The Jackson Laboratory	007908
Oligonucleotides		
<i>Oxtr</i>	Advanced Cell Diagnostics	#411101-C2
<i>Slc17a7</i> , VGLUT1	Advanced Cell Diagnostics	#416631
<i>Gad1</i>	Advanced Cell Diagnostics	#400951
<i>Sst</i>	Advanced Cell Diagnostics	#404631
Recombinant DNA		
pCAGGS-DsRed	Gift from Dr. Christiaan Levelt	N/A
pCAGGS-GCaMP6s	Gift from Dr. Christiaan Levelt	N/A
Software and Algorithms		
Enhanced correlation coefficient algorithm	⁶⁸	N/A
NEST	⁶⁹	RRID:SCR_002963
Model simulations	This paper	https://github.com/comp-neural-circuits/OTmodel
LabView	National Instruments	LabView, RRID:SCR_014325

(Continued on next page)

Continued

REAGENT or RESOURCE	SOURCE	IDENTIFIER
ScanImage	http://scanimage.vidriotechnologies.com/display/SH;jsessionid=06CBF1F1626C333384D74630886127FF ⁷⁰	ScanImage, RRID:SCR_014307
NIS-Elements	Nikon	(NIS-Elements, RRID:SCR_014329)
ImageJ	https://imagej.net/	ImageJ, RRID:SCR_003070
MATLAB	MathWorks	MATLAB, RRID:SCR_001622
Clampfit	Molecular Devices	pClamp, RRID:SCR_011323
AxoGraph	Axograph Scientific	Axograph, RRID:SCR_014284
IGOR Pro	Wave Metrics	IGOR Pro, RRID:SCR_000325
Prism 7	GraphPad	GraphPad Prism, RRID:SCR_002798
Other		
TEAMSTER (Open-source rapid LED switching system for one-photon imaging and photo-activation)	⁷¹	https://github.com/Kolelab/Image-analysis

RESOURCE AVAILABILITY

Lead Contact

Further information and requests for resources and reagents may be directed to and will be fulfilled by the Lead Contact, Christian Lohmann, c.lohmann@nin.knaw.nl.

Materials Availability

This study did not generate new unique reagents.

Data and Code Availability

The datasets generated during this study have not been deposited in a public repository but are available from the Lead Contact on request. This study used standard, custom-built MATLAB programmed scripts that are available from the Lead Contact upon request. The code used for the simulations is available at <https://github.com/comp-neural-circuits/OTmodel>.

EXPERIMENTAL MODEL AND SUBJECT DETAILS

Animal

All experimental procedures were approved by the institutional animal care and use committee of the Royal Netherlands Academy of Arts and Sciences and in agreement with the European Community Directive 2010/63/EU and with the Institutional Animal Care and Use Committee at Florida State University in accordance with state and federal guidelines (Guide for the Care and Use of Laboratory Animals of the National Institutes of Health). We used neonatal C57BL/6J, SST-Cre, SST-Cre;Rosa26-TdTomato and GAD2-Cre;Rosa26-TdTomato males and females mice from postnatal day 9 to 14 (P9-14). The SST-Cre;Rosa26-TdTomato and GAD2-Cre;Rosa26-TdTomato lines were generated by crossing the reporter Rosa26-TdTomato line (The Jackson Laboratory, 007908) with either the SST-Cre (The Jackson Laboratory, 013044) or the GAD2-Cre (The Jackson Laboratory, 010802) lines. Neonatal pups were housed with one mother, with exception of pups coming from in utero electroporation. They were housed with two mothers and the nest trimmed to 6 pups to facilitate the caring behavior of the mothers. Animals were kept in a 12h-12h light/dark cycle with food and water *ad libitum*. All the experiments were performed during the light cycle. No effects related to sex were observed. No animal was excluded from the analysis.

METHOD DETAILS

In utero electroporation and surgery

In utero electroporation was performed as described previously²³. To perform calcium imaging of layer 2/3 pyramidal cells, GCaMP6s was cloned into pCAGGS (Addgene plasmid 40753⁷²) and used in combination with DsRed in pCAGGS for visualization (gift from Christiaan Levelt). Pups were in utero electroporated at embryonic day (E) 16.5 after injection of the GCaMP6s (2 μg/μl) and DsRed (1 μg/μl) vectors into the ventricles. Electrode paddles were positioned to target the subventricular zone and 50 V pulses of 50 ms duration were applied.

For *in vivo* experiments, surgery for craniotomy was performed as described previously^{7,33}. Pups were kept at 36–37°C and anesthetized with 2% isoflurane and lidocaine was applied into the skin before neck muscle removal. A head bar was fixed above the V1/S1 region. Isoflurane was dropped to 0.7% before the imaging session. This lightly anesthetized state, which is characterized by rapid and shallow breathing and a relatively high heart rate, was maintained throughout the imaging session. During experiments in the absence of anesthesia, pups were kept undisturbed in the dark and covered by a custom-made holder that prevents heat loss and mimic the conditions in the nest, for one hour before the imaging session started. The welfare of the pup was monitored to minimize distress during the whole imaging session.

Virus injection

Virus injections were performed at P0–1. Virus injected were pAAV1-Syn-GCaMP6s (AV-1-PV2824, UPenn viral core) and pAAV1-hSyn-DIO-hM4D(Gi)-mCherry (produced by Fred Winter³³). SST-Cre neonatal mice were anesthetized by cold-induced hypothermia and kept cold in a stereotactic frame for pups (RWD Life Science). Stereotactic injections targeting V1 were performed with a microinjection pipet (Nanoject II, Drummond; volume 27 nl; mix of 1:1 AAV1-hSyn-DIO-hM4D(Gi)-mCherry and AAV1-Syn-GCaMP6; from Bregma in mm: 0.3 posterior, 1.4 lateral). Immediately after injection, pups were kept warm on a heating pad and placed back to their mother after they awoke from anesthesia.

Wide-field imaging

In utero electroporated or virus injected pups were used for calcium imaging of visual and somatosensory cortex. Calcium events were recorded with a Movable Objective Microscope (MOM, Sutter Instrument). Time-lapse recordings were acquired with a 4x objective (0.8 NA, Olympus) and blue light excitation from a Xenon Arc lamp (Lambda LS, Sutter Instrument Company). A CCD camera (Evolution QEi, QImaging) was controlled by custom-made LabVIEW (National Instruments) based software and images were acquired at a frame rate of 20 Hz.

Clozapine (Tocris) was injected subcutaneously (0.5 mg/kg) and oxytocin was applied five minutes after clozapine injection.

2-photon imaging

Bolus load of the calcium indicator Oregon Green 488 BAPTA-1 AM (OGB-1, Invitrogen) was performed as described⁷. Imaging was performed by using a two-photon microscope (MOM, Sutter, or A1RMP, Nikon) and a mode-locked Ti:Sapphire laser (MaiTai, Spectra Physics or Chamaleon, Coherent, λ = 810 nm). Consecutive xyt-stacks were acquired at a frame rate of 4–7 Hz (pixel size 0.3–0.6 μm) through a 40x (0.8 NA, Olympus) or a 16x (0.8 NA, Nikon) water-immersion objective, controlled by ScanImage⁷⁰ or NIS-Elements AR4.51.00 software (Nikon).

For *in vivo* experiments, oxytocin (1 μM, Sigma) and the oxytocin receptor antagonist (desGly-NH₂,d(CH₂)₅[D-Tyr²,Thr⁴]OVT, 250 μM, synthesized and kindly donated by Dr. Maurice Manning, University of Toledo) was diluted in cortex buffer solution⁷ and applied topically at the craniotomy. The craniotomy was filled with approximately 300 μl of solution and that volume was kept constant until the end of the experiment.

Patch-clamp experiments

Acute 300 μm coronal slices of the visual or somatosensory cortex were dissected between P9–P14. Pups were sacrificed by decapitation and their brains were immersed in ice-cold cutting solution (in mM): 2.5 KCl, 1.25 NaH₂PO₄, 26 NaHCO₃, 20 Glucose, 215 Sucrose, 1 CaCl₂, 7 MgCl₂ (Sigma), pH 7.3–7.4, bubbled with 95%/5% O₂/CO₂. Slices were obtained with a vibratome (Microm HM 650V, Thermo Scientific) and subsequently incubated at 34°C in artificial cerebrospinal fluid (ACSF, in mM): 125 NaCl, 3.5 KCl, 1.25 NaH₂PO₄, 26 NaHCO₃, 20 Glucose, 2 CaCl₂, 1 MgCl₂ (Sigma), pH 7.3–7.4. After 45 minutes, slices were transferred to the electrophysiology setup, kept at room temperature and bubbled with 95%/5% O₂/CO₂. For patch-clamp recordings, slices were transferred to a recording chamber and perfused (3 ml/min) with ACSF solution bubbled with 95%/5% O₂/CO₂ at 34°C.

Layer 2/3 pyramidal cells and interneurons were identified using an IR-DIC video microscope (Olympus BX51WI). GAD2⁺ and SST⁺ interneurons were identified by the TdTomato protein fluorescence from the transgenic mice GAD2-Cre;Rosa26-TdTomato and SST-Cre;Rosa26-TdTomato, respectively. Quick change between bright-field imaging and epifluorescence was achieved using a foot-switch device TEAMSTER⁷¹. Whole-cell voltage or current-clamp recordings were made with a MultiClamp 700B amplifier (Molecular Devices), filtered with a low pass Bessel filter at 10 kHz and digitized at 20–50 kHz (Digidata 1440A, Molecular Devices). Series resistance was assessed during recordings and neurons showing a series resistance > 30 MΩ or a change > 30% were discarded. Digitized data were analyzed offline using Clampfit 10 (Molecular Devices), Igor (WaveMetrics) and AxoGraph (Axograph Scientific).

Spontaneous and miniature IPSCs were recorded at a holding potential of 10 mV with glass pipettes (3–6 M Ω) containing (in mM): 115 CsCH₃SO₃, 10 HEPES, 20 CsCl, 2.5 MgCl₂, 4 ATP disodium hydrate, 0.4 GTP sodium hydrate, 10 phosphocreatine disodium hydrate, 0.6 EGTA (Sigma), pH 7.3. For sIPSC recordings during selective silencing of SST⁺ interneurons, clozapine N-oxide (CNO) (10 μ M, Tocris) was administered 1 minute prior to oxytocin (1 μ M, Sigma). mIPSCs were recorded in the presence of tetrodotoxin (0.5 μ M, Tocris). The oxytocin receptor antagonist desGly-NH₂,d(CH₂)₅[D-Tyr²,Thr⁴]OVT (50 μ M, synthesized and kindly donated by Dr. Maurice Manning, University of Toledo) was applied for 5–10 minutes before oxytocin wash-in. sEPSCs were recorded at a holding potential of –60 mV (with junction potential correction) with an intracellular solution containing (in mM): 122 potassium gluconate, 10 HEPES, 13 KCl, 10 phosphocreatine disodium hydrate, 4 ATP magnesium salt, 0.3 GTP sodium hydrate (Sigma), pH 7.3. Oxytocin-induced currents in GAD2⁺ and SST⁺ interneurons were recorded at a holding potential of –60 mV (with junction potential correction) in the presence of 10 μ M SR95531, 10 μ M NBQX, 50 μ M D-AP5 (Tocris). Current-clamp recordings of SST⁺ interneurons were performed using the same K⁺ gluconate-based intracellular solution and in the presence of the synaptic blockers mentioned above. After breaking the seal, variable current injection was applied to keep the cells at –60 mV. The injected current was kept constant from the time of oxytocin wash-in.

RNAscope

Fresh frozen brain tissue from C57BL/6J mice was sectioned in the sagittal plane at 20 μ m in 6 series on SuperFrost Plus microscope slides and stored at –80°C until further processing. RNA transcripts were detected with RNAscope 2.5HD Duplex Assay (Cat. No. 322430, Advanced Cell Diagnostics (ACD), Hayward, CA). Synthetic oligonucleotide probes complementary to the nucleotide sequence 1198 – 2221 of *Oxtr* (NM_001081147.1; ACD Cat. No. 411101-C2), 464 – 1415 of *Slc17a7* (VGLUT1; NM_182993.2; ACD Cat. No. 416631), 62 – 3113 of *Gad1* (NM_008077.4; ACD Cat. No. 400951) and 18 – 407 of *Sst* (NM_009215.1; ACD Cat. No. 404631) were used. Slides were fixed for 2 hours in ice cold 4% paraformaldehyde (pH 9.5) followed by increasing concentrations of ethanol and dehydration in 100% ethanol overnight at –20°C. Slides were air-dried for 10 minutes and boiled for 5 minutes in a target retrieval solution (ref. 322001, ACD), followed by 2 room temperature water rinses and a rinse in 100% ethanol. Slides were air-dried, after which targeted sections were incubated with Protease Plus solution (ref. 322331, ACD) for 15 minutes at 40°C, followed by room temperature water rinses. These prepared slides were then probed for 2 hours with individual probe mixtures (*Oxtr* in the red channel 2 and the other probes in the blue-green channel 1) at 40°C. Unbound probes were rinsed off in wash buffer and slides were stored overnight in 5X SSC at room temperature. Signal amplification and detection were performed using the detailed instructions provided in the RNAscope 2.5HD Duplex Assay. Sections were counterstained with Gill's hematoxylin (American Mastertech Scientific, Inc. Lodi, CA) and coverslipped with Vectamount (Vector Laboratories, Inc. Burlingame, CA). Images were captured with brightfield microscopy (Keyence BZ-X710, Keyence Corp., Osaka, Japan).

Model

We simulated a large-scale computational model of the visual cortex³⁷ in the NEST framework⁶⁹. We focused only on modeling the cortical network of excitatory and inhibitory neurons with 25% of the inhibitory population corresponding to SST⁺ neurons in L2/3, receiving excitatory input from the thalamus. To achieve network activity similar to that described for the developing cortex^{7,62}, we adjusted the intrinsic membrane properties and synaptic weights in the model based on measurements from the present study (Table S1) and applied an external current of 50 pA (to excitatory neurons) or 40 pA (to SST⁺ interneurons) and a sinusoidal background input to the excitatory population to generate spontaneous activity. The oxytocin effect was modeled by increasing the resting membrane potential of SST⁺ interneurons from –60.8 mV to –56.3 mV as the change observed in our experiments (Figure 6A). After simulating the system for 60 s in baseline condition, we modeled application of oxytocin and simulated again for 60 s. Correlations are computed between the voltage traces of excitatory units.

QUANTIFICATION AND STATISTICAL ANALYSIS

2-photon imaging analysis

Images were analyzed with ImageJ (NIH) and custom-written MATLAB scripts (MathWorks) as described previously⁶³. First, to remove movement artifacts and align all recordings we performed an image alignment step based on the enhanced correlation coefficient algorithm⁶⁸. $\Delta F/F_0$ stacks were generated by subtracting and dividing each frame by the mean fluorescence (F_0). Regions of interest (ROIs) were placed on cells that showed clear activity and were visible in all recordings. Glial cells in the field of view showed elevated basal intensity and were not active. All included ROIs were neuronal. $\Delta F/F_0$ traces were obtained by calculating the mean intensity within the ROI for each frame. Increases in fluorescence intensity, which reflect increases in the intracellular calcium concentration due to action potential firing, were then detected automatically for all ROIs and subsequently verified manually. The detection threshold was adjusted for each experiment (at least 2x the standard deviation of the signal in the absence of events) but remained the same within an experiment.

Pearson correlation coefficients were computed from the $\Delta F/F_0$ stacks. The total number of pairs of cells (computed as $N(N - 1) / 2$) was balanced across conditions (oxytocin – 8806 pairs; cortex buffer – 8023 pairs). In Figure 2E each x-coordinate corresponds to a window of length 7 minutes around the time point. The y-coordinate of the line is computed as the average across all animals of the condition over the correlation coefficients computed from the window. The shaded area is the standard error of the mean (computed as $\hat{\sigma} / \sqrt{N}$, where $\hat{\sigma}$ is the estimated standard deviation over animals and N is the number of animals). In Figure 2F, we averaged the

correlation coefficients computed from the windows over all animals and time points before or after oxytocin application. The filled contour plot was made by plotting pairwise correlations after oxytocin (average of 40 minutes period after oxytocin) against baseline correlations (average of 40 minutes period before oxytocin).

For the matrix correlation analysis, we computed the squared distance between the baseline matrix, c_{ij}^{BL} , computed for the entire baseline period of 45 minutes, and the correlation matrix computed from a shifting 7-minute slice centered at time point t , c_{ij}^t , and then summing over all the element-wise differences of all matrix entries, $MSD = \sum_{ij} (c_{ij}^t - c_{ij}^{BL})^2$. To remove any potential drift that occurs

already during the baseline and that might distort the MSD analysis, we performed a linear regression on the baseline MSD and subtracted the linear contributions from all time points. To further pool across multiple animals, we normalized the squared distances by the mean and standard deviation of the baseline period.

Wide-field imaging analysis

Network events were detected automatically. First, $\Delta F/F_0$ stacks were generated using a moving average across 500 frames as F_0 . The detection threshold was 12% $\Delta F/F_0$, which was at least 3x larger than the standard deviation of the noise during inactivity for all recordings. Pixels below threshold were reduced to zero. Network events were defined as groups of at least 300 non-zero pixels that were connected in time and/or space. Since the frame rate was 20 Hz and the pixel size 7.68 μm (area covered by 1 pixel: 59 μm^2), this criterion included events of e.g., > 1 s duration that covered on average > 885 μm^2 of cortical surface. Since this criterion was chosen empirically, we investigated how robust our findings were with respect to this criterion. We performed analyses where we varied the total number of connected pixels that defined a network event on a subset of the data. We found that the number of detected events and the changes observed in frequency after oxytocin application were very robust across different pixel numbers between 200 and 800 pixels (not shown). Since wide-field microscopy is inherently prone to scattered light, we found that the area that network events covered across the cortex was overestimated when we used the 12% cutoff. Therefore, we restricted the area to those pixels that reached 67% of the maximal $\Delta F/F_0$ value for each event (Figure S6).

Recordings from un-anaesthetized animals showed increased movement artifacts. Therefore, we restricted our analysis to frequency and amplitude of network events in traces generated from the entire area of V1. Traces were long-pass filtered to remove high-frequency movement artifacts. Network events were automatically detected using MATLAB's "Find peaks" function where the parameters prominence and peak were optimized for detecting events during the baseline period and kept constant throughout the experiment.

Electrophysiological analysis

m/sIPSCs and sEPSCs were detected using an Igor-based tool SpAcAn (Igor Pro 7, WaveMetrics). Frequency timelines of postsynaptic currents were built by calculating the frequency of 50- or 90 s bins. The 20%–80% rise time was calculated for each IPSC event and the rise rate was determined as amplitude/rise time (pA/ms). Excitability of SST⁺ interneurons was assessed with a one-step ramp protocol, from –100 pA to 140 pA at a rate of 96 pA/second. Single action potentials (APs) were elicited by injecting moderate pulses of current (< 1 nA, < 15 ms). Changes in membrane potential upon oxytocin treatment were calculated as the voltage difference between the trace exhibiting the peak effect and the last trace of baseline condition. A minority of cells that did not exhibit a depolarization (6%) were discarded for subsequent analyses. A voltage timeline was built by calculating the baseline membrane potential of 45 s bins. For analysis of SST⁺ interneuron excitability, the duration of the ramp was divided into 175-millisecond bins and the mean inter-spike interval (ISI) was calculated for each period bin. Then, the instantaneous frequency (ISI⁻¹) was plotted against the mean current injected within the same bin. AP features were determined as follows: (1) overshoot was quantified as the amplitude of the AP above 0 mV. (2) Amplitude was calculated as the voltage difference between the peak of the AP and its threshold. (3) Width was determined at half the amplitude of the AP. (4) ΔTime was described as the time difference between the onset of pulse injection and the time point when the membrane potential reached the action potential threshold. (5) $dVdt^{-1}$ was defined as the first derivative of the voltage trace with respect to time.

RNAscope analysis

Quantification was done on the 40x images. The total number of cells was determined by the nucleus visualization given by Gill's hematoxylin staining. *Oxtr*⁺/*VGLUT1*⁺/*Gad1*⁺ neurons were manually identified and counted with ImageJ.

Statistics

All data are shown as mean \pm SEM. The number of animals and the test used for each analysis is specified in the Results section. To determine statistical differences we used Prism 7 (GraphPad). Sets of data ≥ 6 were tested for normality with a Shapiro-Wilk test, then a paired or unpaired t test was applied for two-group comparisons. Comparisons between more than two groups were performed with one or two-way ANOVAs. For not normally distributed data or data < 6, the non-parametric Wilcoxon and Mann-Whitney tests were applied for paired or unpaired experiments, respectively, for two-group comparisons. Datasets with more than two groups were analyzed using the Kruskal-Wallis and Friedman test.

4 Discussion

In the publications that compose this dissertation, we have used various techniques from computational neuroscience to investigate the brain at multiple levels of abstraction.

- Starting at the molecular level, we synthesized existing experimental insights on the interactions between neurotrophic factors into a mathematical model (Kirchner *et al.*, 2021). Mathematical analysis allowed us to identify the model's key characteristics and demonstrate how to map the molecular model onto a well-established phenomenological model of activity-dependent synaptic plasticity.
- Using the phenomenological model of synaptic plasticity at the dendrite level, we were able to explain the emergence of species-specific types of synaptic organization in the developing visual cortex (Kirchner *et al.*, 2021). Consistent with the model's predictions, the synaptic organization in the visual cortex of the macaque was recently demonstrated to resemble the synaptic organization in the ferret visual cortex (Ju *et al.*, 2020).
- At the circuit level, we used a feedforward model of visual pathway development to investigate the functional role of high-synchronicity-events in receptive field refinement (Wosniack *et al.*, 2021). Our model predicted a previously unnoticed property of high-synchronicity-events that they adapt their amplitude to the amplitude of preceding events, which we were able to verify by reanalyzing the experimental data.
- To better understand the effect of the hormone oxytocin on spontaneous activity in the developing cortex, we constructed a recurrent neural network model with an excitatory and an inhibitory population (Maldonado *et al.*, 2021). When calibrated with biologically-realistic parameters, we demon-

strate that a slight depolarization of a small (~25%) subpopulation of inhibitory cells is sufficient to explain the observed changes in spontaneous activity at the population level.

By mathematically connecting the models underlying these projects, in this dissertation, I demonstrate the ability of computational modeling to provide a unified language for explanations in neuroscience. Taken together, my research illustrates that interactions between spontaneous activity and synaptic plasticity are well-suited to instruct and support the maturation of the cortex at multiple levels of abstraction.

Open Questions and Outlook

The value of computational models reveals itself through the models' ability to describe biology, connect multiple experimental findings into a single framework, and extract principles beyond these multiple experimental observations (Abbott, 2008). Beyond the published work that forms the basis of this dissertation, I have contributed to several additional research projects that expand the published methods and are now in preparation for publication. These projects center on further aspects of brain development, such as

1. the impact of the Fragile X mutation on the circuit-level mechanism generating spontaneous activity during development.
2. the interactions between synaptic activity and dendrite growth in the developing cortex.
3. the emergence of multisensory processing in the developing higher-order cortex of mouse pups.

I briefly summarize the question and preliminary results from these studies and explain their relation to my published work that constitutes this dissertation.

Impact of a single gene mutation on circuit structure and spontaneous activity in the developing cortex

Zhuo-Shi Liu^{†1}, Jan Hendrik Kirchner[†], Juliette Cheyne, Christian Lohmann, and Julijana Gjorgjieva

Studying how circuits wire up in the brain during development helps us understand how the brain processes sensory information and generates behavior, which is important for understanding normal behaviors and brain disorders. Before an organism perceives its environment, spontaneous activity in the developing brain organizes and refines its circuitry (Kirkby *et al.*, 2013). Changes in this activity can lead to malformations in its wiring. Alterations of this type have been observed in a mutant mouse model of the Fragile X syndrome, where a single genetic mutation leads to changes in cortical inhibition and recruitment of additional neurons in spontaneous activity (Cheyne *et al.*, 2019; Gonçalves *et al.*, 2013). We do not understand exactly how spontaneous activity comes about, especially whether and how certain genes might affect it (Yap *et al.*, 2018).

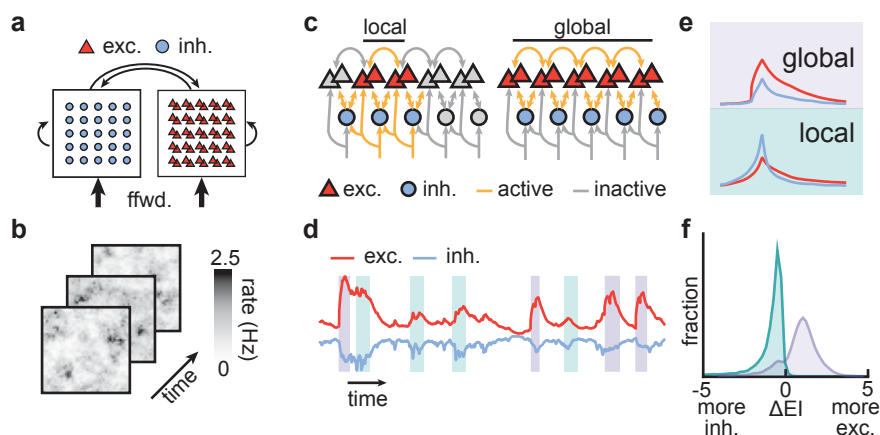


Figure 4.1: A computational model produces local and global events through differential inhibitory control. (a) Schematic of our recurrent network model with excitatory (E, red) and inhibitory (I, blue) cells arranged in a grid and locally connected with a Gaussian profile. (b) Three frames from spatially structured feedforward input. (c) Proposed mechanism for the generation of local and global events. (d) Averaged E and I activity as a function of time. Local and global events are highlighted in green and purple. (e) Average E and I activity at global and local events. (f) Histogram of E-I activity differences during the peak of local and global events.

We investigated how biologically realistic, spontaneous activity can emerge in recurrent networks with excitatory and inhibitory neurons and background input representing input from the sensory periphery. The model derives from the work

[†] indicates equal contribution.

4 Discussion

published in Maldonado *et al.* (2021). Our model accurately capture two distinct classes of spontaneous activity: Local (L-)events, and Global (H-)events, which match with experimentally characterized activity originating in the sensory periphery of the cortex (Leighton *et al.*, 2021; Siegel *et al.*, 2012) (Fig. 4.1a-c). When stimulation stems from the periphery, inputs onto inhibitory units are dominant, and only a limited portion of the excitatory units activates (Fig. 4.1c). Conversely, activation from within the cortex triggers dominant excitation that spreads laterally without restriction (Fig. 4.1c). Consistent with experimental data, we thus find that the differential drive onto excitation and inhibition can exhibit a powerful control over spontaneous activity in the developing cortex (Fig. 4.1d-e).

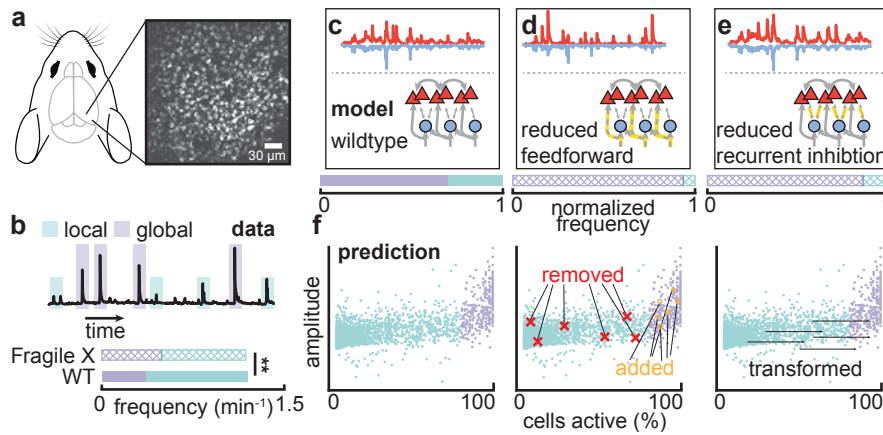


Figure 4.2: Two hypothesis for perturbed ratio of local and global events. (a) Field of view from calcium image experiments in the developing mouse visual cortex. Reanalyzed data from Cheyne *et al.* (2019). (b) Top: Example calcium trace averaged across the recorded cells, with local and global events highlighted. Bottom: Comparison of average frequency on local and global events in wildtype (lower) and Fragile X (upper) animals. (c–e) Averaged activity traces from excitatory (red) and inhibitory (blue) cells in the baseline model (c), the reduced feedforward model (d) and the reduced inhibition model (e). Bar plot below indicates observed change in frequency of local and global events as in b. (f) Model prediction about the relationship between amplitude and fraction of cells active per event.

We next reanalyzed calcium imaging data from the developing cortex of Fragile X and wildtype mice (Cheyne *et al.*, 2019) (Fig. 4.2a). Our analysis revealed spontaneous activity with an increase in global and a decrease in local events (Fig. 4.2b). Using our recurrent model, we explored two plausible mechanisms that lead to this altered activity: weakened feedforward input vs. reduced recurrent inhibitory connectivity (Fig. 4.2c-e). These alternatives make different experimentally-testable predictions for the relative ratio between local and global events (Fig. 4.2f). We are thus able to leverage computational modeling to propose two concrete mechanisms

capable of explaining part of the Fragile X phenotype and articulating the central role that inhibition might play in the disorder.

Beyond the Fragile X mutation, the proposed model allows us to investigate a host of modulating factors on characteristics of spontaneous activity. Further research could leverage this approach to explore the role of connectivity profiles, intrinsic excitability, and correlations in shaping spontaneous activity and the implications for receptive field refinements in development. Dissecting the influence of these factors in a model could guide experimental work and might eventually suggest approaches to understand and perhaps even treat disorders derived from altered circuit structure during development.

Activity-dependent dendrite growth through formation and removal of synapses

Jan Hendrik Kirchner^{†2}, Lucas Euler[†], and Julijana Gjorgjieva

Neurons can perform different computations depending on the shape of their dendrites and the formation of synapses with other neurons (Stuart *et al.*, 2016). Throughout brain development, dendrites grow and integrate into multiple networks simultaneously. Many experiments have shown that neural activity and synapse formation influence dendrite growth (Niell *et al.*, 2004; Podgorski *et al.*, 2021). Yet, computational models of dendrite growth have mostly assumed random branching (Kliemann, 1987), implemented activity-independent growth cones (Luczak, 2006), or generated dendrite morphologies based on abstract mathematical constraints (Torben-Nielsen *et al.*, 2014; van Veen *et al.*, 1992). These approaches can produce highly accurate neuronal morphologies and capture neurons at different developmental stages (Cuntz, 2016; Koene *et al.*, 2009). Still, they don't allow us to study how changes in the morphology of a neuron might constrain its functioning. Consequently, we cannot answer questions about the relationship between morphological variability and the firing patterns of individual neurons with these models.

^{2†} indicates equal contribution.

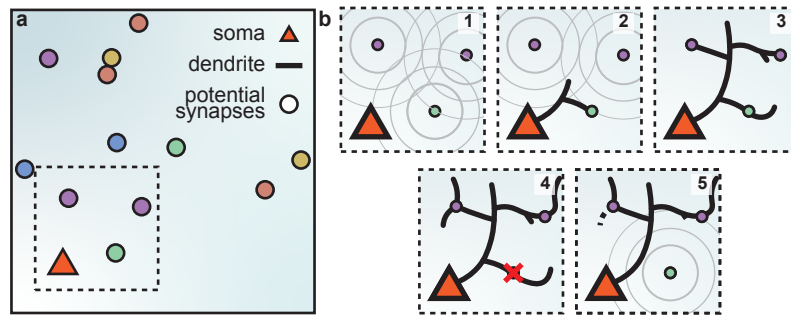


Figure 4.3: A model of dendrite growth for a cortical pyramidal neuron driven by spontaneous activity. (a) Schematic of the initial state. Color indicates group identity. (b) Schematic of growth and plasticity model. Soma and synapses correspond to box in a. Signaling molecules diffusing from potential synapses (1) attract dendrite growth and thus promote synapse formation (2) independent of firing pattern (3). Synapses stabilize or disconnect according to local correlations in their activation (4). Stable synapses anchor the dendrite, which would otherwise retract (5).

Based on our published work on activity-dependent synaptic organization (Kirchner *et al.*, 2021), we propose a model in which dendrite growth and retraction stem from combining activity-dependent and -independent cues from potential synaptic partners (Fig. 4.3a). A newly formed synaptic contact is either stabilized or removed according to our local plasticity rule for synaptic organization (Kirchner *et al.*, 2021) (Fig. 4.3b). The corresponding branch retracts if a synapse gets removed from the dendrite, thus connecting neural activity and dendritic shape in a dynamical system.

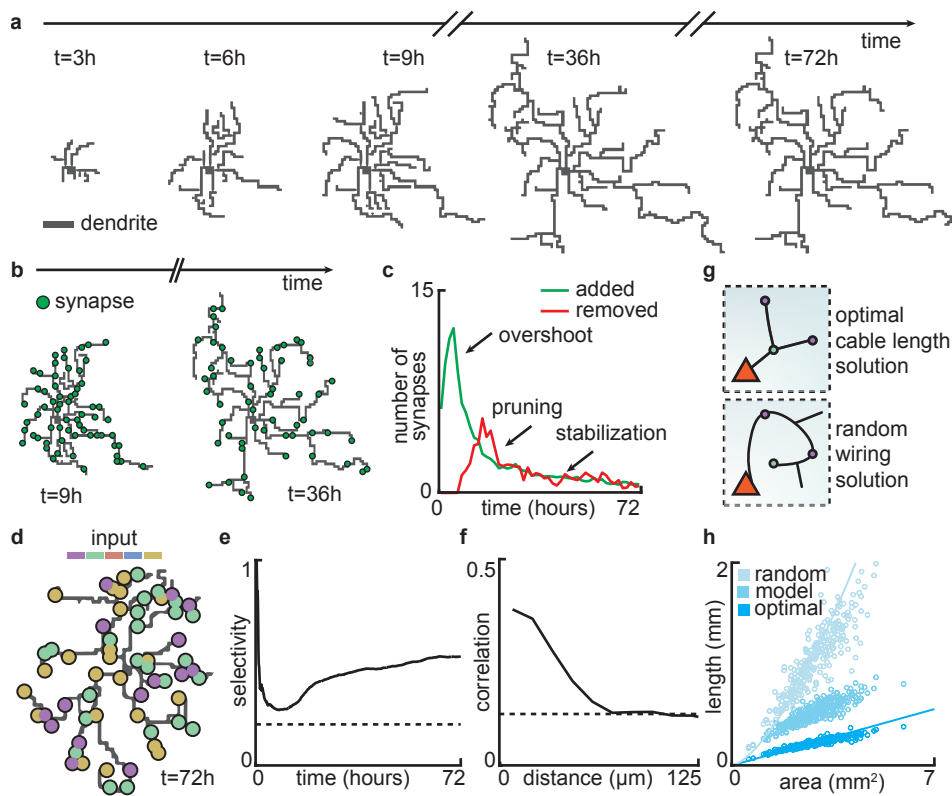


Figure 4.4: Spontaneous activity and a local plasticity rule drive balanced growth and retraction of dendrites and synapse formation in distinct phases. (a) Example of dendrite at five time points in our model. (b) Same dendrite as in a with formed synapses (green circle) superimposed. (c) Added synapses (green) and pruned synapses (red) as a function of time. Note the three emerging phases (overshoot, pruning, and stabilization). (d) Example of dendrite tree with synapses superimposed. Color indicates group identity. (e) Global group selectivity of dendrites as a function of time. Dashed line indicates chance level. (f) Average local correlation as a function of distance between pairs of synapses at $t=72h$. (g) Schematic illustrating optimal and random dendritic wiring. (h) Tree length as a function of area occupied in the optimal, simulated and random scenario. Lines correspond to analytic predictions.

Stable dendritic morphologies emerge naturally in this model through three sequential phases of growth (overshoot, pruning, and stabilization) (Fig. 4.4a-c). Dendrites only retain inputs that match the activity of their neighbors, while mismatched inputs are pruned (Fig. 4.4d). Thus, the dendrite becomes more selective for some input patterns over time (Fig. 4.4e), and nearby synapses are more likely to be correlated than distant synapses (Fig. 4.4f). Dendrite growth is determined by the nearest available synaptic partner (Fig. 4.3). As a consequence, dendrites approximate optimal wiring length (Fig. 4.4g,h). In summary, our mechanistic model captures diverse phenomena related to dendrite growth and suggests specific ways in which synaptic formation and removal control both form and function.

In this project, we have focused on the development of a few dendrites in a two-dimensional sheet of cortex to identify principles of dendrite development. However, with more powerful hardware becoming cheaper and more widely accessible (Sevilla *et al.*, 2022), a large-scale simulation of hundreds or thousands of neurons interacting and developing in parallel might soon be feasible. Such a model would allow the detailed investigation of reciprocal interactions between local dendritic plasticity and circuit-wide spontaneous activity.

Correlated spontaneous activity drives emergence of multi-sensory integration in the developing higher-order cortex

Jan Kirchner, Deyue Kong, Marina Wosniack, Paloma Maldonado, Alessandra Raspanti, Nawal Zabouri, Gertjan Houwens, Christian Lohmann, and Julijana Gjorgjieva

Not only the primary visual (V1) but also the somatosensory cortex (S1) and other cortical and subcortical areas in the developing rodent brain exhibit patterns of spontaneous activity before the onset of sensory experience (Golshani *et al.*, 2009). These patterns generally become more localized and sparse as the brain develops (Golshani *et al.*, 2009; Rochefort *et al.*, 2009; Siegel *et al.*, 2012). However, spontaneous events in S1 are sparser than their counterparts in V1 before eye-opening (Golshani *et al.*, 2009; Rochefort *et al.*, 2009), implying an earlier maturation of S1 relative to V1. V1 and S1's spontaneous activity propagates to higher cortical areas, with a common target being the rostralateral cortex (RL) (Glickfeld *et al.*, 2017; Wang *et al.*, 2007). The adult RL integrates multi-sensory inputs (visual and tactile), and ~60% of its neurons are bimodal (Olcese *et al.*, 2013). Furthermore, the visual and tactile maps are topographically aligned in RL, meaning they share a common coordinate system (Olcese *et al.*, 2013).

Since spontaneous activity is known to instruct various aspects of organization in the developing brain, we asked whether it might be involved in the refinement of connections between V1, S1, and RL. We expanded a published model (Wosniack *et al.*, 2021) to include the two primary cortices, one higher-order cortex, and feedforward connections between them (Fig. 4.5a,b). Using insights from the experimental data, we generate spontaneous activity with biologically realistic statistics as input to the system (Fig. 4.5c).

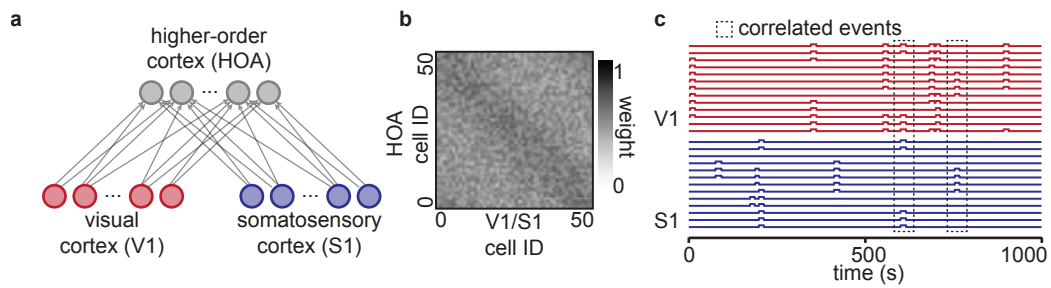


Figure 4.5: Model set-up and assumptions. (a) Schematic of a three population feed-forward model of the developing visual (V1), somatosensory (S1) and higher-order cortex (HOA). (b) Example of random initial connectivity matrix between V1 and HOA (connectivity matrix for S1 and HOA is chosen identically) with bias along the diagonal. (c) Sample of spontaneous events in V1 (top) and S1 (bottom) across cells as a function of time. Boxes highlight two spatiotemporally correlated events in V1 and S1.

Using this model, we investigated the emergence of bimodal RL neurons (Fig. 4.6a). We found that bimodal RL neurons develop when sufficient correlation between events in V1 and S1 exists (Fig. 4.6b) and could detect this correlation in experimentally recorded data (Fig. 4.6c,d). Furthermore, we found that the mixture of bimodal and unimodal neurons observed in biology is optimal for information decoding when visual and somatosensory activity is correlated (Fig. 4.6e,f).

4 Discussion

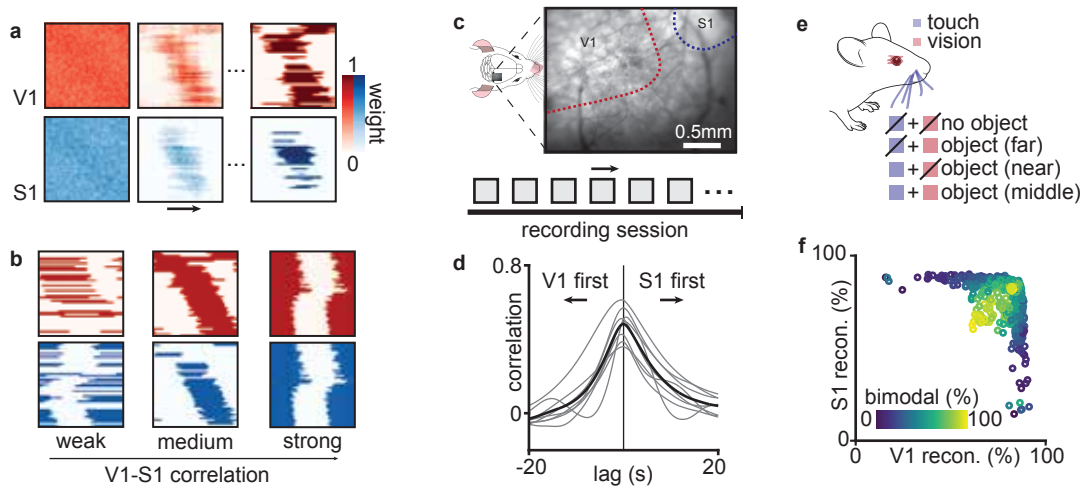


Figure 4.6: Emergence of bimodal neurons through biologically realistic correlated activity and optimal decoding. (a) Example of refinement of connectivity matrix between V1 and HOA (top) and S1 and HOA (bottom). (b). Example of connectivity matrices in steady state from simulations with low (left) to high (right) correlation between V1 and S1. (c) Schematic of the widefield experiments. An area encompassing V1 and S1 imaged over a 100 min recording session. (d) Correlation between activity in the somatosensory and the visual cortex as a function of the lag. Individual animals (grey) and average (black) superimposed. Vertical black line indicates zero lag. (e) Schematic of different possible combinations of sensory stimulation. (f) S1 and V1 reconstruction as a function of the percentage of bimodal cells.

Thus, by combining theory and experiments, we find that activity-dependent plasticity can instruct cross-cortical wiring in the developing cortex and produce circuits that efficiently integrate information from multiple modalities. Future research could elucidate how different higher-order cortices manage to specialize in processing different aspects of multisensory stimuli (Murakami *et al.*, 2017) or how the processed stimuli might inform downstream tasks like decision making and motor planning.

Simplicity in the developing brain

The work in this dissertation is based on the idea that computational models can connect different levels of abstraction. In the projects highlighted in the previous sections, I have looked at how this principle applies to different areas, such as neurodevelopmental disorders, the temporal dynamics of dendrite development, or the relationship between primary and higher-order cortices. Intriguingly, the previously published models naturally extend to these areas, demonstrating their broad explanatory potential (Abbott, 2008).

Despite the different focus of each project, the work presented in this thesis shares a methodological core. When creating a computational model, I attempt to *only* include the essential aspects that produce a given phenomenon. This allows the model to be general enough to be applied to different systems, while still being specific enough to describe complex biological phenomena. This principle of parsimony (Occam's razor; Sober, 2015) is well-known in philosophy and science alike. However, the principle is not always applicable (Webb, 1996). Some philosophers go as far as to argue that it is impossible to create a simple model of how the brain works at the highest levels of abstraction (McGinn, 1989). In this closing section of my dissertation, I want to lay out an argument for why we might have a more optimistic outlook on the future of neuroscience.

Building a brain is an amazing feat. Not only is the resulting, adult brain extremely complex, but the process of creating it is also very intricately constrained. In particular:

1. The genetic code that controls brain development does not specify the exact connectivity of the mature brain (Price *et al.*, 2017; Witvliet *et al.*, 2021). Instead, the code must be able to sequentially *bootstrap* the brain into function, using the immature brain's basic structure and activity to gradually build a more sophisticated brain (Richter *et al.*, 2017).
2. Faced with an adversarial environment, the developing brain needs to respond robustly to severe perturbations. Malnourishment, minor genetic mutation, or assault by predators are not uncommon and are compensated for by the appropriate alterations to development (Chapman *et al.*, 1993; Zheng *et al.*, 2014).
3. Despite the need for acute robustness to adversarial inputs, the developing brain nonetheless needs to be able to absorb and internalize the specifics of its environment flexibly (Berkes *et al.*, 2011; Roy *et al.*, 2020). In particular, the highly protracted development of the human brain illustrates how the brain must be able to adapt to new experiences as they arise throughout life.

Given the complex and opposing constraints that exist, it is surprising that brain development is something that can be modeled computationally. Additionally, it is impressive that simple models can explain a lot about brain development. A hint for why we might find comparatively simple explanations comes from recent advances in artificial intelligence (Team *et al.*, 2021; Valle-Perez *et al.*, 2018; Wang *et al.*, 2016). A system confronted with a wide range of diverse tasks is incentivized to develop robust learning routines (Wang *et al.*, 2016), which allow the system to flexibly act in novel environments (Team *et al.*, 2021). Intriguingly, this astonishing ability of artificial systems stems from an implicit bias towards simple solutions, which tend to

4 Discussion

generalize much better than more complex solutions (Valle-Perez *et al.*, 2018). Note that *simplicity* in this context has the technical meaning of *mathematically concise*, and not necessarily *composed of few components* (Rasmussen *et al.*, 2000).

Could the brain also be biased towards simple solutions? The work in this dissertation demonstrates that, sometimes, we can characterize developmental processes with mathematically concise computational models. Suppose this type of simplicity is a foundational aspect of brain development. In that case, future research will uncover increasingly concise but expressive computational models that can explain both normal function and developmental disorders. Thus, the discovery of simple computational models might be a step toward a unified understanding of how the brain develops.

Bibliography

1. Abbott, L. F. Theoretical neuroscience rising. *Neuron* **60**, 489–495 (2008).
2. Adoff, M. D., Climer, J. R., Davoudi, H., Marvin, J. S., Looger, L. L. & Dombeck, D. A. The functional organization of excitatory synaptic input to place cells. *Nature Communications* **12**, 3558 (2021).
3. Ashaber, M., Tomina, Y., Kassraian, P., Bushong, E. A., Kristan, W. B., Ellisman, M. H. & Wagenaar, D. A. Anatomy and activity patterns in a multifunctional motor neuron and its surrounding circuits. *eLife* **10**, e61881 (2021).
4. Barde, Y. A., Edgar, D. & Thoenen, H. Purification of a new neurotrophic factor from mammalian brain. *The EMBO Journal* **1**, 549–553 (1982).
5. Berkes, P., Orbán, G., Lengyel, M. & Fiser, J. Spontaneous cortical activity reveals hallmarks of an optimal internal model of the environment. *Science* **331**, 83–87 (2011).
6. Bollmann, J. H. & Engert, F. Subcellular topography of visually driven dendritic activity in the vertebrate visual system. *Neuron* **61**, 895–905 (2009).
7. Borges, J. L. & Casares, A. B. *On exactitude in science (A. Hurley, Trans.)* (1946).
8. El-Boustani, S., Ip, J. P. K., Breton-Provencher, V., Knott, G. W., Okuno, H., Bito, H. & Sur, M. Locally coordinated synaptic plasticity of visual cortex neurons in vivo. *Science* **360**, 1349–1354 (2018).
9. Bureau, I., Shepherd, G. M. G. & Svoboda, K. Circuit and plasticity defects in the developing somatosensory cortex of FMR1 knock-out mice. *The Journal of Neuroscience* **28**, 5178–5188 (2008).
10. Burkitt, A. N. A Review of the Integrate-and-fire Neuron Model: I. Homogeneous Synaptic Input. *Biological Cybernetics* **95**, 1–19 (2006).
11. Chapman, B. & Stryker, M. P. Development of orientation selectivity in ferret visual cortex and effects of deprivation. *The Journal of Neuroscience* **13**, 5251–5262 (1993).
12. Cheyne, J. E., Zabouri, N., Baddeley, D. & Lohmann, C. Spontaneous Activity Patterns Are Altered in the Developing Visual Cortex of the Fmr1 Knock-out Mouse. *Frontiers in Neural Circuits* **13**, 57 (2019).
13. Cuntz, H. in *Dendrites* 487–504 (2016).

Bibliography

14. Dayan, P. & Abbott, L. *Theoretical neuroscience: computational and mathematical modeling of neural systems* (2005).
15. Ebner, C., Clopath, C., Jedlicka, P. & Cuntz, H. Unifying Long-Term Plasticity Rules for Excitatory Synapses by Modeling Dendrites of Cortical Pyramidal Neurons. *Cell Reports* **29**, 4295–4307.e6 (2019).
16. Frank, A. C., Huang, S., Zhou, M., Gdalyahu, A., Kastellakis, G., Silva, T. K., Lu, E., Wen, X., Poirazi, P., Trachtenberg, J. T. & Silva, A. J. Hotspots of dendritic spine turnover facilitate clustered spine addition and learning and memory. *Nature Communications* **9**, 422 (2018).
17. Froemke, R. C. & Young, L. J. Oxytocin, Neural Plasticity, and Social Behavior. *Annual Review of Neuroscience* **44**, 359–381 (2021).
18. Fu, M., Yu, X., Lu, J. & Zuo, Y. Repetitive motor learning induces coordinated formation of clustered dendritic spines in vivo. *Nature* **483**, 92–95 (2012).
19. Ge, X., Zhang, K., Gribizis, A., Hamodi, A. S., Sabino, A. M. & Crair, M. C. Retinal waves prime visual motion detection by simulating future optic flow. *Science* (2021).
20. Gerstner, W., Kistler, W. M., Naud, R. & Paninski, L. *Neuronal Dynamics: From Single Neurons to Networks and Models of Cognition* (2014).
21. Glickfeld, L. L. & Olsen, S. R. Higher-Order Areas of the Mouse Visual Cortex. *Annual Review of Vision Science* **3**, 251–273 (2017).
22. Gökçe, O., Bonhoeffer, T. & Scheuss, V. Clusters of synaptic inputs on dendrites of layer 5 pyramidal cells in mouse visual cortex. *eLife* **5**, e09222 (2016).
23. Golshani, P., Gonçalves, J. T., Khoshkhou, S., Mostany, R., Smirnakis, S. & Portera-Cailliau, C. Internally Mediated Developmental Desynchronization of Neocortical Network Activity. *Journal of Neuroscience* **29**, 10890–10899 (2009).
24. Gonçalves, J. T., Anstey, J. E., Golshani, P. & Portera-Cailliau, C. Circuit level defects in the developing neocortex of Fragile X mice. *Nature Neuroscience* **16**, 903–909 (2013).
25. Grinevich, V., Desarménien, M. G., Chini, B., Tauber, M. & Muscatelli, F. Ontogenesis of oxytocin pathways in the mammalian brain: late maturation and psychosocial disorders. *Frontiers in Neuroanatomy* **8** (2015).
26. Hammock, E. & Levitt, P. Oxytocin receptor ligand binding in embryonic tissue and postnatal brain development of the C57BL/6J mouse. *Frontiers in Behavioral Neuroscience* **7** (2013).

27. Harward, S. C., Hedrick, N. G., Hall, C. E., Parra-Bueno, P., Milner, T. A., Pan, E., Laviv, T., Hempstead, B. L., Yasuda, R. & McNamara, J. O. Autocrine BDNF–TrkB signalling within a single dendritic spine. *Nature* **538**, 99–103 (2016).
28. Hedrick, N. G., Harward, S. C., Hall, C. E., Murakoshi, H., McNamara, J. O. & Yasuda, R. Rho GTPase complementation underlies BDNF-dependent homo- and heterosynaptic plasticity. *Nature* **538**, 104–108 (2016).
29. Hopfield, J. J. & Tank, D. W. Computing with Neural Circuits: A Model. *Science* **233**, 625–633 (1986).
30. Iacaruso, M. F., Gasler, I. T. & Hofer, S. B. Synaptic organization of visual space in primary visual cortex. *Nature* **547**, 449–452 (2017).
31. Iascone, D. M., Li, Y., Sömbül, U., Doron, M., Chen, H., Andreu, V., Goudy, F., Blockus, H., Abbott, L. F., Segev, I., Peng, H. & Polleux, F. Whole-Neuron Synaptic Mapping Reveals Spatially Precise Excitatory/Inhibitory Balance Limiting Dendritic and Somatic Spiking. *Neuron* **106**, 566–578.e8 (2020).
32. Jang, J., Song, M. & Paik, S.-B. Retino-cortical mapping ratio predicts columnar and salt-and-pepper organization in mammalian visual cortex. *Cell Reports* **30**, 3270–3279.e3 (2020).
33. Je, H. S., Yang, F., Ji, Y., Nagappan, G., Hempstead, B. L. & Lu, B. Role of pro-brain-derived neurotrophic factor (proBDNF) to mature BDNF conversion in activity-dependent competition at developing neuromuscular synapses. *Proceedings of the National Academy of Sciences* **109**, 15924–15929 (2012).
34. Jia, H., Rochefort, N. L., Chen, X. & Konnerth, A. Dendritic organization of sensory input to cortical neurons in vivo. *Nature* **464**, 1307–1312 (2010).
35. Jia, H., Varga, Z., Sakmann, B. & Konnerth, A. Linear integration of spine Ca²⁺ signals in layer 4 cortical neurons in vivo. *Proceedings of the National Academy of Sciences* **111**, 9277–9282 (2014).
36. Ju, N., Li, Y., Liu, F., Jiang, H., Macknik, S. L., Martinez-Conde, S. & Tang, S. Spatiotemporal functional organization of excitatory synaptic inputs onto macaque V1 neurons. *Nature Communications* **11**, 697 (2020).
37. Katoh-Semba, R., Takeuchi, I. K., Semba, R. & Kato, K. Distribution of Brain-Derived Neurotrophic Factor in Rats and Its Changes with Development in the Brain. *Journal of Neurochemistry* **69**, 34–42 (1997).
38. Kerlin, A., Mohar, B., Flickinger, D., MacLennan, B. J., Dean, M. B., Davis, C., Spruston, N. & Svoboda, K. Functional clustering of dendritic activity during decision-making. *eLife* **8**, e46966 (2019).

Bibliography

39. Kim, N., Bahn, S., Choi, J. H., Kim, J. S. & Rah, J.-C. Synapses from the motor cortex and a high-order thalamic nucleus are spatially clustered in proximity to each other in the distal tuft dendrites of mouse somatosensory cortex. *Cerebral Cortex* (2021).
40. Kirchner, J. H. & Gjorgjieva, J. Emergence of local and global synaptic organization on cortical dendrites. *Nature Communications* **12**, 4005 (2021).
41. Kirchner, J. H. & Gjorgjieva, J. Emergence of synaptic organization and computation in dendrites. *Neuroforum* **28**, 21–30 (2022).
42. Kirkby, L., Sack, G., Firl, A. & Feller, M. B. A role for correlated spontaneous activity in the assembly of neural circuits. *Neuron* **80**, 1129–1144 (2013).
43. Kleindienst, T., Winnubst, J., Roth-Alpermann, C., Bonhoeffer, T. & Lohmann, C. Activity-Dependent Clustering of Functional Synaptic Inputs on Developing Hippocampal Dendrites. *Neuron* **72**, 1012–1024 (2011).
44. Kliemann, W. A stochastic dynamical model for the characterization of the geometrical structure of dendritic processes. *Bulletin of Mathematical Biology* **49**, 135 (1987).
45. Koene, R. A., Tijms, B., van Hees, P., Postma, F., de Ridder, A., Ramakers, G. J. A., van Pelt, J. & van Ooyen, A. NETMORPH: A Framework for the Stochastic Generation of Large Scale Neuronal Networks With Realistic Neuron Morphologies. *Neuroinformatics* **7**, 195–210 (2009).
46. Kowiański, P., Lietzau, G., Czuba, E., Wańkow, M., Steliga, A. & Moryś, J. BDNF: A Key Factor with Multipotent Impact on Brain Signaling and Synaptic Plasticity. *Cellular and Molecular Neurobiology* **38**, 579–593 (2018).
47. La Fata, G., Gärtner, A., Domínguez-Iturza, N., Dresselaers, T., Dawitz, J., Poorthuis, R. B., Aversa, M., Himmelreich, U., Meredith, R. M., Achsel, T., Dotti, C. G. & Bagni, C. FMRP regulates multipolar to bipolar transition affecting neuronal migration and cortical circuitry. *Nature Neuroscience* **17**, 1693–1700 (2014).
48. Larsen, D. D. & Callaway, E. M. Development of layer-specific axonal arborizations in mouse primary somatosensory cortex. *Journal of Comparative Neurology* **494**, 398–414 (2006).
49. Laurent, G. On the value of model diversity in neuroscience. *Nature Reviews Neuroscience* **21**, 395–396 (2020).
50. Laviv, T. & Yasuda, R. Imaging neuronal protein signaling dynamics in vivo. *Current Opinion in Neurobiology* **69**, 68–75 (2021).
51. Lee, K. F. H., Soares, C., Thivierge, J.-P. & Béïque, J.-C. Correlated Synaptic Inputs Drive Dendritic Calcium Amplification and Cooperative Plasticity during Clustered Synapse Development. *Neuron* **89**, 784–799 (2016).

52. Lee, K.-S., Vandemark, K., Mezey, D., Shultz, N. & Fitzpatrick, D. Functional synaptic architecture of callosal inputs in mouse primary visual cortex. *Neuron* **101**, 421–428.e5 (2019).
53. Lee, R., Kermani, P., Teng, K. K. & Hempstead, B. L. Regulation of Cell Survival by Secreted Proneurotrophins. *Science* **294**, 1945–1948 (2001).
54. Leibrock, J., Lottspeich, F., Hohn, A., Hofer, M., Hengerer, B., Masiakowski, P., Thoenen, H. & Barde, Y.-A. Molecular cloning and expression of brain-derived neurotrophic factor. *Nature* **341**, 149–152 (1989).
55. Leighton, A. H., Cheyne, J. E., Houwen, G. J., Maldonado, P. P., De Winter, F., Levelt, C. N. & Lohmann, C. Somatostatin interneurons restrict cell recruitment to retinally driven spontaneous activity in the developing cortex. *Cell Reports* **36**, 109316 (2021).
56. Leighton, A. H. & Lohmann, C. The wiring of developing sensory circuits—from patterned spontaneous activity to synaptic plasticity mechanisms. *Frontiers in Neural Circuits* **10**, 71 (2016).
57. Letzkus, J. J., Kampa, B. M. & Stuart, G. J. Learning rules for spike timing-dependent plasticity depend on dendritic synapse location. *Journal of Neuroscience* **26**, 10420–10429 (2006).
58. Levenstein, D., Alvarez, V. A., Amarasingham, A., Azab, H., Gerkin, R. C., Hasenstaub, A., Iyer, R., Jolivet, R. B., Marzen, S., Monaco, J. D., Prinz, A. A., Quraishi, S., Santamaria, F., Shivkumar, S., Singh, M. F., Stockton, D. B., Traub, R., Rotstein, H. G., Nadim, F. & Redish, A. D. On the role of theory and modeling in neuroscience. *arXiv* (2020).
59. Lohmann, C. & Wong, R. O. L. Regulation of dendritic growth and plasticity by local and global calcium dynamics. *Cell Calcium* **37**, 403–409 (2005).
60. Lu, B., Pang, P. T. & Woo, N. H. The yin and yang of neurotrophin action. *Nature Reviews Neuroscience* **6**, 603–614 (2005).
61. Lu, H., Park, H. & Poo, M.-M. Spike-timing-dependent BDNF secretion and synaptic plasticity. *Philosophical Transactions of the Royal Society B: Biological Sciences* **369**, 20130132 (2014).
62. Lucion, A. B. & Bortolini, M. C. Mother–Pup Interactions: Rodents and Humans. *Frontiers in Endocrinology* **5**, 17 (2014).
63. Luczak, A. Spatial embedding of neuronal trees modeled by diffusive growth. *Journal of Neuroscience Methods* **157**, 132–141 (2006).
64. Maldonado, P. P., Nuno-Perez, A., Kirchner, J. H., Hammock, E., Gjorgjieva, J. & Lohmann, C. Oxytocin Shapes Spontaneous Activity Patterns in the Developing Visual Cortex by Activating Somatostatin Interneurons. *Current Biology* **31**, 322–333.e5 (2021).

Bibliography

65. Marder, E. Theoretical musings. *eLife* **9**, e60703 (2020).
66. Marlin, B. J., Mitre, M., D'amour, J. A., Chao, M. V. & Froemke, R. C. Oxytocin enables maternal behaviour by balancing cortical inhibition. *Nature* **520**, 499–504 (2015).
67. McBride, T. J., Rodriguez-Contreras, A., Trinh, A., Bailey, R. & DeBello, W. M. Learning Drives Differential Clustering of Axodendritic Contacts in the Barn Owl Auditory System. *Journal of Neuroscience* **28**, 6960–6973 (2008).
68. McGinn, C. Can we solve the Mind–Body problem? *Mind* **98**, 349–366 (1989).
69. McLaughlin, T. & O'Leary, D. D. M. Molecular gradients and development of retinotopic maps. *Annual Review of Neuroscience* **28**, 327–355 (2005).
70. Mel, B. *The Clusteron: Toward a Simple Abstraction for a Complex Neuron in Advances in Neural Information Processing Systems* **4** (1991).
71. Miller, T. V. & Caldwell, H. K. Oxytocin during Development: Possible Organizational Effects on Behavior. *Frontiers in Endocrinology* **6** (2015).
72. Molnár, Z., Luhmann, H. J. & Kanold, P. O. Transient cortical circuits match spontaneous and sensory-driven activity during development. *Science* **370**, eabb2153 (2020).
73. Murakami, T., Matsui, T. & Ohki, K. Functional Segregation and Development of Mouse Higher Visual Areas. *Journal of Neuroscience* **37**, 9424–9437 (2017).
74. Nagappan, G., Zaitsev, E., Senatorov, V. V., Yang, J., Hempstead, B. L. & Lu, B. Control of extracellular cleavage of ProBDNF by high frequency neuronal activity. *Proceedings of the National Academy of Sciences* **106**, 1267–1272 (2009).
75. Naskar, S., Narducci, R., Balzani, E., Cwetsch, A. W., Tucci, V. & Cancedda, L. The development of synaptic transmission is time-locked to early social behaviors in rats. *Nature Communications* **10**, 1195 (2019).
76. Niculescu, D., Michaelsen-Preusse, K., Güner, Ü., van Dorland, R., Wierenga, C. J. & Lohmann, C. A BDNF-mediated push-pull plasticity mechanism for synaptic clustering. *Cell Reports* **24**, 2063–2074 (2018).
77. Niell, C. M., Meyer, M. P. & Smith, S. J. In vivo imaging of synapse formation on a growing dendritic arbor. *Nature Neuroscience* **7**, 254–260 (2004).
78. Okun, M. & Lampl, I. Instantaneous correlation of excitation and inhibition during ongoing and sensory-evoked activities. *Nature Neuroscience* **11**, 535–537 (2008).
79. Okun, M. & Lampl, I. Instantaneous correlation of excitation and inhibition during ongoing and sensory-evoked activities. *Nature Neuroscience* **11**, 535–537 (2008).

80. Olcese, U., Iurilli, G. & Medini, P. Cellular and synaptic architecture of multisensory integration in the mouse neocortex. *Neuron* **79**, 579–593 (2013).
81. Park, H. & Poo, M.-m. Neurotrophin regulation of neural circuit development and function. *Nature Reviews Neuroscience* **14**, 7–23 (2013).
82. Payeur, A., Béïque, J.-C. & Naud, R. Classes of dendritic information processing. *Current Opinion in Neurobiology* **58**, 78–85 (2019).
83. Perovic, M., Tesic, V., Mladenovic Djordjevic, A., Smiljanic, K., Loncarevic-Vasiljkovic, N., Ruzdijic, S. & Kanazir, S. BDNF transcripts, proBDNF and proNGF, in the cortex and hippocampus throughout the life span of the rat. *AGE* **35**, 2057–2070 (2013).
84. Podgorski, K., Toth, T. D., Coleman, P., Opushnyev, S., Brusco, J., Hogg, P., Edgcumbe, P. & Haas, K. Comprehensive imaging of synaptic activity reveals dendritic growth rules that cluster inputs. *bioRxiv*, 2021.02.11.430646 (2021).
85. Poirazi, P., Brannon, T. & Mel, B. W. Pyramidal neuron as two-layer neural network. *Neuron* **37**, 989–999 (2003).
86. Poirazi, P. & Papoutsi, A. Illuminating dendritic function with computational models. *Nature Reviews Neuroscience* **21**, 303–321 (2020).
87. Pollen, A. A., Dobberfuhr, A. P., Scace, J., Igulu, M. M., Renn, S. C. P., Shumway, C. A. & Hofmann, H. A. Environmental Complexity and Social Organization Sculpt the Brain in Lake Tanganyikan Cichlid Fish. *Brain, Behavior and Evolution* **70**, 21–39 (2007).
88. Prescott, S. A., Ratté, S., De Koninck, Y. & Sejnowski, T. J. Pyramidal Neurons Switch From Integrators In Vitro to Resonators Under In Vivo-Like Conditions. *Journal of Neurophysiology* **100**, 3030–3042 (2008).
89. Price, D. J., Jarman, A. P., Mason, J. O. & Kind, P. C. *Building brains: an introduction to neural development* (2017).
90. Pulikkottil, V. V., Somashekar, B. P. & Bhalla, U. S. Computation, wiring, and plasticity in synaptic clusters. *Current Opinion in Neurobiology* **70**, 101–112 (2021).
91. Rajamani, K. T., Wagner, S., Grinevich, V. & Harony-Nicolas, H. Oxytocin as a Modulator of Synaptic Plasticity: Implications for Neurodevelopmental Disorders. *Frontiers in Synaptic Neuroscience* **10** (2018).
92. Rall, W. Theory of Physiological Properties of Dendrites. *Annals of the New York Academy of Sciences* **96**, 1071–1092 (1962).
93. Rasmussen, C. & Ghahramani, Z. Occam’s razor. *Advances in neural information processing systems* **13** (2000).

Bibliography

94. Redondo, R. L. & Morris, R. G. M. Making memories last: the synaptic tagging and capture hypothesis. *Nature Reviews Neuroscience* **12**, 17–30 (2011).
95. Richter, L. M. & Gjorgjieva, J. Understanding neural circuit development through theory and models. *Current Opinion in Neurobiology* **46**, 39–47 (2017).
96. Rochefort, N. L., Garaschuk, O., Milos, R.-I., Narushima, M., Marandi, N., Pichler, B., Kovalchuk, Y. & Konnerth, A. Sparsification of neuronal activity in the visual cortex at eye-opening. *Proceedings of the National Academy of Sciences* **106**, 15049–15054 (2009).
97. Rossi, L. F., Harris, K. D. & Carandini, M. Spatial connectivity matches direction selectivity in visual cortex. *Nature* **588**, 648–652 (2020).
98. Roy, A., Wang, S., Meschede-Krasa, B., Breffle, J. & Van Hooser, S. D. An early phase of instructive plasticity before the typical onset of sensory experience. *Nature Communications* **11**, 11 (2020).
99. Rumsey, C. C. & Abbott, L. F. Synaptic Democracy in Active Dendrites. *Journal of Neurophysiology* **96**, 2307–2318 (2006).
100. Schneider, A., Hagerman, R. & Hessel, D. Fragile X syndrome—From genes to cognition. *Developmental Disabilities Research Reviews* **15**, 333–342 (2009).
101. Scholl, B., Wilson, D. E. & Fitzpatrick, D. Local order within global disorder: synaptic architecture of visual space. *Neuron* **96**, 1127–1138.e4 (2017).
102. Schoonover, C. E., Tapia, J.-C., Schilling, V. C., Wimmer, V., Blazeski, R., Zhang, W., Mason, C. A. & Bruno, R. M. Comparative Strength and Dendritic Organization of Thalamocortical and Corticocortical Synapses onto Excitatory Layer 4 Neurons. *The Journal of Neuroscience* **34**, 6746–6758 (2014).
103. Sevilla, J., Heim, L., Ho, A., Besiroglu, T., Hobbhahn, M. & Villalobos, P. Compute Trends Across Three Eras of Machine Learning. *arXiv* (2022).
104. Siegel, F., Heimel, J. A., Peters, J. & Lohmann, C. Peripheral and central inputs shape network dynamics in the developing visual cortex in vivo. *Current Biology* **22**, 253–258 (2012).
105. Sober, E. *Ockam's Razor: A User's Manual* (Cambridge University Press Cambridge, 2015).
106. Spruston, N., Schiller, Y., Stuart, G. & Sakmann, B. Activity-Dependent Action Potential Invasion and Calcium Influx into Hippocampal CA1 Dendrites. *Science* **268**, 297–300 (1995).
107. Stafford, B. K., Sher, A., Litke, A. M. & Feldheim, D. A. Spatial-Temporal Patterns of Retinal Waves Underlying Activity-Dependent Refinement of Retinofugal Projections. *Neuron* **64**, 200–212 (2009).

108. Sterratt, D. C., Groen, M. R., Meredith, R. M. & Ooyen, A. v. Spine Calcium Transients Induced by Synaptically-Evoked Action Potentials Can Predict Synapse Location and Establish Synaptic Democracy. *PLOS Computational Biology* **8**, e1002545 (2012).
109. Stevens, C. & Zador, A. When is an Integrate-and-fire Neuron like a Poisson Neuron? *Advances in Neural Information Processing Systems* **8** (1995).
110. Strata, P. & Harvey, R. Dale's principle. *Brain Research Bulletin* **50**, 349–350 (1999).
111. Stringer, C., Pachitariu, M., Steinmetz, N., Reddy, C. B., Carandini, M. & Harris, K. D. Spontaneous behaviors drive multidimensional, brainwide activity. *Science* **364**, eaav7893 (2019).
112. Stuart, G., Spruston, N. & Hausser, M. *Dendrites* (2016).
113. Sutor, B. & Luhmann, H. J. Development of excitatory and inhibitory post-synaptic potentials in the rat neocortex. *Perspectives on Developmental Neurobiology* **2**, 409–419 (1995).
114. Takahashi, N., Kitamura, K., Matsuo, N., Mayford, M., Kano, M., Matsuki, N. & Ikegaya, Y. Locally synchronized synaptic inputs. *Science* **335**, 353–356 (2012).
115. Team, O. E. L., Stooke, A., Mahajan, A., Barros, C., Deck, C., Bauer, J., Synowski, J., Trebacz, M., Jaderberg, M., Mathieu, M., *et al.* Open-ended learning leads to generally capable agents. *arXiv preprint arXiv:2107.12808* (2021).
116. Teng, H. K., Teng, K. K., Lee, R., Wright, S., Tevar, S., Almeida, R. D., Kermani, P., Torkin, R., Chen, Z.-Y., Lee, F. S., Kraemer, R. T., Nykjaer, A. & Hempstead, B. L. ProBDNF Induces Neuronal Apoptosis via Activation of a Receptor Complex of p75NTR and Sortilin. *Journal of Neuroscience* **25**, 5455–5463 (2005).
117. Tiriach, A., Smith, B. E. & Feller, M. B. Light prior to eye-opening promotes retinal waves and eye-specific segregation. *Neuron* **100**, 1059–1065.e4 (2018).
118. Torben-Nielsen, B. & De Schutter, E. Context-aware modeling of neuronal morphologies. *Frontiers in Neuroanatomy* **8**, 92 (2014).
119. Tzilivaki, A., Kastellakis, G. & Poirazi, P. Challenging the point neuron dogma: FS basket cells as 2-stage nonlinear integrators. *Nature Communications* **10**, 1–14 (2019).
120. Vaidyanathan, R. & Hammock, E. A. Oxytocin receptor dynamics in the brain across development and species. *Developmental Neurobiology* **77**, 143–157 (2017).

Bibliography

121. Valle-Perez, G., Camargo, C. Q. & Louis, A. A. Deep learning generalizes because the parameter-function map is biased towards simple functions. *arXiv preprint arXiv:1805.08522* (2018).
122. Van Veen, M. & van Pelt, J. A model for outgrowth of branching neurites. *Journal of Theoretical Biology* **159**, 1–23 (1992).
123. Wang, J. X., Kurth-Nelson, Z., Tirumala, D., Soyer, H., Leibo, J. Z., Munos, R., Blundell, C., Kumaran, D. & Botvinick, M. Learning to reinforcement learn. *arXiv preprint arXiv:1611.05763* (2016).
124. Wang, Q. & Burkhalter, A. Area map of mouse visual cortex. *Journal of Comparative Neurology* **502**, 339–357 (2007).
125. Webb, G. I. Further experimental evidence against the utility of Occam's razor. *Journal of Artificial Intelligence Research* **4**, 397–417 (1996).
126. Weiler, S., Guggiana Nilo, D., Bonhoeffer, T., Hübener, M., Rose, T. & Scheuss, V. Orientation and direction tuning align with dendritic morphology and spatial connectivity in mouse visual cortex. *Current Biology* (2022).
127. Willshaw, D. J., Von Der Malsburg, C. & Longuet-Higgins, H. C. How patterned neural connections can be set up by self-organization. *Proceedings of the Royal Society B: Biological Sciences* **194**, 431–445 (1976).
128. Wilson, D. E., Whitney, D. E., Scholl, B. & Fitzpatrick, D. Orientation selectivity and the functional clustering of synaptic inputs in primary visual cortex. *Nature Neuroscience* **19**, 1003–1009 (2016).
129. Wilson, H. R. & Cowan, J. D. Excitatory and inhibitory interactions in localized populations of model neurons. *Biophysical Journal* **12**, 1–24 (1972).
130. Winnubst, J., Cheyne, J. E., Niculescu, D. & Lohmann, C. Spontaneous activity drives local synaptic plasticity in vivo. *Neuron* **87**, 399–410 (2015).
131. Witvliet, D., Mulcahy, B., Mitchell, J. K., Meirovitch, Y., Berger, D. R., Wu, Y., Liu, Y., Koh, W. X., Parvathala, R., Holmyard, D., Schalek, R. L., Shavit, N., Chisholm, A. D., Lichtman, J. W., Samuel, A. D. T. & Zhen, M. Connectomes across development reveal principles of brain maturation. *Nature* **596**, 257–261 (2021).
132. Wong, R. O. L. Retinal Waves and Visual System Development. *Annual Review of Neuroscience* **22**, 29–47 (1999).
133. Woo, N. H., Teng, H. K., Siao, C.-J., Chiaruttini, C., Pang, P. T., Milner, T. A., Hempstead, B. L. & Lu, B. Activation of p75NTR by proBDNF facilitates hippocampal long-term depression. *Nature Neuroscience* **8**, 1069–1077 (2005).

134. Wosniack, M. E., Kirchner, J. H., Chao, L.-Y., Zabouri, N., Lohmann, C. & Gjorgjieva, J. Adaptation of spontaneous activity in the developing visual cortex. *eLife* **10**, e61619 (2021).
135. Yang, J., Siao, C.-J., Nagappan, G., Marinic, T., Jing, D., McGrath, K., Chen, Z.-Y., Mark, W., Tessarollo, L., Lee, F. S., Lu, B. & Hempstead, B. L. Neuronal release of proBDNF. *Nature Neuroscience* **12**, 113–115 (2009).
136. Yap, E.-L. & Greenberg, M. E. Activity-Regulated Transcription: Bridging the Gap between Neural Activity and Behavior. *Neuron* **100**, 330–348 (2018).
137. Zheng, J.-J., Li, S.-J., Zhang, X.-D., Miao, W.-Y., Zhang, D., Yao, H. & Yu, X. Oxytocin mediates early experience-dependent cross-modal plasticity in the sensory cortices. *Nature Neuroscience* **17**, 391–399 (2014).

5 List of scientific communications

Peer-reviewed publications

1. Kirchner, J.H. & Gjorgjieva, J. Emergence of local and global synaptic organization on cortical dendrites. *Nature Communications* **12**, 4005 (2021).
2. Kirchner, J.H. & Gjorgjieva, J. Emergence of synaptic organization and computation in dendrites. *Neuroforum* **28**, 21–30 (2022).
3. Maldonado, P.P., Nuno-Perez, A., Kirchner, J.H., Hammock, E., Gjorgjieva, J. & Lohmann, C. Oxytocin Shapes Spontaneous Activity Patterns in the Developing Visual Cortex by Activating Somatostatin Interneurons. *Current Biology* **31**, 322–333.e5 (2021).
4. Wosniack, M.E., Kirchner, J.H., Chao, L.-Y., Zabouri, N., Lohmann, C. & Gjorgjieva, J. Adaptation of spontaneous activity in the developing visual cortex. *eLife* **10**, e61619 (2021).

Peer-reviewed poster presentations

1. Euler, L., Gjorgjieva, J. & Jan Hendrik Kirchner. Activity-dependent dendrite growth through formation and removal of synapses. *Poster presentation at Computational and Systems Neuroscience (Cosyne) conference, Lisbon, Portugal* (2022).
2. Jan Hendrik Kirchner & Gjorgjieva, J. Activity-dependent synaptic plasticity shapes dendritic synaptic inputs on developing cortical neurons. *Poster presentation at Computational and Systems Neuroscience (Cosyne) conference, Lisbon, Portugal* (2019).
3. Jan Hendrik Kirchner & Gjorgjieva, J. Dendritic plasticity rules in spontaneously active cortical neurons. *Poster presentation at Bernstein Conference, Berlin, Germany* (2018).
4. Jan Hendrik Kirchner, Paloma Maldonado, A.N.-P., Lohmann, C. & Gjorgjieva, J. Neuromodulatory control of spontaneous activity and circuit maturation in development. *Poster presentation at Computational and Systems Neuroscience (Cosyne) conference, online* (2021).

5 List of scientific communications

5. Liu, Z., Jan Hendrik Kirchner, Cheyne, J., Lohmann, C. & Gjorgjieva, J. Impact of single gene mutation on circuit structure and spontaneous activity in the developing cortex. *Poster presentation at Computational and Systems Neuroscience (Cosyne) conference, Lisbon, Portugal (2022)*.
6. Wosniack, M. E., Jan Hendrik Kirchner, Chao, L.-Y., Siegel, F., Lohmann, C. & Gjorgjieva, J. Spontaneous activity patterns in the developing mouse visual cortex in vivo guide retinotopic refinement of network connectivity. *Poster presentation at Computational and Systems Neuroscience (Cosyne) conference, Denver, CO, USA (2018)*.

Oral presentations

1. Jan Hendrik Kirchner & Gjorgjieva, J. Dendritic plasticity driven by spontaneous activity organizes synaptic inputs. *Invited talk at EITN workshop on synaptic plasticity, Paris, France (2020)*.
2. Jan Hendrik Kirchner & Gjorgjieva, J. Local and global organization of synaptic inputs on cortical dendrites. *Contributed talk at Neuromatch 1.0, online (2020)*.
3. Jan Hendrik Kirchner & Gjorgjieva, J. Local and global organization of synaptic inputs on cortical dendrites. *Workshop presentation and poster presentation at Computational and Systems Neuroscience (Cosyne) conference, Denver, CO, USA (2020)*.
4. Jan Hendrik Kirchner & Gjorgjieva, J. Origins and functional implications of dendritic synaptic clustering. *Workshop organizer and workshop presentation at Bernstein Conference 2019, Berlin, Germany (2019)*.
5. Wosniack, M.E., Jan Hendrik Kirchner, Maldonado, P., Zabouri, N., Lohmann, C. & Gjorgjieva, J. Spontaneous activity and multi-sensory integration in the developing higher-order cortex. *Contributed talk at Computational and Systems Neuroscience (Cosyne) conference, Denver, CO, USA (2020)*.

6 Acknowledgments

I thank my advisor, Prof. Dr. Gjorgjieva, for her invaluable help and mentorship through this project. I thank Prof. Dr. Lohmann and Prof. Dr. Kaschube for their work as my thesis advisory committee members and their helpful comments and suggestions. Finally, I want to thank my family, friends, and colleagues for their support in every step of my research.

7 Appendix

Emergence of local and global synaptic organization on cortical dendrites

Kirchner, J. H. & Gjorgjieva, J. Emergence of local and global synaptic organization on cortical dendrites. *Nature Communications* 12, 4005 (2021).

Emergence of synaptic organization and computation in dendrites

Kirchner, J. H. & Gjorgjieva, J. Emergence of synaptic organization and computation in dendrites. *Neuroforum* 28, 21–30 (2022).

Adaptation of spontaneous activity in the developing visual cortex

Wosniack, M. E., Kirchner, J. H., Chao, L.-Y., Zabouri, N., Lohmann, C. & Gjorgjieva, J. Adaptation of spontaneous activity in the developing visual cortex. *eLife* 10, e61619 (2021).

Oxytocin Shapes Spontaneous Activity Patterns in the Developing Visual Cortex by Activating Somatostatin Interneurons

Maldonado, P. P., Nuno-Perez, A., Kirchner, J. H., Hammock, E., Gjorgjieva, J. & Lohmann, C. Oxytocin Shapes Spontaneous Activity Patterns in the Developing Visual Cortex by Activating Somatostatin Interneurons. *Current Biology* 31, 322–333.e5 (2021).